AD

USAAMRDL TECHNICAL REPORT 71-20

DESIGN AND EXPERIMENTAL EVALUATION OF A HIGH-TEMPERATURE RADIAL TURBINE

By

Glenn S. Calvert
Stephen C. Beck
Ülo Okapuu

May 1971

EUSTIS DIRECTORATE
U. S. ARMY AIR MOBILITY RESEARCH AND DEVELOPMENT LABORATORY
FORT EUSTIS, VIRGINIA

Approved for public release;
distribution unlimited.

D D C
JUL 20 1971
C

DISCLAIMERS

DOCUMENT CONTROL DATA - R & D

(Security classification of title, body of abstract and indexing annotation must be entered when the overall report is classified)

1 ORIGINATING ACTIVITY (Corporate author)	2a. REPORT SECURITY CLASSIFICATION
Pratt and Whitney Aircraft	Unclassified
Florida Research and Development Center	2b. GROUP
West Palm Beach, Florida	

3 REPORT TITLE

Design and Experimental Evaluation of a High-Temperature Radial Turbine

4 DESCRIPTIVE NOTES (Type of report and inclusive dates)

Final Report - Phase II

5. AUTHOR(S) (First name, middle initial, last name)

Glenn S. Calvert
Stephen C. Beck
Ülo Okapuu

6. REPORT DATE	7a. TOTAL NO. OF PAGES	7b. NO. OF REFS
May 1971	224	4

8a. CONTRACT OR GRANT NO.	9a. ORIGINATOR'S REPORT NUMBER(S)
DAAJ02-68-C-0003	
b. PROJECT NO.	USAAMRDL Technical Report 71-20
Task 1G162203D1413	
c.	9b. OTHER REPORT NO(S) (Any other numbers that may be assigned this report)
d.	PWA FR-4058

10. DISTRIBUTION STATEMENT

Approved for public release; distribution unlimited.

11. SUPPLEMENTARY NOTES	12. SPONSORING MILITARY ACTIVITY
	Eustis Directorate
	U. S. Army Air Mobility R&D Laboratory
	Fort Eustis, Virginia 23604

13. ABSTRACT

This report describes the design, fabrication and test of a radial turbine designed to produce 219.6 Btu/lb stage work at 87.5% efficiency, with a 5:1 stage pressure ratio. Turbine inlet gas conditions at design point were 257.5 psia and 2300°F. The resulting turbine configuration consisted of an air-cooled, 12-bladed rotor designed for 67,000 rpm, and a 20-vaned air-cooled nozzle section of a reflex-type (supersonic) design. Both parts were designed as IN100 (PWA 658) investment castings.

As part of the preliminary design effort, a fabrication study was conducted to evaluate feasible methods of casting the turbine nozzle and rotor. Results showed that the nozzle section could be cast as an integral assembly, but fabrication of the rotor as an integral casting was much more difficult. Bicasting was evaluated as an alternate method of fabricating the rotor, and results showed substantial advantages for the bicasting technique. However, neither method could produce designed rotor properties, and testing was conducted with structurally limited rotors.

A test rig was designed and fabricated by the contractor. The test rig consisted of a supercharged gas generator, which had the capability of controlling the turbine load by varying the compressor flow rate.

Burner testing preceded turbine testing. Aviation gasoline was used to avoid carbon buildup, and a temperature distribution of ΔTVR = 1.14 was achieved with a modified PT6 engine flame tube.

Rotor structural limitations precluded turbine testing at engine design conditions. The maximum test value of turbine inlet temperature was 2045°F, and the maximum rpm was approximately 53,000. Measured performance at turbine inlet temperatures of 1000° to 1200°F showed that efficiency levels were within -0.8 to +2.3 efficiency points of the predicted values (87.5% efficiency, $\Delta H/\theta$ of 41.3 Btu/lb at design point). It was concluded that the aerodynamic performance of the cooled radial turbine substantiated its potential for application in advanced small gas turbine engines.

DD FORM **1473** REPLACES DD FORM 1473, 1 JAN 64, WHICH IS OBSOLETE FOR ARMY USE.

14. KEY WORDS	LINK A		LINK B		LINK C	
	ROLE	WT	ROLE	WT	ROLE	WT
Cooled Radial Turbine Design						
Cooled Radial Turbine Performance						
High Temperature						
High Pressure Ratio						
Fabrication Study, Bicasting						

5016-71

The research described herein was conducted by the
Florida Research and Development Center of Pratt and
Whitney Aircraft under the terms of Contract DAAJ02-
68-C-0003. The work was performed under the technical
management of Mr. Edward T. Johnson, Propulsion Division,
Eustis Directorate, US Army Air Mobility Research and
Development Laboratory.

The object of this research effort was to design,
fabricate, and experimentally test a radial turbine
capable of driving an 18:1 pressure ratio compressor
while operating at 2300°F turbine inlet temperature
with an efficiency of 87.5%. Included in this report
is the final design of the rotor and nozzle (developed
from the Phase I effort reported in USAAVLABS Report
No. 68-69); the fabrication development of the rotor;
the testing of the combustor and fuel control system;
and cold and hot gas testing of the rotor.

Appropriate technical personnel of this Directorate
have reviewed this report and concur with the conclu-
sions contained herein.

The findings and recommendations outlined herein will
be taken into consideration in the planning of future
radial turbine programs.

Task 1G162203D14413
Contract DAAJ02-68-C-0003
USAAMRDL Technical Report 71-20
May 1971

DESIGN AND EXPERIMENTAL EVALUATION OF A HIGH-TEMPERATURE
RADIAL TURBINE

Phase II

Final Report

.

By

Glenn S. Calvert
Stephen C. Beck
Ülo Okapuu

Prepared by

Pratt & Whitney Aircraft
Florida Research and Development Center
West Palm Beach, Florida

for

EUSTIS DIRECTORATE
U. S. ARMY AIR MOBILITY RESEARCH AND DEVELOPMENT LABORATORY
FORT EUSTIS, VIRGINIA

ABSTRACT

Tnis report describes the design, fabrication and test of a radial turbine designed to produce 219.6 Btu/lb stage work at 87.5% efficiency, with a 5:1 stage pressure ratio. Turbine inlet gas conditions at design point were 257.5 psia and 2300°F. The resulting turbine configuration consisted of an air-cooled, 12-bladed rotor designed for 67,000 rpm, and a 20-vaned air-cooled nozzle section of a reflex-type (supersonic) design. Both parts were designed as IN100 (PWA 658) investment castings.

As part of the preliminary design effort, a fabrication study was conducted to evaluate feasible methods of casting the turbine nozzle and rotor. Results showed that the nozzle section could be cast as an integral assembly, but fabrication of the rotor as an integral casting was much more difficult. Bicasting was evaluated as an alternate method of fabricating the rotor, and results showed substantial advantages for the bicasting technique. However, neither method could produce designed rotor properties, and testing was conducted with structurally limited rotors.

A test rig was designed and fabricated by the contractor. The test rig consisted of a supercharged gas generator, which had the capability of controlling the turbine load by varying the compressor flow rate.

Burner testing preceded turbine testing. Aviation gasoline was used to avoid carbon buildup, and a temperature distribution of ΔTVR = 1.14 was achieved with a modified PT6 engine flame tube.

Rotor structural limitations precluded turbine testing at engine design conditions. The maximum test value of turbine inlet temperature was 2045°F, and the maximum rpm was approximately 53,000. Measured performance at turbine inlet temperatures of 1000° to 1200°F showed that efficiency levels were within -0.8 to +2.3 efficiency points of the predicted values (87.5% efficiency, ΔH/θ of 41.3 Btu/lb at design point). It was concluded that the aerodynamic performance of the cooled radial turbine substantiated its potential for application in advanced small gas turbine engines.

FOREWORD

The work described in this report was accomplished for the Eustis Directorate, U. S. Army Air Mobility Research and Development Laboratory, under Contract DAAJ02-68-C-0003, Task 1G162203D14413, during the period 18 July 1967 to 31 August 1970. The program was divided into two phases: (1) preliminary design of a high-temperature radial turbine; and (2) final design, fabrication and test of the turbine. The work completed under Phase I was reported by USAAVLABS Technical Report 68-69 (DDC No. AD-688164) dated January 1969. This report covers the work completed under Phase II and summarizes pertinent information from Phase I.

This program was conducted by three elements of the United Aircraft Corporation: the Forida Research and Development Center of Pratt & Whitney Aircraft (FRDC); the Connecticut Operations of Pratt & Whitney Aircraft; and United Aircraft of Canada, Ltd. (UACL). FRDC was the prime contractor for the program, and both UACL and Connecticut Operations had major contributing roles.

Mr. Edward T. Johnson of the Eustis Directorate was the contract technical monitor.

v

TABLE OF CONTENTS

TABLE OF CONTENTS (Concluded)

LIST OF ILLUSTRATIONS

LIST OF ILLUSTRATIONS (Continued)

LIST OF ILLUSTRATIONS (Continued)

LIST OF ILLUSTRATIONS (Continued)

LIST OF ILLUSTRATIONS (Continued)

LIST OF ILLUSTRATIONS (Continued)

LIST OF ILLUSTRATIONS (Concluded)

LIST OF TABLES

LIST OF SYMBOLS

Symbol		Units
BHPCR	Measured turbine power corrected for parasitic losses	hp
Co'	Ideal spouting velocity	ft/sec
Corrected $N/\sqrt{\theta}$	Speed parameter corrected for gamma effects	
Corrected PR_{T-T}	Total-to-total pressure ratio corrected for gamma effects	
HP (parasitic)	Horsepower consumed by bearings, windage, and cooling air pumping in the rotor	hp
M	Mach No.	
M_R	Relative Mach No.	
N	Speed	rpm
N_S	Specific speed $= \dfrac{N\sqrt{Q_{exit}}}{(\Delta H')3/4}$	
P_{inlet}	Vane inlet total pressure	psia
PR	Pressure ratio	
PR_{T-T}	Total-to-total pressure ratio	
PS5	Static pressure at Station 5	psia
PT5	Total pressure at Station 5	psia
P3A	Static pressure in cavity behind compressor	psia
P4A	Static pressure in cavity behind turbine	psia
Q_{exit}	Volume flow rate at turbine exit	cfs
RIT	Rotor inlet stagnation temperature	°R
T_{avg}	Average temperature at combustor discharge	°R

Symbol		Units
T_{exit}	Mixed temperature at rotor exit (exhaust orifice temperature corrected for heat loss in exhaust pipe)	°R
T_{in}	Combustor inlet temperature	°R
TIT	Turbine (vane) inlet stagnation temperature	°R
T_{max}	Maximum local temperature in any circumferential location	°R
TT4	Total temperature at Station 4	°R
U	Rotor tip speed	ft/sec
W	Same as W_{tcr}	lb/sec
W_{bl}	Bleed air flow rate	lb/sec
W_{bp}	Backplate cooling air flow rate	lb/sec
W_{burn}	Burner airflow	lb/sec
W_c	Compressor inlet air flow rate	lb/sec
W_{inlet}	Vane inlet flow rate	lb/sec
W_r	Rotor cooling air flow rate	lb/sec
W_{sh}	Shroud cooling air flow rate	lb/sec
W_t	Turbine exhaust flow rate	lb/sec
W_{tcr}	Turbine rotor inlet flow rate	lb/sec
$\alpha 5(av)$	Area averaged exit gas angle at rotor discharge. Positive value indicates same rotation as rotor; negative value indicates opposite rotation	deg
γ	Ratio of specific heats, C_p/C_v	

LIST OF SYMBOLS (Continued)

Symbol		Units
ΔH	Actual enthalpy drop across turbine based on measured turbine work	Btu/lb
ΔH_c	Total enthalpy rise across compressor based on measured temperatures at compressor inlet and discharge stations	ft-lb/lb
$\Delta H'$	Isentropic enthalpy drop = $C_p \times TT4 \left[1 - \left(\dfrac{PT5}{PT4}\right)^{\frac{\gamma-1}{\gamma}} \right]$ (total-to-total)	ft-lb/lb
$\Delta M/M$	Nondimensional distance	
ΔTVR	Delta temperature variation ratio, $\dfrac{T_{max} - T_{in}}{T_{avg} - T_{in}}$	
δ	Normalized turbine inlet pressure = PT4/ standard atmosphere pressure (14.7)	
η_B	Combustion efficiency	pct
Corrected η_{T-T}	Total-to-total turbine efficiency corrected for clearance effects	pct
Predicted η_{T-T}	Design predicted total-to-total turbine efficiency	pct
η_{T-T}	Total-to-total turbine efficiency	pct
θ	Normalized rotor inlet temperature, $\dfrac{RIT}{518.69}$	
ϕ	Cooling effectiveness, $TT4-T_{metal}/TT4-T_{cooling\ air}$	

LIST OF SYMBOLS (Concluded)

RIG STATION DESIGNATIONS

1	Rig inlet
2	Compressor inlet
3	Burner inlet
3a	Cavity behind compressor rear face
4	Burner discharge
4a	Cavity behind turbine rear face
5	Turbine discharge

INTRODUCTION

Radial turbines can offer greater stage-work capacity than axial turbines and at higher efficiencies. If this advantage can be coupled with a capability to accommodate high turbine inlet temperatures, radial turbines will permit appreciable simplification of small gas turbine engines for use in future Army vehicles. The objective of this program was to develop the technology for high-temperature radial turbines to a level that would permit a potential small-engine manufacturer to make a choice between the radial and axial turbine.

A 2-year, two-phase program was conducted involving the design and testing of a cooled, single-stage, radial-inflow turbine with the following design conditions: turbine inlet temperature of 2300°F, total-to-total aerodynamic efficiency of 87.5%; gas flow of approximately 5 lb/sec; and stage work parameter ($\Delta H/\theta$) of 41.3 Btu/lb.

The objective of the first phase was to evolve, through iterative aerodynamic-structural-heat transfer analyses, a preliminary turbine design to meet performance objectives. The first phase included cold-flow turbine tests to verify the selected numbers of nozzle vanes and rotor blades, water-flow tests to help in assessing the effect of cooling air ejection at the rotor leading edge, and a fabrication study to establish the existing state of the art for casting radial turbines and to uncover any potential fabrication problem areas. A detailed account of the Phase I effort was published in USAAVLABS Technical Report 68-69 (January 1969); pertinent information from that phase is summarized in this report.

In the second phase, the turbine design was finalized and fabrication of the turbine hardware was completed. Burner testing and modification were conducted to establish a suitable exit temperature profile. A casting development program was added to Phase II when the trial rotors of the Phase I fabrication study did not meet the required specifications. Cold flow turbine tests were conducted to determine the operating characteristics of the rig, and the cooled radial turbine was hot tested under various conditions to measure the performance level.

PHASE II, TASK 1 - DETAIL DESIGN OF HOT TURBINE

TASK SUMMARY

The objective of this task was to finalize the Phase I preliminary design for the turbine nozzle, rotor, backplate, and shroud. Included in this task were stress analyses, heat transfer analyses, aerodynamic analyses (where applicable), and the preparation of detailed manufacturing drawings. The details of the design procedures were presented in the Phase I report.

The Phase II final geometries for the parts designed in this task were essentially the same as the Phase I final geometries. The Phase II predicted stress and metal temperatures were slightly different from those published in Phase I, but the basic stress and thermal patterns were not changed.

The structural design goal for the nozzle, shroud and backplate was a 300-hr stress-rupture life. Conventional elastic stress analyses were used to design these parts. In the case of the turbine nozzle, the 200-hr stress-rupture life was not indicated by the elastic analysis (which did not account for stress relaxation due to plastic redistribution of the material), and a plastic stress analysis was required to show that the nozzle design met the original goal. The turbine rotor stress analysis was accomplished with a UACL finite element technique (described in a later paragraph) with design criteria of 1% creep in 100 hr and burst at 130% design speed.

GENERAL DESIGN CONCEPTS

The radial turbine was designed as the gas generator turbine for a hypothetical twin-spool turboshaft engine in the 5 lb/sec airflow class. The basic engine cycle had an overall pressure ratio of 18:1 and a turbine inlet temperature of 2300°F. Table I shows the other basic design assumptions for the engine and the gas generator radial turbine.

Figure 1 shows the mean line design parameters for the radial turbine. Since the direction of rotation of the axial power turbine in the assumed engine was not specified, the exit swirl from the gas generator turbine was chosen to be zero. The absolute exit Mach No. was chosen to be 0.43, and the rotor hub radius at exit was set at 1.0 in. Due to the hostile thermal environment, the aerodynamic design of the turbine was intentionally compromised to relieve the high stress levels in the rotor. For example, it was recognized that the choice of +6.5 deg incidence (to minimize rotor blade length) would cost several points in design point efficiency. The number of rotor blades was similarly below optimum, to reduce hub stresses and cooling air requirements.

2

TABLE I. HYPOTHETICAL ENGINE DESIGN PARAMETERS
(SEA LEVEL, STATIC)

ASSUMED ENGINE

Pressure Ratio	18:1
Compressor	1 AX + 1 CENT
Centrifugal PR	10:1
Centrifugal Ns	80
Overall Efficiency	81%
Gas Generator Turbine	1 Radial
Power Turbine (Free Shaft, Front Drive)	1 Axial

GAS GENERATOR TURBINE

Inlet Pressure	257.5 psia
Inlet Temperature	2300°F
Inlet Flow Rate	4.90 lb/sec
Rotational Speed	67,000 rev/min
Enthalpy Drop	219.6 Btu/lb
Target Efficiency (Total)	0.875
Total Pressure Ratio	5.165

As shown in Figure 2, the basic components of the turbine were the rotor, the backplate assembly, the nozzle, and the shroud assembly. The downstream duct with its struts and centerbody was a test rig part, and did not simulate any specific engine configuration. The rotor (A) was a single-piece casting that was overhung from the gas generator shaft (to the left in the figure). The backplate assembly, which consisted of the lower backplate (B), upper backplate (C), and air cover (D), was bolted to the bearing housing. The backplate was designed in two concentric parts to permit unrestricted radial growth, thus reducing thermal stresses. The radial nozzle (E), also bolted to the bearing housing, was an integral casting with 20 hollow vanes. The stationary shroud ring (F) was held concentric with the nozzle by means of radial dogs and slots.

Stresses in the shroud ring were relieved by the pressure balance piston (G).
An air cover (H), which channelled the shroud cooling air, completed the shroud
assembly. The shroud ring and the upper backplate formed face seals with the
nozzle casting, the sealing force being maintained by the large pressure
difference between the cooling air and the hot primary gas stream.

NOZZLE FINAL DESIGN

The final nozzle design was an integral casting of IN100 (PWA 658), having 20
hollow vanes with cooling inserts and two platform heat shields as shown in
Figure 3. The airfoil and insert geometries are defined in Figure 4.

Referring to Figure 3, the nozzle was cooled by two separate streams of cooling
air which, after having cooled the backplate and shroud, converged in the nozzle
vanes and were ejected into the primary gas stream ahead of the rotor. Back-
plate cooling air amounting to 3% of primary flow, at 850°F and 257.5 psia, was
progressively admitted into the space formed by the backplate and its air cover.
In this area it passed through a number of channels machined into the surface
of the upper backplate, then through holes in the nozzle support cylinder, and
finally into the nozzle insert at an estimated temperature of 1080°F and 250 psia.
Shroud cooling air, also 3%, was similarly admitted into the space between the
shroud ring and its air cover, passed through a number of channels machined
into the shroud at its outer radius, and flowed into the nozzle inserts at the
same nominal pressure as the backplate coolant. To allow for small pressure
differences between the two vane coolant supplies, a dividing wall was placed
at the insert midspan. The backplate and shroud cooling streams merged
inside the vanes, combined to cool the vanes, and then were ejected together
through slits in the vanes into the mainstream. The quantity of air required
to cool these stationary components was therefore 6% of the primary flow at
the nozzle leading edge. This air was ejected upstream of the rotor and was
not completely lost to the gas generator cycle.

The following paragraphs present more detailed information on the aerodynamic,
heat transfer, and structural analyses for the nozzle.

Nozzle Aerodynamic Design

The Phase II final nozzle design used 20 airfoils of the reflex type. In this type
of vane, shown schematically in Figure 5, the suction surface downstream of
the throat is a streamline in a compressible, adiabatic, free vortex flow field,
with sidewall and vane friction effects included. At the leading edge, the
incidence calculated by potential flow analysis was zero. All aerodynamic
parameters for the nozzle design were calculated by potential flow analyses,
results of which are presented in Figure 6, 7, and 8.

4

The original selection of 20 nozzle vanes was verified during the Phase I cold-flow tests, which showed that 20 vanes were slightly more efficient than either 15 or 25 vanes of similar design at a stage pressure ratio of about 5:1.

Nozzle Heat Transfer Design

The nozzle, due to its small size, presented a formidable design challenge. The internal cooling passage configuration producing a satisfactory vane metal temperature distribution was one of considerable complexity (Figure 9). Cooling air from the shroud and backplate emerged from the insert, impinged onto the vane, and was split into two parts. One part, amounting to 2% of the primary stream, was ejected onto the suction surface of the vane, where it formed a cooling film. The remaining 4% passed over internal fins and was ejected onto the pressure surface of the vane in an accelerating region of the nozzle channel.

The platform heat shields (Figure 3) represented an interesting design solution to the problem of excessive radial thermal gradients in the platforms. The problem existed because combustor liner cooling air was expected to persist as a film into the nozzle channels, where it progressively mixed with the primary stream and increased in temperature in the downstream direction. This was predicted to cause a radial temperature gradient in the platforms (cooler at OD) which would produce excessive hoop stresses. The introduction of additional cooling air midway through the nozzle channel, which was one possible way of reducing this radial thermal gradient, would have lowered the average temperature in the platforms to the point where the temperature difference between platforms and vanes would have caused excessive shear stresses at their junction. The heat shields, which extended part way into the nozzle channels, reduced the radial thermal gradient by preventing overcooling of the outer portions of the platforms; and at the same time,they reduced the temperature difference between platforms and vanes.

Calculated gas side heat transfer coefficients for the vanes are presented in Figure 10, and coefficients for the internal cooling passage are presented in Figure 11. The assumed spanwise gas temperature profile at the vane inlet is shown in Figure 12.

Final predicted metal temperatures for the vane and platform are presented in Figures 13 and 14, respectively. For a "hot spot" having a peak temperature of 2600°F, vane metal temperatures would increase by approximately 100°F above those shown. These temperature levels were not expected to cause any endurance problems during the test program.

5

Nozzle Structural Design

An elastic stress analysis of the radial turbine nozzle was carried out. Results presented in Figure 15 indicate that the elastic behavior did not satisfy the 300-hr stress-rupture goal at the vane trailing edge and at the inner portions of the platform. [Mechanical properties for the vane material, IN100 (PWA 658), are presented in Figures 16 and 17.] Two additional analyses were carried out for the vane trailing edge, which was the more severe of the two structural problems. The first of these was a more refined elastic analysis that used a finer nodal breakdown and considered the effects of thermal radiation (which reduced the thermal gradient in the axial direction). Results showed a reduction in the calculated elastic stress from about 50,000 psi to about 43,300 psi. The second analysis was a stress relaxation study, or plastic stress analysis, which accounted for the effects of local stress relief through creep. For conservatism, the previously calculated stress level of 50,000 psi was assumed to exist 36 sec after the application of load. Results of this study presented in Figure 18 showed that initial stresses were quickly relieved and that the design would meet the 300-hr goal. For instance, after 20 hr of steady-state operation at 100% power, the predicted stress in the vane trailing edge has dropped to 20,000 psi, and the time required for stress-rupture at this level would be about 450 hr. Figure 18 gives conservative life estimates when applied to cyclic operation. If it is assumed that a mission consisted of 2 hr operation at 100% power, the predicted life remaining after ten missions (20 hr total operation) would be greater than 450 hr. A more realistic life study would indicate considerably longer life, since only about 15% of the engine operating time would be spent at 100% power.

Predicted deflections at design conditions for selected locations on the nozzle are shown in Figure 19.

ROTOR FINAL DESIGN

The Phase II final rotor design was an IN100 (PWA 658) casting having 12 hollow blades cooled by 3% cooling air flow, most of which made a double pass through the blades. Figures 20 and 21 define the rotor geometry.

The final number of rotor blades (12) was selected on the basis of a Phase I trade-off study that considered the effect on the hypothetical cycle of using 10-, 12-, and 14-blade rotor designs. Phase I aerodynamic tests of 10-, 12-, and 14-blade rotors showed a 0.4% efficiency penalty for the 12-blade rotor compared to the 14-blade design, and a 0.9% efficiency advantage for the 12-blade rotor over the 10-blade design. For the hypothetical engine cycle, the 12-blade rotor gave a calculated SFC of 0.4213 lb/hp-hr compared to 0.4210 lb/hp-hr for the cycle using the 14-blade rotor. This small SFC penalty was acceptable in return for the lower rotor stresses and reduced cooling air requirements of the 12-blade design.

6

The two-pass blade cooling design was selected over a simpler, single-pass design for both heat transfer and aerodynamic reasons. The single-pass configuration studied consisted of a cooling passage that carried the coolant from the hub to the blade tips, where it was ejected radially outward. Calculated metal temperatures for the two-pass configuration were significantly lower than the single-pass design with the same cooling air flow. Aerodynamically, the single-pass design was less desirable because the Phase I water tests showed that tip ejection of the coolant tended to aggravate flow separation at the blade tips.

The following paragraphs, in conjunction with the Phase I report, describe the aerodynamic, heat transfer, and stress analyses of the rotor.

Rotor Aerodynamic Design

One of the reasons that a single-pass cooling design was rejected in favor of a two-pass design was to eliminate the anticipated aerodynamic penalty resulting from exhausting the coolant at the blade tips. A second reason for selecting the two-pass design was the aerodynamic advantage of this configuration. By virtue of its large pressure drop, the high-work radial turbine has a large pressure differential available between the rotor cooling air and the primary gas stream almost anywhere on the rotor. The resulting high ejection velocity can be used for boundary layer control in regions of local mainstream diffusion. In the rotor design, such a region existed on the suction surface of the exducer, over the outer portion of the blade, and the rotor cooling air exhaust was located in this area. There are no quantitative data available to indicate the magnitude of performance improvement that might be expected.

The rotor velocity distribution is defined by Figures 22, 23, and 24. These figures show the predicted relative velocities along a blade in three spanwise locations: along the shroud, at the mean span, and along the hub. The velocities shown were calculated by a potential flow analysis and were used to predict aerodynamic blade loading.

Rotor Heat Transfer Design

In the two-pass cooling configuration shown in Figure 2, cooling air (3%) was introduced into the rotor hub at its downstream face and was guided into the blade cavities through 12 holes. Each blade contained an internal two-pass cooling passage in which the coolant was first guided toward the blade tip, flowing along the back face of the blade. At the tip, some of the cooling air (0.5% total) was bled into the mainstream. The remainder flowed along the shroud side of the blade and was finally ejected at high velocity onto the suction surface of the blade through a part-span slot. This cooling design satisfied two requirements: (1) some cooling was provided at the outer corners of the cooling passage, which otherwise tend to produce stagnant areas where metal temperatures could become excessive, and (2) additional cooling air was provided along the back side of the blade, where the heat input was greater,

7

without requiring any redesign of the shroud-side cooling passage, which was choked at 2.5% cooling air flow.

For cooling air entry location, the downstream face of the rotor was chosen in preference to the flange face to keep the rotating sen. diameter, and therefore, seal leakage, to a low value. This location for the cooling air inlet was adopted to expedite rig testing. In a front-drive engine application, the seal might be located behind the rotor; this would provide a more compact coolant supply system and it would provide for the passage of a free turbine shaft.

Rotor heat transfer analysis was complicated by the anticipated flow separation at the blade leading edge (as observed during the water tests) and the incompletely understood leakage flow pattern between the rotor blades and the backplate. For heat transfer calculations, the potential flow streamlines (presented in Figures 22, 23, and 24) were modified in the star portion of the rotor as shown by the dotted lines in Figures 25, 26, and 27. The modified velocity distributions were estimated from the Phase I water visualization tests. The flow patterns observed in the water tests differ from those predicted by potential flow analysis in that a suction side separation bubble was observed in the water testing and the inlet stagnation streamline was located at the blade tip instead of somewhere downstream of the tip on the pressure side, as predicted by the potential flow calculation. The separated region was believed to be a local phenomenon that would have a more significant effect on the heat transfer coefficients than on the blade loading, and it was therefore considered only for thermal analysis.

In the rotor blade/backplate leakage region, gas side heat transfer coefficients were calculated by considering several possible flow patterns and choosing a coefficient that erred on the conservative side of the average. The mainstream heat transfer coefficients were calculated on the assumption that turbulent flow existed throughout, which should also lead to a conservative design.

Figure 28 shows the predicted gas side static pressure distribution within the rotor, and Figures 29, 30, and 31 show the calculated gas side relative temperatures and heat transfer coefficients along the rotor hub, mean line, and shroud. Heat transfer coefficients for the internal cooling passages were calculated by standard turbulent pipe flow methods as:

$$h = 0.023 \frac{k}{D_H} (R_e)^{.8} (P_R)^{.4}$$

where h = heat transfer coefficient

k = thermal conductivity of the fluid

D_H = hydraulic dia

R_e = Reynolds No.

P_R = Prandtl No.

The resulting coefficients are shown in Figure 32.

The rotor analysis used the calculated heat transfer coefficients in a matrix of 250 internal nodes and 200 external nodes per blade segment, and the resulting metal temperatures are shown in Figure 33. In the cooled portion of the blades, the calculated metal temperatures were about 300 deg lower than the local relative gas temperatures.

Rotor Structural Design

The material specified for the final rotor design was IN100 (PWA 658), which was previously selected in the Phase I preliminary design. Mechanical properties used to determine allowable stresses in the rotor were previously presented in Figures 16 and 17. Rotor design criteria were defined as 30% burst margin and 1% creep in 100 hr.

Stress analysis of the rotor was accomplished with a UACL technique that is initiated by calculating the thickness distributions of two random blade sections, shown in Figure 34 as sections A and B. Each of the two reference sections is first designed as an independent strip element. The radial variation of metal temperature and the corresponding allowable stress criteria for the strip are known from heat transfer analyses and material property data. The tip of the element must have a certain minimum taper angle for manufacturing reasons. This taper angle is continued radially inward (Figure 35) until the allowable stress is reached. In the design of the rotor, the allowable stress in the hub at design conditions was defined as the ultimate tensile strength (UTS) divided by 1.3^2 (corresponding to 130% of design speed); in the blades, the allowable stress was defined as the lower value of either (1) ultimate tensile strength divided by 1.3^2, or (2) the stress that gives 1% creep in 100 hr. At lower metal temperatures, the ultimate tensile strength determines the allowable stress; and at higher metal temperatures (above 1400°F), the 1% creep stress criterion dominates.

The radial location where the allowable stress first occurs is defined as the transition point between the tip portion of the element and the hub portion, which has a thickness distribution that keeps the blade stress always within the maximum allowable. The thickness distribution below the transition point is described by a polynomial of the form

$$T = a + b \cdot z + c \cdot z^2 + d \cdot z^3 \tag{1}$$

The transition points of the two reference sections can be joined by any arbitrary curve (Figure 36) that describes the locus of transition points of all interpolated and extrapolated sections. In the structural design of the turbine rotor, a parabola was used to join the transition points of the radial sections. Each interpolated (and extrapolated) section has its thickness distribution below the transition point described by a polynomial which has coefficients obtained by linear interpolation between (or extrapolation from) coefficients of the reference sections. For instance, in Figure 36, the thickness T at the transition point of section C is

$$T_C = a_C + b_C z + c_C z^2 + d_C z^3 \qquad (2)$$

where the coefficients a_C, b_C, c_C, etc., are obtained by linear interpolation of the similar coefficients in sections A and B as

$$a_C = \frac{(C-B)}{(A-B)} a_A + \frac{(A-C)}{(A-B)} a_B \qquad (3)$$

The rotor blade design procedure thus consists of (1) choosing the reference planes A and B, (2) choosing the shape of the transition-point locus curve, (3) calculating the complete blade thickness distribution, and then (4) carrying out a complete two-dimensional stress analysis. Depending on the results of this analysis, either the reference plane location or the locus of transition points is modified and the process is repeated until the blade stress distribution is satisfactory.

Results from the final rotor stress analysis are presented in Figure 37, which defines the blade thickness distribution, and in Figures 38 and 39, which show stresses and stress ratios (effective stress/UTS) predicted for the rotor at design point. To check for design margin, the same parameters were calculated for a 30% overspeed condition (87,000 rpm) with design point metal temperature distribution. Results are presented in Figures 40 and 41. In Figure 40, the peak stress in the bore has increased only about 5% as a result of an (rpm^2) increase of 69%; this is due to plastic redistribution of material in the hub. The critical location in the rotor appears to be on the back face of the blades, just above the hub. At the 30% overspeed condition, the stresses at this point are approaching the ultimate tensile strength, and failure in this area was predicted at approximately 88,150 rpm.

Calculated radial growths and axial deflections for the rotor at design point are presented in Figure 42.

10

SHROUD FINAL DESIGN

The Phase II final shroud design was a one-piece machined IN100 casting with a cross-sectional profile as shown in Figure 43. Three hundred fins of 0.030-in. height were machined on the cold side of the ring, from R = 3.26 in. to R = 3.93 in. The slots between the fins had a constant width of 0.030 in., and these provided uniformly high convective heat transfer coefficients in the high temperature area. The shroud was positioned against the nozzle at its outer radius, and the higher pressure on the cold side of the shroud provided the sealing force. At its inner radius, the shroud was supported by a piston arrangement that also preloaded the shroud, which reduced the stress levels in the shroud during operation.

Shroud Heat Transfer Design

The shroud was designed to be convectively cooled by 3% airflow at 257.5 psia and 850°F. In the hypothetical engine cycle, this was equivalent to compressor discharge conditions with some pressure loss for the transfer system. Cooling air was guided over the cold (concave) side of the shroud by a contoured sheet metal cover plate. After cooling the shroud, the air entered the nozzle cooling system at a predicted temperature of 1080°F. Calculated metal temperatures for the hot face, midthickness, and cold face at design point conditions are presented in Figure 44.

Shroud Structural Design

Results from the final elastic stress analysis of the shroud are presented in Figure 45. The maximum stresses shown were lower than the 300-hr stress rupture strength of the material, which was the original design goal. (Stress rupture properties are shown for predicted hot-face temperatures, since these yield the most conservative allowable stresses.) The lower curve in Figure 45 shows that temperature gradients in the shroud generally account for half or more of the total predicted stresses.

BACKPLATE FINAL DESIGN

The Phase II final design for the backplate and its supporting structure is defined in Figure 46. In this design, the backplate was segmented into two concentric rings to allow unrestrained radial growth in each part. Sealing at the inter-segment face and at the nozzle backplate face was maintained by the pressure differential between the cold (high pressure) and the hot side. Both backplate parts were machined IN100 castings; the supporting structure was Inconel X.

11

Backplate Heat Transfer Design

The backplate heat transfer design was similar to that for the shroud; cooling was achieved by convection, using 3% cooling airflow at 257.5 psia and 850°F. Cooling air was guided over the cold side of the backplate assembly by a sheet metal cover. At the larger diameters, the coolant flow rate was increased to meet the higher gas-side temperatures. After cooling the backplate, the cooling air entered the nozzle cooling system at a predicted temperature of 1040°F.

Two hundred sixteen fins were machined on the cold side of the upper backplate, with constant-area slots 0.055-in. wide by 0.027-in. deep between fins. These provided closely controlled gaps that maintained uniformly high convective heat transfer coefficients in the high temperature areas.

Calculated design-point metal temperatures for the backplate assembly are shown in Figure 47 for the radial direction and in Figure 48 for the axial direction. As shown in Figure 47, a temperature peak occurs on the upper backplate hot face at a radius of approximately 4 in. This is caused by the main gas stream coming into contact with the upper backplate at a radius slightly higher than 4 in. At that point, no work has been taken out of the main gas stream, and the metal is subjected to rotor inlet gas temperatures. At a radius of about 3.9 in., the gas enters the rotor, work is removed from the gas, and the upper backplate is exposed to decreasing gas temperatures at decreasing radii. The same figure shows a minimum cold face temperature occurring at nearly the same radius. This is primarily the result of injecting part of the 3% cooling flow at a 3.7-in. radius. (See Figure 46.)

Backplate Structural Design

Results from the final elastic stress analysis of the backplate structures are presented in Figures 49 and 50, which show calculated stresses in the radial and axial directions, respectively. Figure 49 shows the calculated stress resulting from both thermal gradients and pressure loads. In the case of the lower backplate, the maximum stresses (without regard to location) were lower than the allowable stress for 300-hr stress rupture based on the predicted hot side temperatures, and the structural design goal was satisfied. In the case of the upper backplate, the calculated cold side and hot side stresses were lower than their respective allowable stresses, and the design goals were satisfied by this design. The lower curve on Figure 49 (stresses due solely to pressure loads) shows that the predicted thermal gradients were the major contributors to the resultant stresses in the upper backplate. Figure 50 shows that the calculated axial stresses in the lower backplate and its support were well below the maximum allowable for 300-hr life.

12

TURBINE STAGE PERFORMANCE PREDICTIONS

The Phase II performance analyses were directed primarily toward refining the off-design performance predictions for the turbine. This work was accomplished by UACL with a semiempirical technique that was developed under an earlier radial turbine program. Results are presented in Figures 51 through 58. Figure 51 compares the Phase II predicted performance with the Phase I predictions. Although design point efficiency (87.5%) was not changed, there were some differences in the predicted efficiency at off-design velocity ratios. At velocity ratios higher than design point, the Phase II predictions showed higher efficiencies than the Phase I predictions, and vice versa at lower-than-design velocity ratios. The performance predicted during Phase I (preliminary design) was assumed to be the same as a similar design previously tested at UACL. The Phase II (detail design) performance was calculated by applying nozzle and rotor loss correlations to this turbine design.

As shown in Figure 52, turbine efficiencies higher than 87.5% were predicted for pressure ratios lower than the 5.1:1 design value, or at normalized speeds higher than design. These trends were caused by a nonoptimum (positive) design point incidence at the leading edge, which was the result of reducing the rotor tip diameter. This compromise was desirable to reduce rotor stresses to an acceptable level. If the turbine had been designed for a less hostile environment, the design point would lie closer to the peak efficiency point.

Figure 53 shows the predicted nozzle flow characteristics as a function of stage total pressure ratio. The normalized flow is shown to increase with pressure ratio until a choked condition is reached. The turbine design point lies within the choked regime.

Figure 54 presents the predicted turbine efficiency as a function of velocity ratio and stage pressure ratio. The turbine design point, at a velocity ratio of 0.65, lies below the best efficiency point, which was predicted to occur at a velocity ratio of approximately 0.8. As previously discussed, this was the result of compromising the aerodynamic performance to reduce rotor stresses to a manageable level.

Figure 55 presents the predicted exit swirl angles as a function of stage total pressure ratio and corrected speed, and shows that the turbine was designed for zero exit swirl at the design point. For a turbine that has been stress-limited to velocity ratios below optimum (such as the present design), some increase in rotor efficiency might result from designing for a modest counter swirl at the exit (i.e., opposite to turbine rotation), which would reduce the rotor aerodynamic loading. However, zero exit swirl was selected to demonstrate performance under the most severe conditions that would be expected in an engine design, and to avoid any implication that the performance was dependent upon a specially favorable exhaust system.

Figure 56 shows the normalized enthalpy drop as a function of pressure ratio and corrected speed. This curve was compiled from the efficiency predictions in Figure 52 and the isentropic enthalpy available to the stage. The constant $N/\sqrt{\theta}$ trends are characteristic of radial turbines. Likewise, the normalized torque curves presented in Figure 57 have been derived from the predicted work per pound of air (Figure 56) and the predicted flow characteristics (Figure 53). The torque trends shown are typical of radial turbines.

Figure 58 presents a universal performance map which has been compiled from the performance characteristics of Figures 52 through 57. This map indicates that the maximum efficiency "island" (92%) is not yet closed, and the peak efficiency may occur at a pressure ratio higher than 6.

PHASE II, TASK 2 -
CASTING DEVELOPMENT AND FABRICATION OF HOT TURBINE

TASK SUMMARY

This task consisted of effort in two categories:

1. Development of rotor casting techniques

2. Fabrication of hot test hardware

The casting development program was added to this task after the Phase I Fabrication Study showed low material properties in experimental rotors cast by conventional investment techniques. Two types of rotors were evaluated in the development program: (1) bicast rotors and (2) integrally cast rotors similar to those made in Phase I except in the final design configuration. Experimental evaluation included both metallographic inspection and destructive spin testing.

Results from this task showed advantages for both the bicast and integral cast techniques, but neither process could produce a rotor to meet all design specifications. All rotors tested in Task 3 were made by the bicasting process.

BACKGROUND

During Phase I of the program, three investment casting vendors experimented with trial rotors in an effort to define the fabrication problems that would be experienced later. The trial rotors were integral castings of IN100 (PWA 658), the material selected for the rotor design. Most of the samples were 11-in.-diameter rotors with 0.020-in.-thick blade walls at the leading edge. (A typical sample rotor is shown in Figure 59.) Early rotors showed casting deficiencies, such as failure to fill blade tips, core breakage, and shrinkage. Later castings were improved in these respects, but the results from metallurgical tests were disappointing. Table II presents a summary of results from these tests, which indicated low creep-rupture life and ductility (elongation) and unacceptable scatter in all properties. These problems were believed to be caused by undesirable grain formation, which was difficult to control because of the different cooling rates of the thin blades and the thick hub section.

To operate at design conditions with a reasonable burst margin, the minimum rotor properties had to meet the PWA material specifications. The trial rotors did not meet these specifications, and in Phase II the radial turbine contract was modified to add a casting development effort to the basic program.

TABLE II. SUMMARY OF METALLURGICAL TEST RESULTS			
Property	Range of Data	Average Value	PWA 658 Min Spec
Yield Strength, psi	0 to 118,000	93,000	95,000
Ultimate Strength, psi	100,000 to 132,000	122,000	115,000
Tensile Elongation, %	0 to 11	4	5
Creep-Rupture Life (1400°F), hr	0 to 36	14	23
Elongation Prior to Rupture (1400°F), %	0 to 3.3	1.2	2

PHASE II CASTING DEVELOPMENT PROGRAM

The Phase II casting development program was planned as a dual approach in which both integral-cast and bicast rotors were to be evaluated. Bicasting represented a departure from normal casting practice in that the blades were cast individually and then a hub of the same material was cast onto the blades. The potential advantages of a successful bicasting process over the more conventional integral-casting technique are significant. With individually cast blades, inspection of the blade passage is simplified, and the yield factor is increased since the loss of one blade does not require the rejection of other undamaged blades, as is the case with integrally cast parts. In addition, bicasting offers a potential solution to the differential cooling problem of the integral rotor: the blades and the hub can be poured under different conditions to achieve desirable grain formation in both types of parts.

Bicasting Experience

The first bicast pieces to be metallurgically evaluated were rectangular test bars, 8 by 2 by 5/8 in. Two different types of bicast joints were made: a simple butt joint (Figure 60) and a chevron joint (Figure 61). Both of these joints were similar in appearance, indicating that the chevron "tang" had lost its identity in the remelted zone. Tensile and creep-rupture data from 17 test bars were encouraging (Tables III and IV) and indicated that PWA 658 (IN100) specification properties were available with a satisfactory degree of repeatability.

The second type of test specimen to be evaluated was taken from an uncored (solid blade) rotor section. Figure 62 shows a cross section of this part. Along the original platform base (shown by the dotted lines), a good metallurgical bond appeared to exist in the radial direction. In the shallow slotted areas along the

sides of the platform, there appeared to be no metallurgical bonding. (Figure 63 shows an individual blade with the slots along the platform sides; these depressions were intended to give some mechanical bond in the absence of any metallurgical bond.)

Two specimens were taken from the blade centerline of the rotor shown in Figure 62 so that the original blade platform surface was located in the gage length of the metallurgical test specimen (Figure 64). One of these specimens was tested for tensile properties, the other for creep-rupture properties. In both cases, the experimental properties were acceptable. (See Tables III and IV.) These data, in conjunction with the test bar data previously generated, indicated that the bicasting process had the potential to produce rotors with design material properties.

During Phase II of the program, a bicast solid blade rotor was being used to verify a redesigned spin arbor when the rotor failed at 76,400 rpm. This single point was the only burst data for bicast rotors resulting from this task, since the rotors originally intended for spin test were used to replace rotors damaged in rig tests. Stress analysis had predicted a burst speed of 82,660 rpm for a solid blade rotor, which implied that the effective strength of the fractured rotor was about 15% below design. Inspection of the rotor fragments (Figure 65) indicated that there was incomplete metallurgical bonding in the circumferential direction. It was concluded that this was the primary cause of the reduced burst strength.

The production advantages of the bicast process were verified during the fabrication of four air-cooled rotors. In the final batch of blades cast for this program, a yield of 24 good blades from a total of 30 blades was achieved. Also, inspection of individual blades for core position and core integrity was considerably easier than conducting the same inspection for a complete rotor assembly.

During the preparation of the bicast rotors for rig testing, conventional inspection techniques did not reveal the incomplete metallurgical bonding in the rotors. Both X-ray and Zyglo (fluorescent penetrant) inspections were used on the test rotors, and neither method revealed the unbonded areas between blades. It was later concluded that the incomplete blade/hub bond was responsible for some of the spin-testing difficulties that were encountered during proof spin tests and destructive spin tests. These difficulties consisted of an apparent instability (at speeds in the 35,000 to 55,000 rpm range) such as would be expected from an out-of-balance part. (Shaft movement was observed through an oscilloscope presentation of two electromagnetic proximity probes located at right angles to each other.) After the bonding problem was established, it was concluded that the blades were deflecting unsymmetrically during rotation, causing the out-of-balance condition observed on the oscilloscope.

On the basis of the bicasting experience in Phase II, it was concluded that the process offers significant advantages in the production of geometrically correct air-cooled radial turbine rotors, but additional development is required to solve the incomplete bonding problem. It was also concluded that new inspection techniques are needed to detect incomplete blade-to-hub bonds.

17

TABLE III. TEST RESULTS FROM BICAST CREEP-RUPTURE SPECIMENS (1400°F)

Specimen No.	Source	Stress (ksi)	Life (hr)	Elongation (%)	Meet Specification?	Remarks
1	Test Bar*	70	18.5	0.7	No, but see Remarks	Failed outside junction area
2	Test Bar*	85	3.1	0.0	No, but see Remarks	Failed outside junction area
3	Test Bar*	85	0.1	0.0	No, but see Remarks	Failed outside junction area
4	Test Bar*	85	12.0	1.2	No, but see Remarks	Failed outside junction area
5	Test Bar*	85	29.3	2.1	Yes	
6	Test Bar	85	231.8	7.8	Yes	
7	Test Bar	85	80.7	5.4	Yes	
8	Test Bar	85	10.7	3.4	No	
9	Test Bar	85	94.5	6.1	Yes	
10	Test Bar	85	210.2	2.5	Yes	
11	Rotor	85	26.0	1.4	Life yes, % elongation no	Uncored rotor
PWA Specification (minimums)		85	23.0	2.0		

*Shrinkage observed in casting outside of bicast junction area.

18

TABLE IV. TEST RESULTS FROM BICAST TENSILE SPECIMENS

Specimen No.	Source	Test Temperature (°F)	Yield Strength (ksi)	Ultimate Strength (ksi)	Elongation (%)	Meet Specification?	Remarks
1	Test Bar*	1400	-	104.9	2.0	No, but see Remarks	Failed outside junction area
2	Test Bar*	1400	-	89.8	-	No, but see Remarks	Failed outside junction area
3	Test Bar*	1400	112.3	121.0	4.0	Yes	Failed outside junction area
4	Test Bar*	70	102.2	115.8	10.0	Yes	Failed outside junction area
5	Test Bar*	70	106.8	112.8	5.0	No, but see Remarks	Failed outside junction area
6	Test Bar	1400	103.8	141.5	7.0	Yes	
7	Test Bar	1400	95.0	123.5	4.0	Yes	
8	Rotor	1400	112.2	131.6	4.0	Yes	Uncored rotor
Pᵥ A Specification (minimums)		1400	94.0	112.0	2.0		
		70	95.0	115.0	5.0		

*Shrinkage observed in casting outside of bicast junction area.

19

Integral Casting Experience

During the casting development program, four integral rotors were fabricated. The first two rotors were uncored, and the latter two were cored. Figure 66 shows typical grain patterns in an uncored rotor. In general, the long axially oriented grains in the blade section shown in Figure 66 are undesirable for a radially stressed part such as this turbine rotor.

Hub shrinkage was the primary problem with the first solid-blade rotor (Figure 67). The shrinkage problem was resolved on the second solid rotor, and the casting vendor proceeded to the cored rotor configurations. On the first cored rotor attempt, the blade tips failed to fill completely, indicating that the pour temperature was too low. No core breakage was experienced on this rotor, but some core shift was observed on several blades. In the second cored rotor attempt, a higher pour temperature was used. Improvement was noted in the tip-fill problem, although some blades still failed to fill. One core was broken, and the missing portion of the core was located in the hub near the surface. This part was salvaged as a spin-test specimen (Figure 68) by machining away the broken core and filling the void with weld-deposited Hastelloy-W material. The incomplete blade tips were also weld-repaired, and the part was spin-tested to destruction. Burst occurred at 88,660 rpm, and growth measurements taken at intermediate speeds showed acceptable ductility. Predicted burst speed for this type of rotor (cored) was 86,200 rpm, indicating that the integral rotor was capable of producing design material properties.

Because of contract limitations, the integral casting development effort was stopped after the destructive spin-test. In the present state of development, the burst strength of the integral rotor appears acceptable, but the problems of high scrap rate, incomplete tip fill, and core shift and breakage remain.

FABRICATION OF TURBINE NOZZLES AND ROTORS

Three nozzle sections and four rotors were fabricated for testing in Phase II, Task 3. The following paragraphs describe the procedures developed to solve unusual fabrication problems that arose from either the complexity of the design or the problems associated with welding IN100, which is generally regarded as an unweldable material. Figure 69 shows cracks in a typical weld on IN100.

The integral nozzle casting (shown after machining in Figure 70) presented some fabrication problems during early casting trials. These problems were primarily shrinkage and cracking in the thin trailing edges of the airfoils. These problems were solved in a reasonable development period by adjusting conventional invest-ment casting parameters, such as mold preheat, pouring temperature, and gating design. The platforms and attachment areas of the nozzle were machined after casting to remove approximately 0.060-in. machining stock. On the gas-path surfaces, the only machining required was a hand-blending operation on the pressure side of the airfoil trailing edges. This operation was necessary to achieve uniformity of the 20 throat areas.

The cooling inserts, which were also IN100, were cast without cooling air holes. The holes were later machined by multiple electro-discharge electrodes as shown in Figure 71.

Attachment of the inserts into the nozzle airfoils was accomplished with a nickel-base braze (Coast Metals No. 50). Prior to brazing, the parts were nickel-plated on the mating surfaces (nominally 0.006-in. plating on the insert, 0.0013-in. on the nozzle casting). This plating was found to be necessary to obtain a satisfactory braze joint. The brazing process is described in detail in Appendix I.

The final step in the preparation of a nozzle casting for test was the welding of heat shields and sheet metal transition ducts to the nozzle casting. A nozzle assembly is shown in Figure 72, complete with test instrumentation.

Like the nozzle section, the turbine rotors were cast with finished dimensions on the gas-path side and a minimum of 0.060-in. machining stock on the other surfaces. Referring to Figure 20, the profile behind the rotor flange was machined on a lathe using a template and follower. The internal passages were then filled with wax, and the area between the blades was filled with a low temperature bismuth-lead eutectic (Cerrobend). The 15-deg angle cone in the hub and the 0.590-in.-diameter bore were machined on a lathe. The lathe was also used to machine the OD of the blade tips and the blade contour using a template. The 0.295-in.-diameter bore in the small end of the hub was machined in jig bore. Both the 0.590- and 0.295-in. diameters were ground to the finished dimensions to eliminate any roughness in the bore that might create undesirable stress concentrations. On the fourth and last rotor machined, some blade tips were slightly deformed while machining the OD. For this reason, the blade cooling cavities should be filled with the eutectic, instead of wax, during the blade profile machining operation.

Welding was required to close the core support holes on the turbine back side and at the blade tips (Figure 73). For the rear core support holes, a counter-bore of 0.312-in. diameter by 0.060-in. depth was machined prior to depositing Nichrome V weld material to close the hole. The same weld material was used to close the blade tips. After welding, the rotors were given a 10-hr, 2000°F stress-relieving heat treatment in a hydrogen atmosphere.

Prior to the third turbine build, a welding procedure was developed to improve the blade-to-hub circumferential bonding at the blade roots and increase hoop strength. (The incomplete bonding problem became apparent after the destruction of a bicast rotor in the spin pit; see previous discussion under this task.) This procedure consisted of machining a 0.150-in.-deep by 0.150-in.-wide welding groove between the blades in the star portion of the rotor. A similar groove was machined on the back side of the rotor, along the original blade platform surface. Pie-shaped sections of a scrap rotor were used to make trial welds. The welding grooves were machined into these sections and trial welds were made with Hastelloy W and Nichrome V. The trial welds were sectioned and inspected under a microscope for cracks. In this welding operation, Hastelloy W produced better trial welds than Nichrome V. Hastelloy W was therefore used to fill the grooves (Figures 74 and 75). The last two bicast rotors (tested in Builds 3 and 4) incorporated this welding procedure.

Fabrication of the rotor was completed by electro-discharge machining two 0.020-in.-diameter tip bleed holes (shown in Figure 71) and one 0.156-in.-diameter cooling air inlet hole for each blade as shown in Figure 76.

21

After machining, each rotor was returned to the casting vendor for removal of residual core material, which tended to remain in certain areas of the cooling cavity.

The final operation in the preparation of rotors for test consisted of balancing and spin-testing to 110% of the anticipated rig operating speed. Details of the balance and spin procedures are given in Appendix II.

PHASE II, TASK 3 - HOT TESTING

TASK SUMMARY

Burner tests and turbine tests were conducted under this task. The burner tests were conducted to achieve an acceptable temperature distribution and to determine combustion efficiency. After 10 burner tests, the objectives of the combustor program were satisfied and turbine testing was started. The turbine testing was originally scheduled for 10 builds and tests with the objective of obtaining performance data at various conditions up to and including design conditions. Because of rotor fabrication problems (see previous section) and contract limitations, the turbine test program was foreshortened to 4 builds and tests. Performance data showed some scatter, and indicated that turbine efficiencies were approximately 0.8 point below to 2.3 points above the predicted values (87.5% efficiency, $\Delta H/\theta$ of 41.3 Btu/lb at design point). It was concluded that the measured performance levels of the radial turbine were high enough to substantiate its potential for application in advanced small gas turbine engines.

TURBINE AND BURNER TEST RIG

The contractor-furnished test rig that was used in the turbine and burner test programs is shown in Figures 77 and 78. The turbine test rig was a supercharged gas generator that duplicated the turbine environment of the hypothetical engine (257.5 psia and 2300°F at the turbine inlet). Pressurized inlet air was supplied by compressor bleed air taken from a facility gas turbine engine. Key design features of the turbine test rig included the following:

1. Adjustable brake (compressor) inlet guide vanes (IGV)

2. Single-stage centrifugal compressor

3. Pipe diffusers (two designs with different numbers of diffusers)

4. Bleed air discharge

5. High-temperature burner

6. Oil-cooled and -lubricated bearing package with film damping

7. Integrally cast, air-cooled nozzle vanes

8. Cast, air-cooled turbine rotor

9. Air-cooled shroud and backplate

In operation, the brake was designed to serve two purposes: it absorbed the power generated by the turbine and it raised the pressure of the inlet air (90 psia) to the hypothetical engine compressor discharge pressure (257.5 psia). It was designed to accept approximately twice as much air as the turbine design flow

(nominally 5 lb/sec). The excess air discharged through the bleed air line. This feature of the rig design provided an increased range of turbine test data as compared to a design in which the compressor and turbine airflow rates are equal.

The adjustable brake IGV's and the two pipe diffuser designs were required to utilize the wide range of test conditions (made possible by the bleed air system) without operating the brake in surge conditions.

The basis of the burner design was the UACL PT6 flame tube and fuel system. To this were added a sheet metal duct that established the proper gas flow path for efficient burner operation and a transition piece to turn the hot gases in a radially inward direction. The outer shell of the rig supported the entire test assembly.

To operate the high-speed (67,000 rpm) bearing system in a high-temperature environment, it was necessary to provide appreciable cooling within the bearing package. This was accomplished by designing a cylindrical cooling-oil flow path that enveloped the bearing assembly and maintained acceptable temperatures in this area. Oil-film damping was provided at the brake bearing to damp out the first two critical speeds (approximately 10,000 and 25,000 rpm), which were passed through in accelerating to design speed.

Primary control of the rig was achieved with a PT6 fuel control and a bleed air control valve. Secondary control points were the adjustable brake IGV's and a turbine backpressure control valve. Turbine power was determined from the calculated compressor work, corrected for bearing, windage, and rotor pumping losses.

In the burner test configuration (Figure 78), the turbine rotating assembly was replaced by a temperature/pressure traversing probe assembly, which was used to measure total temperature and total pressure at the nozzle leading edge. An indexing gearbox was used to advance the probes in equal circumferential increments, and multiple probes located at different axial positions provided spanwise temperature data.

BURNER TESTING

Burner Test Facility

External views of the assembled burner rig are presented in Figures 79 and 80, and Figure 81 shows the burner test rig installed on the test stand.

The test facility for the burner test program is shown schematically in Figure 82. Rig inlet air was supplied by a JT3 (J57) facility engine at flow rates up to 4 lb/sec and pressures up to 90 psia during the burner tests.

Rig cooling air was supplied from a 350-psia facility air supply. After passing through an air dryer, the cooling air was metered to the rig by automatic controllers, which maintained a constant pressure differential across the backplate and shroud. Fuel nozzle cooling air was supplied by the same source and controlled

24

by means of a pressure regulator. An automatic abort system was installed to shut off fuel flow to the rig in the event that cooling air pressure dropped below a preselected pressure level.

Fuel flow to the rig was delivered by a UACL PT6 fuel pump and control unit. The control pressure signal for the fuel control originated in the burner. This system provided a nearly constant fuel-air ratio for small changes in the rig air supply. An automatic overtemperature abort system was installed that sensed burner exit temperature through three platinum/platinum-rhodium aspirated thermocouples. This system aborted the rig in a fuel-off, air-on mode.

Burner Test Rig Instrumentation

At low temperature locations throughout the burner rig, all of the pressure and temperature measurements were taken with conventional instrumentation. At the higher temperature locations, between burner exit and turbine exhaust, special instrumentation in the form of a traversing probe assembly and an automatic traversing mechanism was designed and fabricated for these tests. Figure 83 shows a typical total temperature/total pressure probe. The probe assembly consisted of two platinum tubes (to withstand high temperatures) welded together. The aspirated thermocouple was designed to enclose the thermocouple assembly with an inner tube having metal temperatures approximately equal to mainstream gas temperatures, thus reducing radiation errors to a negligible value. Figure 84 shows the three-probe assembly as used in the burner tests; Figure 85 shows the spanwise spacing of the probes. The traversing assembly in the burner test rig is shown in Figure 86.

The traversing assembly was actuated by a specially designed actuator shown in Figure 87. This actuator was an indexing gearbox that could be stepped manually or automatically at angular intervals as small as 1.5 deg. During the burner tests, a 3-deg interval was used to record circumferential temperature data.

Figure 88 shows the locations of the basic instrumentation used to measure burner performance.

Burner Performance Calculations

The burner performance was evaluated in terms of two basic parameters, delta temperature variation ratio (ΔTVR) and combustion efficiency. ΔTVR is defined in the list of symbols.

The average gas temperature was calculated as an arithmetic average based on temperature readings from probes located at 25%, 50%, and 75% span at 3-deg intervals around the circumference. The midspan reading was assumed to exist at a constant value from 25% to 75% span, and the other two temperature readings were assumed to exist at constant values from 0% to 25% and 75% to 100% span.

The second basic burner performance parameter, combustion efficiency, was defined as

$$\eta_B = \frac{\text{Measured Temperature Rise}}{\text{Ideal Temperature Rise}}$$

where   Measured Temperature Rise was an arithmetic average value calculated from traverse data at the burner exit and from fixed burner inlet temperature readings.

Ideal Temperature Rise was determined as a function of relative humidity, inlet air temperature, fuel-air ratio, and the lower heating value of the fuel. Figure 89 shows the ideal temperature rise for dry air and aviation gasoline. This value was corrected (lowered) to account for the energy required to raise the temperature of the water vapor fraction (determined from relative humidity readings) from burner inlet temperature to the final burner exit temperature.

Burner Tests

Ten burner assemblies were evaluated, and the results of these tests are summarized in Table V and Appendix III. The initial burner configuration tested consisted of a PT6 flame tube design that had been modified with increased wall thickness (to extend durability) and with decreased hole area (to restore design pressure drop at high burner pressure). This burner was tested with unheated inlet air (110° to 150°F) and JP5 fuel. Excessive carbon deposits were experienced with the first and the subsequent three builds (Figure 90), even though the hole pattern was modified to increase the airflow to the areas of carbon formation. For the fifth and sixth builds, the fuel was changed from JP5 to JP7, and a standard thin-wall PT6 burner (including standard PT6 hole area) was used in lieu of the original heavy-wall burner, which had become distorted. In addition, a facility preheater was installed in the inlet line, and the inlet air temperature was raised above 350°F for the fifth and all subsequent tests. Results from the fifth build showed a modest improvement in the temperature pattern, but the carbon formation was still unacceptable (Figure 91). For the seventh build, aviation gasoline was substituted for JP7, and the carbon formation problem was solved (Figure 92). In addition, the temperature pattern was improved. It was concluded that aviation gasoline should be used for subsequent burner tests and for the hot turbine testing. Build 8 incorporated a modified hole pattern, and two tests were conducted: one with bleed flow and one without bleed flow. Although the temperature patterns in both cases were distorted by a plugged fuel nozzle, the patterns were essentially unchanged. It was concluded that the temperature distribution was not affected by changes in the bleed airflow. Build 9 used the Build 8 hole pattern and a new set of fuel nozzles, and the temperature pattern achieved (ΔTVR = 1.14) surpassed the goal (ΔTVR = 1.2). Figure 93 shows the Build 9 hole pattern, and the measured temperature distribution is included in Appendix III. For Build 10, a heavy-wall burner (0.029 in. instead of 0.017 in. for standard PT6 engine flame tube) was fabricated with the Build 9 hole pattern and tested under nearly identical conditions. Unaccountably, Build 10 results showed a lower quality temperature pattern, and it was concluded that the thin-wall burner should be used for the turbine tests.

26

TABLE V. SUMMARY OF BURNER TEST PROGRAM

Assembly	Test	Airflow (lb/sec)	Bleed Flow (lb/sec)	Fuel/Air Ratio	Burner Exit Average T_{in} (°F)	Burner Average P_t (psia)	Burner Average T_{out} (°F)	Maximum Local T_{out} (°F)	ΔTVR	Ideal T_{out} (°F)	Calculated Efficiency (%)	Fuel Type	Remarks
Build 1	1-1	2.88	-	0.0128	123	111	1343	2196	1.70	1353	99.6	JP-5	Carbon deposits. Heavy walled burner (Builds 1 to 4),
Build 2	2-1	3.16	-	0.0173	112	124	1490	2294	1.58	1318	114	JP-5	Carbon deposits.
Build 3	3-1	3.35	-	0.017	97	114	1438	2238	1.60	1288	112	JP-5	Carbon deposits.
Build 4	4-1	3.20	-	0.017	153	111	1424	1976	1.43	1327	108	JP-5	Carbon deposits.
Build 5	5-1	2.99	-	0.012	508	104	1408	1668	1.29	1338	108	JP-7	Carbon deposits. Thin-walled burner (Builds 5 to 9).
Build 6	6-1	2.50	THERMOCOUPLE FAILURE: NO DATA AVAILABLE									JP-7	Carbon deposits.
Build 7	7-1	2.29	-	0.021	350	97	1704	2045	1.25	1683	101	AVGAS	Carbon problem improved.
Build 8	8-1	2.46	-	0.017	375	94	1577	2020	1.37	1489	108	AVGAS	No carbon deposits in burner. Plugged fuel nozzle produced cold spot, otherwise temperature pattern good. Temperature pattern unaffected by use of bleed air. (Tests 8-1 and 8-2.)
Build 8	8-2	1.85	1.63	0.023	382	80	1870	2210	1.23	1827	103	AVGAS	
Build 9	9-1	1.81	-	0.024	354	95	2028	2265	1.14	1883	109	AVGAS	No carbon deposits; good temperature pattern.
Build 10	10-1	2.22	-	0.024	352	98	1966	2360	1.24	1883	105	AVGAS	New heavy-walled burner. Carbon deposits; degraded temperature pattern. (Tests 10-1 and 10-2.)
Build 10	10-2	2.27	-	0.024	353	98	2047	2620	1.34	1882	111	AVGAS	

27

The calculated combustion efficiency was over 100% for nearly every burner test (Table V). This discrepancy, which is common in burner testing, was attributed to sampling errors (radiation errors in an aspirating probe of the type used are negligible).

TURBINE TESTING

Turbine Test Facility

Figures 94 and 95 show front and rear views, respectively, of the turbine test rig installed in the test facility.

A schematic of the turbine test facility is presented in Figure 96. Like the burner test configuration, air was supplied to the turbine test rig by bleed air from a JT3 (J57) facility engine. Lubricating oil was delivered to the front (brake) and rear (turbine) bearings by electric motor-driven facility pumps. A small heat exchanger was used to maintain the proper operating temperature. Oil was also circulated through a jacket surrounding the bearing package for cooling the area. During Builds 1 and 2, oil was scavenged from the bearing compartment by high-capacity gear pumps. However, the scavenge pumps were unable to depress the bearing cavity pressure to the specified level (10 psia) and they were replaced by a steam ejector system for Builds 3 and 4. Cooling air and seal air were supplied from a 350-psig facility air supply. The backplate and shroud cooling airflows were set by automatic control valves that maintained a selected delta pressure inside the rig. The turbine rotor and fuel nozzle cooling airflows were set manually.

Fuel flow (aviation gasoline) was provided by the PT6 fuel pump and control, which was operated with a control pressure taken from the rig at the burner inlet and regulated by a manually controlled, variable area orifice.

In addition to the fuel control, three other control modes were provided for adjusting the rig operating point: (1) a motorized butterfly valve in the inlet air line, (2) a motorized butterfly valve in the exhaust line, and (3) a pneumatically operated control valve in the rig bleed line.

The bearing axial thrust loading was controlled by adjusting the pressure in a plenum behind the brake impeller. A bleed valve for decreasing the plenum pressure and a control valve for increasing the plenum pressure were available to provide the selected thrust load.

Turbine Instrumentation

The basic instrumentation plan for the turbine tests is shown in Figure 97. Conventional stationary instrumentation was used throughout the system. Traversing instrumentation at the turbine exhaust station consisted of wedge-type probes (Figure 98) that measured static pressure, total pressure, and total temperature. These probes were traversed in a radial direction at three equally spaced circumferential locations. In addition to moving the probes in a radial direction, the exit air angle was measured by turning the probes about their axes until the static pressures on both sides of the probe were equalized.

Turbine Performance Calculations

Turbine performance was evaluated primarily as turbine efficiency, defined as

$$\eta_{T-T} = \frac{\text{Horsepower Out (corrected)}}{\text{Isentropic Horsepower Available}} = \frac{(W_c \times \Delta H_c/550) + \text{HP (parasitic)}}{(W_{tcr} \times H_{ideal}/550)}$$

where
η_{T-T} = Turbine efficiency, total-to-total.

W_c = Measured compressor (brake) airflow, lb/sec.

ΔH_c = Total enthalpy rise across compressor, ft-lb/lb, based on measured temperatures at compressor inlet and discharge stations.

HP (parasitic) = Horsepower consumed by bearings, windage, and cooling air pumping in the rotor.

W_{tcr} = Rotor inlet flow rate, lb/sec.

ΔH_{ideal} = Total-to-total isentropic enthalpy available, ft-lb/lb, based on calculated rotor inlet temperature, measured vane inlet (burner) pressure, and mass-averaged rotor exit total pressure measured by radially traversing pressure probes.

This definition for turbine efficiency takes into account the work potential of the vane coolant from its point of entry into the mainstream, and the use of vane inlet pressure accounts for the pressure drop across the vane section. The rotor coolant is not considered in this definition of aerodynamic efficiency; it would appear as a penalty in overall engine cycle calculations.

As part of the data analyses, an estimate of the uncertainty in the efficiency calculation was made for a typical data point. (See Appendix IV.) Results showed that the rotor inlet flow rate was one of the largest contributors to the ±4.5 efficiency point range of maximum possible error that would reasonably be expected. The normal calculation for rotor inlet flow rate, involving only two flow measurements, is shown in Figure 99. An alternate calculation for rotor inlet flow (Figure 99) required the use of five measured flow rates, and was therefore inherently less accurate than the normal calculation. Most of the flow data showed good agreement (within 4%) between the normal and alternate flow calculations, but in some cases there was a discrepancy of 10 to 30%. In these instances, one or the other flow calculation was selected on the basis of a comparison with predicted nozzle flow rates. The predicted flow rates provided an acceptable check on measured flows, especially in the case of choked conditions at the nozzle throat.

The rotor inlet temperature was determined by calculating the turbine inlet temperature (TIT) at the vane inlet, the cooling air temperature at its point of entry, and then calculating the mixed temperature at the rotor inlet. TIT was determined

by starting with the measured gas temperature at the exhaust orifice and calculating the TIT on the basis of measured horsepower, predicted parasitic losses, and calculated heat loss in the exhaust pipe. The measured temperature at the exhaust station was corrected for the cooling effect of introducing the cooling airflows into the main gas stream. The rotor inlet temperature calculation could also have been based on the mass-averaged temperature as measured by the traversing probes. (See previous subsection.) However, the exhaust orifice temperature provided a more accurate indicator of exhaust temperature. This point is illustrated in Figure 100, where TIT's based on the orifice temperature showed better agreement with measured TIT's (available only in cold-flow tests, where TIT equals brake discharge temperature) than did those based on the traversing measurements.

Efficiency Corrections

The measured turbine efficiencies from Builds 3 and 4 were corrected for the larger-than-design rotor clearances used in those builds. The data used to determine the clearance corrections were taken from an SAE paper,[*] and are shown in Figure 101.

Other available data indicated higher efficiency corrections[**], but the data shown in Figure 101 were selected for conservatism, since the causes of the large variation in reported tip clearance effects are at present not understood.

An additional correction (increasing efficiency) for lower-than-design Reynolds No. could be justified. However, one was not applied because it was a relatively small correction (approximately 0.4 efficiency points for cold-flow data, 0.9 efficiency points for hot-flow data[***]) and the applicability of published data might be questioned, since the Reynolds No. effect is an empirical relationship that depends on design factors such as tip clearance, surface diffusion, and blade loading.

In the determination of predicted efficiencies for comparison with experimental data, corrections were applied to the pressure ratio and normalized speed ($N/\sqrt{\theta}$) to account for the difference in the ratio of specific heats and the geometric dimensions between the test condition and the design condition.

---

[*] Penny, No·l, ROVER CASE HISTORY OF SMALL GAS TURBINES, SAE Paper No. 634A, The Rover Co., LTD., January 1963.

[**] Futral, Samuel M., Jr., and Donald L. Holeski, EXPERIMENTAL RESULTS OF VARYING THE BLADE-SHROUD CLEARANCE IN A 6.02-INCH RADIAL-INFLOW TURBINE, NASA TND-5513, January 1970.

Watanabe, Ariga, and Mashimo, EFFECT OF DIMENSIONAL PARAMETERS ON PERFORMANCE CHARACTERISTICS OF A RADIAL-INFLOW TURBINE, ASME Paper No. 70-GT-90, January 1970.

[***] Nusbaum, N. J., and C. A. Wasserbauer, EXPERIMENTAL PERFORMANCE EVALUATION OF A 4.59-INCH RADIAL TURBINE OVER A RANGE OF REYNOLDS NUMBERS, NASA TND-3835, February 1967.

Build 1 Objectives

The test objectives of Turbine Build 1 were (1) to establish performance charac-
teristics of the brake and to determine the rig characteristics under different con-
trol modes during a series of cold-flow tests, and (2) to obtain turbine aerody-
namic performance data under both cold- and hot-flow conditions.

Build 1 Configuration

The turbine test rig configuration for Build 1 was the same as that previously
shown in Figure 77 with the exception that the slip ring was not used. The test
stand and primary instrumentation were previously described in this section.

Build 1 Operational Summary

Approximately 23 hr of cold-flow testing were accumulated on Turbine Build 1,
15 of which were spent in establishing rig operating procedures. Turbine traverse
data near the design point (cold) were obtained during the other 8 hr of cold-flow
testing.

During facility checkout, several of the metal bellows on the internal air and oil
service lines ruptured and were replaced with spare bellows sections.

Seven hours of hot testing were completed, with turbine inlet temperatures ranging
from about 950° to 2045°F and rig speeds as high as 53,000 rpm. During the
30 hr of test time accumulated with Turbine Build 1, no abrupt changes were noted
in either the rig operating characteristics or in the recorded performance levels.
After approximately 3 hr of running (cold flow), the strain gage reading from the
thrust-measuring load ring was lost. These points were significant in assessing
the pertinency of the Build 1 performance data (see following discussion). For the
remainder of the test, the thrust was estimated from the thrust data recorded before
the strain gage failure. Testing was terminated when the turbine bearing chip
detector gave a positive indication. Examination of the chip detector showed
numerous metal chips (Figure 102) in the bearing lubrication system, and the rig
was dismounted and disassembled.

During Build 1, the scavenge pumps were unable to depress the bearing cavity
pressure to the desired level (10 psia), and the tests were conducted at a higher
pressure level. The net effect of this situation was an increase in the leakage
rate of labyrinth seal air into the system.

Build 1 Test Results and Conclusions (Mechanical)

Inspection of the rig parts showed evidence of FOD to the brake impeller and
especially in the vane trailing edge and rotor leading edge regions. The turbine
bearing showed spalling of the balls and races (Figure 103), and the instrumented
load spacer was buckled, which could account for the loss of the strain gage read-
ing early in the cold-flow testing. In addition, there was evidence that the rotor
had rubbed both the backplate and the shroud.

31

Figures 104, 105, and 106 show FOD at the brake impeller, turbine vane trailing edge, and turbine rotor leading edge and tips, respectively. The appearance of the damaged parts indicated that a gradual erosion process had taken place, rather than an abrupt catastrophic failure. This observation, in conjunction with the operational experience (which did not indicate any abrupt changes in rig behavior), led to the conclusion that the performance data were recorded after the erosion process had started.

The exact cause of the FOD could not be determined, but two sources were primarily suspected: foreign objects in the inlet air line, and a thrust overload, which could have resulted in the buckled load ring in the bearing package. A laboratory analysis of particles found in the rig matched a similar analysis of particles taken from the air inlet line. The primary constituent was iron oxide, presumably formed in the carbon steel pipeline between the rig and the slave engine. The second possible cause of the FOD was the overstressed load ring. A buckling failure would have allowed the turbine to run too far rearward and the blade end wall would have rubbed the backplate. This rubbing could have produced enough metal particles to start the erosion process. The rotor-to-shroud rubbing was probably caused by rotor deflections resulting from the backplate rub or loss of balance during the erosion process. Regardless of which suspected FOD source initiated the damage, it was concluded that the erosion process started early enough to invalidate the turbine aerodynamic performance data from Build 1. It was also concluded that the test facility and test rig should be modified to preclude a recurrence of the FOD and load ring failure experienced with this build.

Build 1 Test Results and Conclusions (Aerodynamic)

During the cold-flow testing, rig operating procedures were developed, and the surge line of the brake with the 26-pipe diffuser and inlet guide vanes set at 0-deg prewhirl was established for use in later turbine tests. Data from this testing is shown in Figure 107.

The data accumulated with Build 1 at pressure ratios ranging from 3.2-6.1:1 indicated that measured efficiencies were approximately 7 to 15 points below predicted (Figure 108). However, in view of the evidence that the erosion damage began early in the testing, it was concluded that the Build 1 aerodynamic data were not representative of the turbine design.

Build 2 Objectives

The test objective of Turbine Build 2 was to obtain turbine aerodynamic performance data under both hot- and cold-flow conditions.

Build 2 Configuration

The test rig and test facility for Build 2 incorporated three modifications. Two of the modifications were directed toward prevention of FOD from outside sources: (1) 50-μ screening was installed in the rig inlet line (Figure 96), in all cooling air lines, and in the rig itself just upstream of the burner (Figure 109);

and (2) the instrumented load ring was redesigned with heavier sections to prevent buckling (Figure 110). The third modification consisted of replacing the bellows sections of the interval service lines (air and oil) with heavier metal bellows to prevent recurrence of the bellows failure that had been experienced during Build 1. An original and replacement bellows section are shown in Figure 111. The slip ring was not used.

Primary instrumentation for Build 2 was the same as for Build 1.

Build 2 Operational Summary

The performance of the thrust-measuring load ring was again troublesome. Prior to starting rig rotation, the strain gage signal was lost and the problem was diagnosed as an inaccessible electrical short inside the rig. It was decided to continue with the testing of Turbine Build 2 using a manual calculation of residual axial thrust based on measured pressures and disk area.

Shortly after starting rotation of Build 2, high vibration levels were encountered at a rig speed of 31,000 rpm and the rig was immediately shut down. Examination of the turbine exducer indicated that a rotor-to-shroud rub had occurred, and the rig was dismounted and disassembled.

Scavenging of the bearing cavity continued to be a problem even though additional scavenge pumps had been added to the system.

Build 2 Test Results and Conclusions (Mechanical)

Inspection of the rig parts showed rub damage to the turbine rotor (Figure 112) and turbine shroud (Figure 113). Metal particles from the turbine rub were thrown into the vane trailing edges (Figure 114), but the immediate shutdown prevented the extensive vane damage sustained in Turbine Build 1. After Zyglo and dimensional inspections it was concluded that the damaged parts could be salvaged for testing in Turbine Build 3.

The cause of the failure was attributed to a reversal of the axial thrust while accelerating the rig to the first operating point. The turbine bearing was designed as an angular contact ball bearing, which can only take axial thrust in one direction. An axial thrust reversal would unload the bearing and allow the turbine rotor to move downstream, rubbing the shroud. It was concluded that the manual calculation of thrust was not adequate for rig testing, and a faster backup technique would be required for subsequent tests. In addition, the unsatisfactory performance of the load ring indicated that additional modifications should be made to improve its reliability.

Build 2 Test Results and Conclusions (Aerodynamic)

The turbine rotor-to-shroud rub occurred before any aerodynamic data were recorded; therefore, there are no aerodynamic performance data from Turbine Build 2.

33

Build 3 Objectives

The test objectives of Turbine Build 3 were (1) to obtain aerodynamic performance data under cold and hot (up to 1900°F) flow conditions and (2) to obtain heat transfer data for the hot section parts: turbine rotor, nozzle, shroud, and backplate.

Build 3 Configuration

The test facility for Build 3 was the same as for Build 2. Six modifications were made to the test rig for Build 3: (1) the turbine rotor was welded at the blade roots; (2) turbine rotor running clearances were increased; (3) thermocouples were installed to record metal temperatures; (4) two new oil scavenge lines were added to the bearing package to increase the flow capacity; (5) the instrumented load ring was modified; and (6) 50-micron screening was installed just upstream of the brake inlet plenum (Figure 109).

Welding of the rotor blade roots was considered desirable when it was concluded during this time period that bicast rotors had an incomplete metallurgical bond in the circumferential direction. (See Figures 74 and 75 and discussion under Phase II, Task 2.) After experimenting with different sizes and types of welds on scrap parts, a satisfactory weld was obtained with a 0.150-in.-wide by 0.150-in.-deep machined slot, filled with Hastelloy-W material. Metallurgical evaluations indicated sound welds on the experimental parts. It was believed that this welding procedure increased the effective burst strength of the rotor, but no quantitative data were available to confirm this belief.

After the rotor rubbing experienced in Build 2, it was decided to use increased running clearances in Build 3 (0.015 in. as compared to the 0.010-in. design value). However, to remove damaged material from the Build 2 rotor, approximately 0.022 to 0.024 in. was machined from the shroud-side profile of the blades. The 0.015-in. axial clearances were set by shimming the shroud. Because of the material removed from the exducer tip profile, there was no feasible way to obtain the desired 0.015-in. clearance in the radial direction, and the turbine was tested with a 0.033-in. radial clearance (Figure 115).

Build 3 had thermocouples installed in the locations shown in Figure 116. The 0.030-in.-diameter thermocouples in the nonrotating parts measured the metal temperatures at a midthickness location, while the 0.010-in.-diameter rotor thermocouples were located at the blade outer surface. Static thermocouples were read directly, and the rotor thermocouples were connected through a high-speed slip ring.

In the fourth and fifth rig modifications, two additional scavenge lines were placed in the bearing cavity to improve oil scavenging, and the instrumentation for the load ring was modified by adding a second strain gage circuit and increasing the size of all electrical leads.

Build 3 Operational Summary

Approximately 10 hr of testing were accumulated with Build 3, about evenly divided between cold-flow and hot-flow testing.

The thermocouples proved to be quite fragile; only 16 of 26 circuits were operating properly at the start of cold-flow testing, and only 8 thermocouples were reading at the end of cold-flow testing. The slip ring, designed to transmit the rotor temperatures, failed twice. It was damaged before the first cold-flow data point was taken, was repaired, and failed for a second time after about 20 min of running. Thermal data resulting from Build 3 was therefore less than anticipated, and no rotor temperatures were recorded.

Satisfactory shaft thrust control was achieved without using the instrumented load spacer, which again performed unreliably in this build. The modified thrust control procedure consisted of maintaining a constant static pressure differential across the brake impeller (10 psi in an upstream direction), preventing a load reversal at the turbine bearing.

The 1900°F inlet temperature test objective was not reached. After 5 hr of hot testing at about 1000° to 1200°F, cooling air was being adjusted prior to increasing the TIT to 1900°F when the slave engine (which supplies the rig inlet air) automatically shut down in an overspeed abort. Aviation gasoline continued to flow into the rig at the rate of 75 lb/hr, the minimum fuel flow at atmospheric pressure. The result was an overtemperature condition, and the rig was shut down. Visual examination of the rotor trailing edges showed some damage, and the test series was ended.

Build 3 Test Results and Conclusions (Mechanical)

Inspection of the rig parts showed damage only in the turbine section. Figure 117 shows the turbine rotor after disassembly; approximately 0.50 in. was missing from each blade tip. This was believed to be the result of an overtemperature condition at shutdown rather than FOD, because there was no smearing of material at the blade tips as was observed in Build 1 as a result of FOD.

The nozzle vanes showed FOD along the trailing edges (Figure 118), but this would be the expected result of losing the overheated rotor blade tips. The vane leading edges showed no evidence of overheating. At the time of the test shutdown, vane cooling air was being adjusted and approximately 4% cooling air was flowing in the vanes. This is believed to have prevented any leading edge damage.

Build 3 Test Results and Conclusions (Thermal)

Metal temperature data from Turbine Build 3 are presented in Table VI, and Figures 119 through 122 show the same data plotted as cooling effectiveness versus percent cooling air.

In Figure 119, which presents shroud metal temperature data, some data scatter is evident since a decreasing effectiveness characteristic with increasing cooling air flow is not possible. In spite of the data scatter, the general level of cooling effectiveness is high enough to conclude that the design effectiveness values would be met at 3% cooling flow (design point).

TABLE VI. SUMMARY OF METAL TEMPERATURE DATA, TURBINE BUILD 3

Data Point	Backplate C/A Temp (°F)	Shroud C/A Temp (°F)	Backplate C/A Flow (%)	Shroud C/A Flow (%)	TIT (°F)	NMT1 (°F)	NMT2 (°F)	NMT6 (°F)	NMT7 (°F)	TSHMT1 (°F)	TSHMT2 (°F)	BPSUPMT (°F)	NSUPMT (°F)
45	255	70	0.97	0.96	1024	725	730	775	760	580	520	590	290
48	215	90	2.03	2.05	1018	735	735	760	735	575	515	565	280
49	283	250	1.65	1.57	1048	750	750	800	780	620	555	605	310
50	300	215	0.87	0.91	1051	760	765	815	765	635	575	640	325

36

Figure 120 shows cooling effectiveness data for the lower backplate and its support. These data show that temperatures in this area are essentially independent of cooling air flow, which was expected since these locations are influenced more by conduction than convective heat transfer. The levels of cooling effectiveness show good agreement with predicted values.

Cooling data for the shroudside nozzle platform are presented in Figures 121 and 122. The data shown in Figure 121 were taken at a location beneath a platform heat shield, which prevented direct contact between the gas stream and the nozzle platform. The data in Figure 122 were taken at a location downstream of the heat shields, where the platform was exposed to the main gas stream. In both figures, some data scatter is present, similar to that previously observed in the shroud cooling data (Figure 119). However, the general levels of measured cooling effectiveness for the nozzle platforms are lower than the predicted values. Since the cooling designs for the other stationary components are adequate (including the shroud, just upstream of the nozzle platform), this suggested the possibility of cooling air leakage between the shroud and the nozzle platform. The shroud/platform junction was a metal-to-metal seal, which could allow cooling air leakage as a result of machining or assembly imperfections, or distortion of either part during operation. Results from this portion of the cooling evaluation were therefore considered inconclusive.

The data from Figures 121 and 122, extrapolated to design conditions, indicate that the platform temperature beneath the heat shield would be approximately 18°F higher than the platform temperature downstream of the heat shields. The predicted temperature difference in these locations was 25°F, with the gradient in the same direction. These data verified that the heat shield had the desired effect of preventing overcooling of the platform outer diameters by the cooling air film injected just upstream of the nozzle section.

Build 3 Test Results and Conclusions (Aerodynamic)

Build 3 test results are summarized in Table VII. Cold-flow data were obtained at pressure ratios of 2.0-3.35:1, and hot-flow data were taken at pressure ratios of 4.1-4.45:1.

To compare experimental performance data with predicted values, the measured efficiencies were corrected for the increased rotor clearances of Build 3. The correction applied was 2.0 efficiency points (increase), which was determined as shown in Figure 123 from previously presented clearance effects (Figure 101) and measured rotor clearances (Figure 115). The resulting performance comparisons are presented in Table VII in the column entitled Corrected η_{T-T} - Predicted η_{T-T}, and in Figure 124.

37

TABLE VII. SUMMARY OF TURBINE BUILD 3 RESULTS

Data Pt No.	N (rpm)	PT4 (psia)	TT4 (°R)	RIT (°R)	PT5 (psia)	PS5 (psia)	T$_{exit}$ (°R)	α5(av) (deg)	PR$_{T-T}$	Corrected PR$_{T-T}$	U/Co'	ΔH/θ (Btu/lb)	W√θ/δ (lb/sec)	WN/δ (lb-rpm/sec)
31	34,090	53.3	710	710	16.0	15.5	535	40.2	3.33	3.04	0.737	31.7	0.696	20,278
32	35,090	52.4	688	683	16.5	15.5	522	39.9	3.18	2.95	0.786	29.8	0.685	20,949
33	35,260	52.5	693	688	16.3	15.5	530	41.8	3.23	2.98	0.783	30.4	0.681	20,863
34	34,110	50.2	685	685	16.5	15.5	530	39.4	3.05	2.83	0.775	29.2	0.689	20,441
35	34,150	50.1	685	685	16.6	15.5	530	42.1	3.03	2.82	0.778	29.0	0.692	20,580
36	32,230	40.6	669	664	16.2	15.3	535	45.8	2.51	2.38	0.808	24.7	0.614	17,447
37	26,300	34.1	640	636	15.9	15.3	537	49.5	2.16	2.07	0.730	21.1	0.606	14,374
38	28,790	35.8	644	640	15.9	15.2	528	49.5	2.25	2.15	0.777	21.3	0.610	15,777
39	19,380	30.0	620	616	15.7	15.1	537	48.9	1.92	1.86	0.589	17.9	0.590	10,482
40	25,880	32.2	636	632	15.7	15.1	536	51.9	2.06	1.98	0.741	20.2	0.571	13,362
41	28,630	35.5	650	646	16.0	15.2	537	49.2	2.23	2.13	0.774	21.7	0.625	16,019
42	29,960	37.3	657	650	16.1	15.2	537	48.1	2.32	2.22	0.789	22.2	0.609	16,277
43	28,620	35.7	650	650	16.1	15.2	538	49.9	2.23	2.13	0.771	21.4	0.603	15,410
44	41,900	71.4	1515	1515	17.0	15.8	1140	12.8	4.21	4.01	0.571	34.3	0.682	16,719
45	41,310	73.2	1484	1468	17.2	16.0	1072	14.8	4.26	4.06	0.571	35.0	0.678	16,641
46								INCOMPLETE DATA						
47								INCOMPLETE DATA						
48	41,860	75.0	1478	1447	17.2	16.0	1066	15.8	4.37	4.12	0.578	34.3	0.681	17,061
49	42,130	73.6	1508	1486	17.2	16.1	1096	16.3	4.30	4.08	0.577	34.8	0.677	16,837
50	42,150	72.7	1511	1498	17.0	15.9	1120	16.7	4.28	4.06	0.575	34.1	0.671	16,648
51	49,210	67.0	1634	1634	16.6	15.7	1226	25.9	4.04	3.89	0.653	35.2	0.666	18,472
52	49,530	74.3	1630	1630	16.9	15.8	1195	24.5	4.40	4.23	0.642	37.5	0.668	18,668
53	50,140	75.2	1632	1632	16.8	15.9	1187	24.5	4.48	4.29	0.647	38.3	0.668	18,888
54	51,470	75.5	1621	1621	17.3	15.9	1181	22.5	4.37	4.20	0.671	38.0	0.664	19,346

Note: The PT4 values shown are below the design value of 257.5 psia due to reduced TIT and horsepower levels during these tests.

TABLE VII. (Concluded)*

Data Pt No.	N/√θ (rpm)	Corrected N/√θ (rpm)	N/√θ (Corr, % design)	Shroud Cooling Air (%)	Backplate Cooling Air (%)	Rotor Cooling Air (%)	w (rotor inlet) (lb/sec)	Torque/δ (ft-lb)	BHPCR (hp)	Corrected η_{T-T} (%)	Predicted η_{T-T} (%)	Corrected η_{T-T} −Predicted η_{T-T}
31	29,143	28,254	95.7	0.0	0.0	0.0	2.161	5.61	132.4	89.4	89.5	-0.1
32	30,584	29,651	100.4	1.9	1.9	3.1	2.132	4.96	118.2	87.0	90.7	-3.7
33	30,624	29,689	100.6	2.0	1.9	0.0	2.116	5.02	120.5	87.7	90.6	-2.9
34	29,688	28,782	97.7	0.0	0.0	3.2	2.050	5.03	111.8	88.0	90.2	-2.2
35	29,723	28,816	98.8	0.0	0.0	0.0	2.056	5.01	111.3	87.8	90.4	-2.6
36	28,620	27,747	94.2	2.1	2.1	3.1	1.498	3.94	67.0	87.8	90.2	-2.4
37	23,848	23,108	78.3	2.3	2.4	3.5	1.270	3.97	46.2	87.6	88.4	-0.8
38	25,895	25,092	85.1	2.2	2.2	3.2	1.335	3.69	19.3	84.3	89.8	-5.5
39	17,765	17,214	58.4	2.7	2.8	4.0	1.104	4.41	33.2	86.7	80.6	+6.1
40	23,424	22,697	77.0	2.5	2.6	3.7	1.135	3.63	39.3	88.6	88.5	+0.1
41	25,632	24,850	84.3	2.0	2.1	2.9	1.354	3.90	51.5	86.9	89.7	-2.8
42	26,733	25,917	97.9	3.8	4.2	3.3	1.380	3.76	54.4	85.5	89.8	-4.3
43	25,572	24,792	84.1	0.0	0.0	0.0	1.310	3.74	49.6	86.0	89.7	-3.7
44	24,521	24,136	81.8	0.0	0.0	0.0	1.940	7.09	275.1	82.5	81.3	+1.2
45	24,551	24,155	81.9	0.9	0.0	2.5	2.008	7.18	281.4	83.6	81.3	+2.3
46			INCOMPLETE DATA									
47			INCOMPLETE DATA									
48	25,044	24,638	83.6	2.0	2.0	0.0	2.081	6.93	282.0	81.0	81.8	-0.8
49	24,886	24,490	83.1	1.5	1.6	0.0	2.003	7.03	282.8	82.8	81.6	+1.2
50	24,800	24,405	81.4	0.9	0.8	0.0	1.954	6.86	272.5	81.4	80.8	+0.6
51	27,725	27,347	92.8	0.0	0.0	0.0	1.713	6.27	268.4	86.2	86.5	-0.3
52	27,941	27,561	93.4	0.0	0.0	0.0	1.906	6.66	317.7	87.6	86.2	+1.4
53	28,267	27,882	94.6	0.0	0.0	0.0	1.929	6.72	328.8	88.6	86.7	+1.9
54	29,121	28,724	97.4	0.0	0.0	0.0	1.933	6.45	324.9	89.2	87.6	+1.6

*Cold flow data are questionable due to low horsepower levels and probable errors in estimating parasitic losses.

39

In Figure 124 the cold-flow efficiencies are generally somewhat lower than the hot-flow efficiencies, when compared to the predicted performance levels. The same trend was evident in the Build 1 data (Figure 108). One basic difference between cold- and hot-flow data can account for the discontinuity between the two types of data; the power levels of the cold-flow data were 1/10 to 1/2 those of the hot-flow data, and the cold-flow data would be more sensitive to errors in estimating the parasitic losses (windage and bearing power consumption) and the losses introduced by internal leakages which could not be taken into account with the hot test rig. A previous program at FRDC with a small cold-flow aerodynamic test rig (the Aerodynamic Research Turbine) showed that experimentally measured windage losses were 2.5 to 3.4 times the predicted values, and measured bearing losses were 3.4 to 3.7 times the predicted values. These errors were attributed to simplifying assumptions such as treating bolted flanges as smooth disks, and assuming constant bearing loads. In the calculation of radial turbine parasitic losses, similar assumptions were used and no experimental loss measurements were conducted. For comparative purposes, the Build 3 cold- and hot-flow performance data were adjusted using the previously determined ratios of measured to calculated parasitic losses, and the results are shown in Figure 125. This figure shows good continuity between cold and hot flow data, fortifying the supposition that the calculated parasitics were low. However, the general level of performance is higher than would be expected, and the magnitude of the error in calculating parasitic losses is probably not as high as that observed in the earlier program. Because of the suspected error in calculating parasitic losses, the hot-flow data (points No. 44 to 54, inclusive) were believed to give a more accurate indication of the turbine aerodynamic performance. On the basis of the corrected efficiency comparisons (Table VII and Figure 124), it was concluded that the experimental performance was within -0.8 to +2.3 efficiency points of the predicted values. Therefore, at the design point conditions, the turbine total-to-total efficiency should be between 86.7 and 89.8%, which is an acceptable value for an advanced small gas turbine engine.

The normalized work parameter, $\Delta H/\sqrt{\theta}$, is directly related to the turbine efficiency, since ΔH equals the efficiency times the isentropic ΔH available to the stage. Based on the measured work parameters and the range of corrected efficiencies projected at design conditions, the work parameter is predicted to range from 40.9 to 42.4 Btu/lb at design point. This range includes the predicted value of 41.3 Btu/lb, and satisfactorily demonstrated the high work capacity of the radial turbine.

The measured rotor exit gas angles (area averaged) presented in Table VII showed fair agreement (generally, 0 to 9 deg) with the values predicted in Figure 54, but the exit swirl measurements for the hot-flow points showed considerably greater difference (generally, 11 to 17 deg). However, the traversing measurements were considered to be relatively low quality data due to sampling errors, inherent susceptibility to clogging and entrapped liquids or leakage in the long instrumentation lines, and the complicating factor of cooling air injection. For these reasons, the exit swirl angle discrepancies were not weighed heavily in the evaluation of the turbine design. Until more precise swirl data are available, it is recommended that the predicted data of Figure 54 be used for engine design studies.

40

Because of the data scatter observed in these tests, an error analysis was undertaken to estimate the magnitude of scatter that should have been expected. Details of this analysis are presented in Appendix IV; results showed that for a typical hot test point, a variation of ±4.5 efficiency points was the maximum possible error that we would reasonably expect to observe. The experimental efficiency variation (compared to predicted values) of less than ±1.6 points for the hot data is therefore an acceptable scatter band for the hot test rig. Conversely, the variation in cold-flow data (±5.8 points compared to predicted values) exceeds the maximum reasonable variation and further justifies the selection of hot-flow data as the more accurate measure of turbine performance.

Build 4 Objectives

The test objectives of Turbine Build 4 were to obtain aerodynamic performance data at three conditions: (1) a scaled-down design point, (2) a 60% power point, and (3) an off-design point with the designed TIT of 2300°F.

The scaled-down design point was selected at the maximum rotor speed that maintained a 30% burst margin with bicast rotors; this speed was approximately 61,000 rpm. The corresponding TIT required to set a scaled design point was 1840°F, with a total-to-total pressure ratio of 5.1:1.

The 60% power point was estimated at 61,000 rpm and about 1900°F TIT, using typical small shaft engine characteristics as a basis for the estimate.

The third target condition was selected at the maximum design TIT of 2300°F, with the rotor speed again limited to 61,000 rpm. This was the maximum power point that could be tested with the reduced strength bicast rotors while maintaining a 30% burst margin. At this condition it would be necessary to overcool the rotor to compensate for the higher relative gas temperatures in the rotor.

Build 4 Configuration

Turbine Build 4 used the fourth and final bicast rotor, which incorporated the blade-root welding procedure previously used in the Build 3 rotor. The third and final nozzle assembly was used for this build. Turbine running clearances were set to a nominal value of 0.015 in. all around at assembly. To achieve the desired radial clearance at the rotor exit, 0.005 in. was machined from the shroud profile.

Turbine Build 4 did not include the hot-section metal thermocouples that were installed in Build 3.

The thrust-measuring load spacer that had proven to be unreliable in the three previous builds was not instrumented for Build 4. Axial thrust was controlled by maintaining a constant pressure differential across the brake, similar to Build 3. To facilitate this control procedure, a second bleed line was added to the plenum behind the brake impeller. This modification was made because the lands on the brake rear face were reduced in height (as a result of previous rubbing) and the brake rear pressures tended to run higher than normal.

The internal 50-μ screen used in Builds 2 and 3 was removed for Build 4 because of loosening of some weld junctions during Build 3.

41

Build 4 Operational Summary

Approximately 2 hr of hot testing were accumulated with the Build 4 assembly before an operational problem caused internal damage to the rig and ended the test series. Data were taken at speeds up to 51,980 rpm, TIT up to 1759°F, and turbine pressure ratio up to 5.2:1. The operational problem occurred with the turbine running at the TIT of 1759°F. While rig data were being recorded, the steam supply to the test stand was suddenly reduced. Steam was used primarily to scavenge oil from the rig bearing cavity, through the use of a steam ejector. Shortly after the loss of steam, the bearing cavity became filled with oil, which leaked past the compressor labyrinth seal into the main airstream. It was concluded that the oil leakage burned in the combustor and raised the TIT to 1950°F, where the automatic overtemperature abort was triggered. The sudden loss of combustion resulted in a rapid rise of the compressor inlet pressure, axial thrust was reversed, and the rig experienced internal damage.

Build 4 Test Results and Conclusions (Mechanical)

Inspection of the rig hardware details showed that the brake had rubbed its backplate, causing damage to both parts (Figures 126 and 127). The turbine rotor and nozzle are shown in Figure 128 after testing. The only significant damage noted to either part was some minor foreign object damage visible on one blade tip which may have been caused by particles from the compressor rub. Oil was found throughout the rig, including the inlet case, which supported the hypothesis that burning oil caused the overtemperature condition.

Build 4 Results and Discussion (Aerodynamic)

Turbine Build 4 test results are summarized in Table VIII, and the corrected efficiencies are compared to predicted performance levels in Figure 129. (The Build 4 clearance correction was 0.7 efficiency points, which was determined by the measured 4% axial and 1% radial clearances and the data presented in Figure 101.) The Build 4 performance data was not consistent with the Build 3 data, either in efficiency level or in the trend of the efficiency vs velocity ratio characteristic. In addition, the data scatter (approximately 14.8 points below to 6.7 points above predicted efficiency levels) exceeded the ±4.5 point maximum efficiency variation that could reasonably be expected, and significant instrumentation errors were suspected. It was concluded that Build 4 performance data could not be used to evaluate turbine performance.

AERODYNAMIC AND MECHANICAL PERFORMANCE SUMMARY

Aerodynamic data taken at turbine inlet temperatures of 1000° to 1200°F indicated that the turbine cooled performance was within -0.8 to +2.3 efficiency points of the predicted values. On this basis, turbine efficiency at design conditions will be between 86.7 and 89.8% (total-to-total) and the work parameter ($\Delta H/\sqrt{\theta}$) will be between 40.9 and 42.4 Btu/lb.

Testing at the design conditions of 67,000 rpm, 2300°F TIT, and 18-atmosphere inlet pressure was precluded by rotor structural limitations, caused by below-specification cast properties. The maximum test value of TIT was 2045°F, and the maximum rpm was approximately 53,000.

TABLE VIII. SUMMARY OF TURBINE BUILD 4 RESULTS

Data Pt No.	N (rpm)	PT4 (psia)	TT4 (°R)	RIT (°R)	PT5 (psia)	PS5 (psia)	Texit (°R)	α5(av) (deg)	PRT-T	Corrected PRT-T	U/Co'	ΔH/θ (Btu/lb)	W√θ/δ (lb/sec)	WN/δ (lb-rpm/sec)
55	29,510	46.4	721	719	16.2	15.3	565	*	2.87	2.68	0.670	23.0	0.675	16,924
56	31,500	49.1	778	765	16.0	15.3	590	34.3	3.08	2.84	0.674	24.9	0.679	17,596
57	49,430	71.1	1849	1776	16.7	15.9	1289	8.5	4.26	4.13	0.619	33.2	0.682	18,219
58	51,980	89.8	1843	1785	17.7	16.4	1258	10.2	5.07	4.87	0.620	37.3	0.667	18,699
59	46,740	93.1	2060	1990	18.2	16.5	1404	7.9	5.13	4.97	0.525	37.9	0.665	15,868
60	42,150	94.9	2219	2142	18.2	17.0	1522	*	5.21	5.09	0.454	37.6	0.678	14,067

* No air angle data available.

Note: The PT4 values shown are below the design value of 257.5 psia due to reduced TIT and horsepower levels during these tests.

TABLE VIII. (Concluded)*

Data Pt No.	$N/\sqrt{\theta}$ (rpm)	Corrected $N/\sqrt{\theta}$ (rpm)	$N/\sqrt{\theta}$ (Corr, % Design)	Shroud Cooling Air (%)	Backplate Cooling Air (%)	Rotor Cooling Air (%)	w (rotor inlet) (lb/sec)	Torque/δ (ft-lb)	BHPCR (hp)	Corrected η_{T-T} (%)	Predicted η_{T-T} (%)	Corrected η_{T-T} - Predicted η_{T-T}
55	25,059	24,302	82.4	1.0	0.0	0.0	1.811	4.59	81.5	71.6	86.4	-14.8
56	25,929	25,179	85.3	3.3	3.5	4.4	1.868	4.84	97.0	73.4	86.6	-13.2
57	26,715	26,405	89.6	3.4	3.7	4.7	1.782	6.29	286.1	77.6	84.8	- 7.2
58	28,019	27,693	93.9	2.7	2.9	3.7	2.197	6.60	398.9	79.5	85.4	- 5.9
59	23,862	23,642	80.2	2.8	3.0	3.8	2.149	7.83	441.5	79.9	78.4	+ 1.5
60	20,742	20,571	69.8	2.8	3.0	3.8	2.154	9.12	472.5	78.4	71.7	+ 6.7

*Note: Questionable data due to suspected instrumentation errors.

44

Figure 130 shows the most probable performance of this turbine design, based on hot test data from Turbine Build 3. It should be noted that this performance is based on a specific cooled efficiency definition shown in Figure 130. It is recognized that several other efficiency definitions are used throughout the industry, and sufficient information is included in the tabular data to calculate turbine efficiency according to other definitions.

Extrapolation of cooling data from the 1035°F (nominal) TIT test condition to the design point indicates that the cooling design is adequate for the turbine shroud and backplate. Data for the nozzle platform was inconclusive, because of data scatter and suspected cooling air leakage between the shroud and the nozzle platform. No cooling data were obtained for the rotor, due to instrumentation failures.

In early testing, the turbine showed a susceptibility to erosion-type foreign object damage on the vane trailing edges and rotor leading edges. However, the problem appeared to be solved by filtering foreign objects from the air inlet system.

CONCLUSIONS

1. Experimental performance of the cooled radial turbine showed efficiencies and work parameters high enough to substantiate its potential for application in advanced small gas turbine engines.

2. The cooling design for the turbine shroud and backplate is adequate for design point operation. No conclusion was reached in regard to the cooling performance of other parts due to suspected cooling air leakage and instrumentation failures.

3. On the basis of a destructive spin test of a single integral-cast rotor, the structural design of the rotor is adequate for design speed operation (67,000 rpm) with the desired burst margin (30%). However, additional test points are required to substantiate this single point.

4. With regard to rotor fabrication techniques, neither bicasting nor integral casting was capable of producing geometrically correct, metallurgically sound rotors with a reasonable yield factor. On the basis of the fabrication work performed under this program, the bicasting technique was shown to possess inherent production advantages (yield and inspection) over the integral casting technique.

5. Improvements in the data scatter experienced in this program can be achieved by sealing potential leakage paths, modifying and supplementing critical instrumentation, measuring parasitic losses, and adding an automatic data recording system.

RECOMMENDATIONS

It is recommended that:

1. The rotor casting development be continued, with emphasis placed on solving the blade-to-hub bonding problem of the bicast technique.

2. When structurally adequate rotors are available, testing with the hot test rig should be resumed. Objectives of future hot tests should include: (1) additional evaluation of the nozzle cooling design, with potential leakage paths sealed; (2) evaluation of rotor cooling design, preceded by a review and modification (if required) of the slip ring system; (3) turbine testing at design conditions; and (4) cyclic testing.

3. To obtain more detailed aerodynamic performance data, it is recommended that this turbine design be evaluated on a component test rig, where critical parameters can be closely controlled and precisely measured.

4. Longer-range programs should consider the inclusion of (1) analytical and experimental studies of the erosion characteristics of high temperature radial turbines, and (2) analytical studies of mixed-flow turbine designs, which may have reduced susceptibility to erosive FOD.
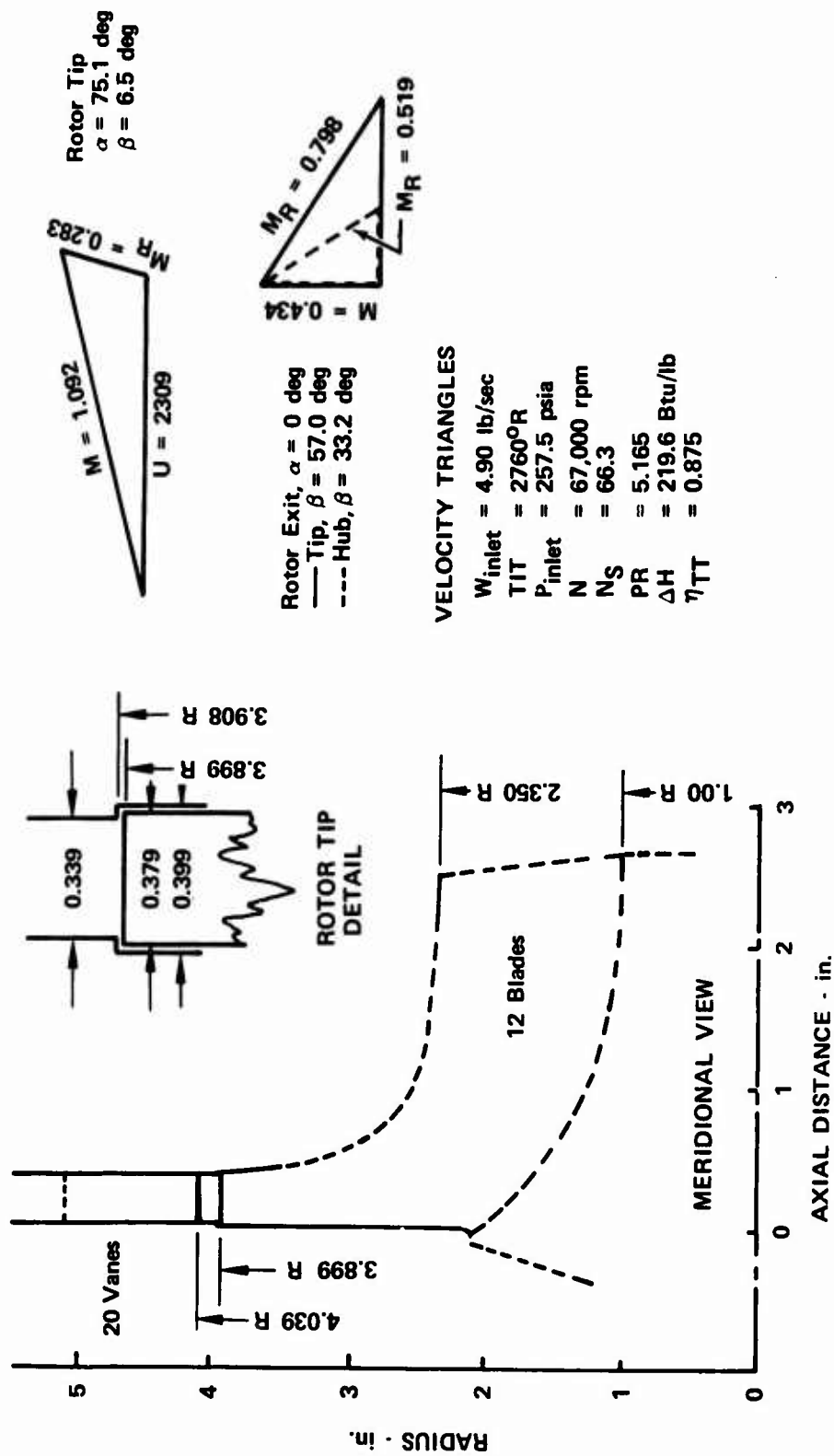
Figure 1. Turbine Mean Line Design Parameters.

48
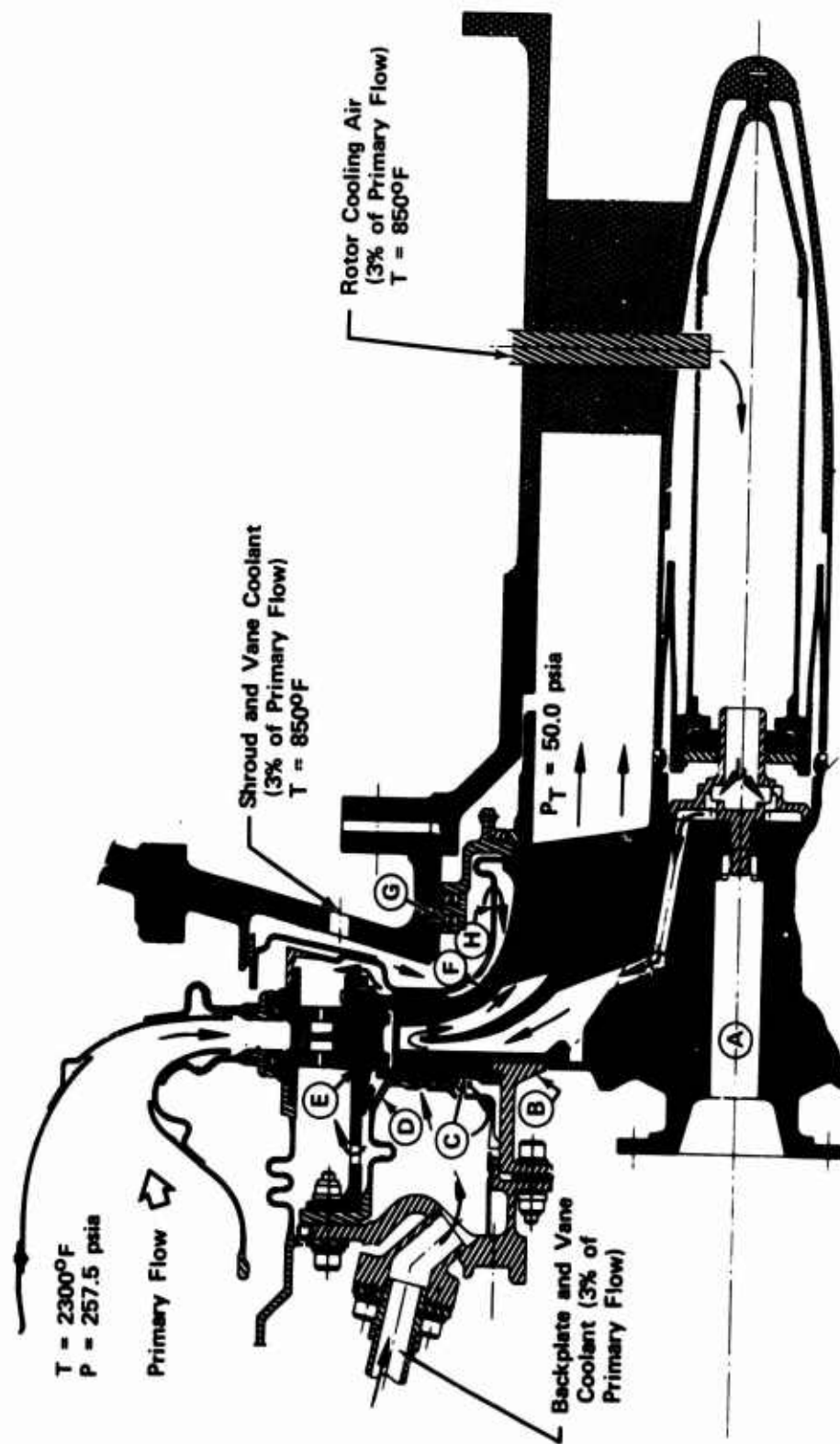
Figure 2. Radial Turbine Hot Section.
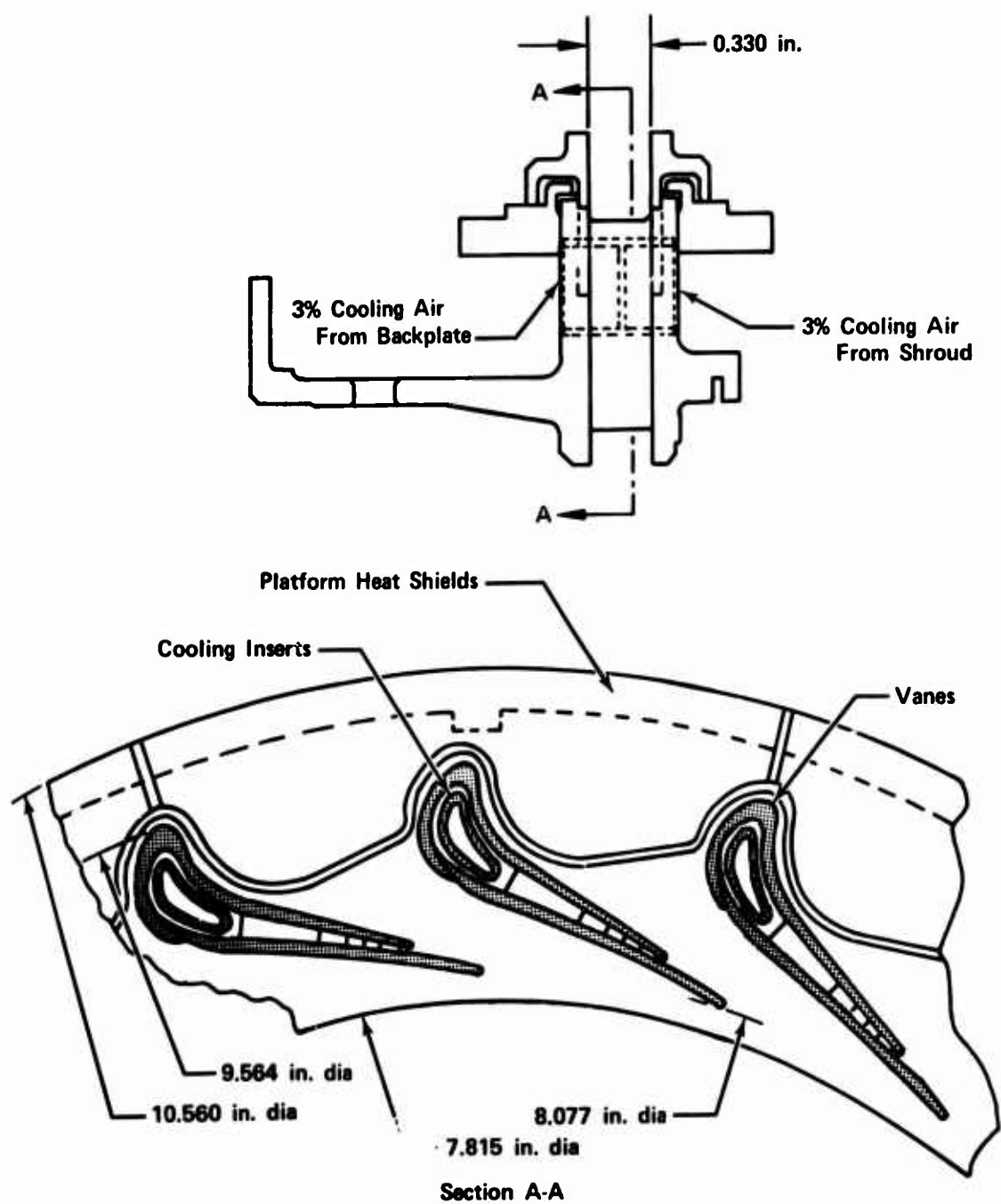
Figure 3. Nozzle Final Design.

	Airfoil Outer Contour		Airfoil Core Contour		Air Passage Contour		Insert Outer Contour	
EMD Profile	A		B		C		D	
Distance x	Y_1	Y_2	Y_3	Y_4	Y_5	Y_6	Y_7	Y_8
0.000	4.0388	4.0798						
0.050	4.0473	4.0958						
0.100	4.0566	4.1106						
0.150	4.0657	4.1225						
0.200	4.0743	4.1327						
0.250	4.0834	4.1407						
0.300	4.0918	4.1464						
0.345	4.0996	4.1975	4.1502	4.1771				
0.400	4.1083	4.2127	4.1543	4.1882				
0.450	4.1156	4.2263	4.1585	4.1987				
0.500	4.1222	4.2396	4.1648	4.2092				
0.550	4.1288	4.2526	4.1726	4.2198				
0.600	4.1349	4.2655	4.1800	4.2300				
0.650	4.1412	4.2784	4.1873	4.2404				
0.700	4.1472	4.2914	4.1947	4.2509				
0.750	4.1532	4.3045	4.2015	4.2614				
0.800	4.1586	4.3175	4.2079	4.2724				
0.850	4.1637	4.3304	4.2137	4.2842				
0.900	4.1684	4.3433	4.2191	4.2964				
0.950	4.1727	4.3565	4.2240	4.3087				
1.000	4.1767	4.3696	4.2283	4.3211				
1.050	4.1797	4.3828	4.2320	4.3334				
1.100	4.1826	4.3957	4.2357	4.3458				
1.150	4.1847	4.4086	4.2389	4.3585				
1.200	4.1869	4.4234	4.2416	4.3713				
1.250	4.1886	4.4412	4.2434	4.3874		4.1893		
1.286							4.3286	4.3286
1.300	4.1906	4.4654	4.2461	4.4083		4.1927	4.2811	4.3763
1.350	4.1933	4.4980	4.2532	4.4380		4.1984	4.2839	4.4027
1.400	4.1973	4.5417	4.2657	4.4741		4.2084	4.2970	4.4360
1.450	4.2047	4.6011	4.2830	4.5200		4.2247	4.3162	4.4781
1.484						4.2412		
1.500	4.2159	4.6933	4.3085	4.5782		4.2506	4.3411	4.5303
1.517					4.2347	4.2630		
1.536			4.3245		4.2536	4.2812		
1.560	4.2333	4.7734	4.3248	4.6500	4.2644	4.3057	4.3696	4.5951
1.577			4.3303					
1.588					4.2965			
1.600	4.2563	4.7821		4.6819			4.4067	4.6187
1.617			4.3515					
1.622					4.3394			
1.634							4.4521	4.5870
1.644							4.5026	4.5026
1.660	4.2964	4.7537		4.6272				
1.667			4.4068					
1.674			4.5187	4.5187				
1.700	4.3540	4.6707						
1.736	4.5140	4.5140						
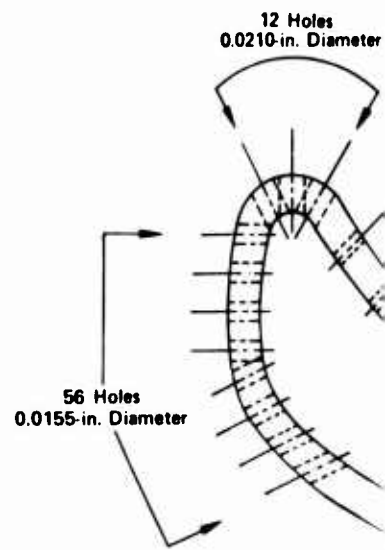
Figure 4. Nozzle Airfoil and Insert Geometries.

51

12 Holes
0.0210-in. Diameter

30 Holes
0.0105-in. Diameter

56 Holes
0.0155-in. Diameter

0.028-in.
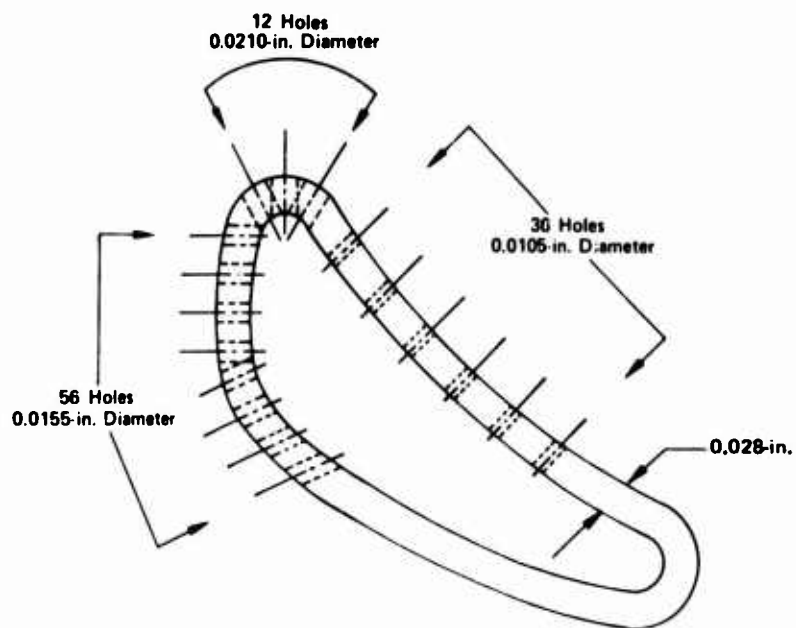
View Showing Insert Only

1.5880

Y_8

Y_7

Y_6 Y_5

Y_2

Y_4

Y_3

Y_1

X

Reference Planes

d Insert Geometries.

Insert Contour
D
Y_8
4.3286
4.3763
4.4027
4.4360
4.4781
4.5303
4.5951
4.6187
4.5870
4.5025
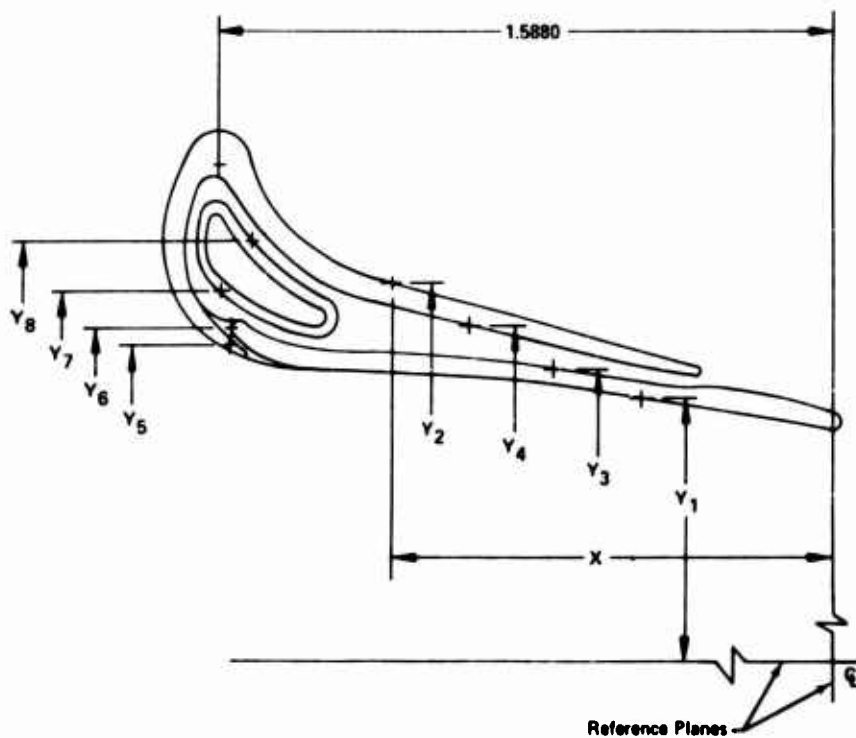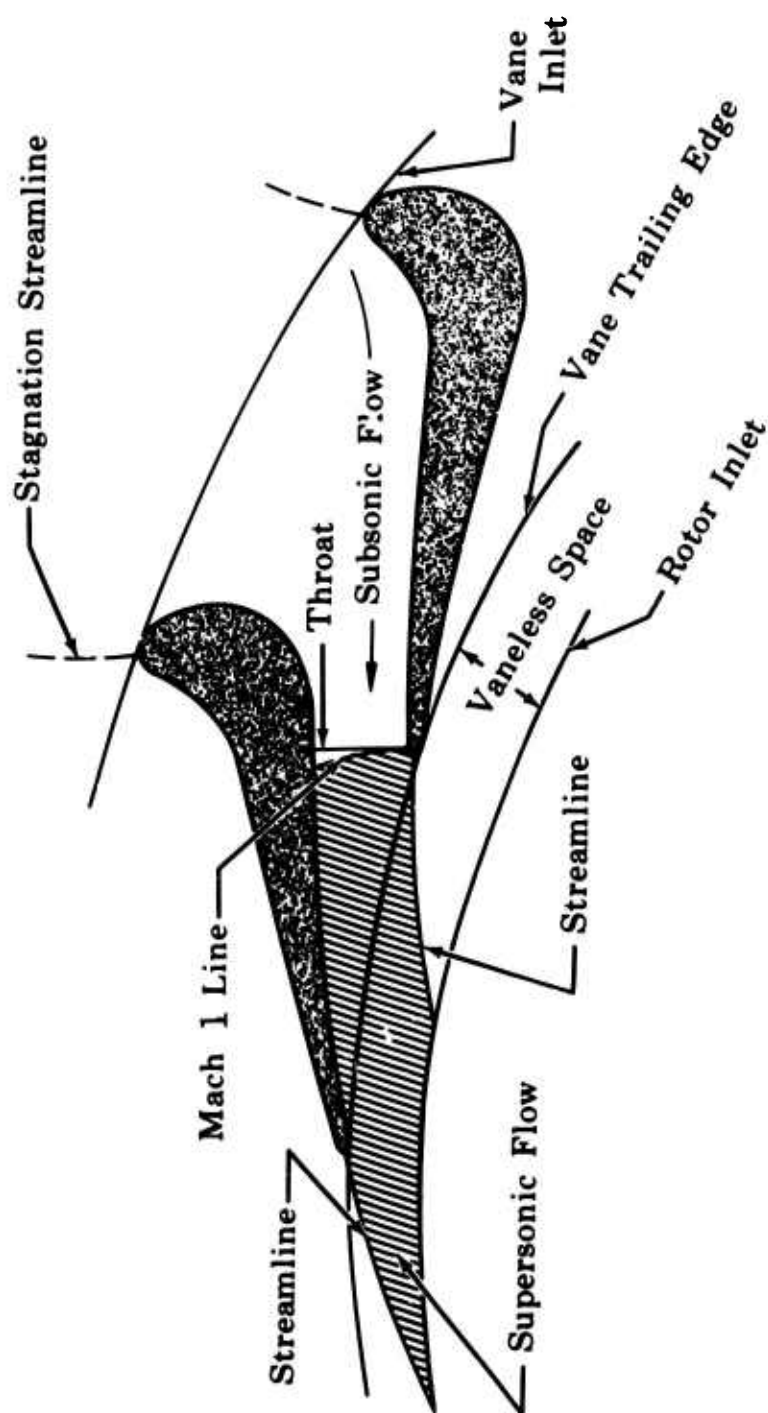
Figure 5. Reflex Vane Schematic.

53
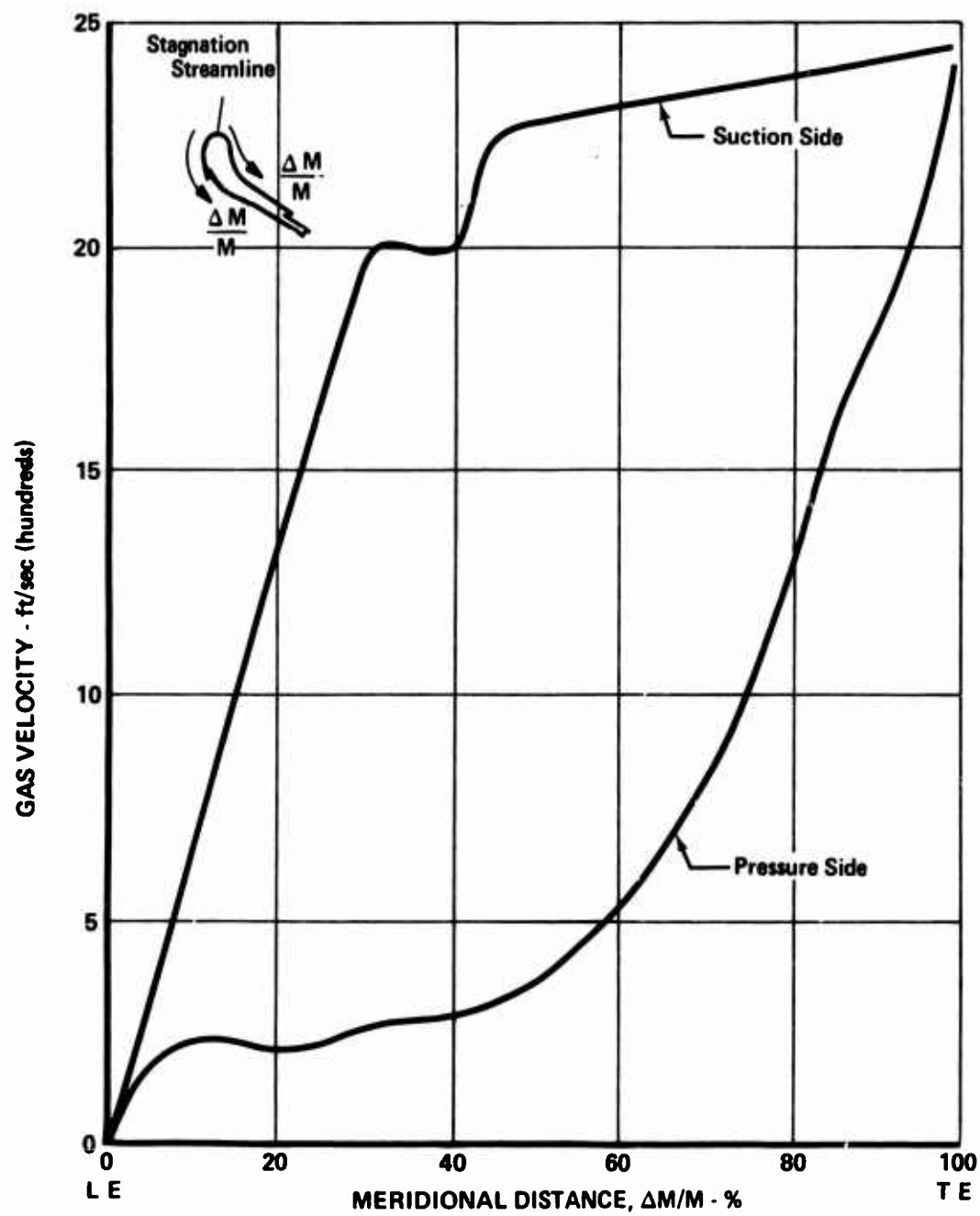
Figure 6. Nozzle Vane Velocity Distribution.

54
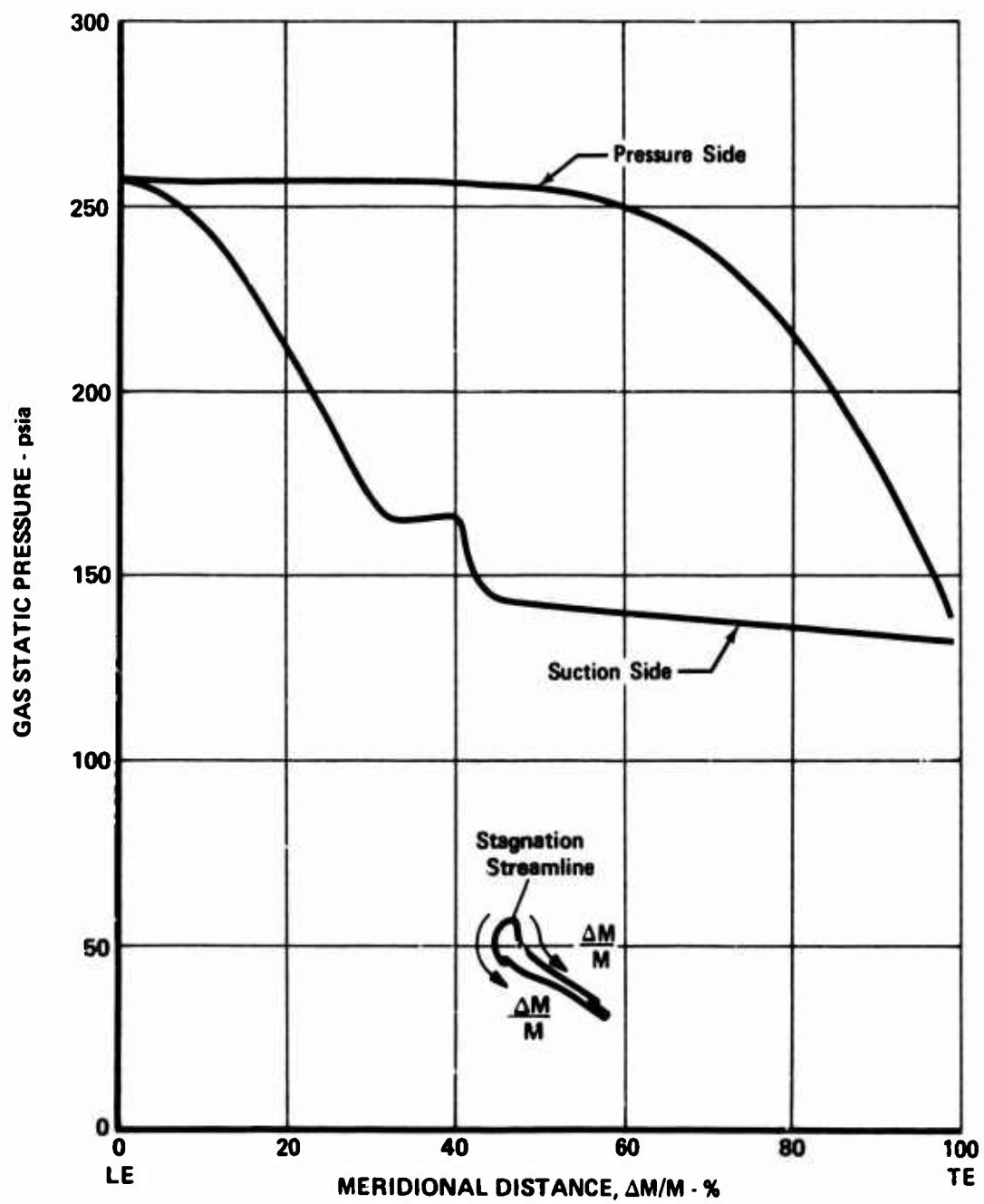
Figure 7. Nozzle Vane Pressure Distribution.
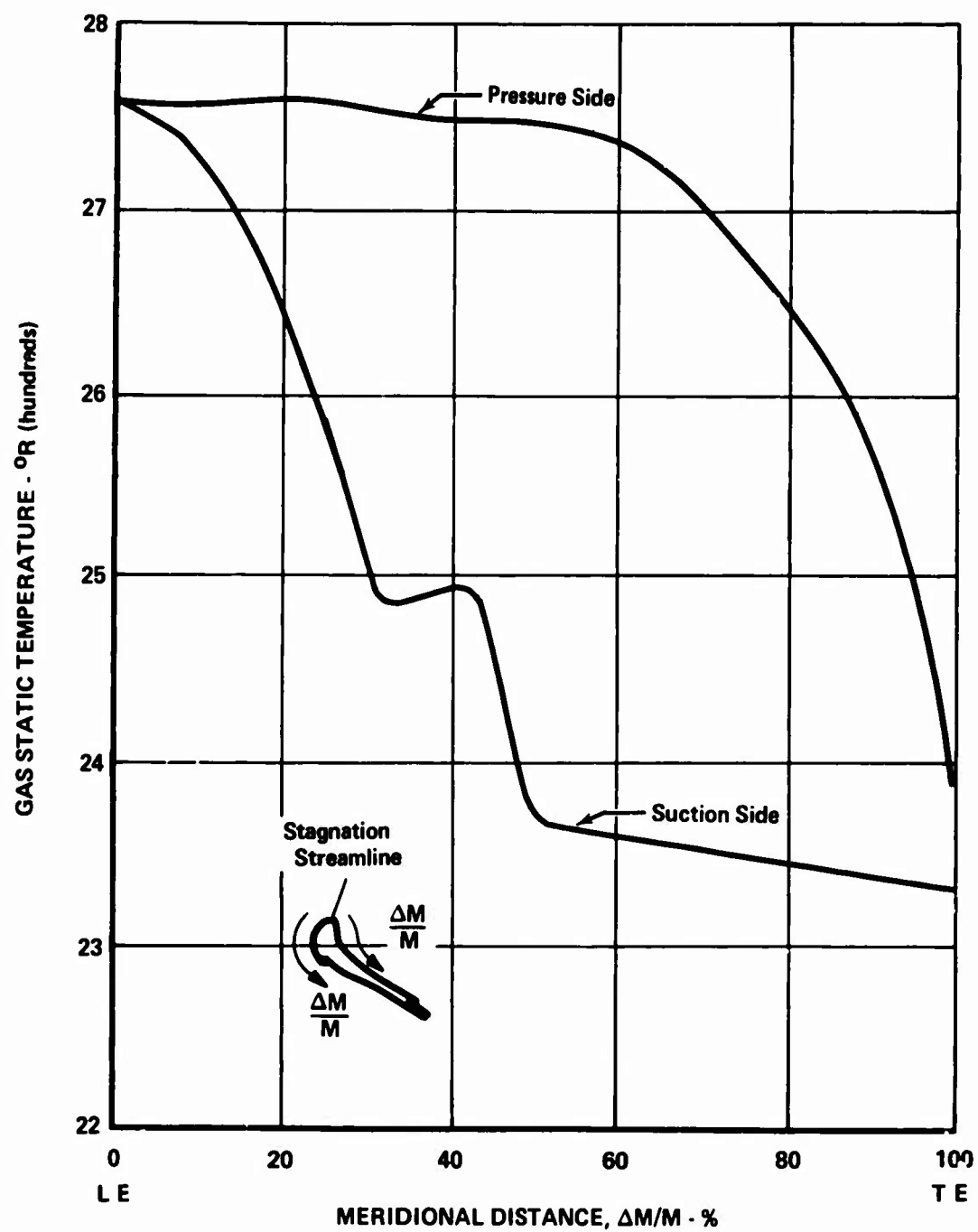
Figure 8.   Nozzle Vane Gas Temperature Distribution.

Insert

5 Fins

2 Fins

3 Fins

4%

2%

Scale
(in.)

0   0.1   0.2   0.3
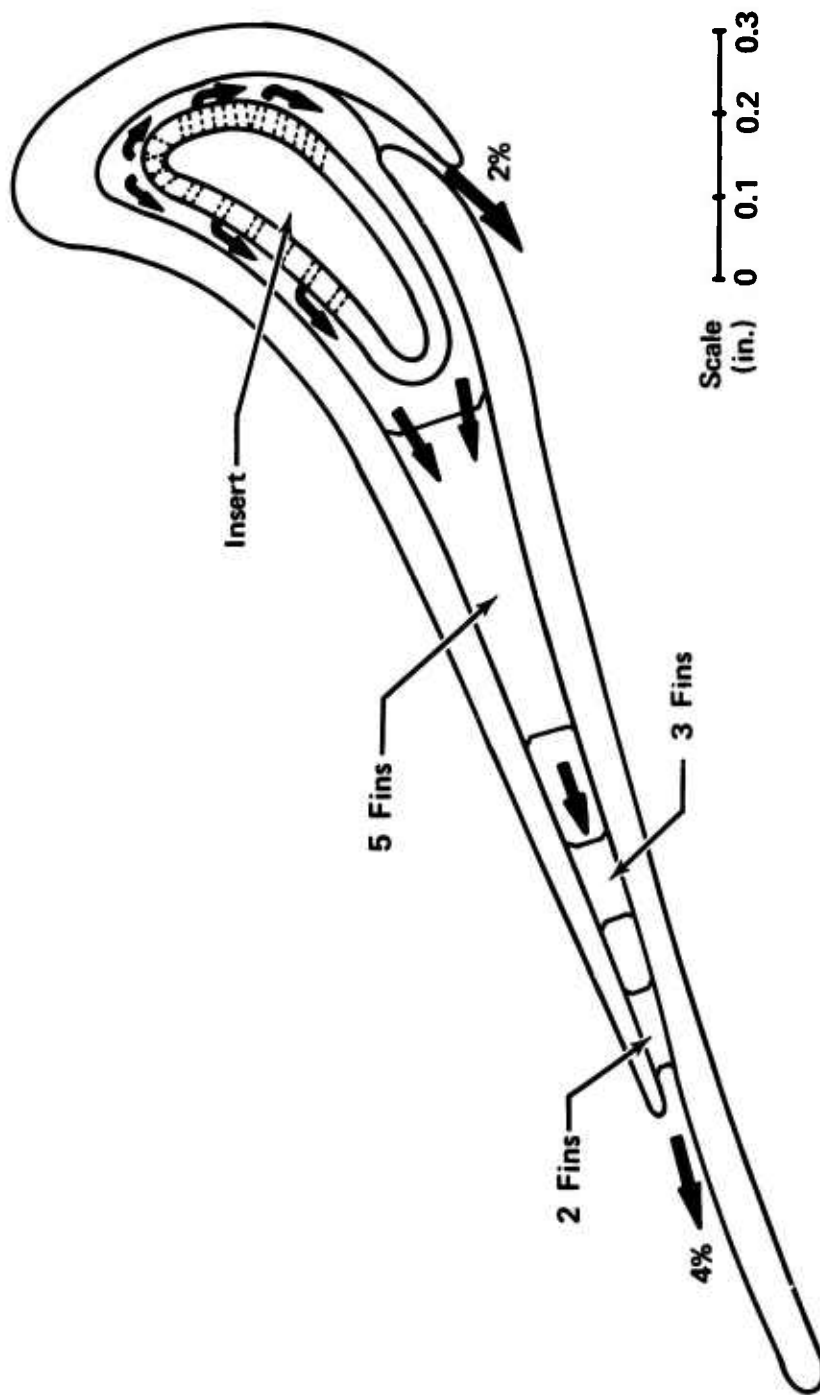
Figure 9.   Nozzle Vane Cooling Configuration.

57

Units: $\frac{Btu}{hr}/ft^2 \cdot {}^oF$
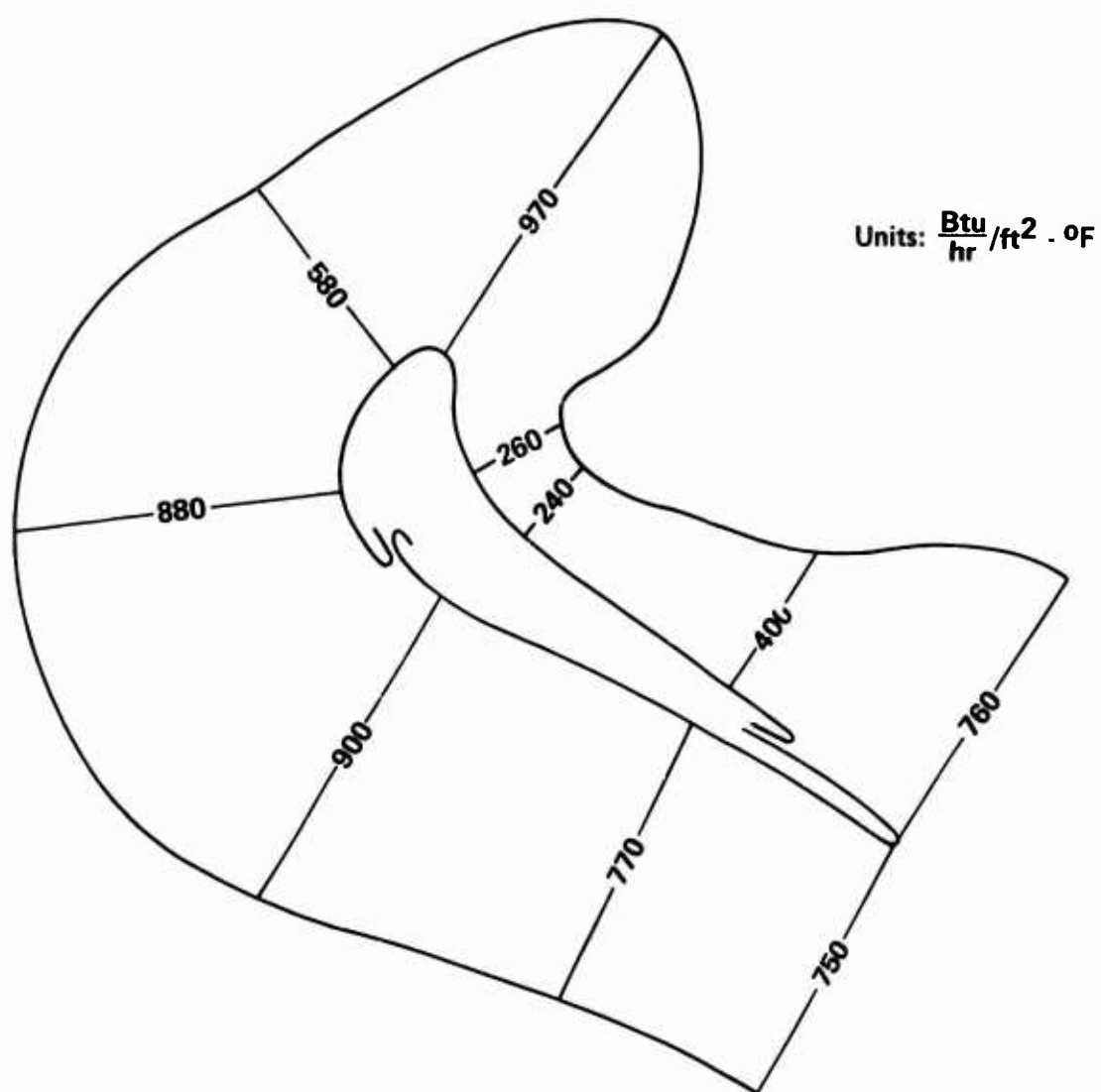
Figure 10.   Nozzle Vane Heat Transfer Coefficients (Gas Side).

58

UNITS: $\frac{Btu}{hr}$ /ft2 . °F
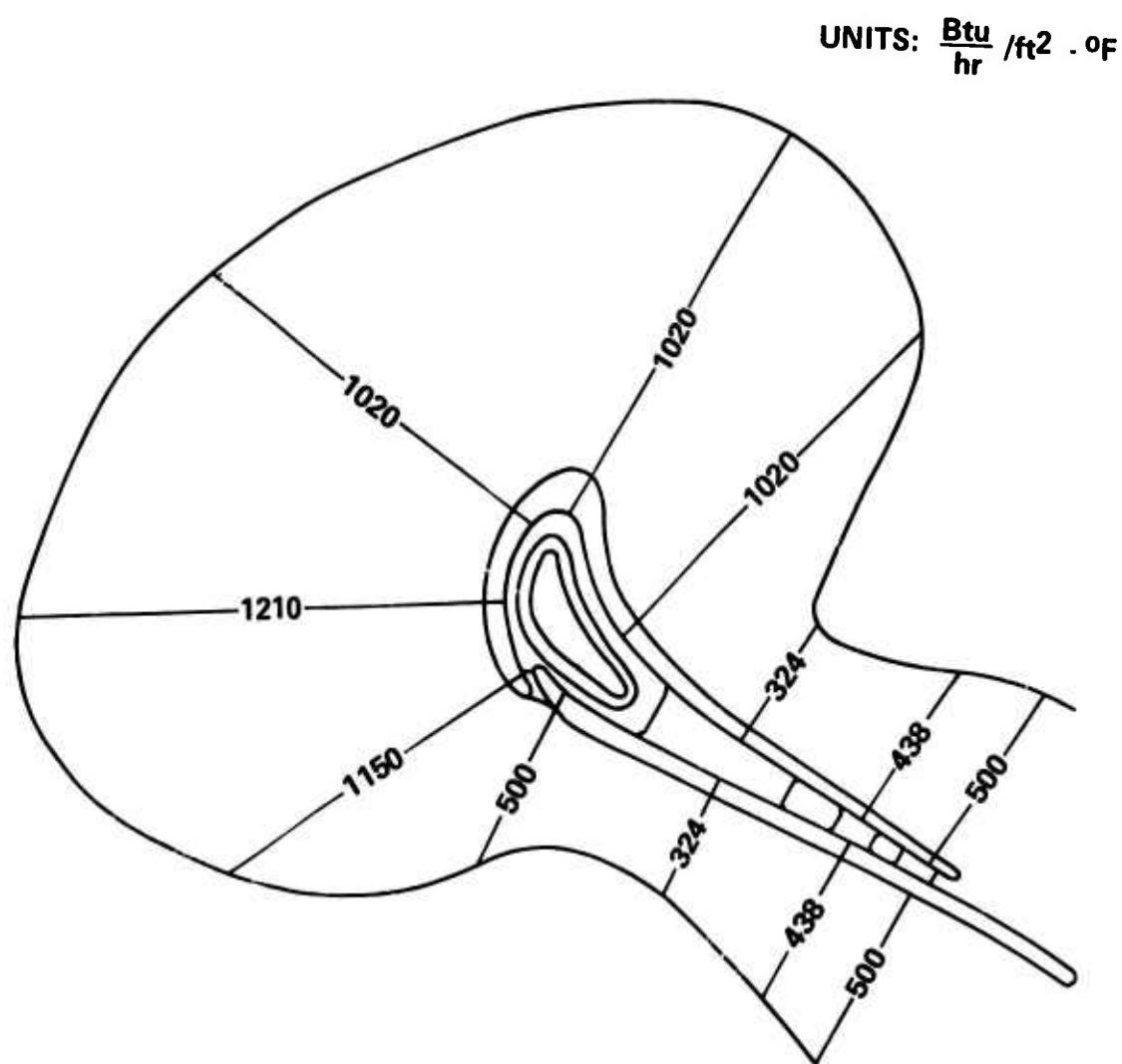
Figure 11. Nozzle Vane Heat Transfer Coefficients (Internal).
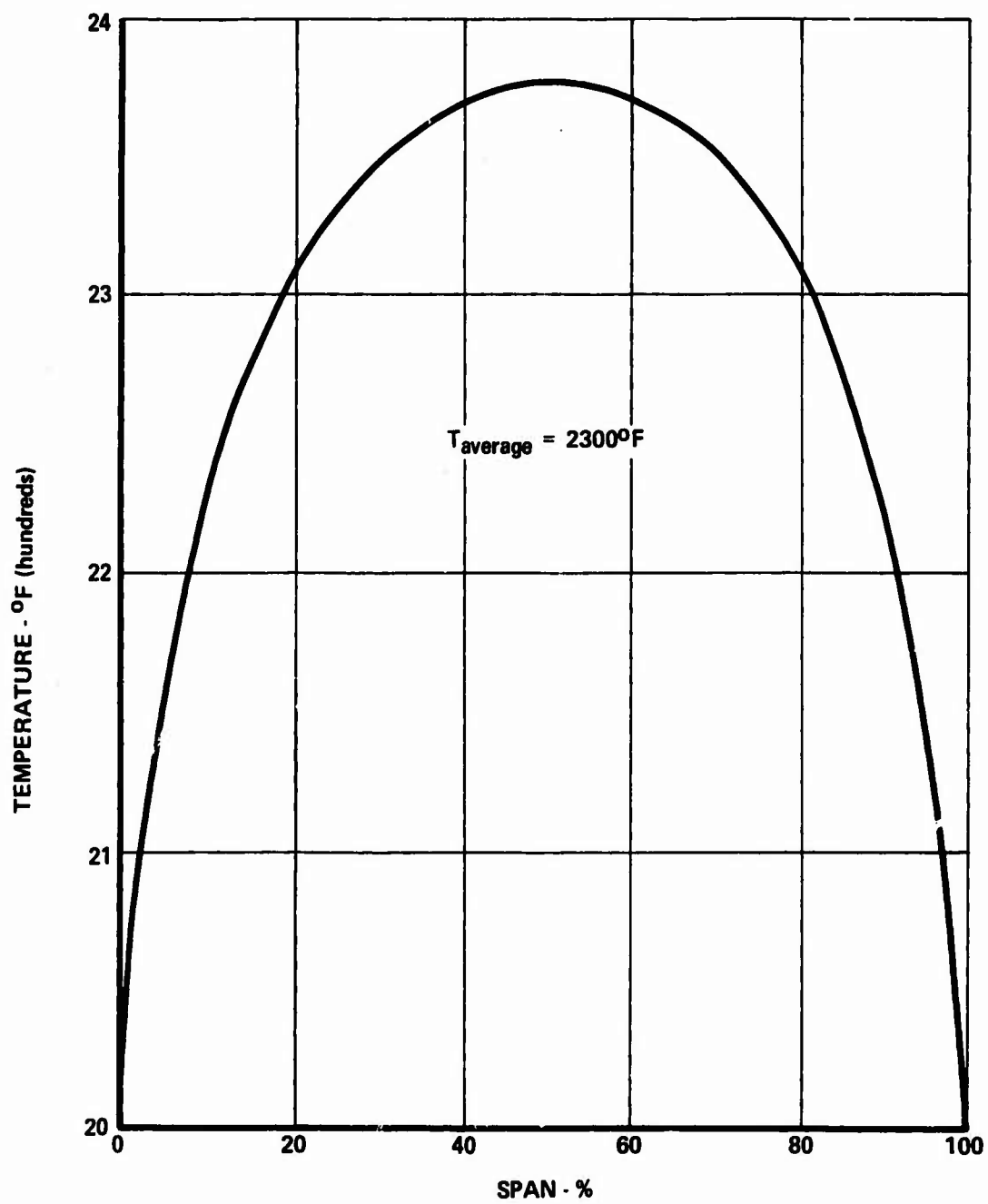
Figure 12.   Nozzle Vane Inlet Gas Temperature Profile.

Vane Midspan Metal Temperature, °F,
for TIT = 2300°F
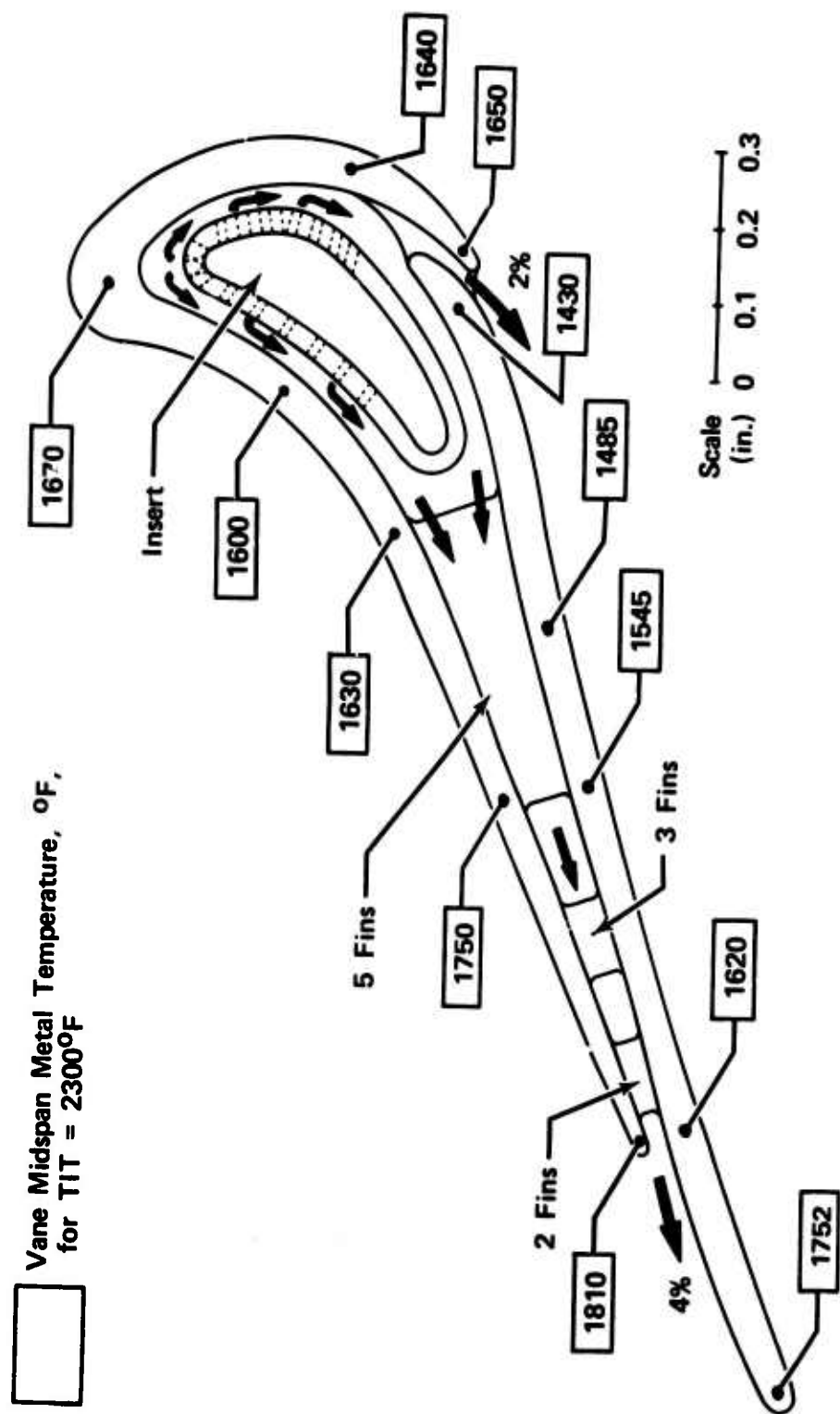
Figure 13. Nozzle Vane Metal Temperatures.

61
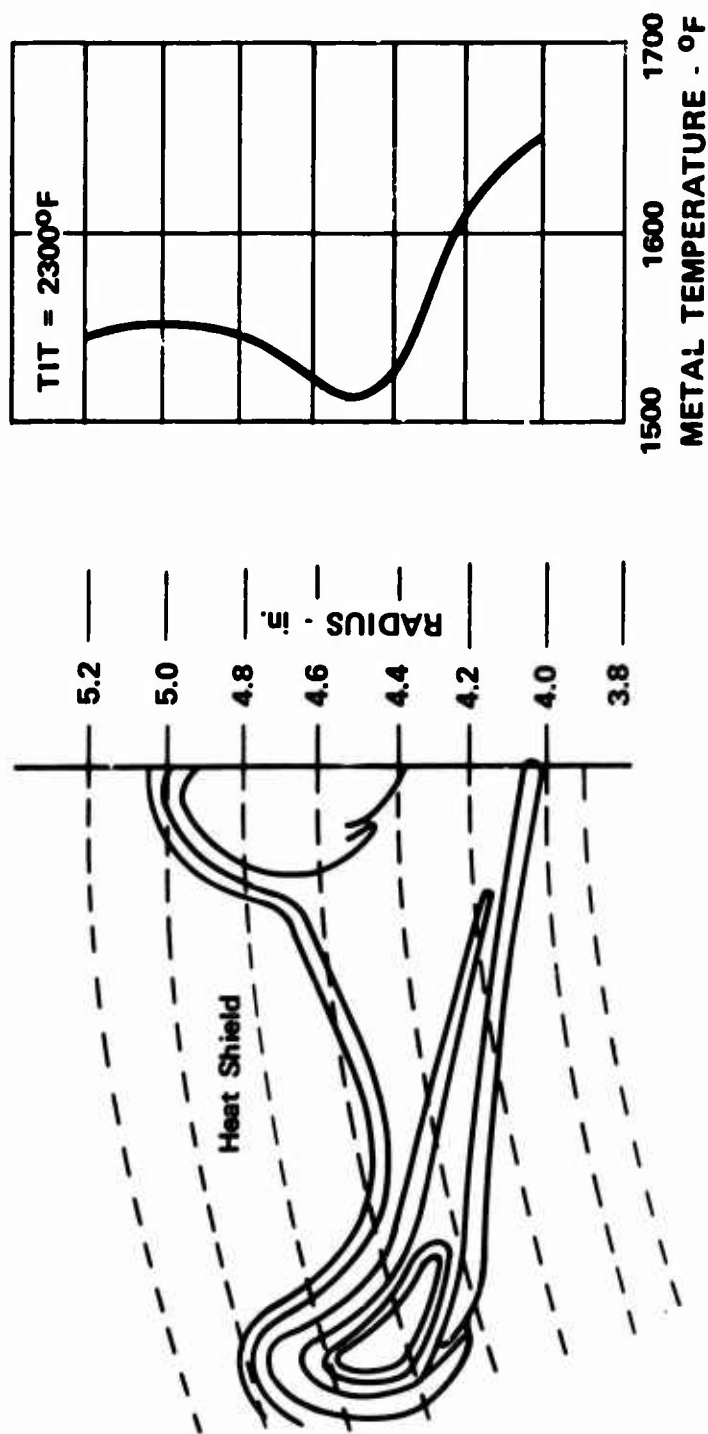
Figure 14. Nozzle Platform Metal Temperatures.
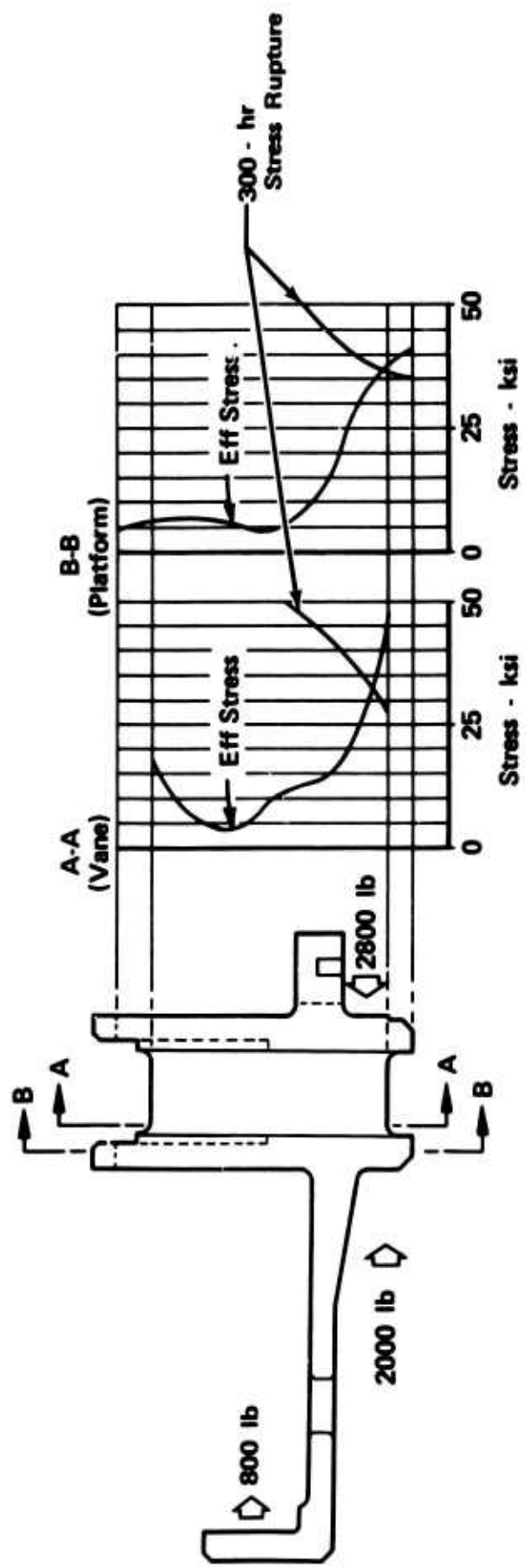
Figure 15. Nozzle Vane and Platform Stress Distribution.
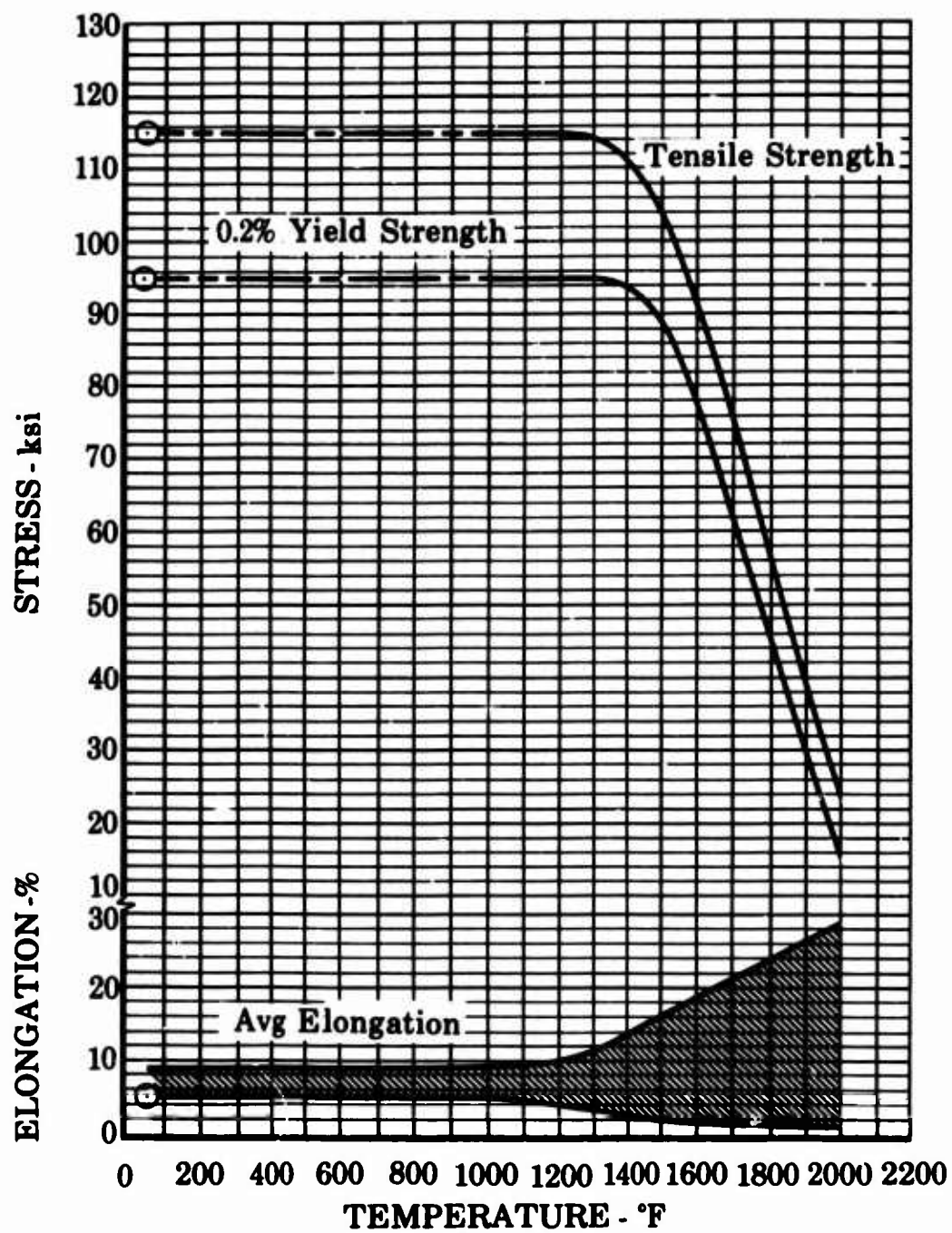
Figure 16. Tensile Properties of IN100 (PWA 658).

64
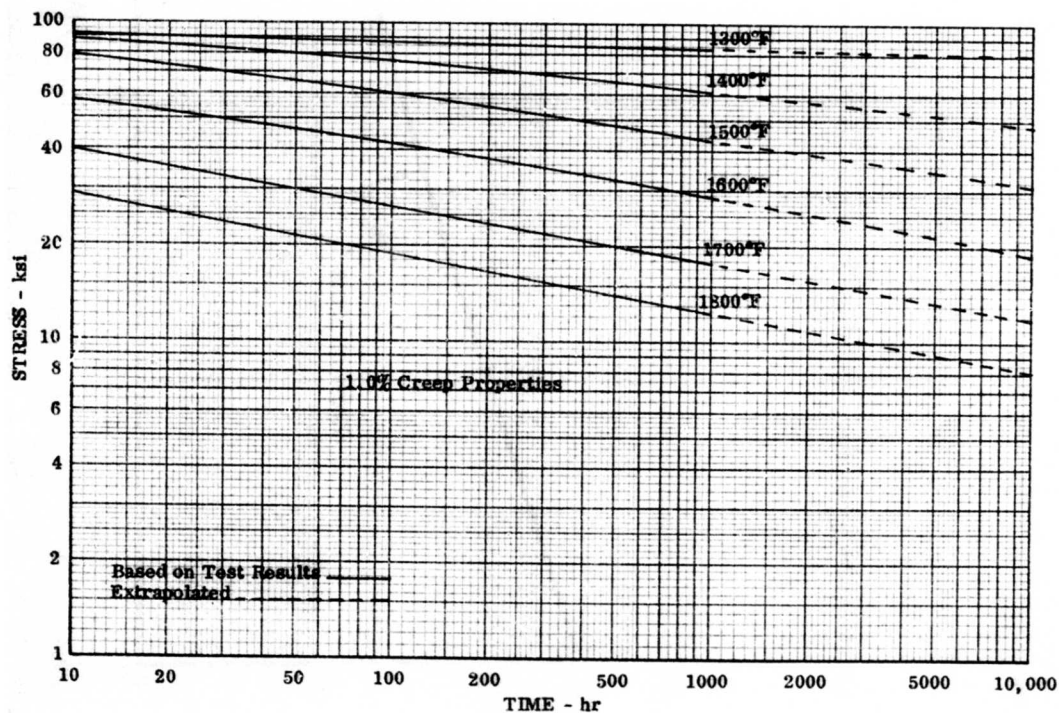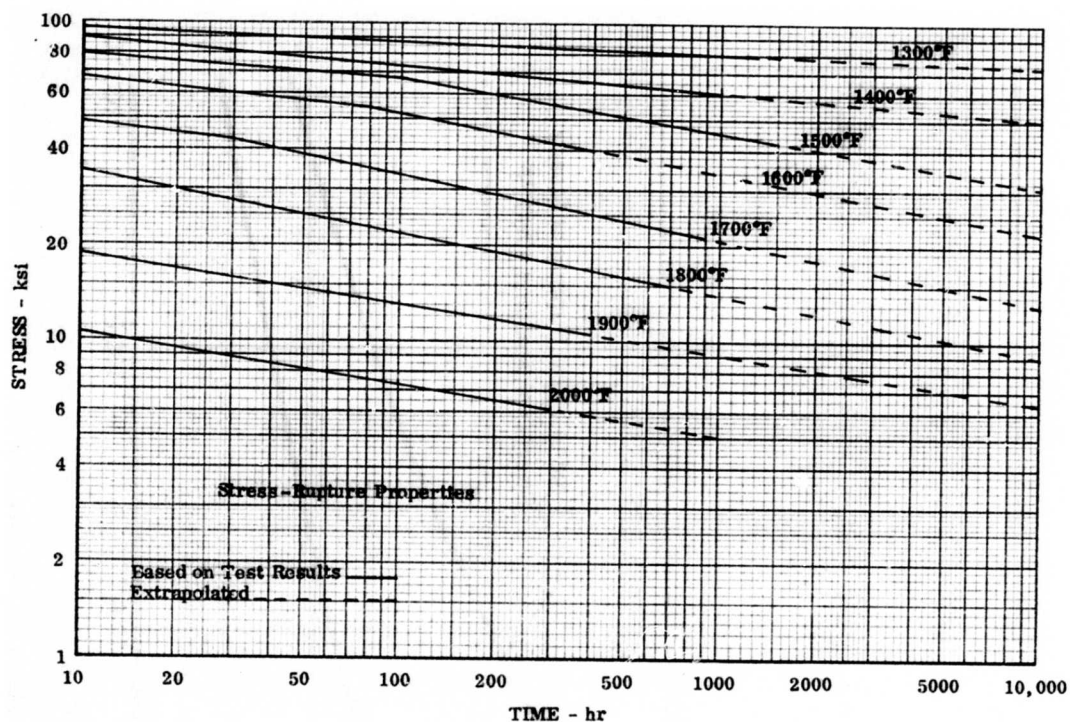
Figure 17. Stress-Rupture and 1% Creep Properties of IN100 (PWA 658).

65
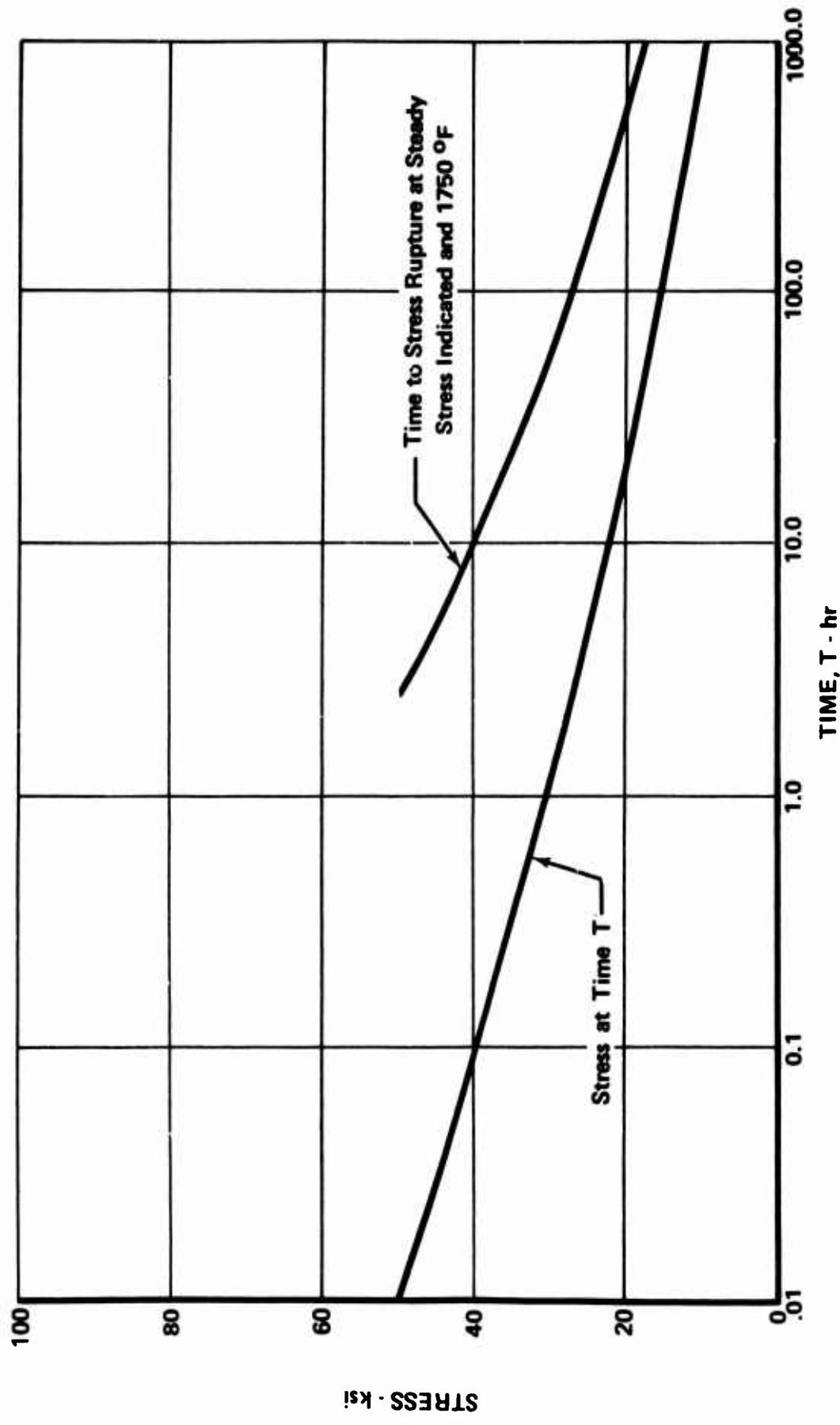
Figure 18. Stress Relaxation Study for Nozzle Vane Trailing Edge.

Time to Stress Rupture at Steady
Stress Indicated and 1750 °F

Stress at Time T

TIME, T - hr

STRESS - ksi
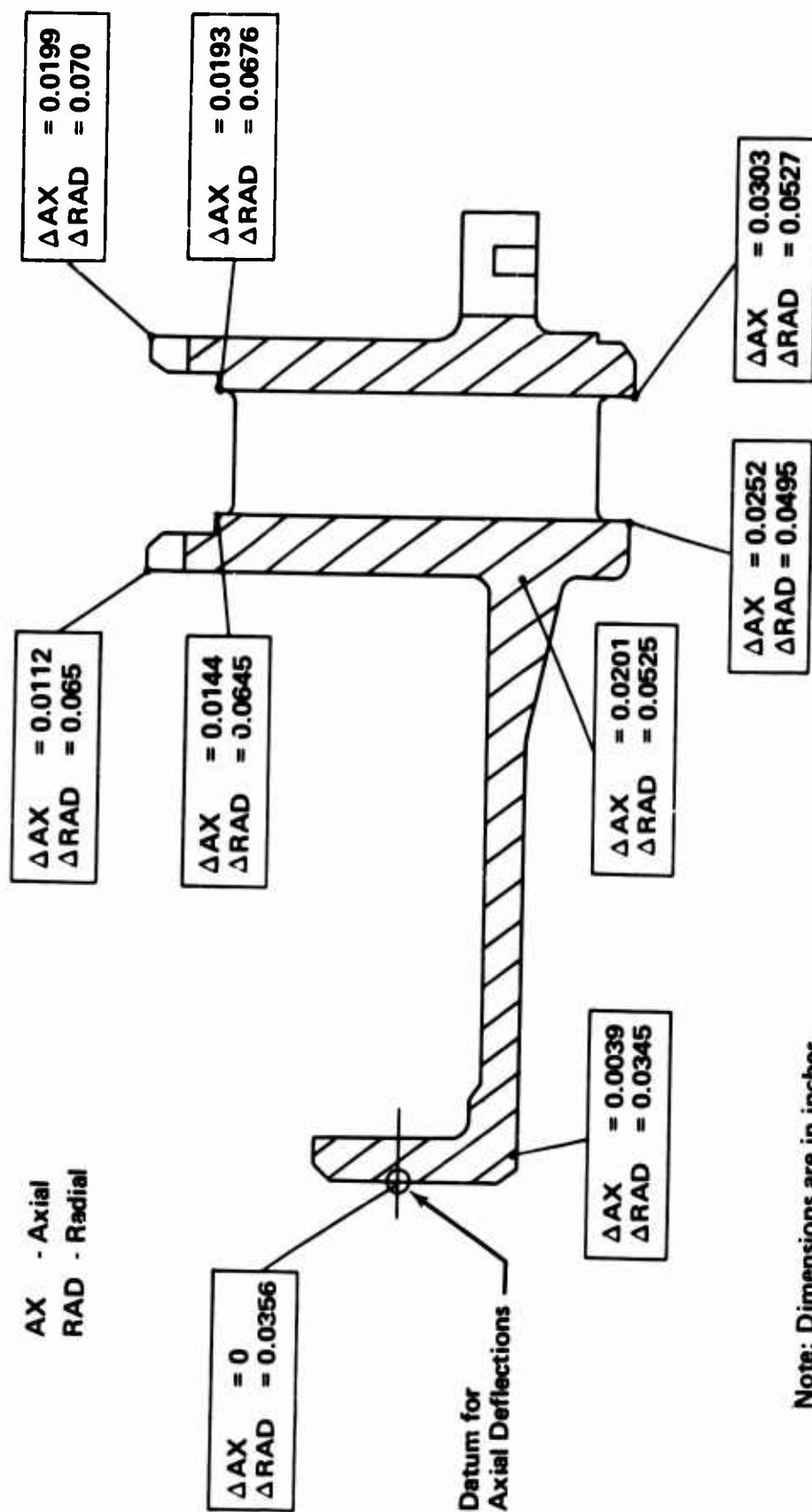
Figure 19. Nozzle Radial and Axial Deflections.

AX   - Axial
RAD - Radial

ΔAX   = 0.0199
ΔRAD = 0.070

ΔAX   = 0.0193
ΔRAD = 0.0676

ΔAX   = 0.0303
ΔRAD = 0.0527

ΔAX   = 0.0112
ΔRAD = 0.065

ΔAX   = 0.0144
ΔRAD = 0.0645

ΔAX   = 0.0201
ΔRAD = 0.0525

ΔAX   = 0.0252
ΔRAD = 0.0495

ΔAX   = 0.0039
ΔRAD = 0.0345

ΔAX   = 0
ΔRAD = 0.0356

Datum for
Axial Deflections

Note: Dimensions are in inches.

67

Figure 20. Rotor Design.
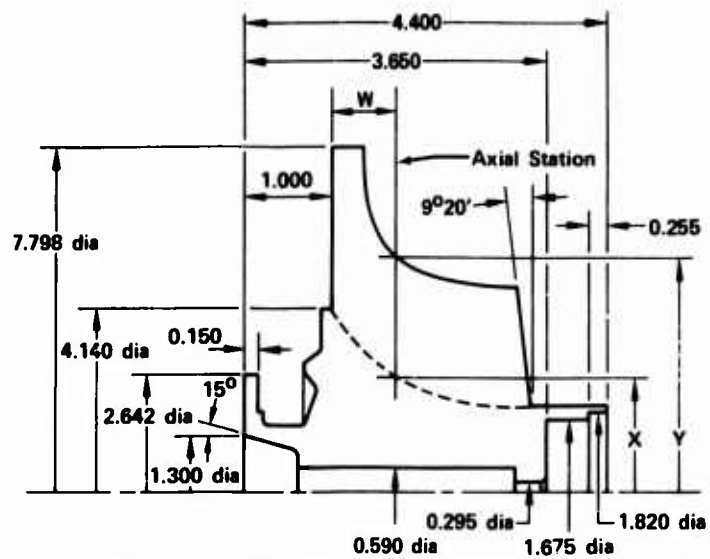
Airfoil Section Data Reference

Station W	F rad	R S	3.950	3.852	3.753	3.654	3.565	3.457	3.358	3.259	3.160	3.062	2.963	2.864	2.765	2.667	2.568	2.469	2.370	2.271
0	0.3951		0.0674	0.0686	0.0699	0.0711	0.0723	0.0735	0.0884	0.1063	0.1267	0.1501	0.1763	0.2059	0.2393	0.2765	0.3180	0.3638	0.4142	0.4691
0.200	0.1810		0.0677	0.0689	0.0701	0.0713	0.0725	0.0738	0.0872	0.1040	0.1231	0.1447	0.1691	0.1965	0.2272	0.2615	0.2995	0.3414	0.3874	0.4375
0.379	0.1933		0.0646	0.0658	0.0670	0.0682	0.0694	0.0707	0.0719	0.0731	0.0762	0.0906	0.1071	0.1256	0.1465	0.1700	0.1963	0.2256	0.2581	0.2941
0.400	0.1940		0.0642	0.0654	0.0667	0.0679	0.0691	0.0703	0.0715	0.0728	0.0740	0.0860	0.1017	0.1194	0.1394	0.1619	0.1871	0.2151	0.2464	0.2809
0.500	0.1930									0.0715	0.0727	0.0739	0.0835	0.0984	0.1152	0.1341	0.1553	0.1790	0.2054	0.2347
0.600	0.1883										0.0718	0.0730	0.0742	0.0849	0.0994	0.1159	0.1343	0.1549	0.1778	0.2033
0.800	0.1871												0.0724	0.0736	0.0759	0.0884	0.1025	0.1182	0.1357	0.1551
0.830	0.1870												0.0722	0.0734	0.0746	0.0852	0.0988	0.1139	0.1308	0.1494
0.900	0.1884												0.0716	0.0729	0.0741	0.0788	0.0912	0.1051	0.1206	0.1377
1.000	0.1896												0.0709	0.0721	0.0733	0.0746	0.0822	0.0946	0.1083	0.1236
1.100	0.1925												0.0702	0.0715	0.0727	0.0739	0.0751	0.0857	0.0980	0.1116
1.200	0.1962															0.0733	0.0745	0.0788	0.0899	0.1022
1.400	0.2036															0.0724	0.0736	0.0748	0.0790	0.0891
1.600	0.2222															0.0709	0.0722	0.0734	0.0746	0.0758
1.800	0.2429															0.0690	0.0703	0.0715	0.0727	0.0739
2.000	0.2580																0.0683	0.0695	0.0695	0.0707
2.200	0.2325																		0.0670	0.0670
2.290	0.2066																		0.0650	0.0650
2.300	0.2020																		0.0650	0.0650
2.400	0.1590																		0.0640	0.0630
2.500	0.1000																		0.0620	0.0610

Basic Camber Line

S

Basic Camber Line at Station W = Zero

F Rad

R

xial Station

0.255

X   Y

1.820 dia

1.675 dia

dia
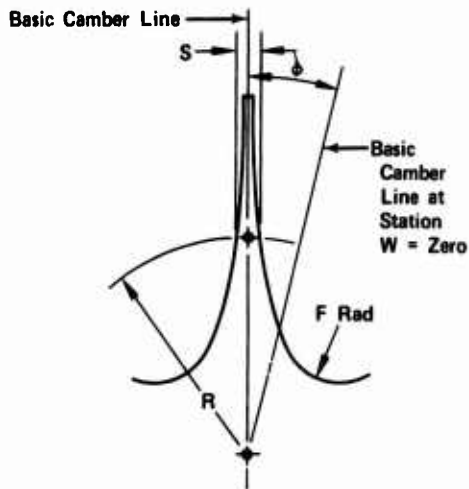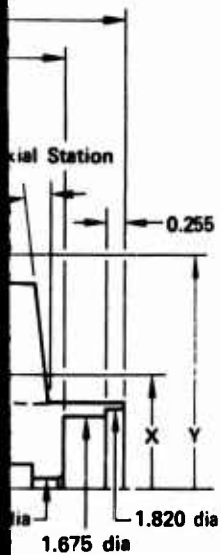
| Airfoil Section Data Reference | | | | | | | | | | | | | | | | | | | | Hub and Tip Profile Ref. | | |
.76C	2.667	2.568	2.469	2.370	2.271	2.173	2.074	1.975	1.876	1.778	1.679	1.580	1.481	1.383	1.284	1.185	1.086	0.988	ϕ	X	Y	Station W
.2393	0.2765	0.3180	0.3638	0.4142	0.4691	0.5286	0.5925	0.6605	0.7325	0.8078	0.8861	0.9667	1.0487	1.1315	1.2141	1.2955	1.3747	1.4505	0°	2.0250	3.8990	0
.2272	0.2615	0.2995	0.3414	0.3874	0.4375	0.4916	0.5496	0.6114	0.6767	0.7451	0.8162	0.8896	0.9646	1.0408	1.1176	1.1943	1.2703	1.3451	0°	1.8080	3.8990	0.200
.1465	0.1700	0.1963	0.2256	0.2581	0.2941	0.3336	0.3767	0.4235	0.4739	0.5278	0.5849	0.6451	0.7081	0.7735	0.8410	0.9102	0.9809	1.0526	0°	1.6240	3.8990	0.379
.1394	0.1619	0.1871	0.2151	0.2464	0.2809	0.3190	0.3605	0.4057	0.4545	0.5067	0.5622	0.6208	0.6822	0.7462	0.8123	0.8804	0.9499	1.0208	0°	1.6050	3.5160	0.400
.1152	0.1341	0.1553	0.1790	0.2054	0.2347	0.2671	0.3027	0.3417	0.3840	0.4296	0.4786	0.5305	0.5854	0.6430	0.7031	0.7653	0.8296	0.8956	0°	1.5240	3.0838	0.500
.0994	0.1159	0.1343	0.1549	0.1778	0.2033	0.2315	0.2627	0.2969	0.3341	0.3745	0.4179	0.4644	0.5136	0.5656	0.6201	0.6769	0.7358	0.7968	0°5'	1.4510	2.8700	0.600
.0759	0.0884	0.1025	0.1182	0.1357	0.1551	0.1766	0.2003	0.2265	0.2552	0.2864	0.3203	0.3568	0.3959	0.4374	0.4814	0.5275	0.5758	0.6262	0°27'	1.3270	2.6397	0.800
.0746	0.0852	0.0988	0.1139	0.1308	0.1494	0.1701	0.1930	0.2181	0.2457	0.2758	0.3084	0.3436	0.3813	0.4215	0.4639	0.5086	0.5554	0.6042	0°31'	1.3110	2.6160	0.830
.0741	0.0788	0.0912	0.1051	0.1206	0.1377	0.1567	0.1776	0.2006	0.2258	0.2534	0.2833	0.3157	0.3604	0.3873	0.4265	0.4679	0.5112	0.5566	0°47'	1.2750	2.5710	0.900
.0733	0.0746	0.0822	0.0946	0.1083	0.1236	0.1404	0.1588	0.1792	0.2014	0.2258	0.2522	0.2808	0.3116	0.3444	0.3793	0.4162	0.4549	0.4954	1°16'	1.2270	2.5210	1.000
.0727	0.0739	0.0751	0.0857	0.0980	0.1116	0.1265	0.1429	0.1609	0.1806	0.2021	0.2254	0.2507	0.2778	0.3085	0.3378	0.3705	0.4048	0.4409	1°57'	1.1850	2.4815	1.100
	0.0733	0.0745	0.0788	0.0899	0.1022	0.1156	0.1303	0.1463	0.1639	0.1829	0.2036	0.2260	0.2500	0.2757	0.3031	0.3320	0.3624	0.3942	2°49'	1.1460	2.4502	1.200
	0.0724	0.0736	0.0748	0.0790	0.0891	0.1003	0.1124	0.1254	0.1395	0.1548	0.1712	0.1889	0.2078	0.2279	0.2492	0.2716	0.2951	0.3197	5°20'	1.0840	2.4080	1.400
	0.0709	0.0722	0.0734	0.0746	0.0758	0.0844	0.0941	0.1046	0.1157	0.1276	0.1403	0.1537	0.1680	0.1831	0.1990	0.2156	0.2328	0.2507	9°10'	1.0420	2.3763	1.600
	0.0690	0.0703	0.0715	0.0727	0.0739	0.0752	0.0775	0.0857	0.0945	0.1038	0.1135	0.1236	0.1342	0.1453	0.1568	0.1686	0.1808	0.1932	14°16'	1.0140	2.3570	1.800
			0.0683	0.0695	0.0707	0.0719	0.0732	0.0744	0.0756	0.0786	0.0860	0.0938	0.1018	0.1099	0.1182	0.1266	0.1351	0.1436	20°34'	0.9980	2.3410	2.000
				0.0670	0.0670	0.0670	0.0670	0.0670	0.0670	0.0670	0.0670	0.0690	0.0750	0.0800	0.0870	0.0930	0.0980	0.1040	27°52'	0.9896	2.3258	2.200
				0.0650	0.0650	0.0650	0.0650	0.0650	0.0640	0.0640	0.0580	0.0600	0.0640	0.0680	0.0740	0.0770	0.0810	0.0860	31°15'	0.9876	2.3191	2.290
				0.0650	0.0650	0.0650	0.0640	0.0640	0.0640	0.0630	0.0580	0.0580	0.0630	0.0670	0.0720	0.0760	0.0790	0.0840	31°38'	0.9876		2.300
				0.0640	0.0630	0.0620	0.0610	0.0600	0.0580	0.0560	0.0540	0.0520	0.0540	0.0550	0.0570	0.0590	0.0610	0.0640	35°30'	0.9876		2.400
				0.0620	0.0610	0.0600	0.0570	0.0550	0.0530	0.0520	0.0500	0.0490	0.0470	0.0460	0.0450	0.0430	0.0430	0.0440	39°21'	0.9876		2.500
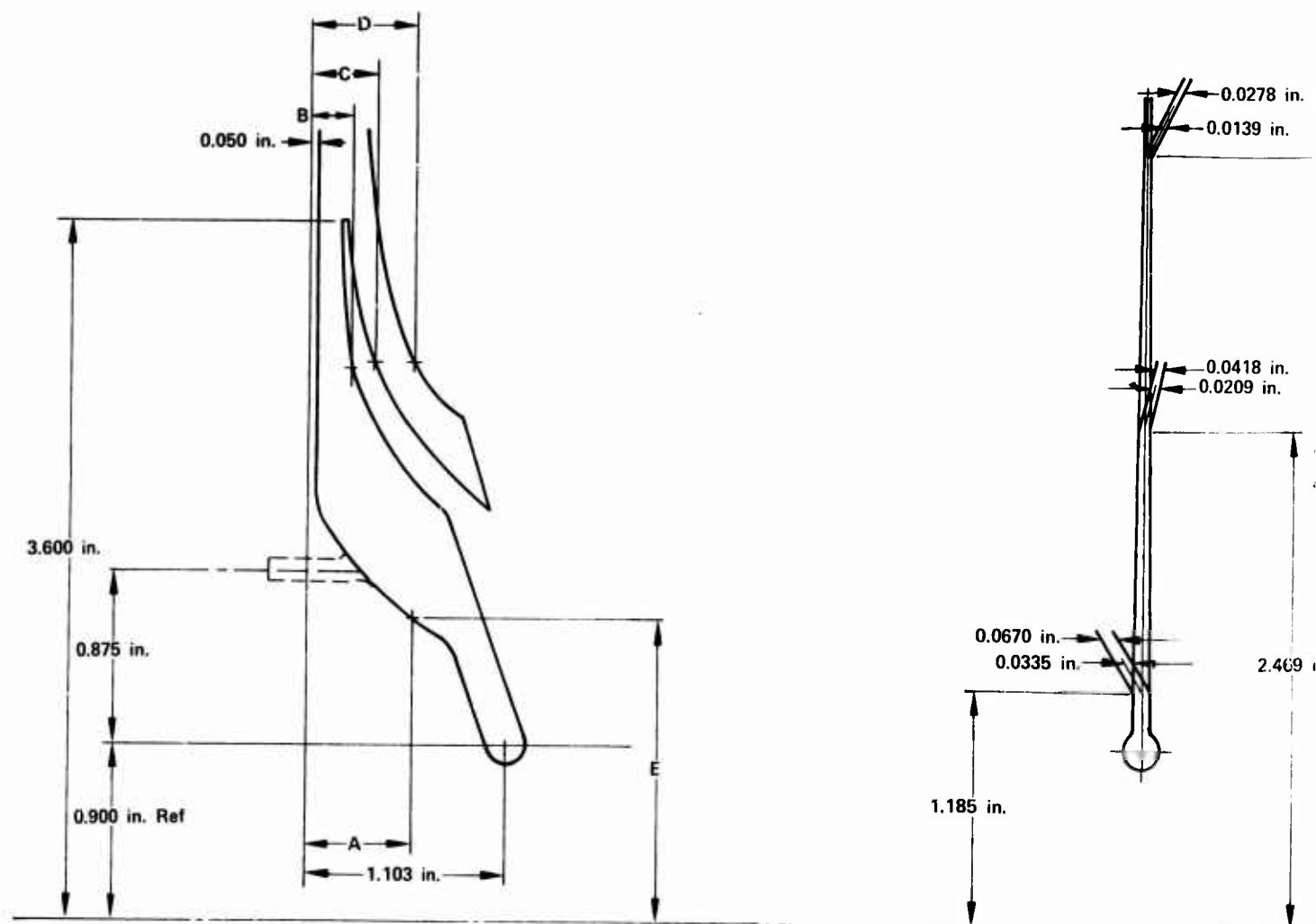
Figure 21. Rotor Cooling Passage Design (Core Geometry).
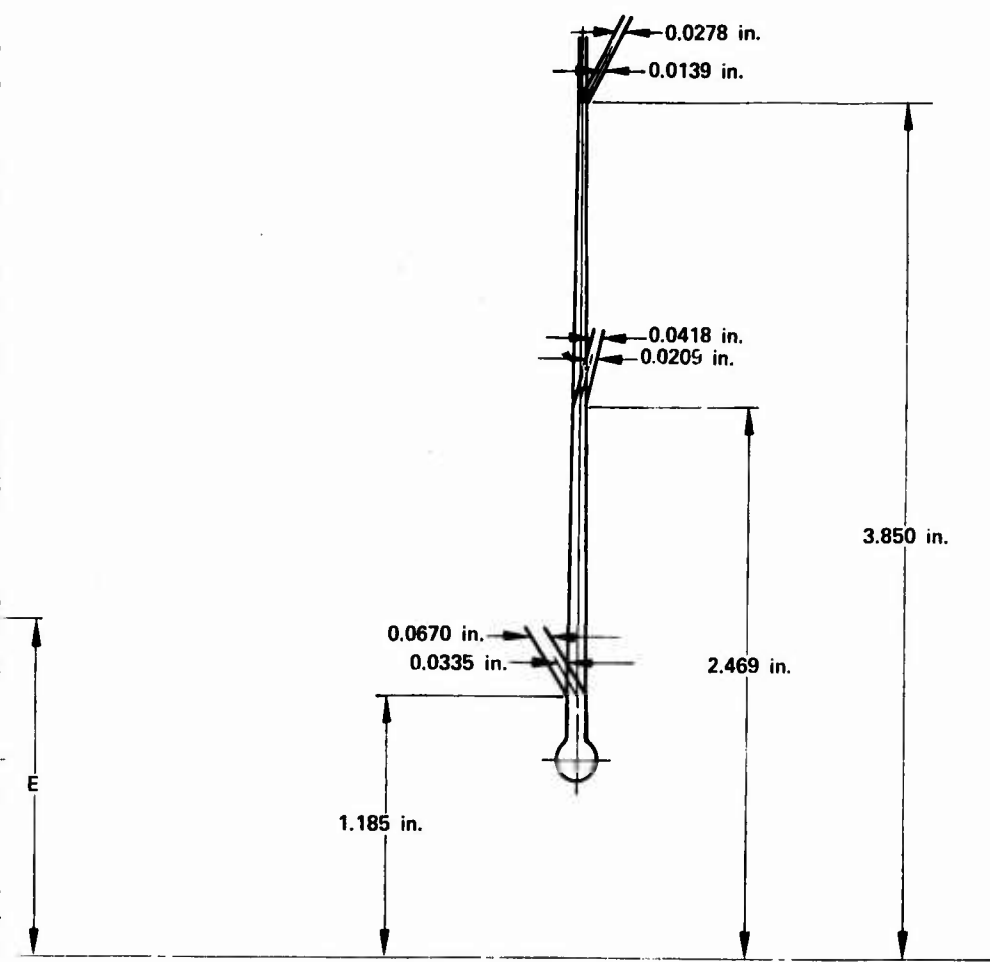
Core Contour Data					
E	B	C	D	E	A
3.899	–	–	0.3290	1.879	0.200
3.555	0.185	0.205	0.3435	1.771	0.300
3.457	0.185	0.205	0.3535	1.670	0.400
3.259	0.185	0.225	0.3940	1.587	0.500
3.062	0.190	0.265	0.4535	1.512	0.600
2.864	0.225	0.330	0.5400	1.446	0.700
2.667	0.290	0.440	0.6935	–	–
2.469	0.395	0.565	1.0000*	–	–
2.271	0.550	0.740	–	–	–
2.074	0.745	1.000	–	–	–
1.975	0.795	1.165*	–	–	–
1.185	1.100	–	–	–	–

*Extended Points

Design (Core Geometry).
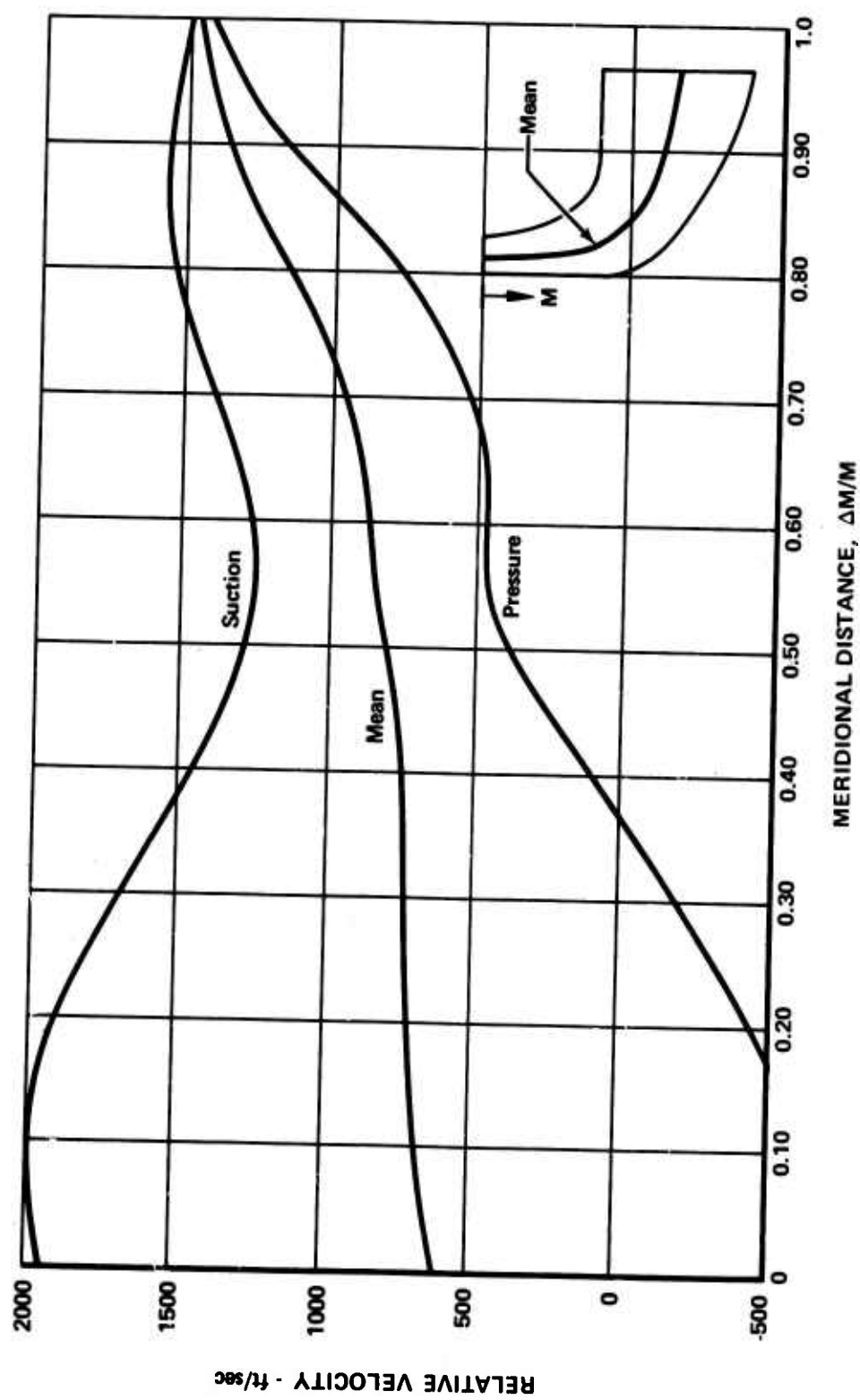
Figure 23. Rotor Velocity Distribution (Mean).

74
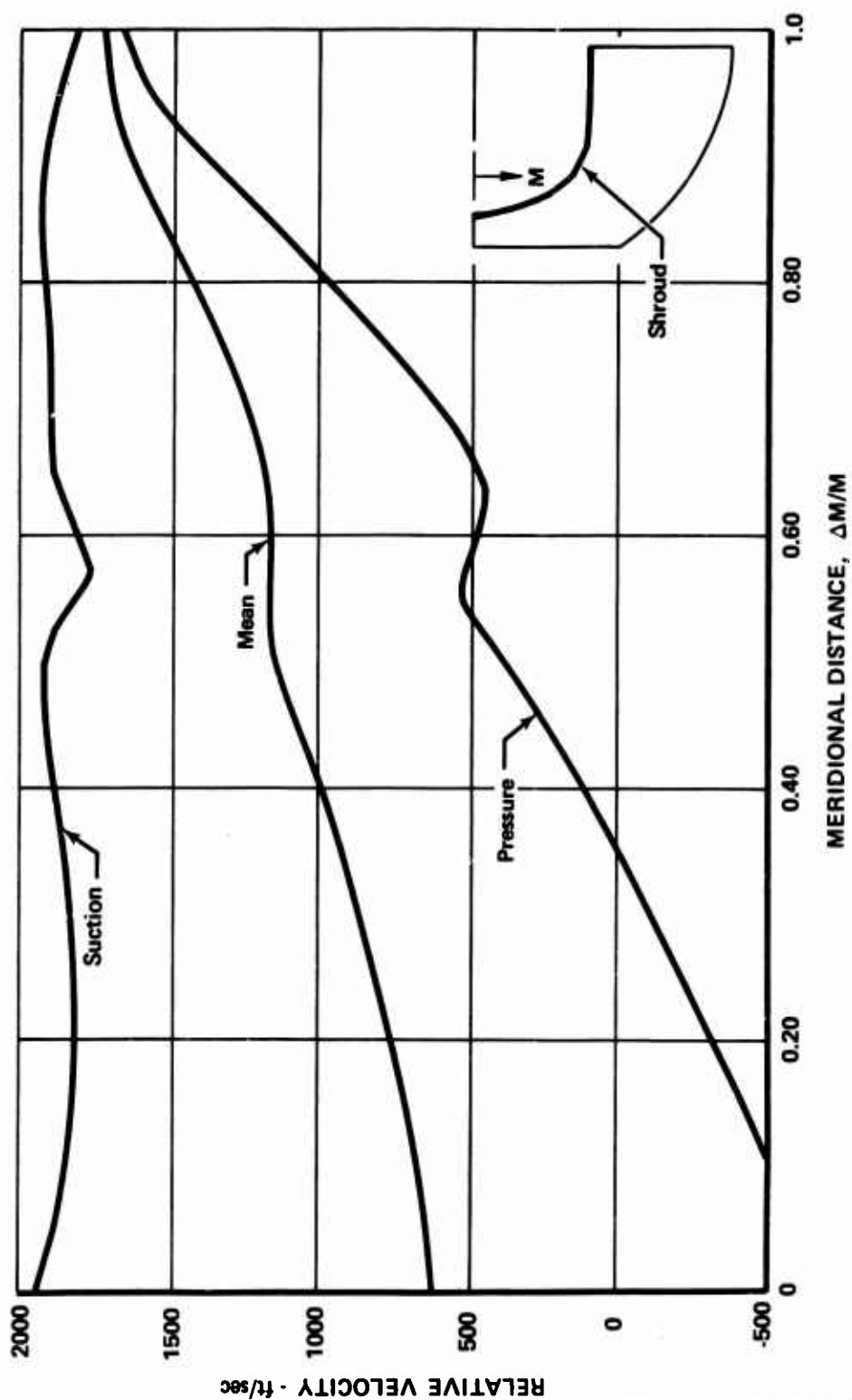
Figure 22. Rotor Velocity Distribution (Shroud Side).
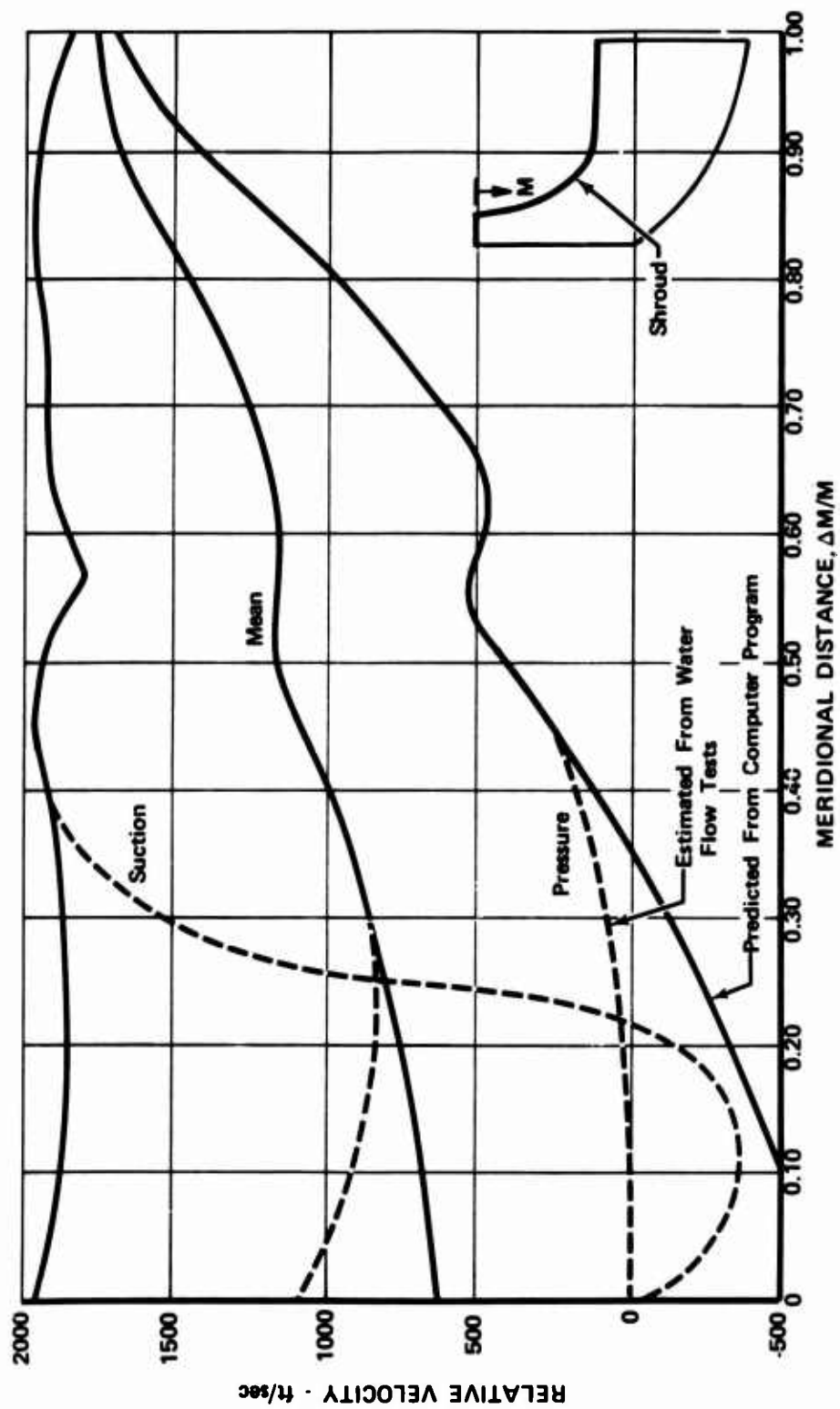
Figure 25. Rotor Velocity Distribution for Heat Transfer Analysis (Shroud Side).
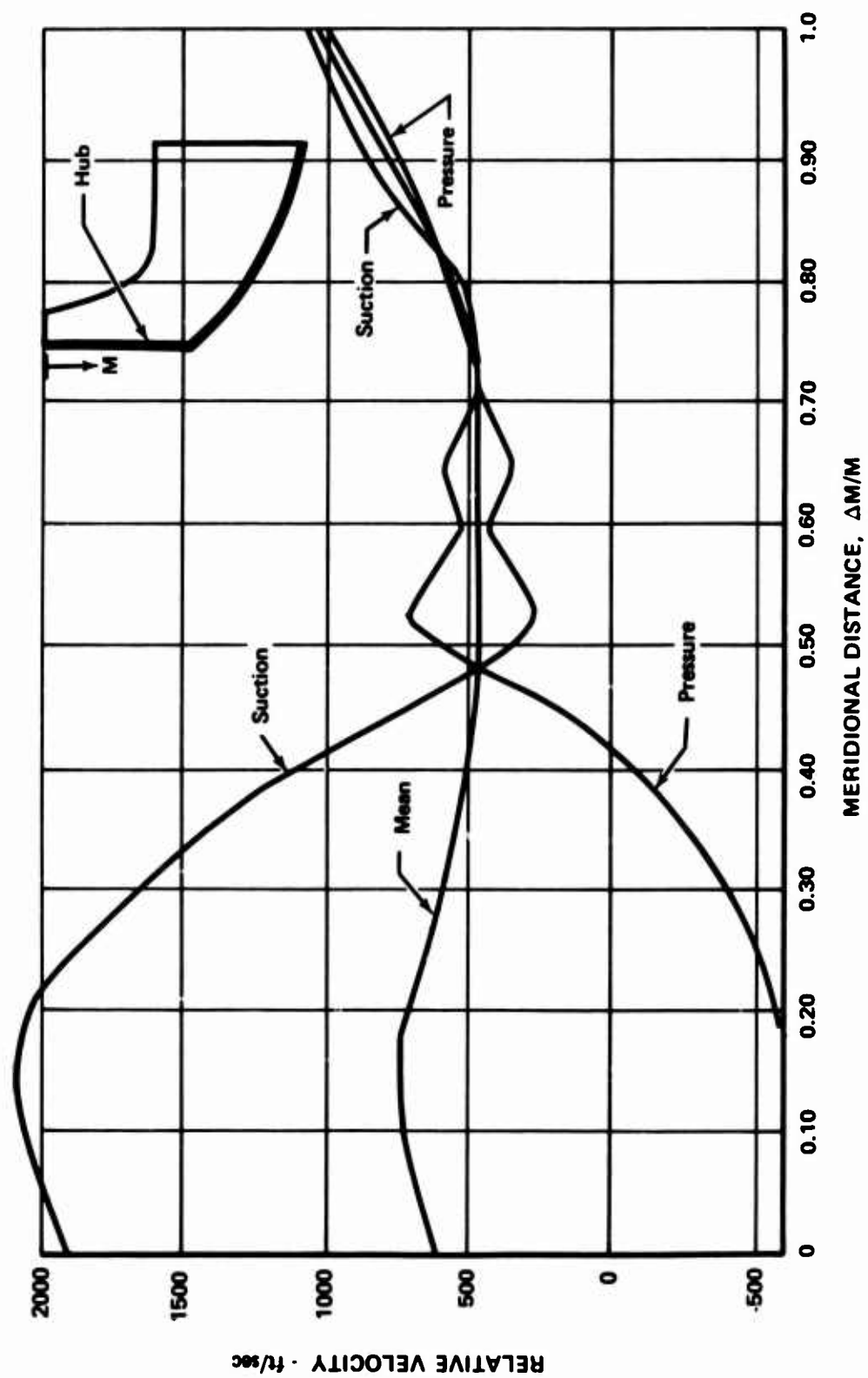
Figure 24. Rotor Velocity Distribution (Hub Side).

75
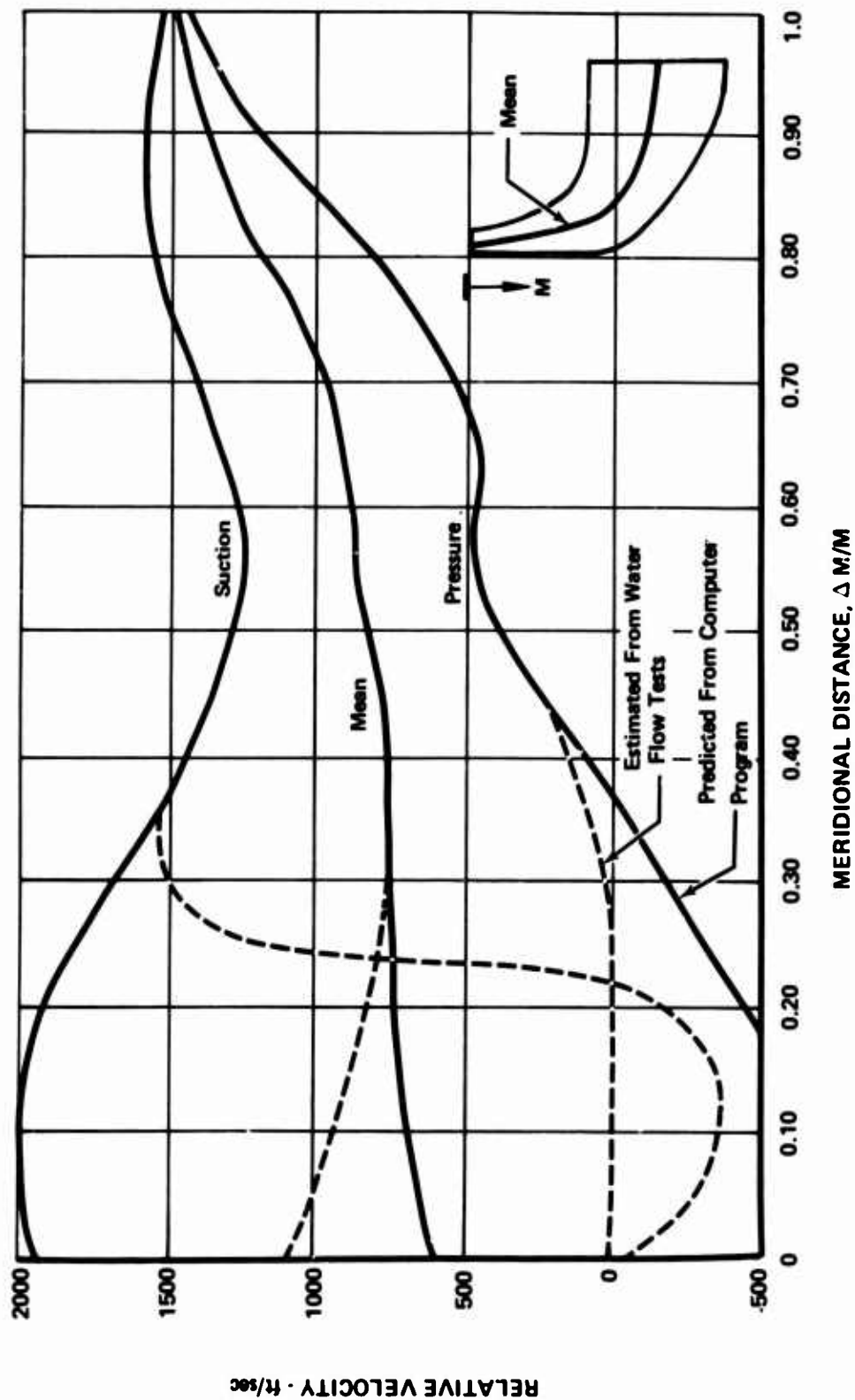
Figure 26. Rotor Velocity Distribution for Heat Transfer Analysis (Mean).

77
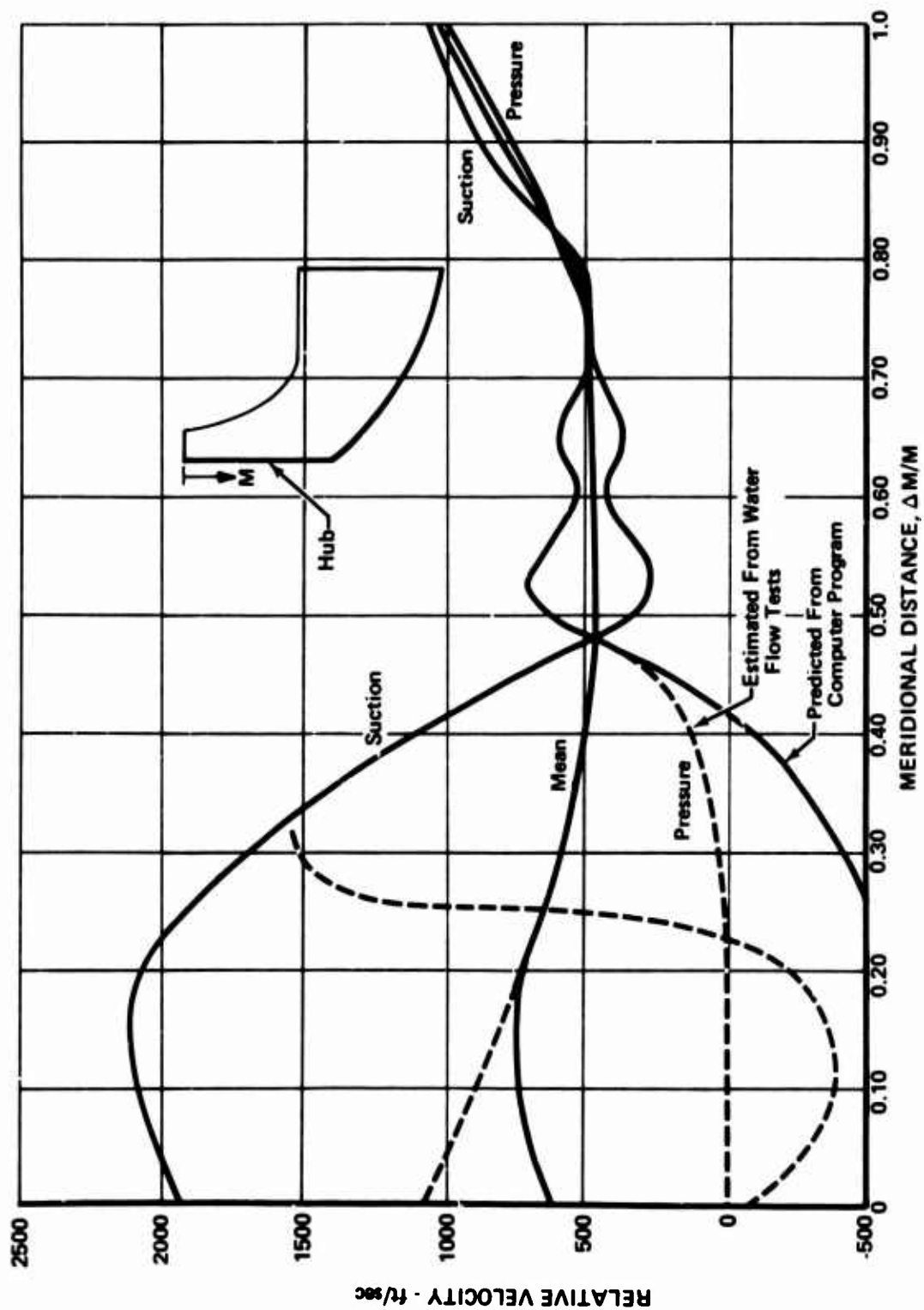
Figure 27. Rotor Velocity Distribution for Heat Transfer Analysis (Hub Side).
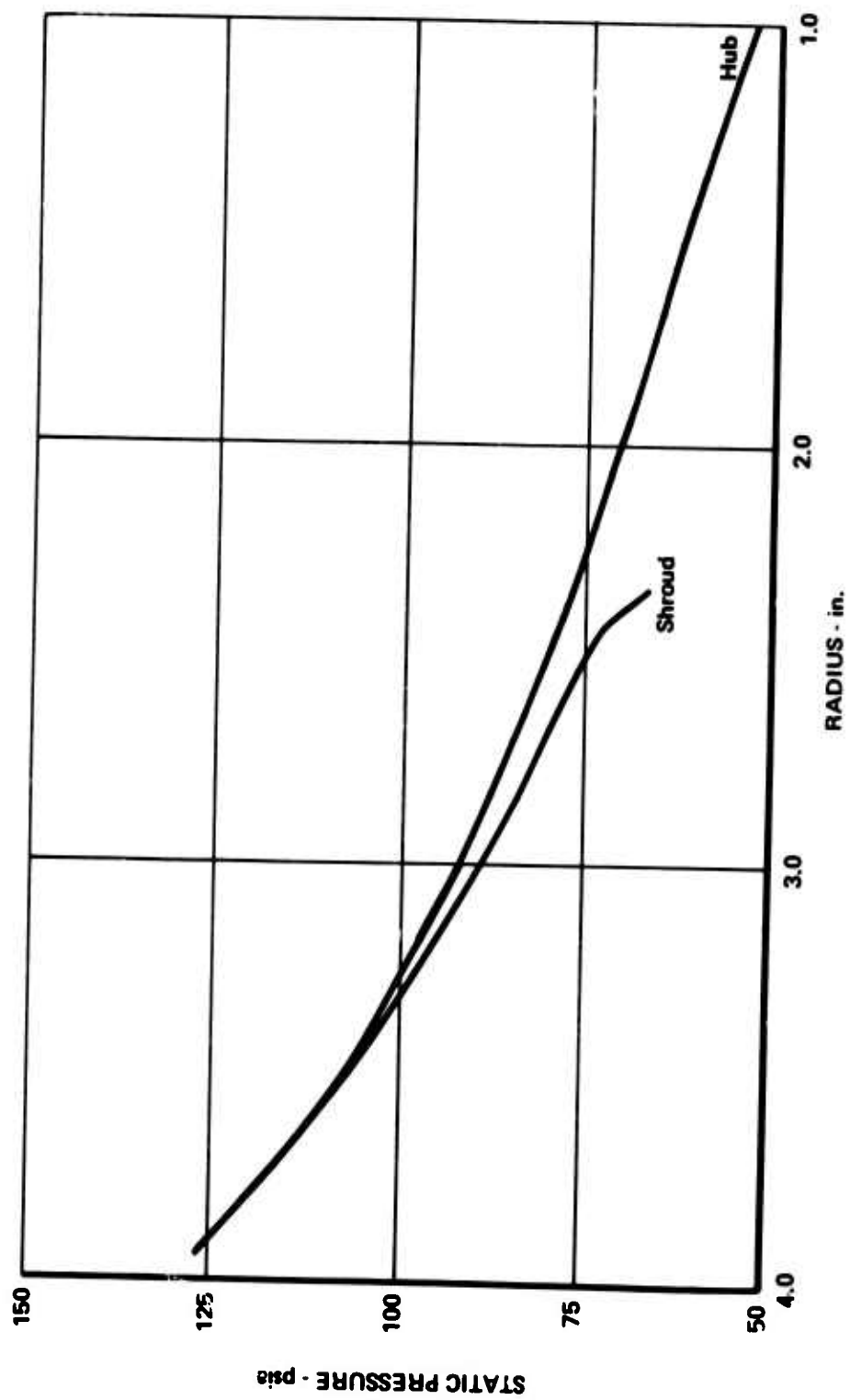
Figure 28. Rotor Static Pressure Distribution.
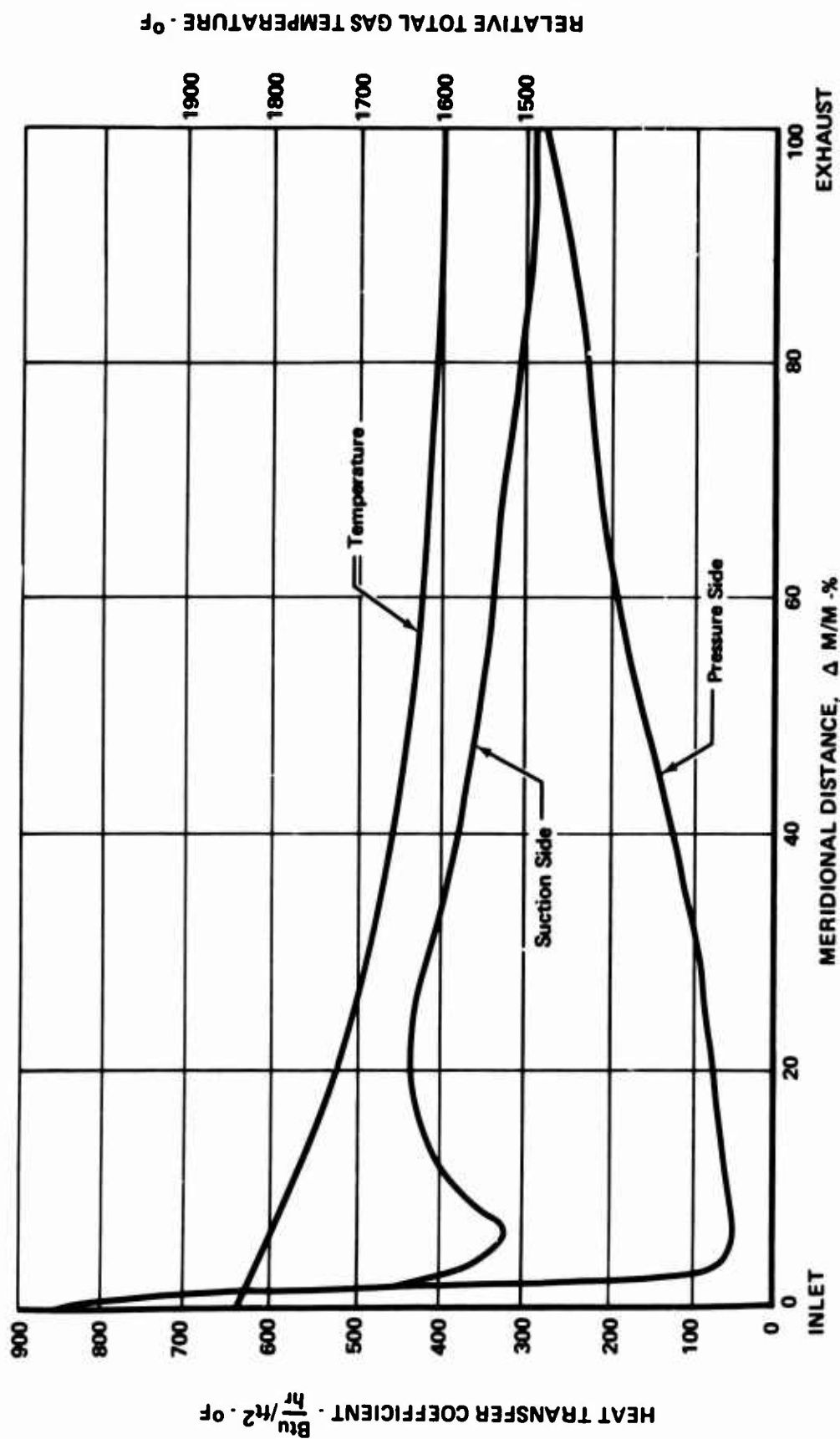
Figure 29. Gas Temperature Distribution and Heat Transfer Coefficients for Rotor Blade (Shroud Side).

80
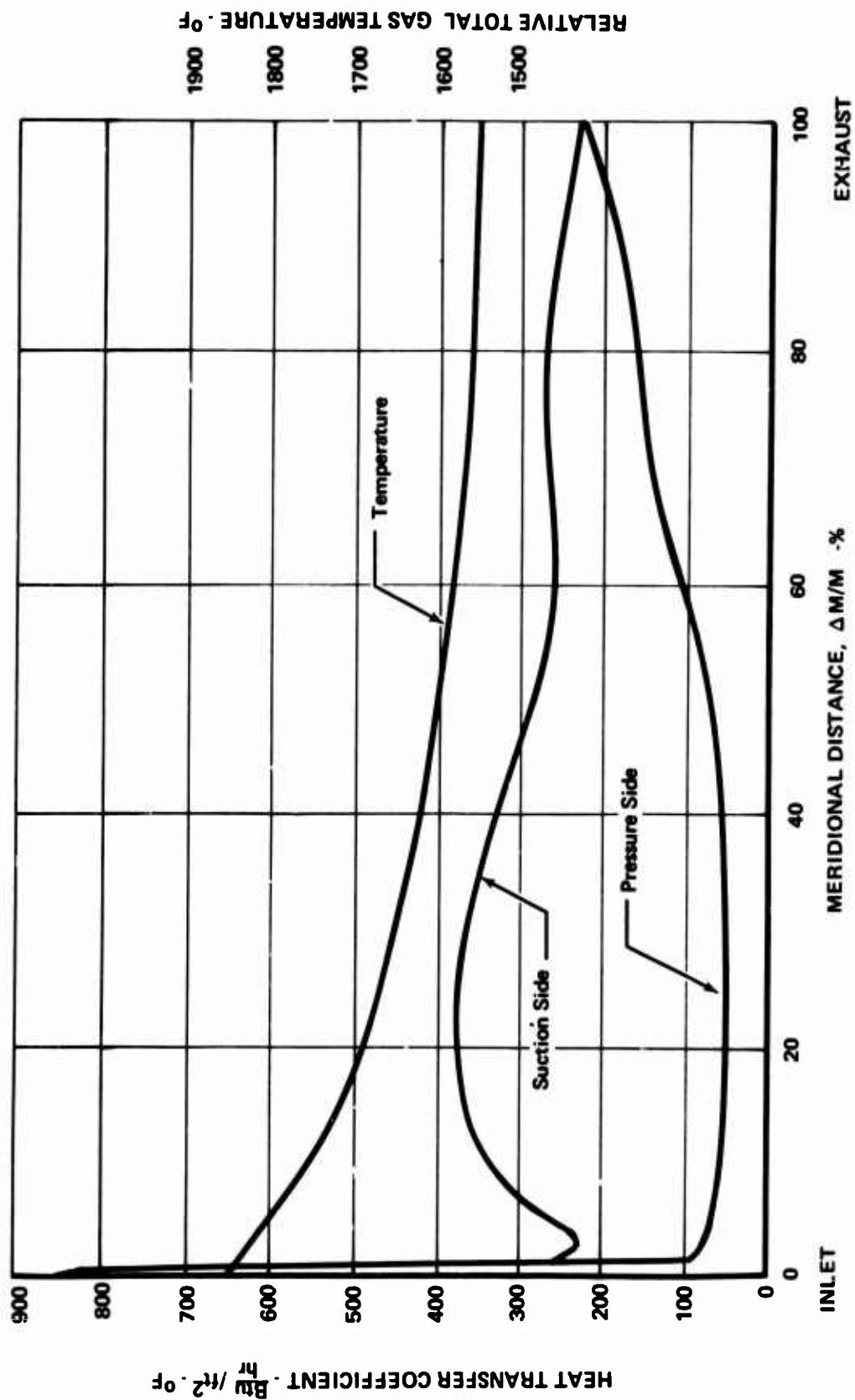
Figure 30. Gas Temperature Distribution and Heat Transfer Coefficients for Rotor Blade (Mean).
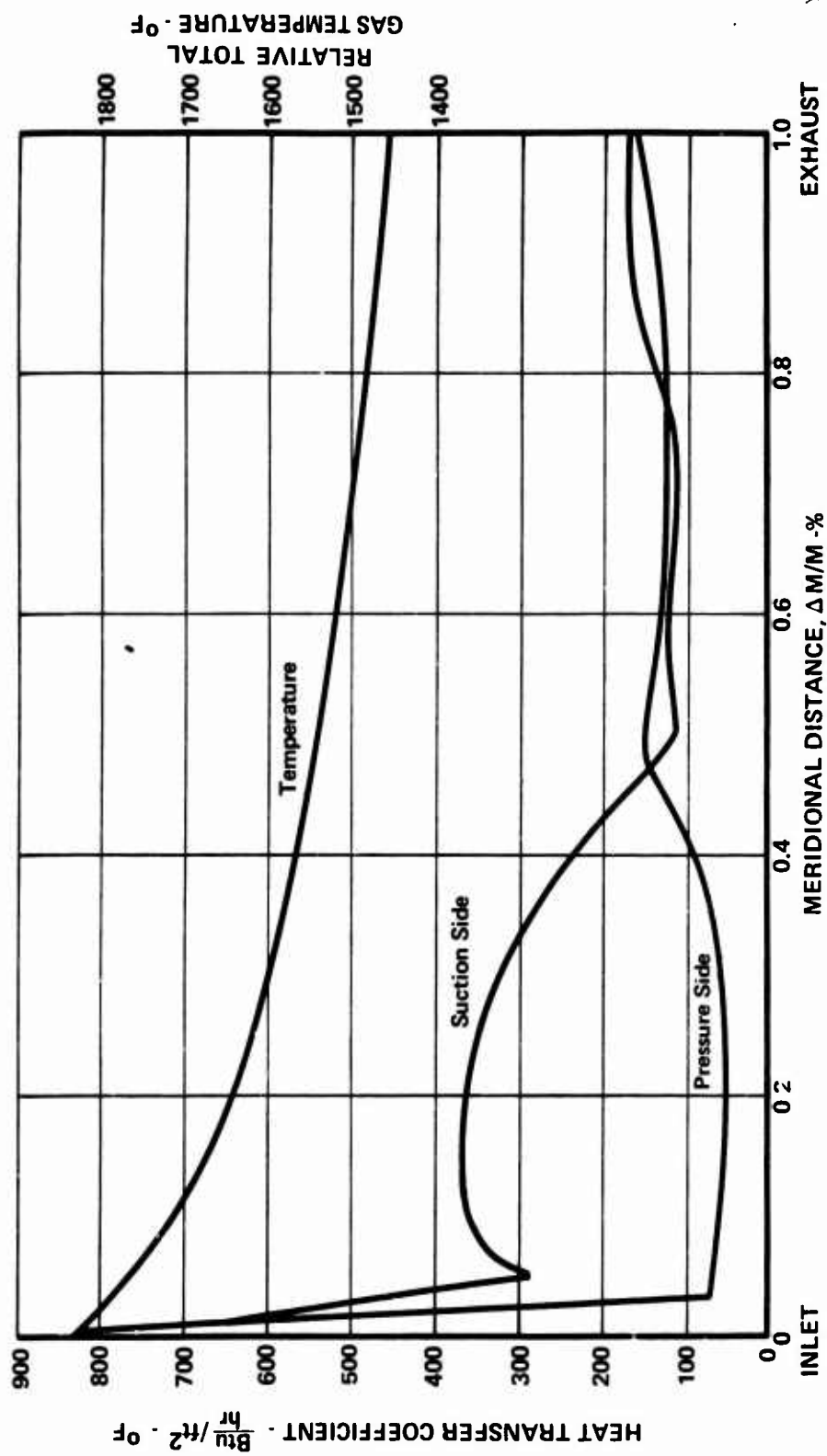
Figure 31. Gas Temperature Distribution and Heat Transfer Coefficients for Rotor Blade (Hub Side).

82
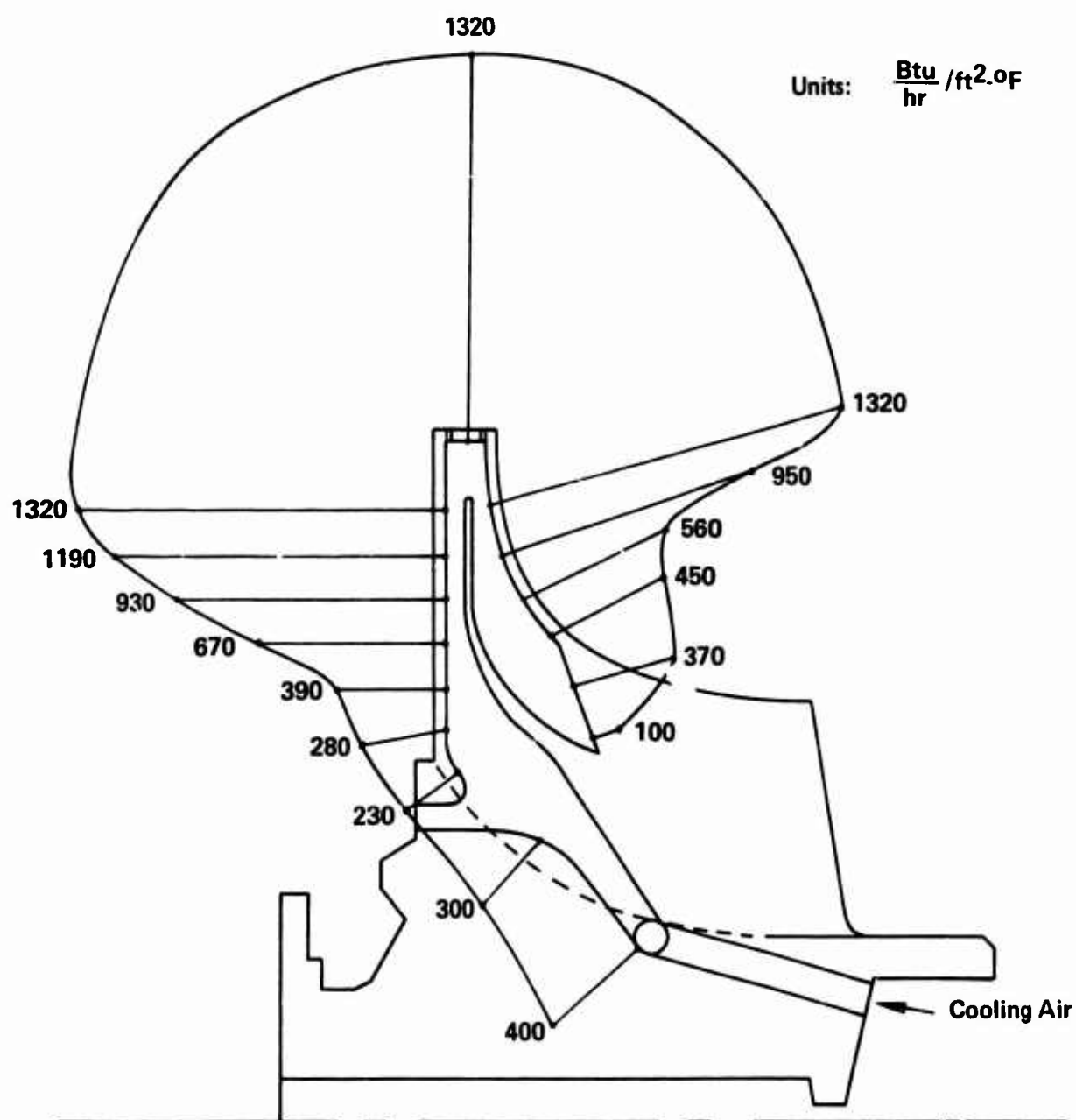
Figure 32. Rotor Internal Heat Transfer Coefficients.
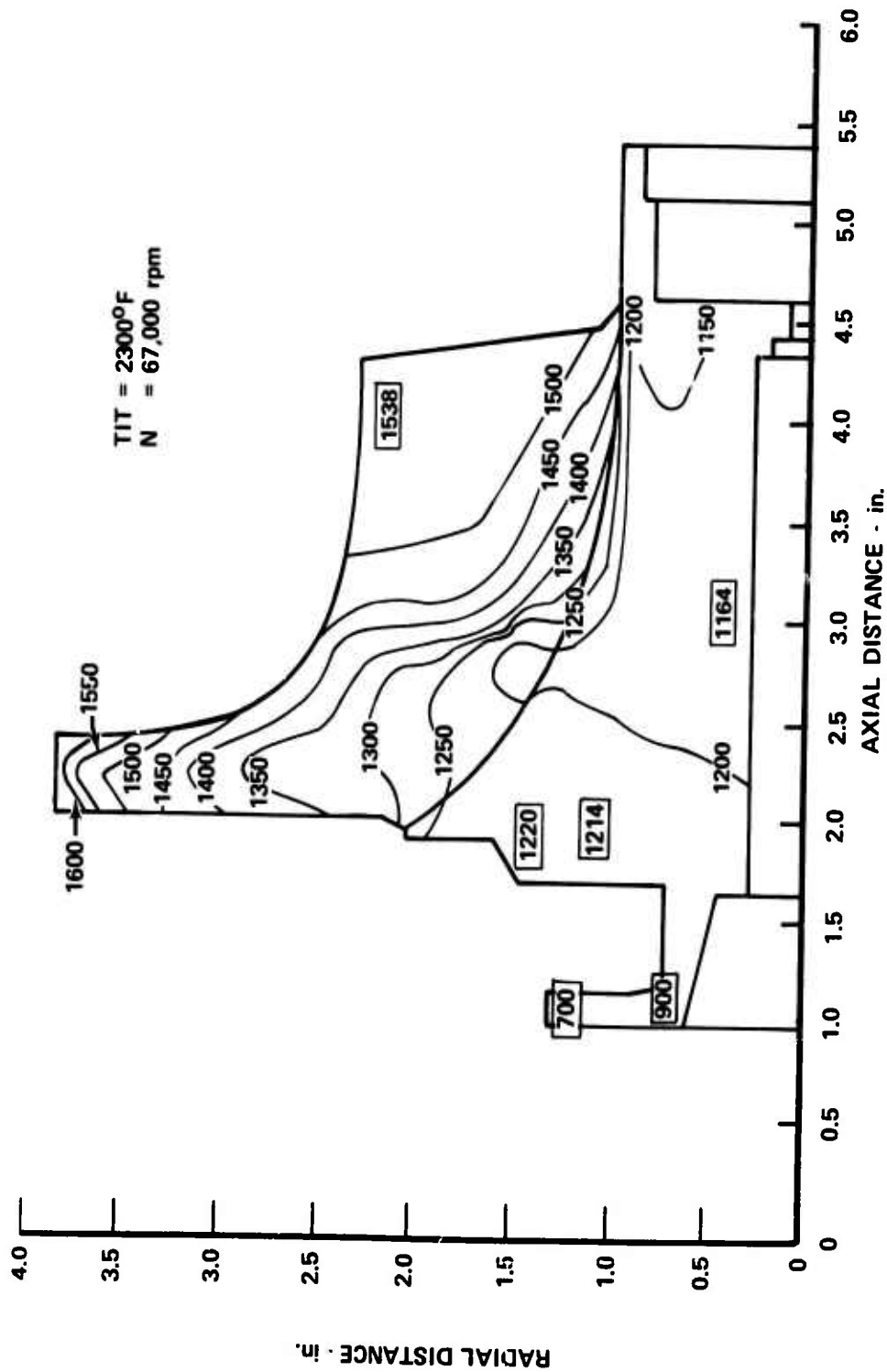
Figure 33. Rotor Temperature Distribution.
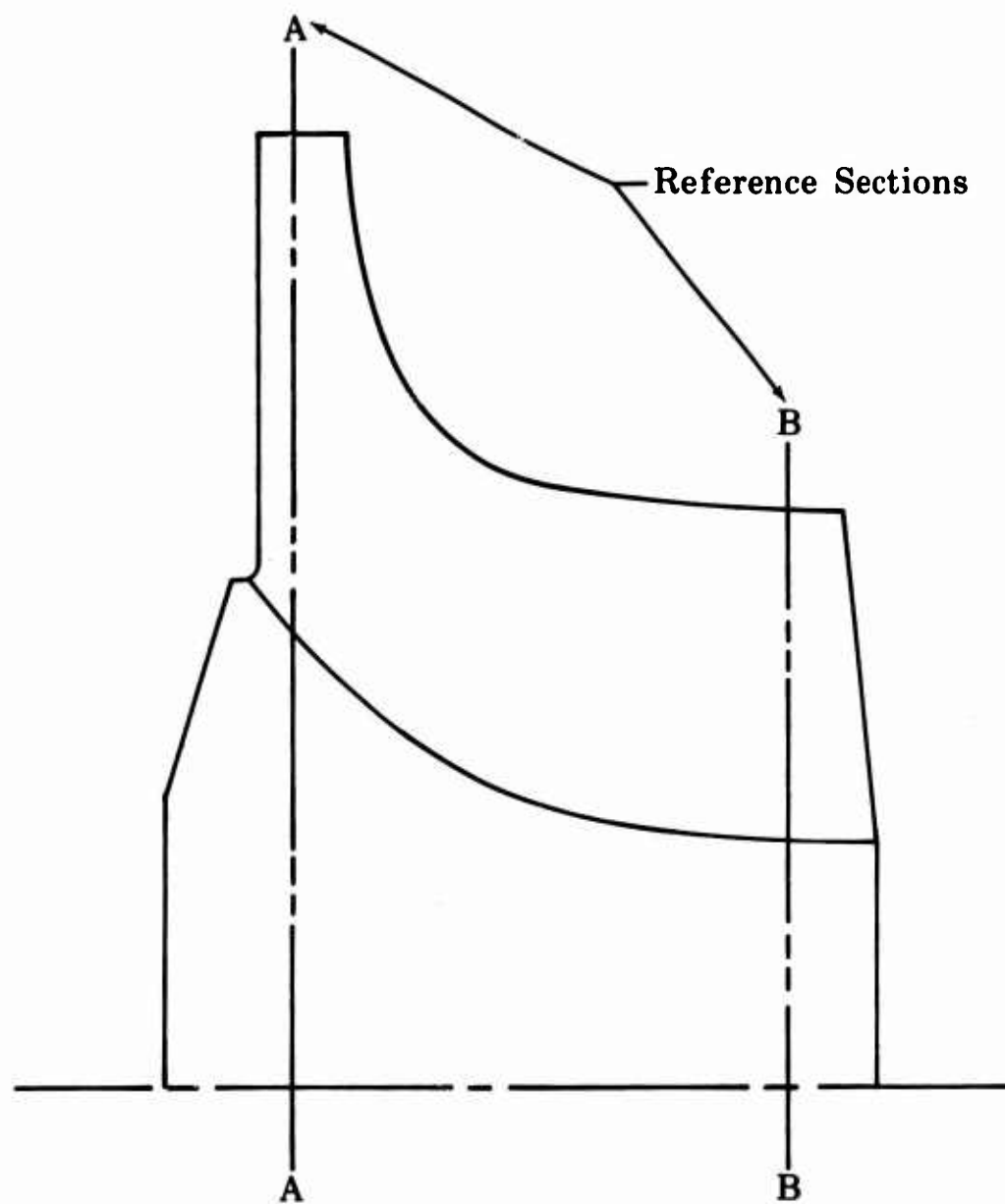
Figure 34. Rotor Stress Model.
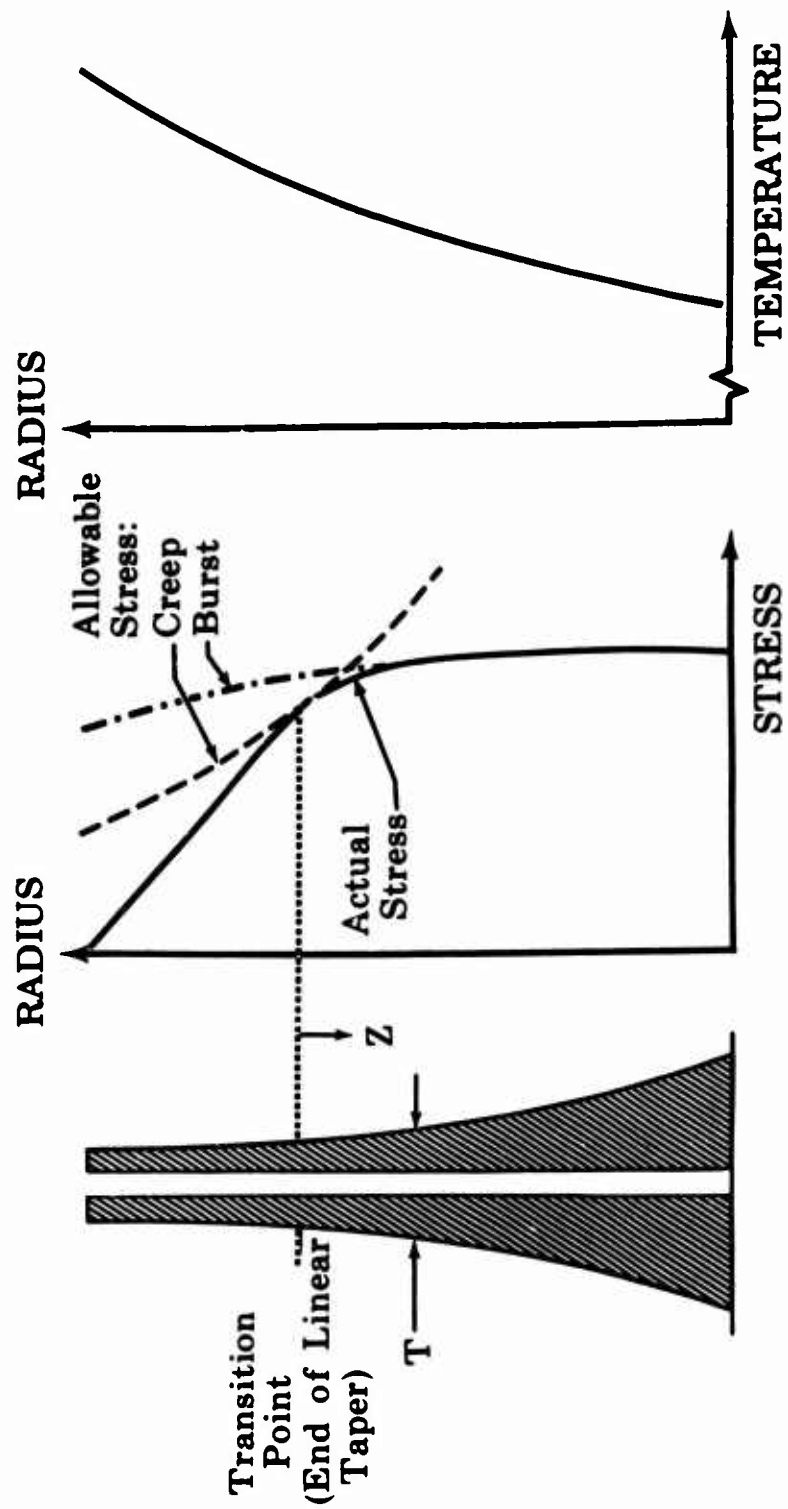
Figure 35. Thickness Distribution in a Reference Section.

86
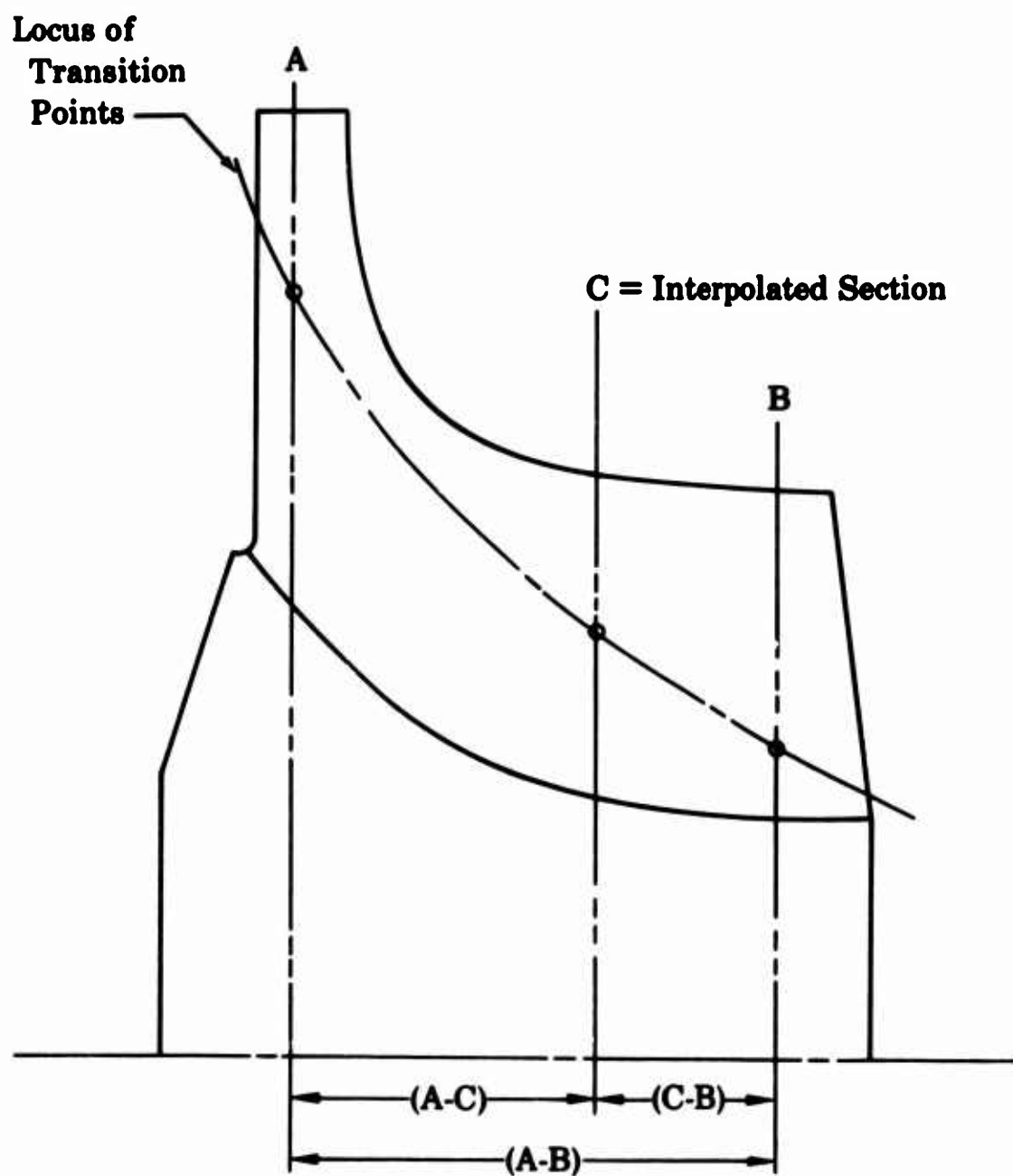
Figure 36. Typical Interpolated Section.
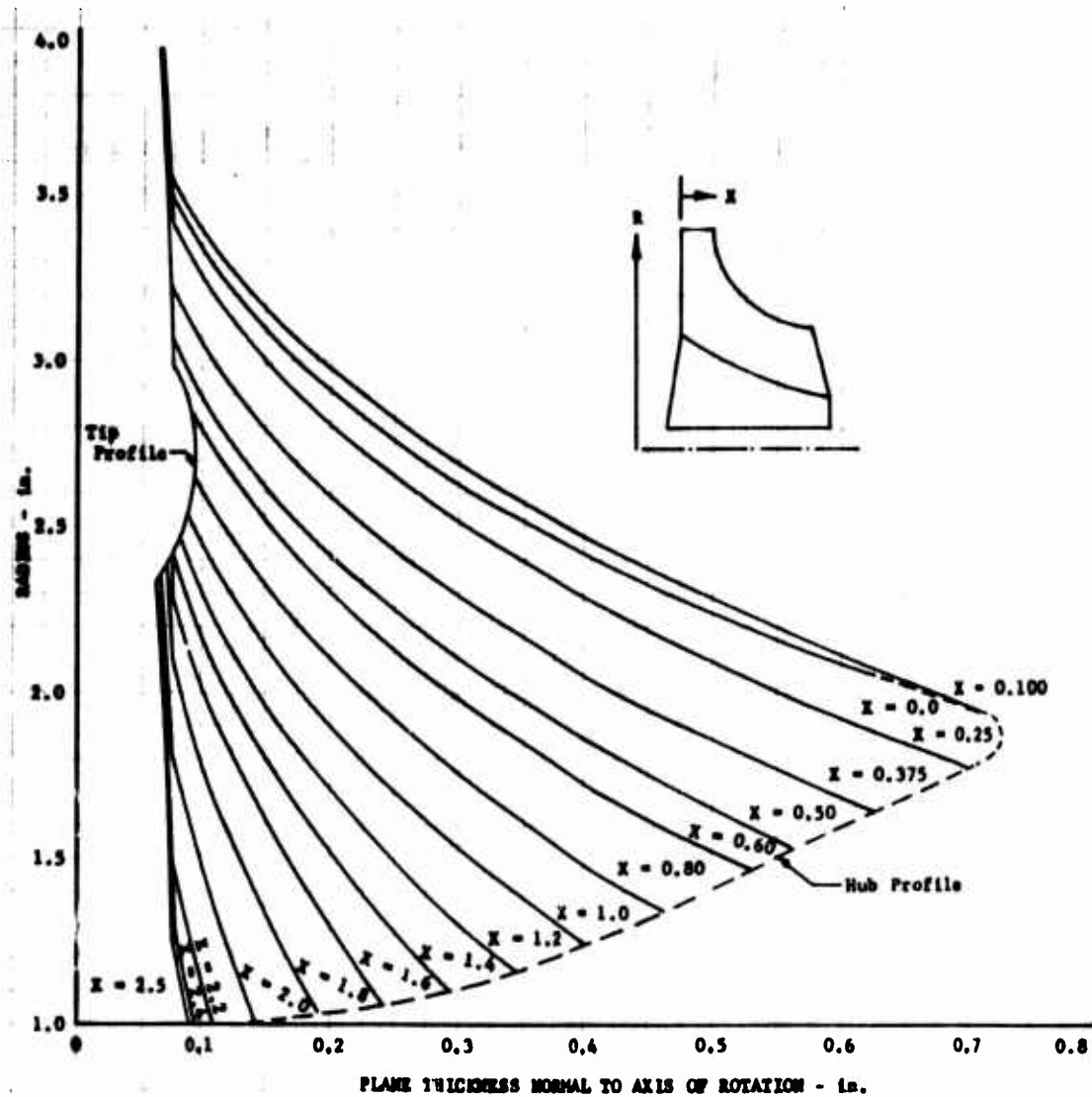
Figure 37. Rotor Blade Thickness Distribution.
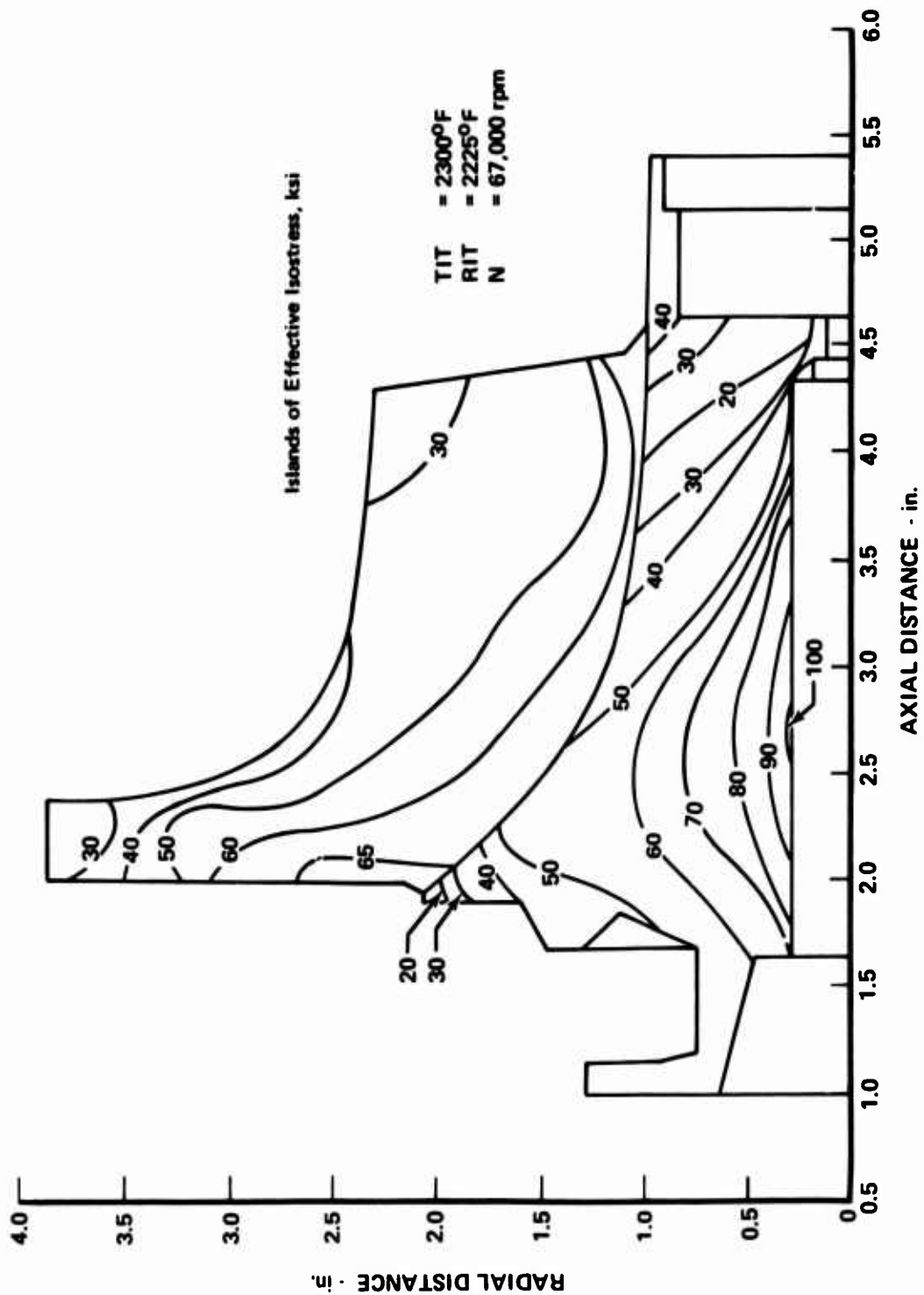
Figure 38. Rotor Stress Distribution (Design Point).

89
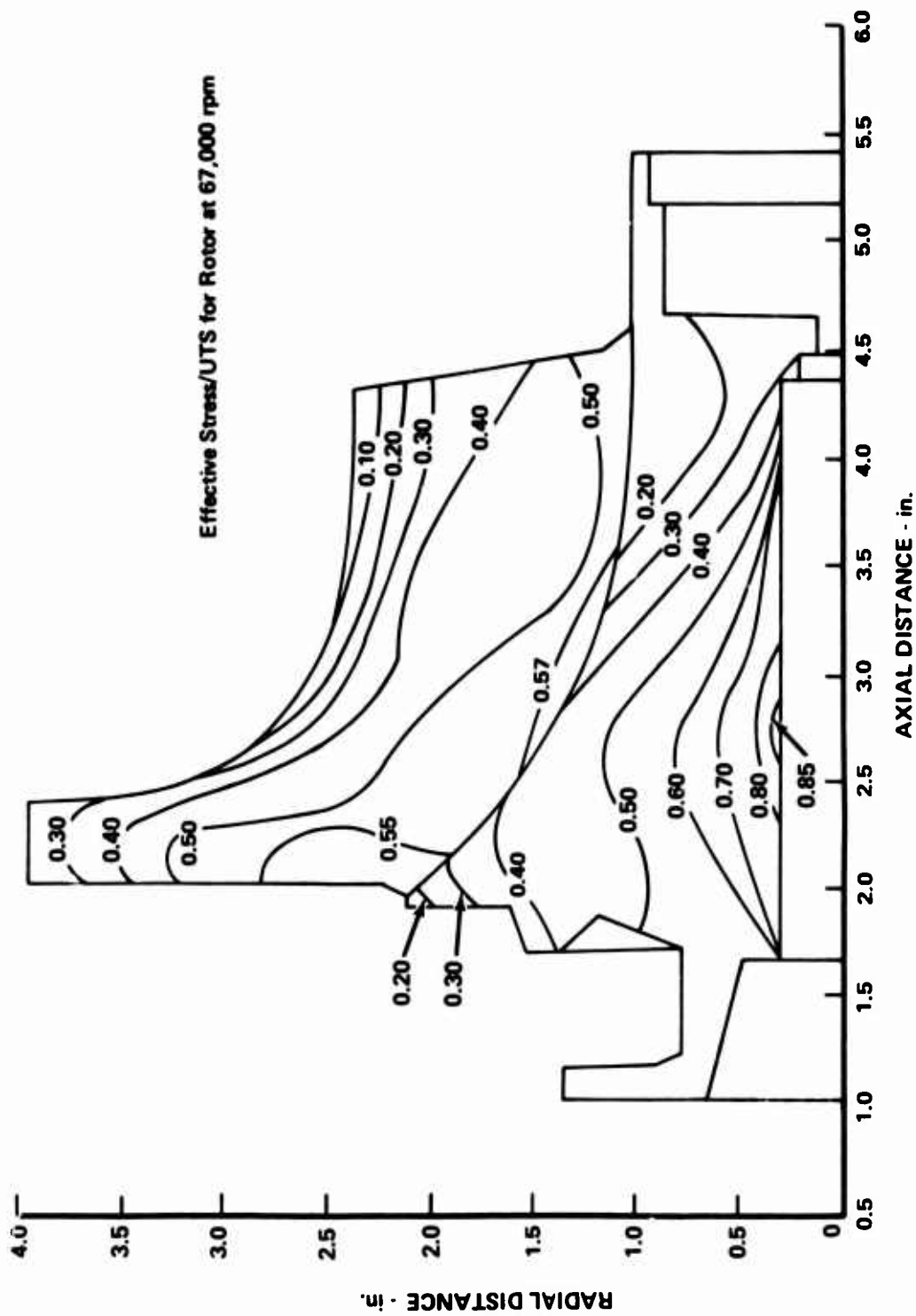
Figure 39.   Rotor Stress Ratio Distribution (Design Point).

90
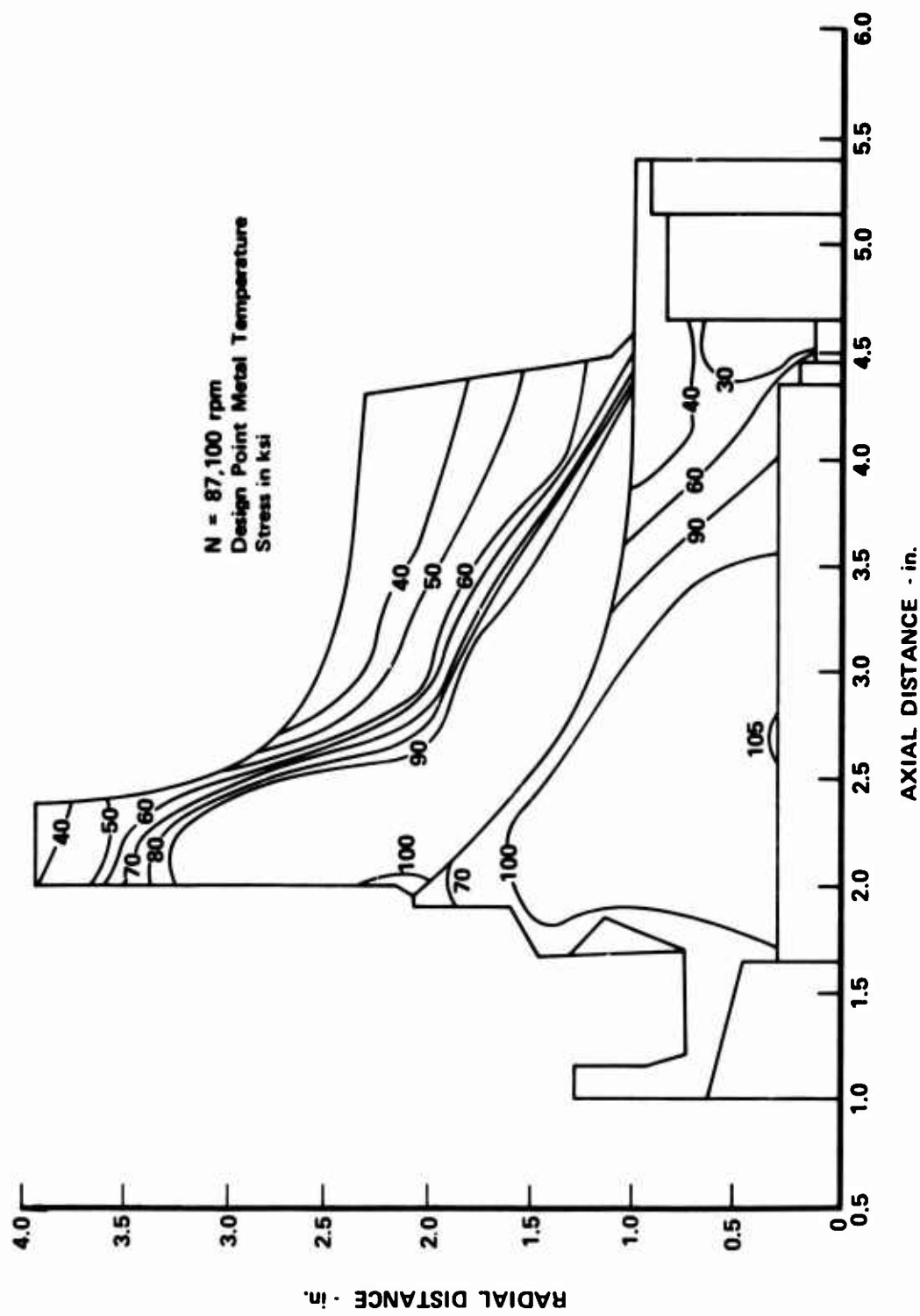
Figure 40.   Rotor Stress Distribution (30% Overspeed).

91
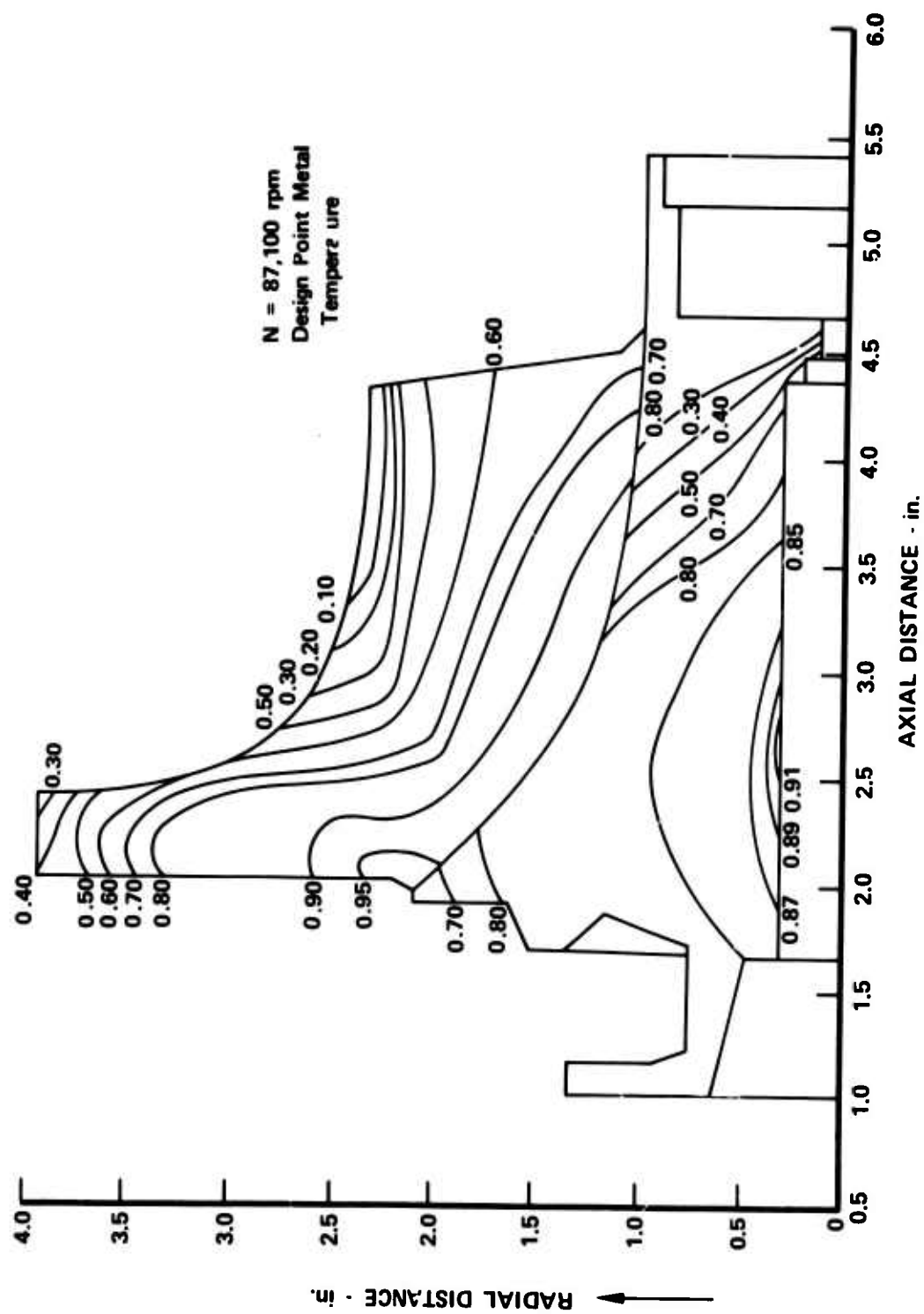
Figure 41. Rotor Stress Ratio Distribution (30% Overspeed).
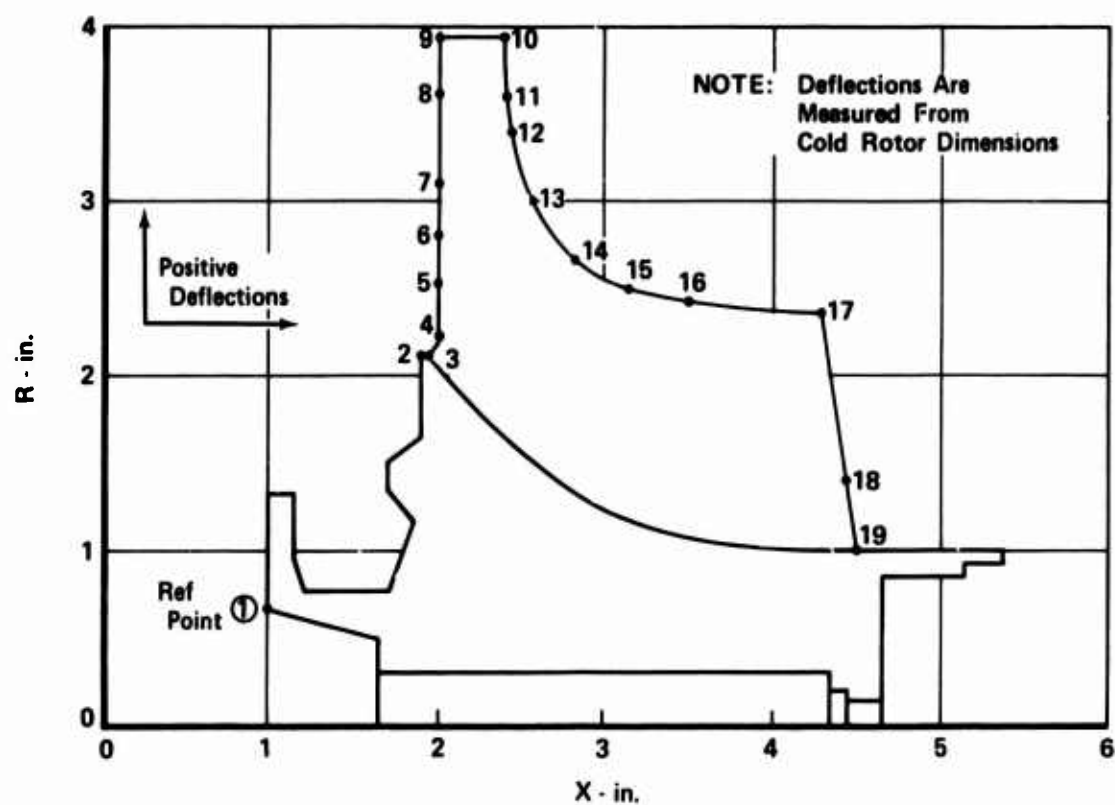
	X	R	Axial Def (in.)	Radial Def (in.)
1	1.000	0.650	0.0	0.0050
2	1.910	2.100	0.0048	0.0222
3	1.950	2.100	0.0052	0.0222
4	2.000	2.200	0.0053	0.0236
5	2.000	2.500	0.0046	0.0275
6	2.000	2.800	0.0041	0.0315
7	2.000	3.100	0.0037	0.0356
8	2.000	3.600	0.0031	0.0425
9	2.000	3.948	0.0026	0.0475
10	2.379	3.948	0.0075	0.0477

	X	R	Axial Def (in.)	Radial Def (in.)
11	2.400	3.600	0.0078	0.0428
12	2.430	3.400	0.0082	0.0400
13	2.550	3.000	0.0097	0.0346
14	2.820	2.660	0.0127	0.0305
15	3.150	2.500	0.0161	0.0291
16	3.500	2.420	0.0202	0.0288
17	4.290	2.350	0.0302	0.0276
18	4.435	1.400	0.0300	0.0146
19	4.500	1.000	0.0289	0.0093

Figure 42. Rotor Deflections (Design Point).

93
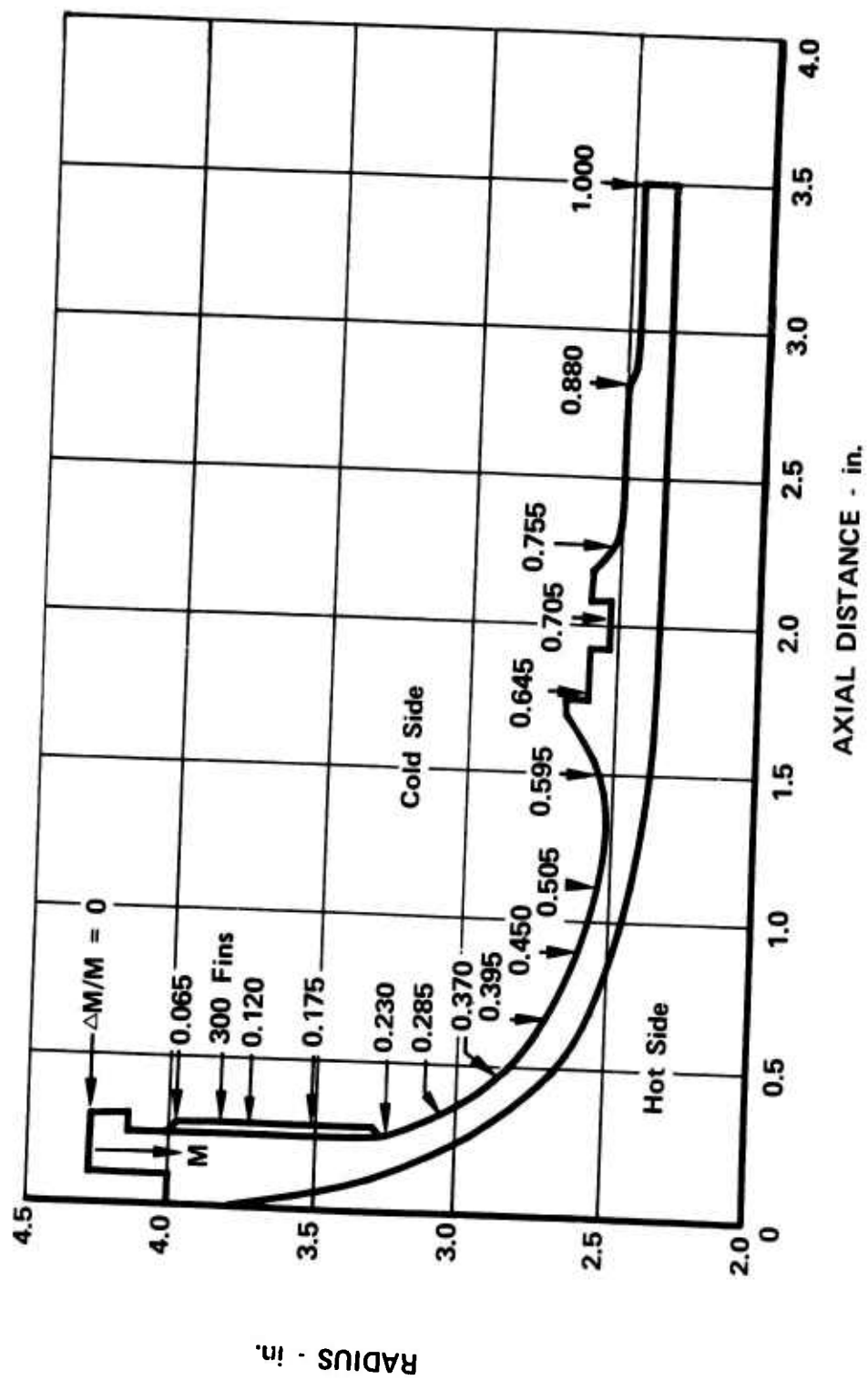
Figure 43. Shroud Design.

94
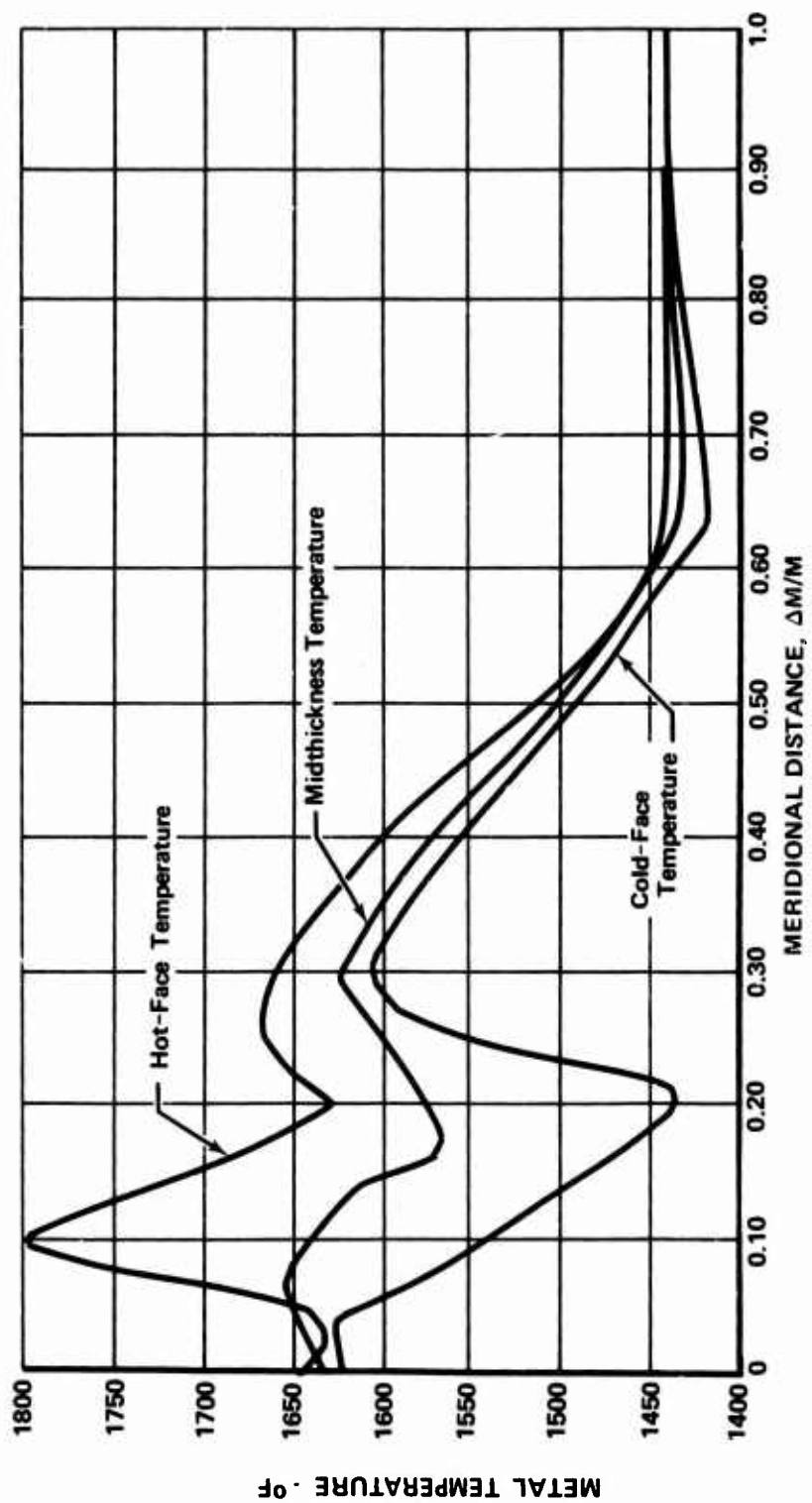
Figure 44. Shroud Temperature Distribution.

95
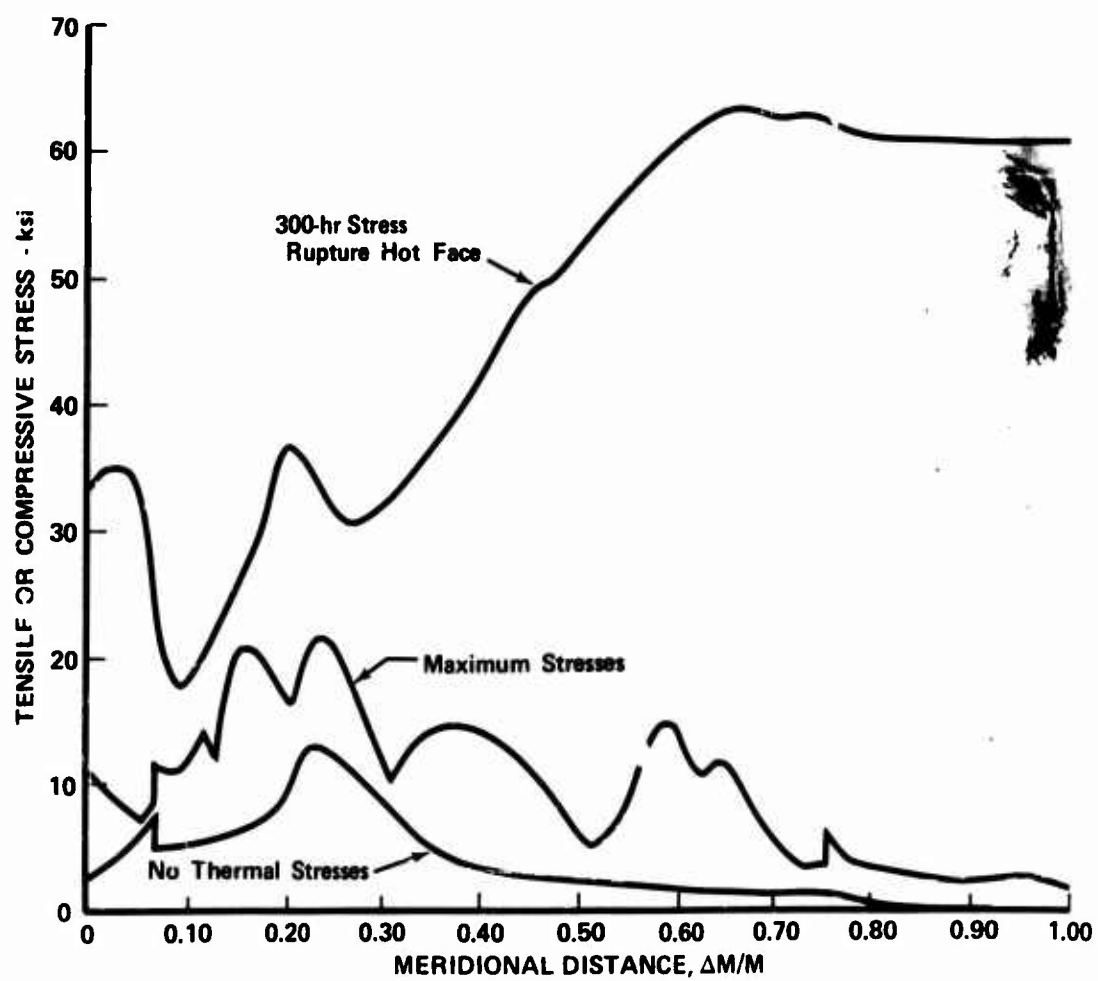
Figure 45. Shroud Maximum Stress Distribution.
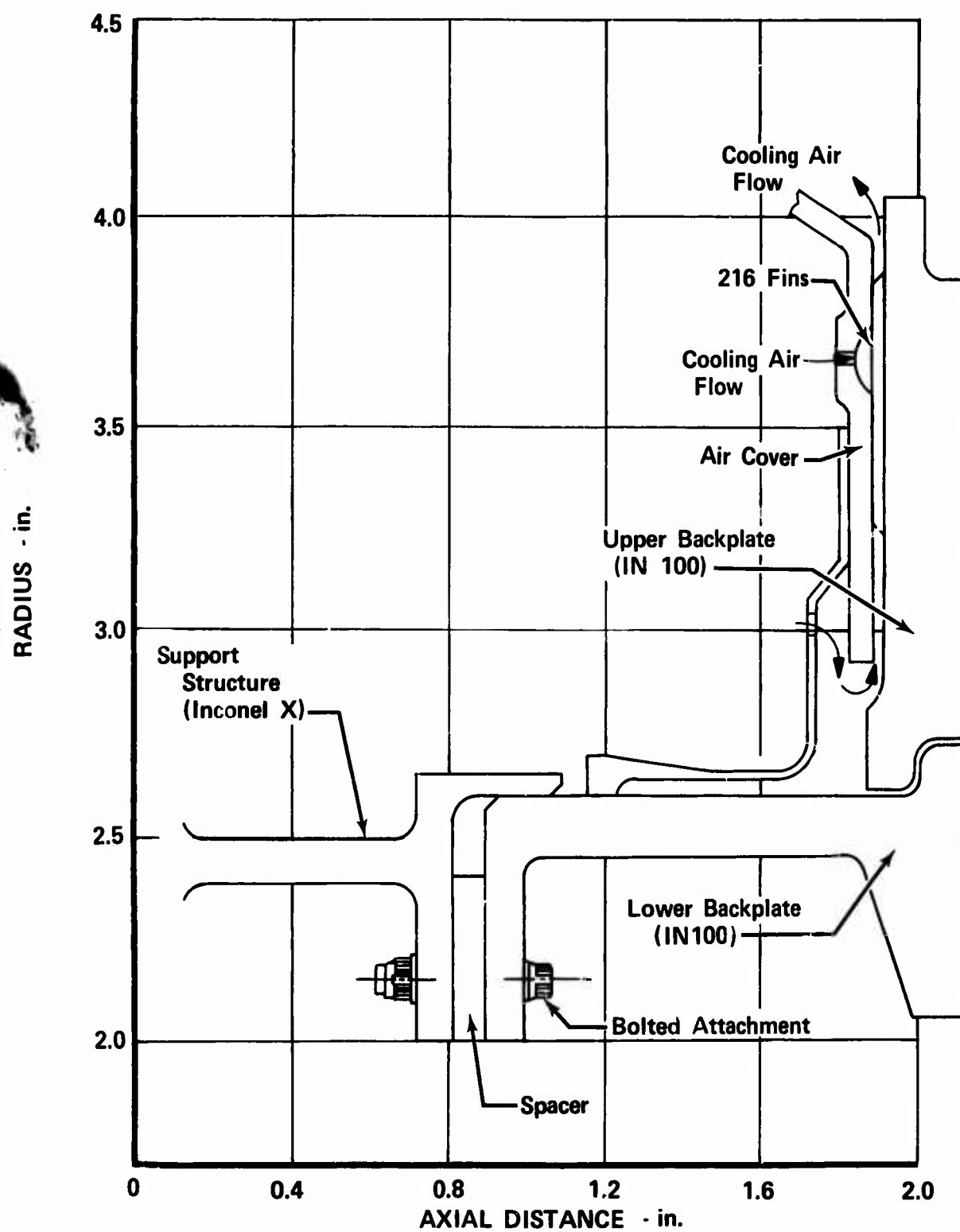
Figure 46. Backplate Design.
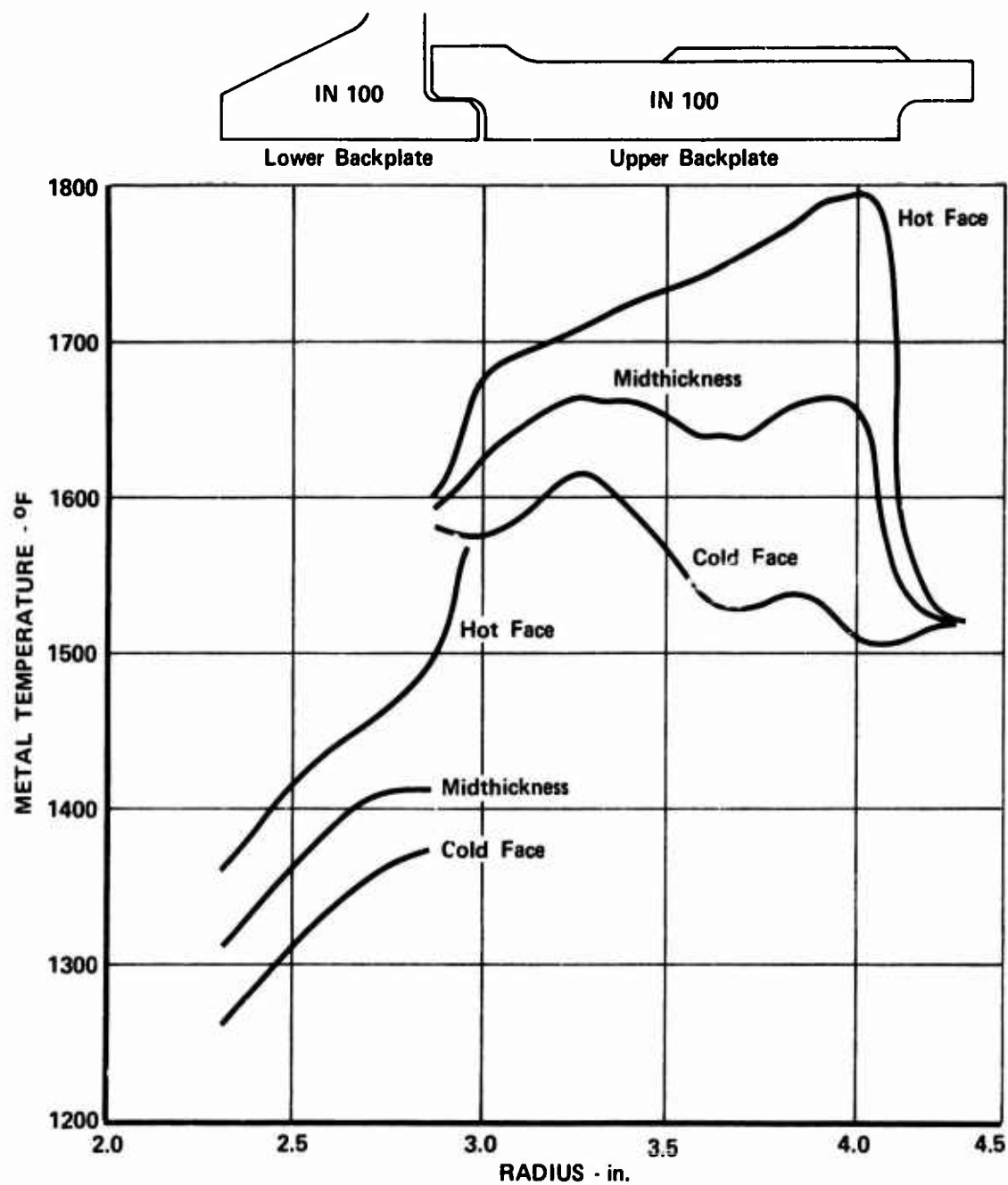
Figure 47. Backplate Metal Temperatures (Radial).

98
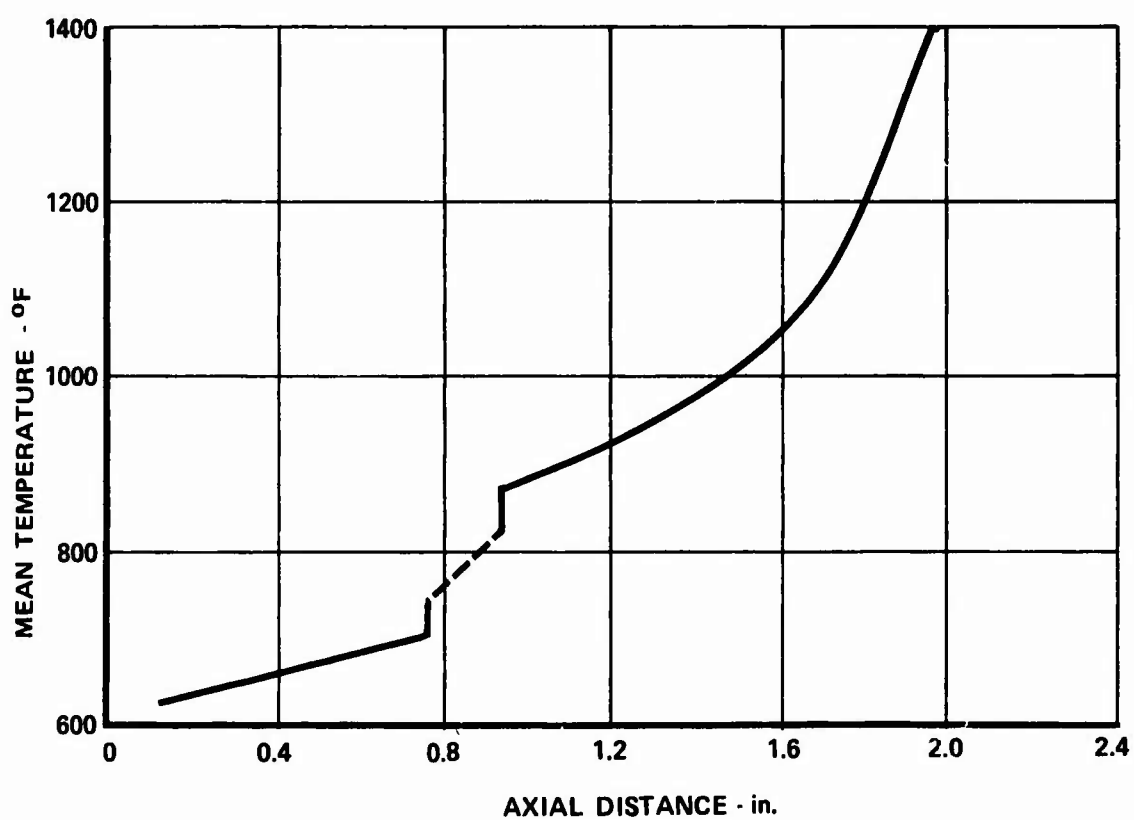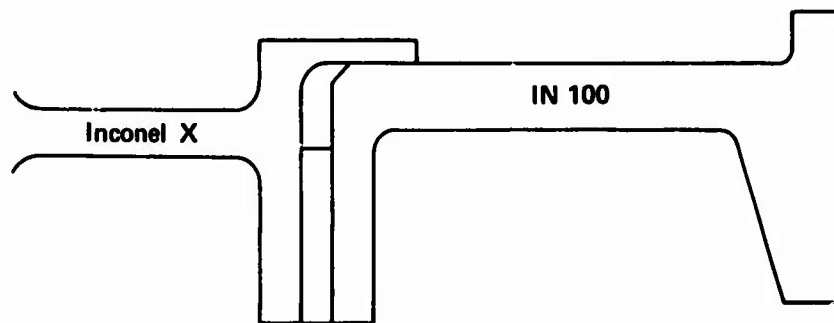
Figure 48. Backplate Metal Temperatures (Axial).
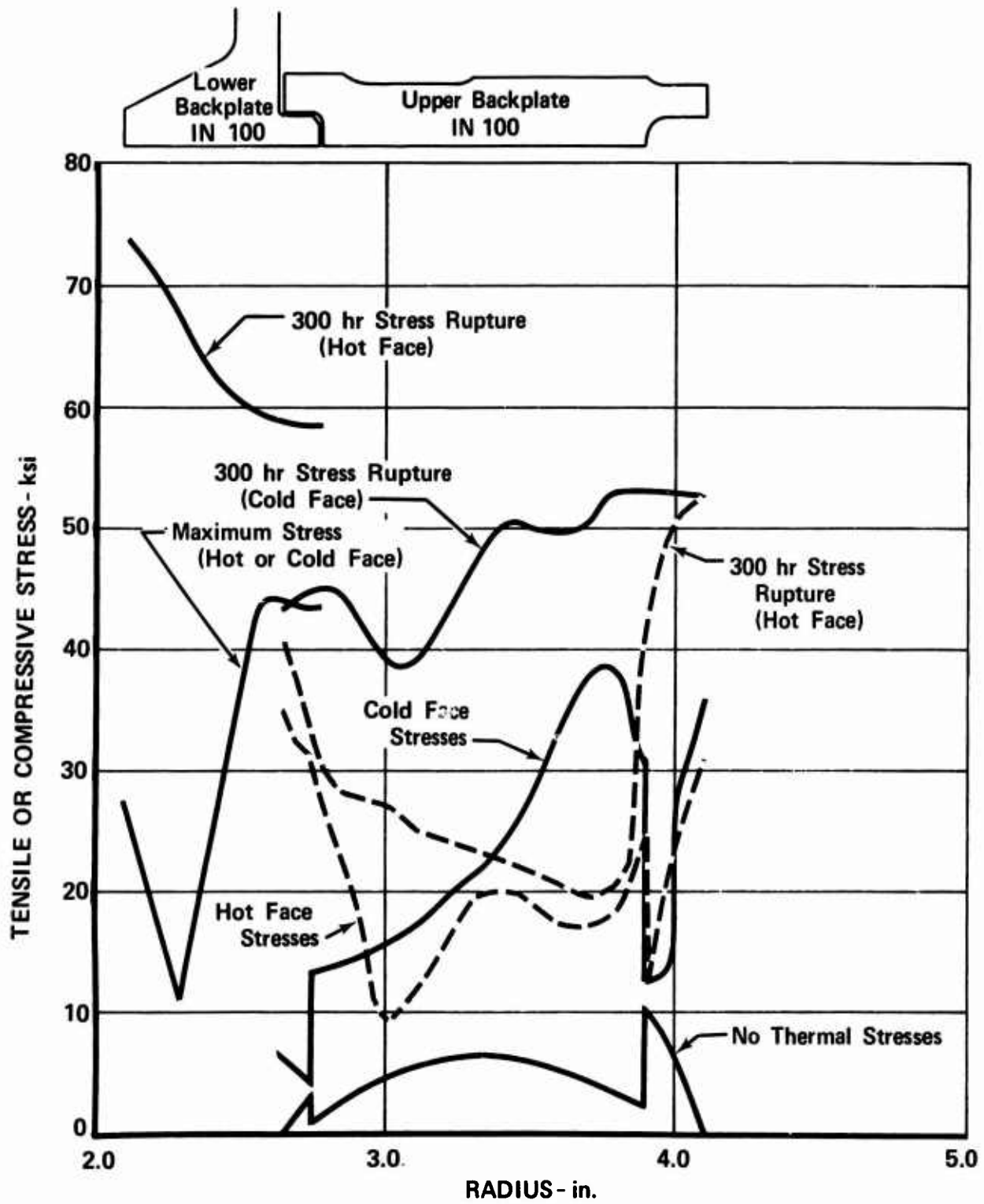
Figure 49. Backplate Stress Distribution (Radial).
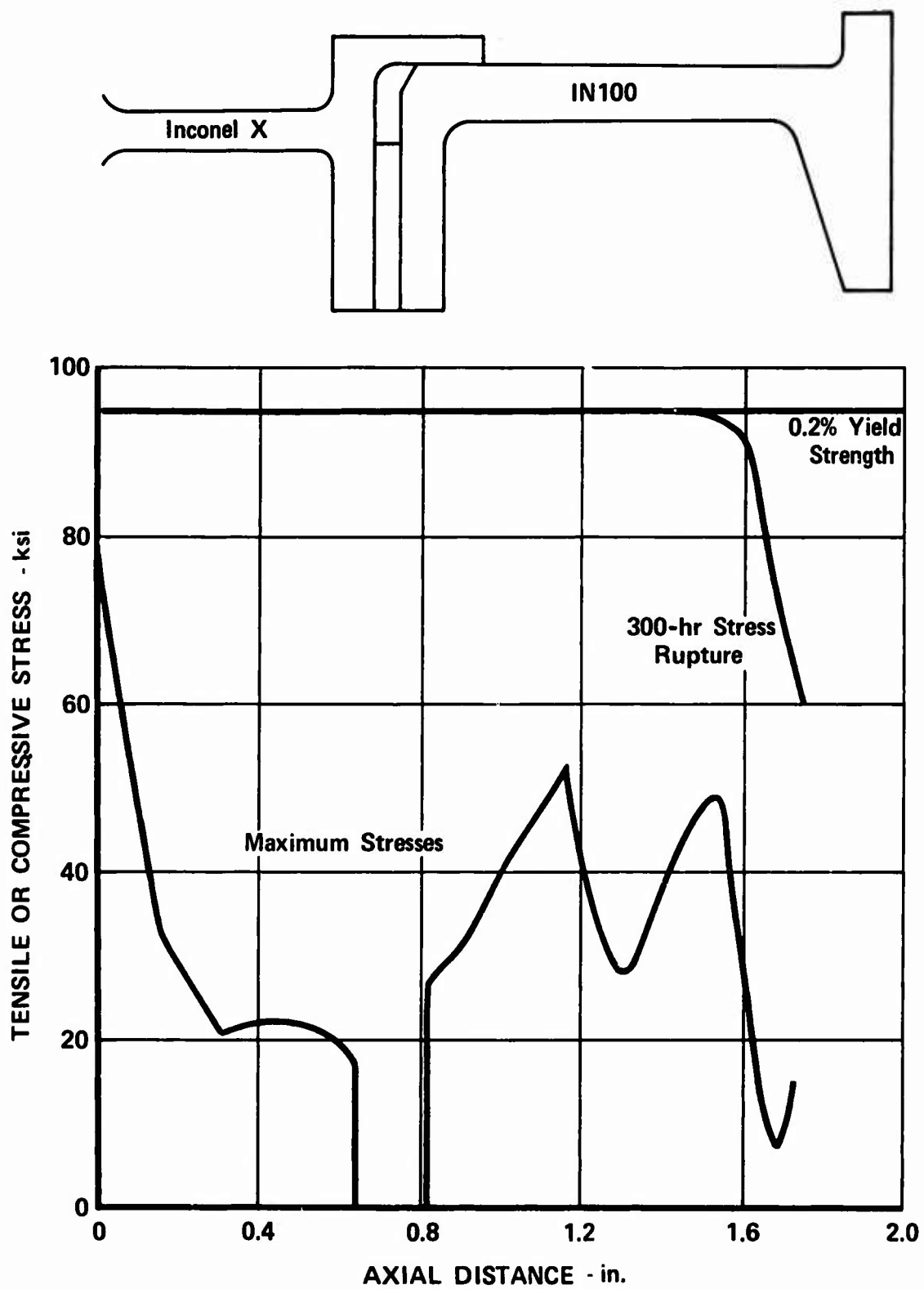
Figure 50. Backplate Stress Distribution (Axial).
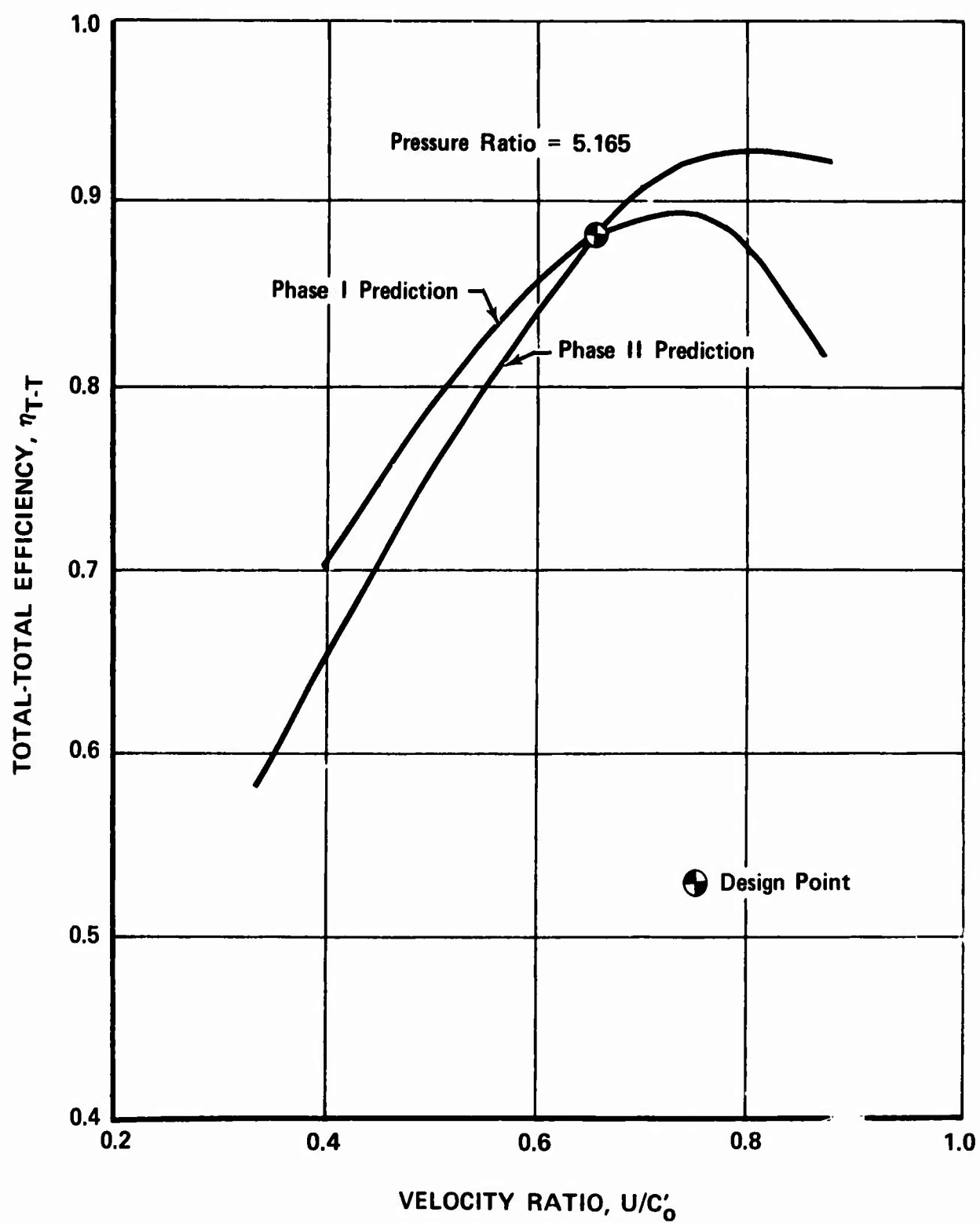
Figure 51. Comparison of Phase I and Phase II Performance Predictions.
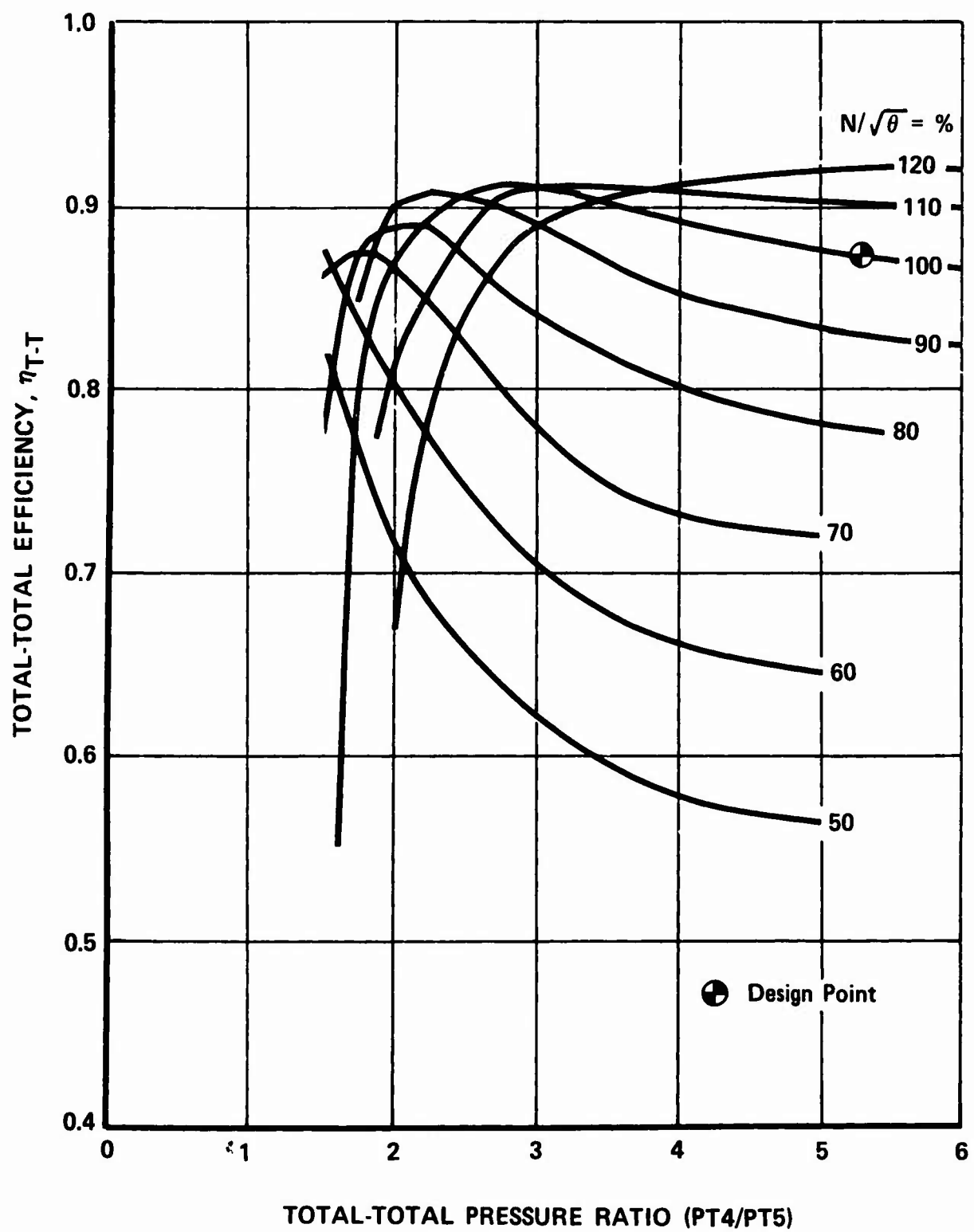
Figure 52. Predicted Stage Performance (Efficiency vs Pressure Ratio).
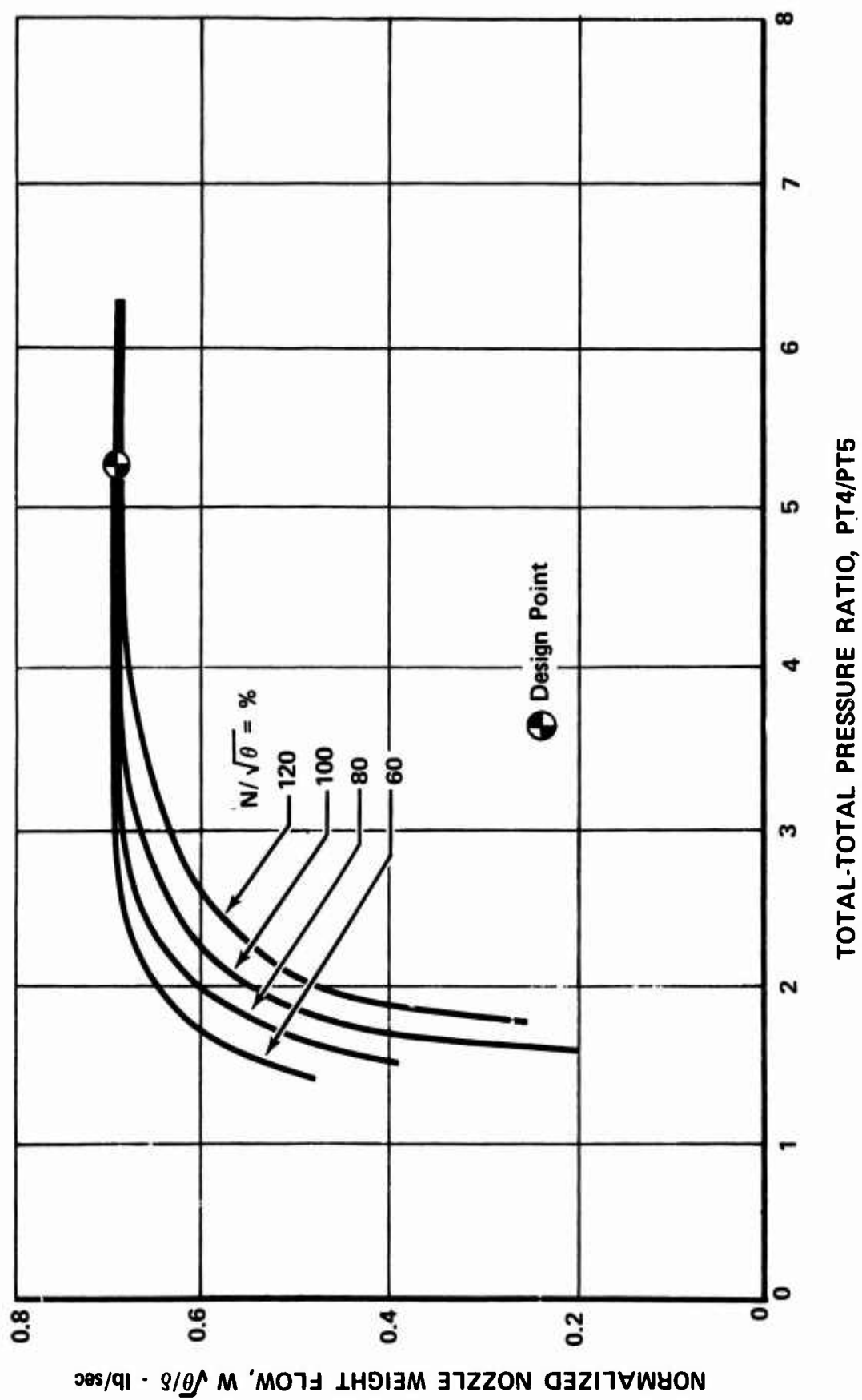
Figure 53. Predicted Stage Performance (Nozzle Weight Flow vs Pressure Ratio).

104
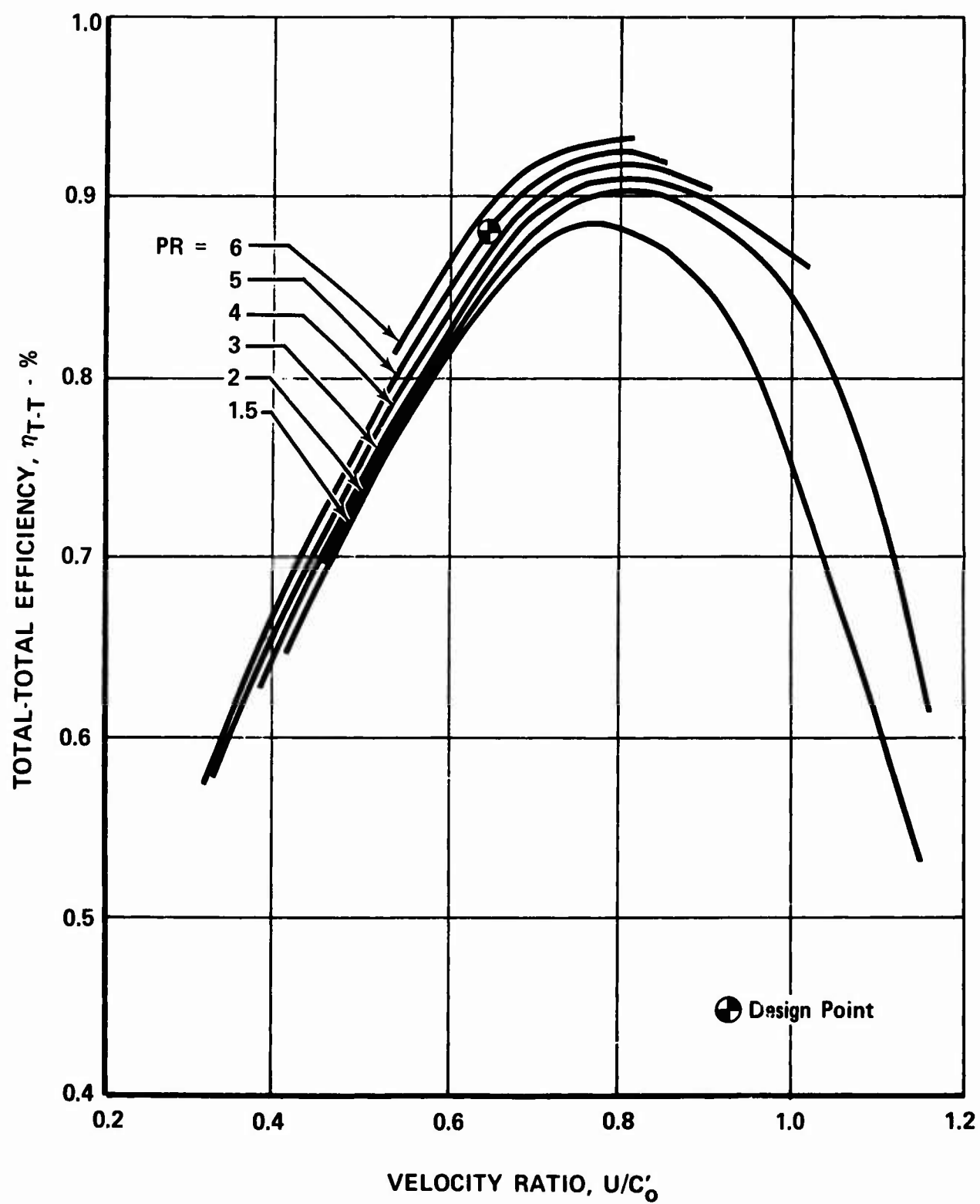
Figure 54. Predicted Stage Performance (Efficiency vs Velocity Ratio).

105
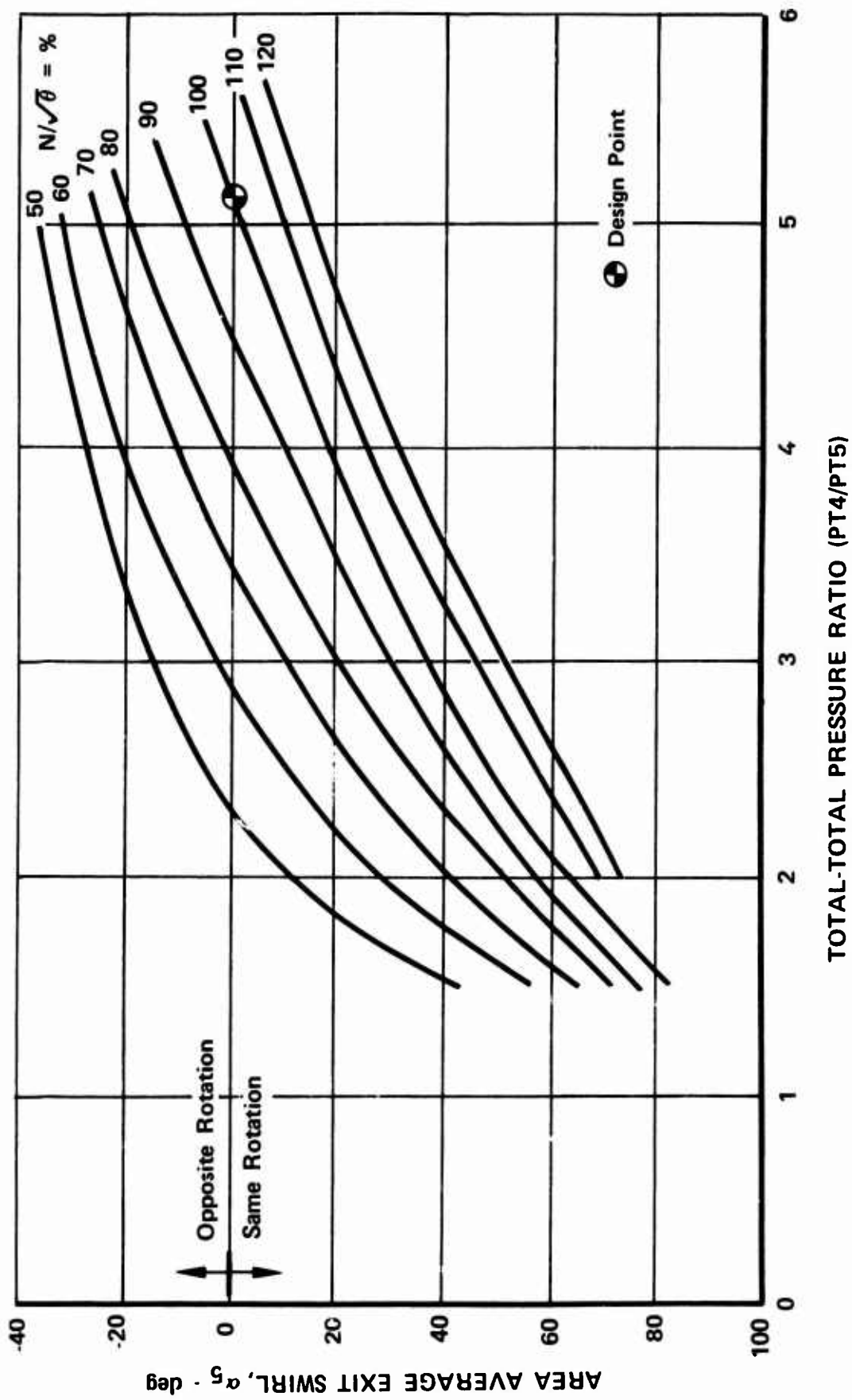
Figure 55. Predicted Stage Performance (Exit Swirl vs Pressure Ratio).

106
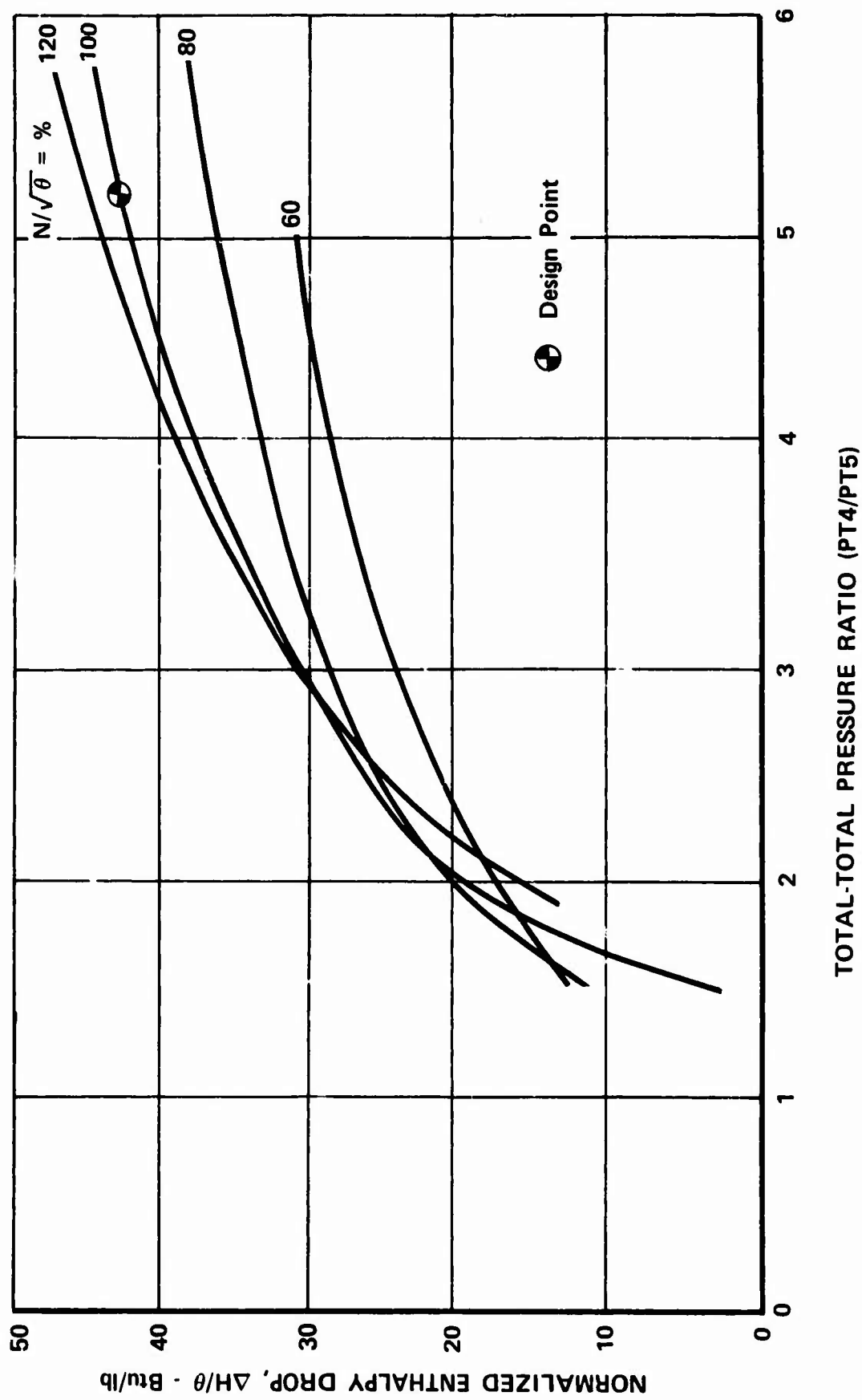
Figure 56. Predicted Stage Performance (Enthalpy Drop vs Pressure Ratio).

107
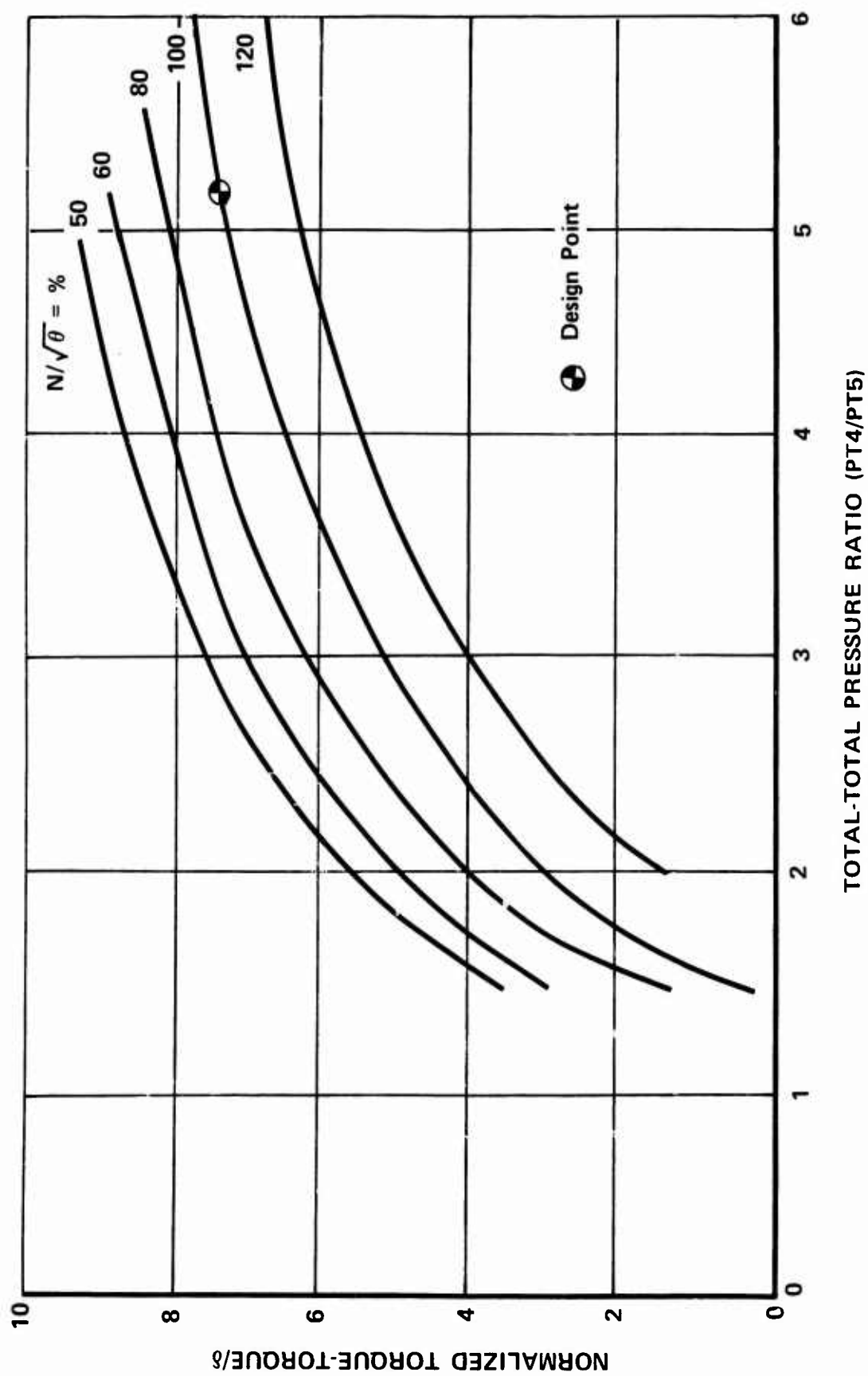
Figure 57. Predicted Stage Performance (Torque vs Pressure Ratio).

108
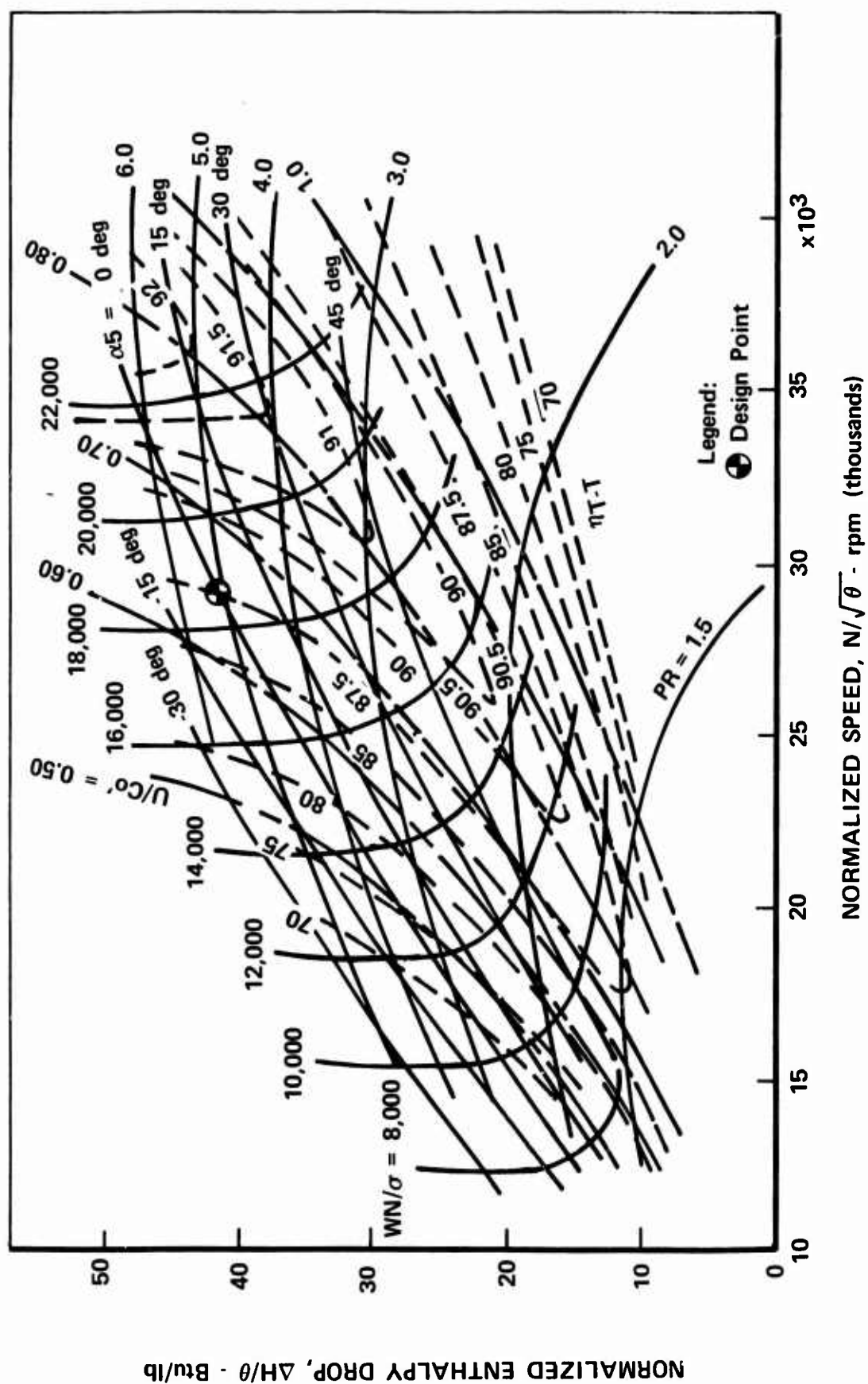
Figure 58. Predicted Stage Performance (Universal Performance Map).
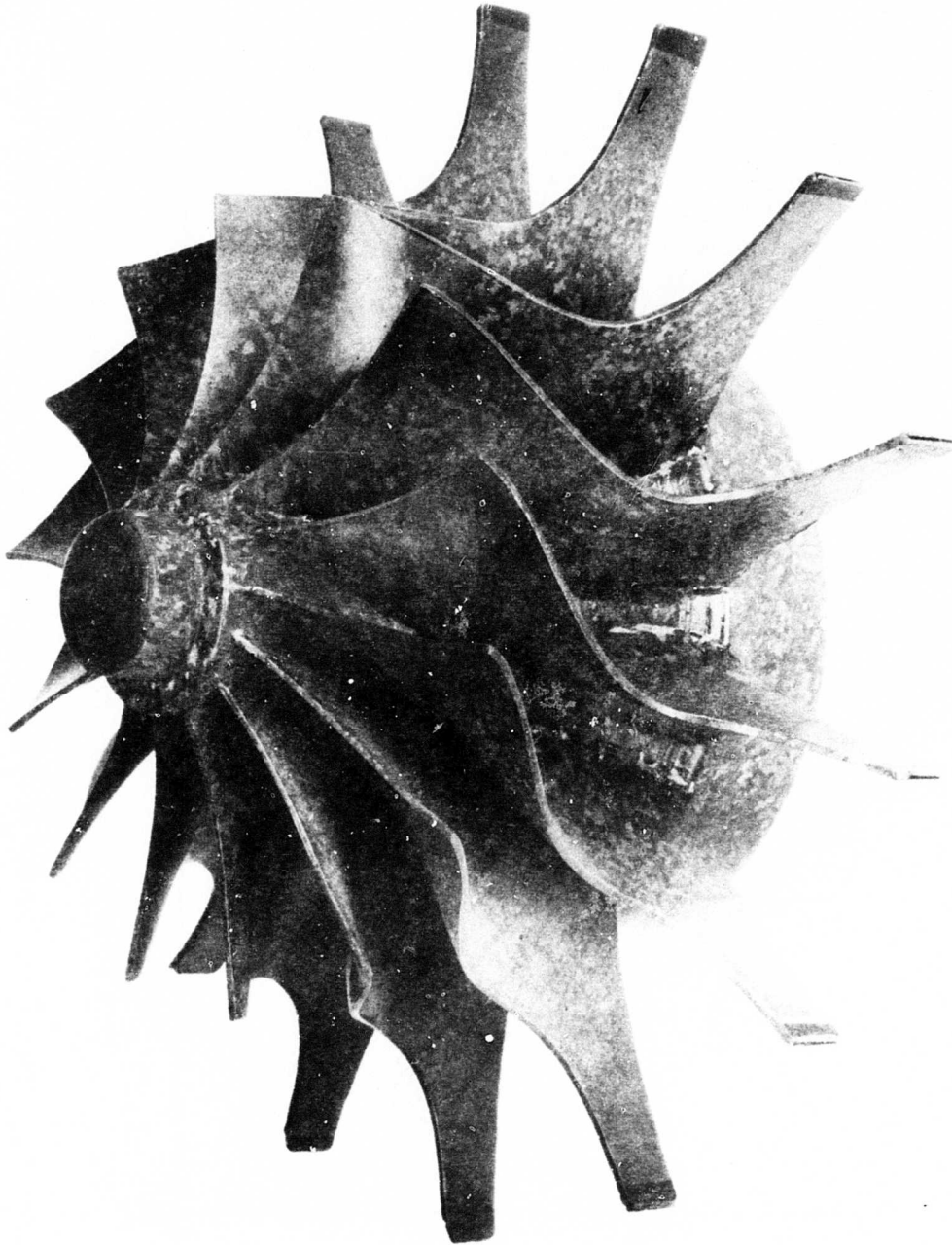
Figure 59. Sample Rotor (11-in. dia).
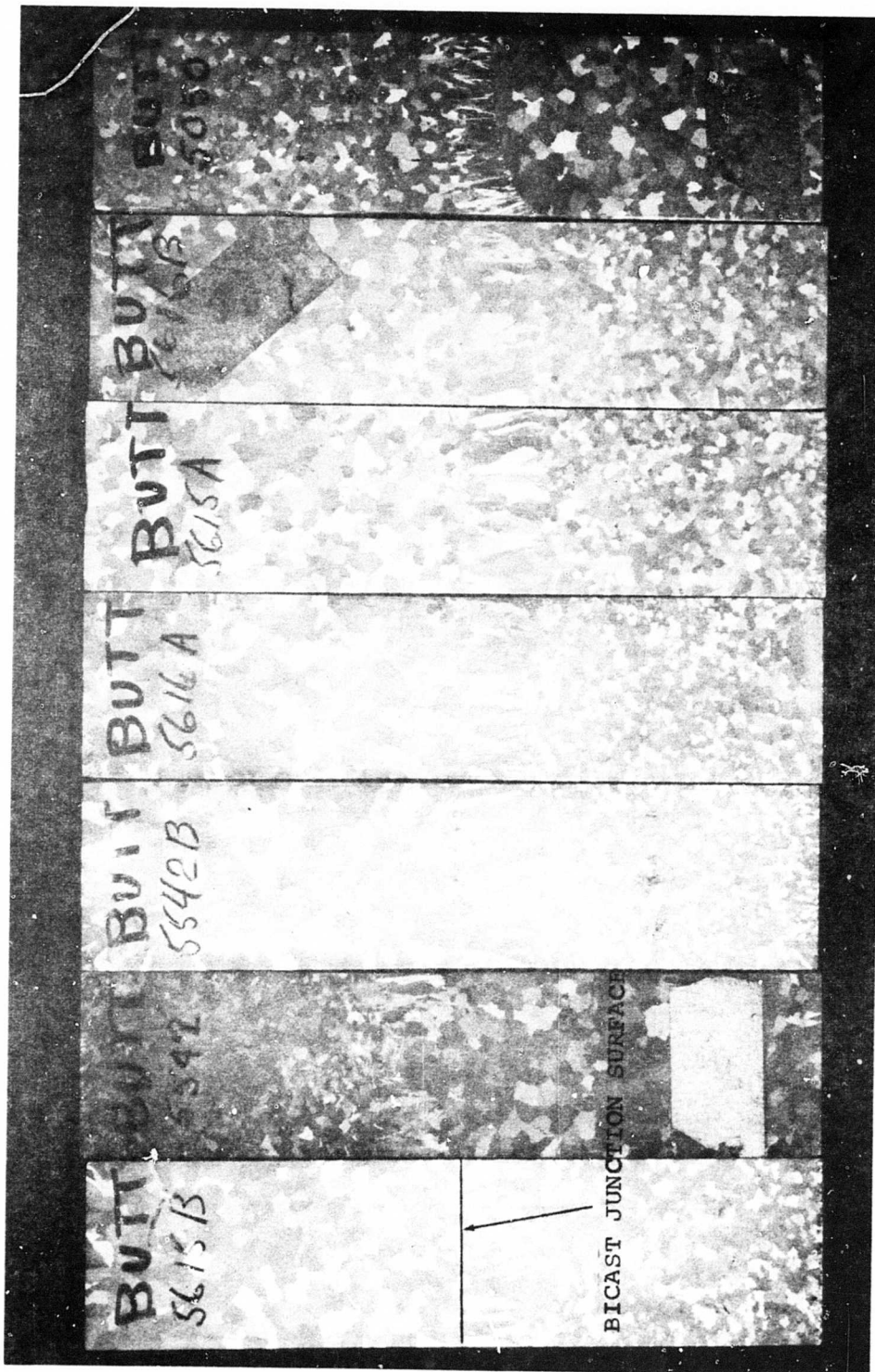
Figure 60. Bicast Test Bars (Butt Joint).
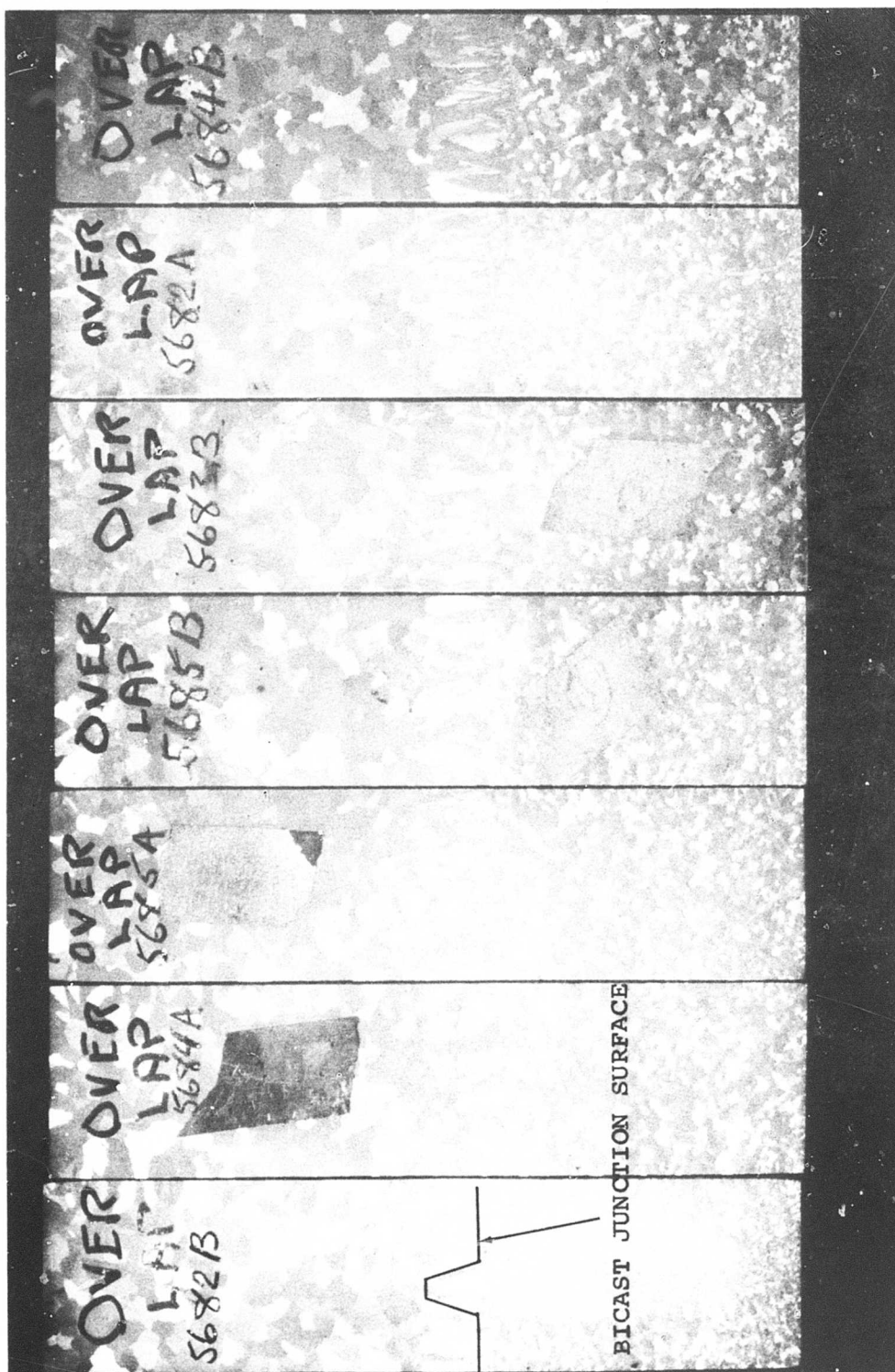
Figure 61. Bicast Test Bars (Chevron Joint).

Depression

Cast-on Hub

Separately
Cast Blade
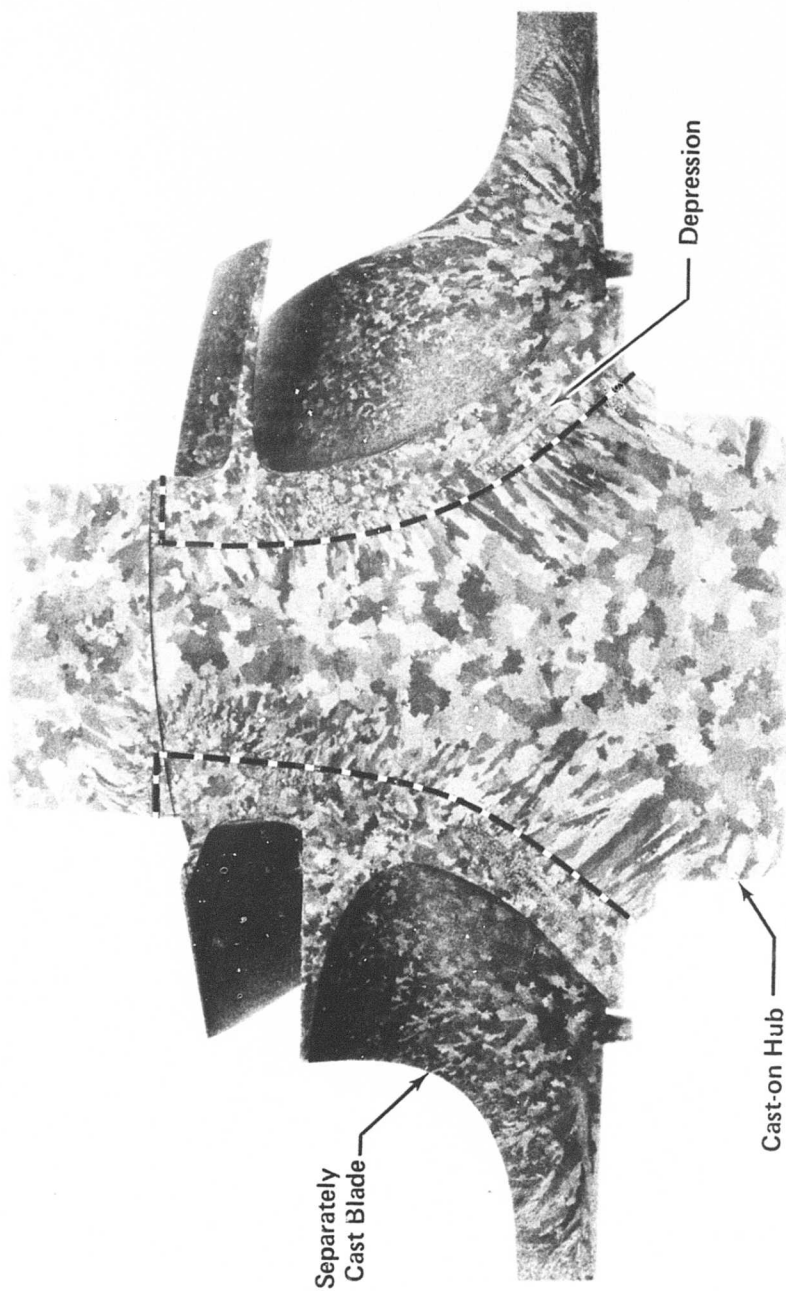
Figure 62. Bicast Rotor Section.

113
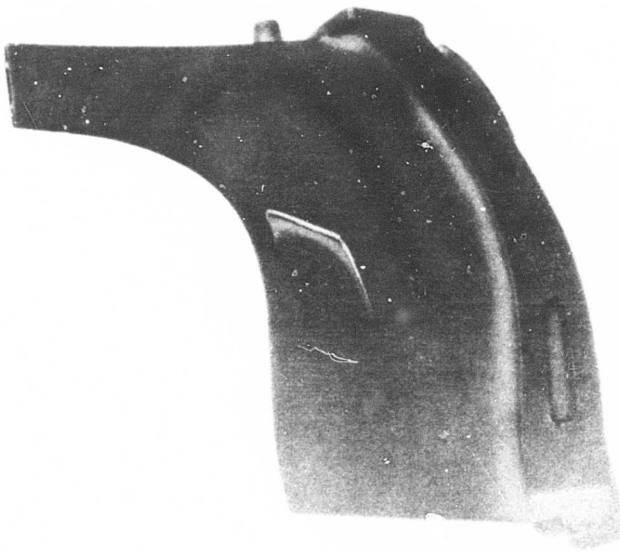
PW. 658 BLADE CASTING
(SUCTION SIDE)
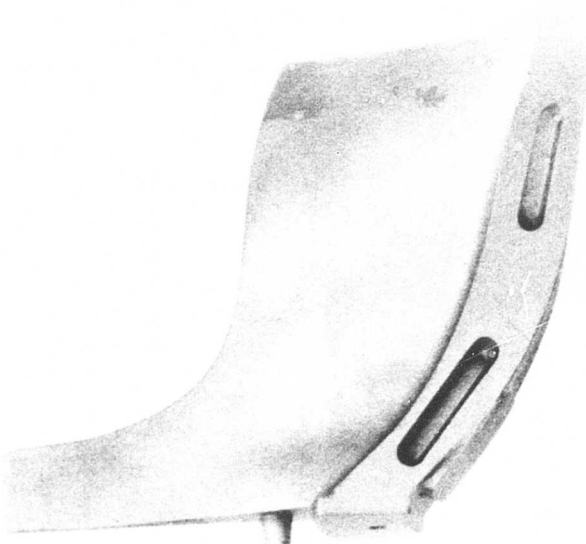
PWA 658 BLADE CASTING
(PRESSURE SIDE)

Figure 63.   Individual Blade Castings.

114
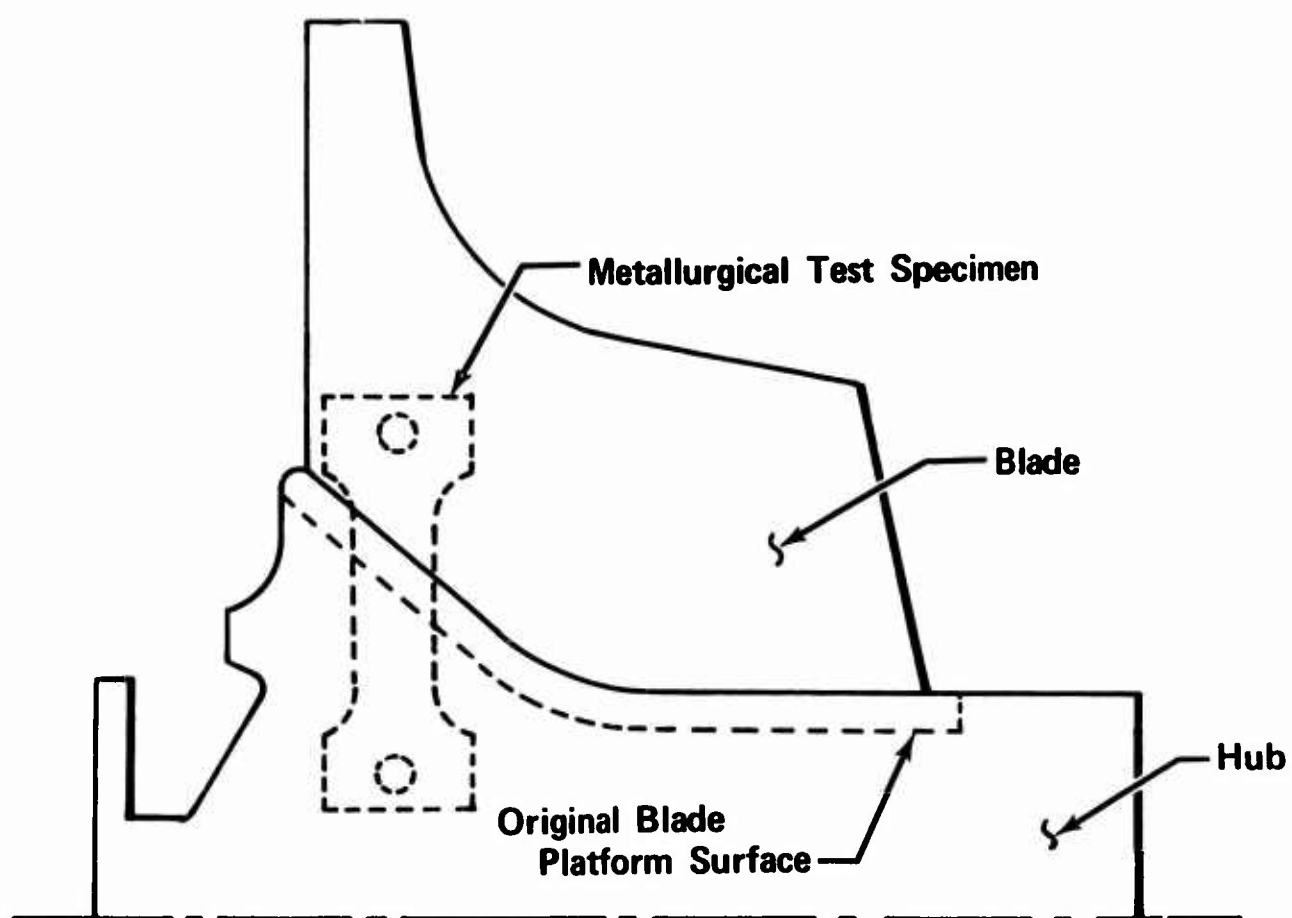
Figure 64. Location of Bicast Metallurgical Specimen.
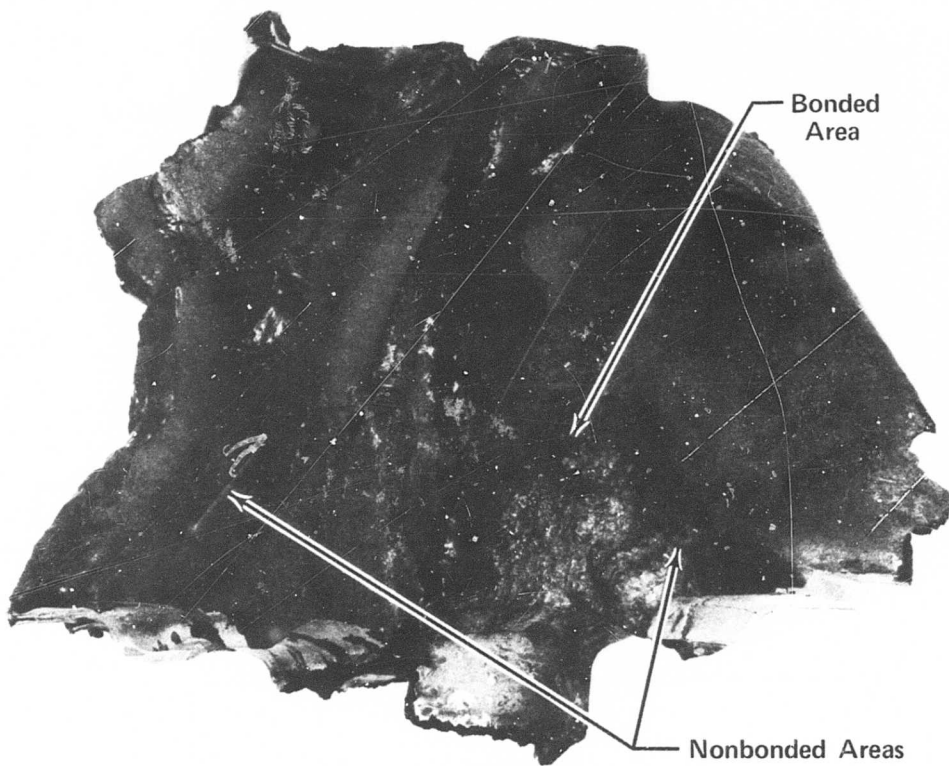
Figure 65.   Fragments From Burst Rotor (Bicast).
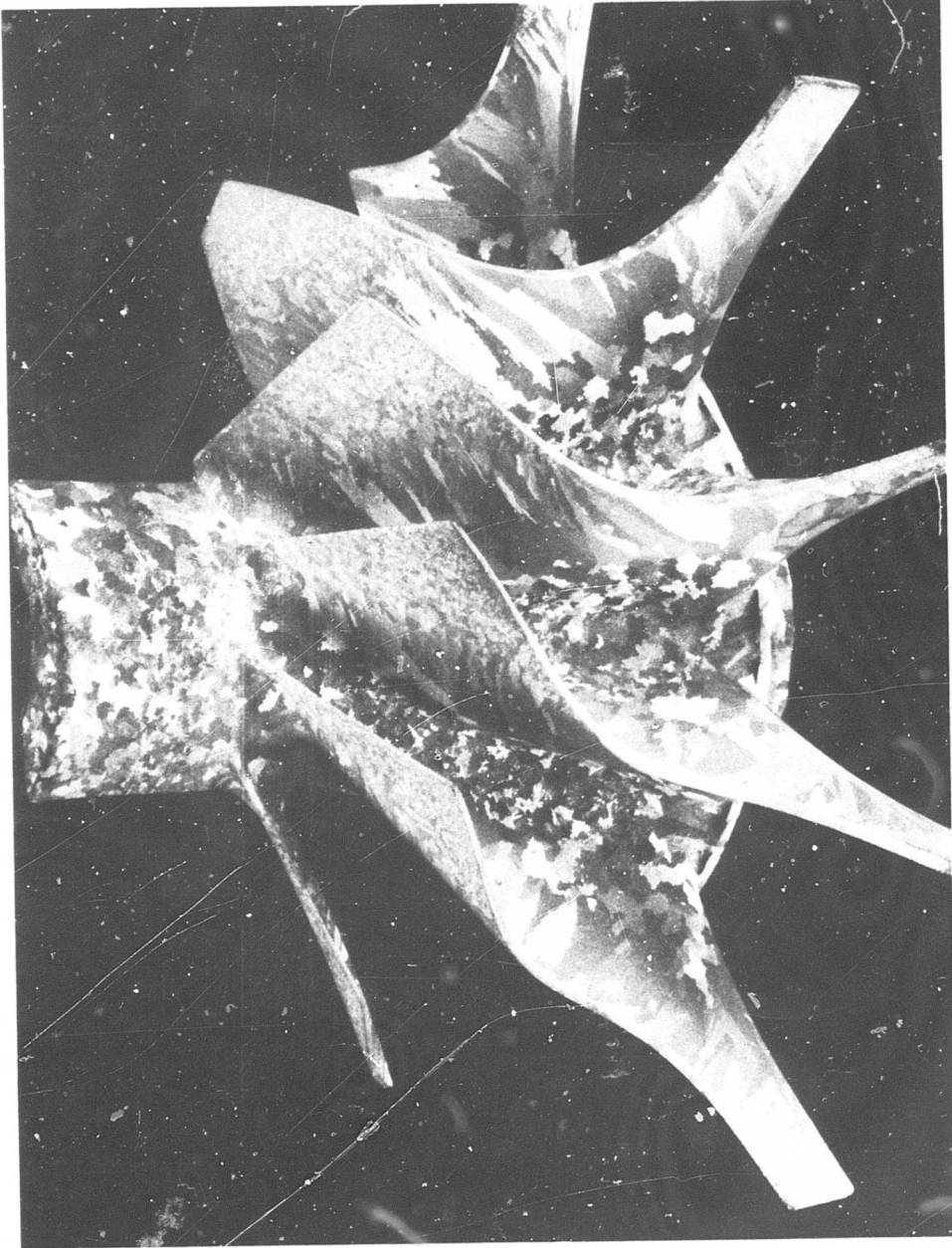
Figure 66.   Integral Rotor (Uncored).

117
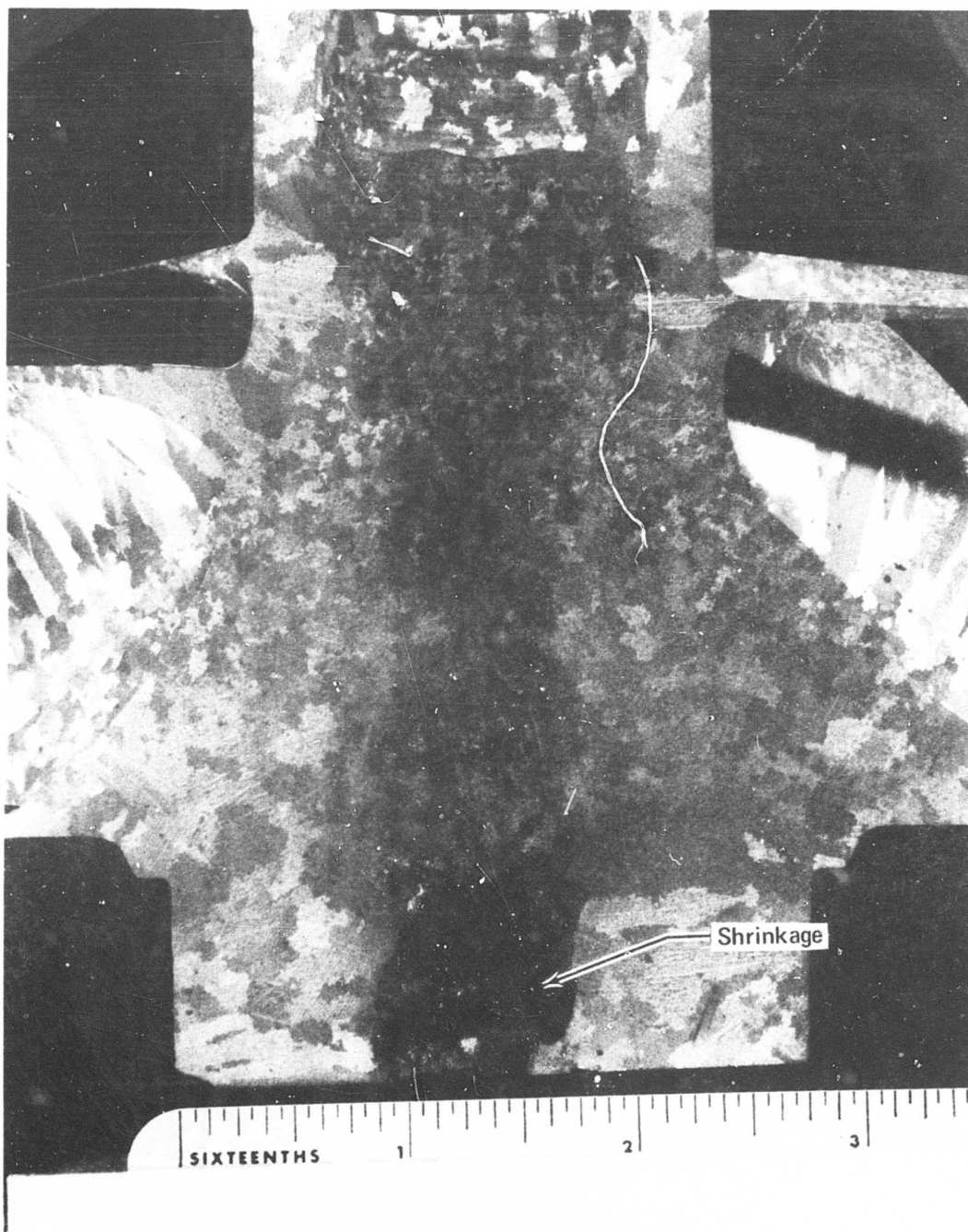
Figure 67. Integral Rotor Section (Uncored).

118
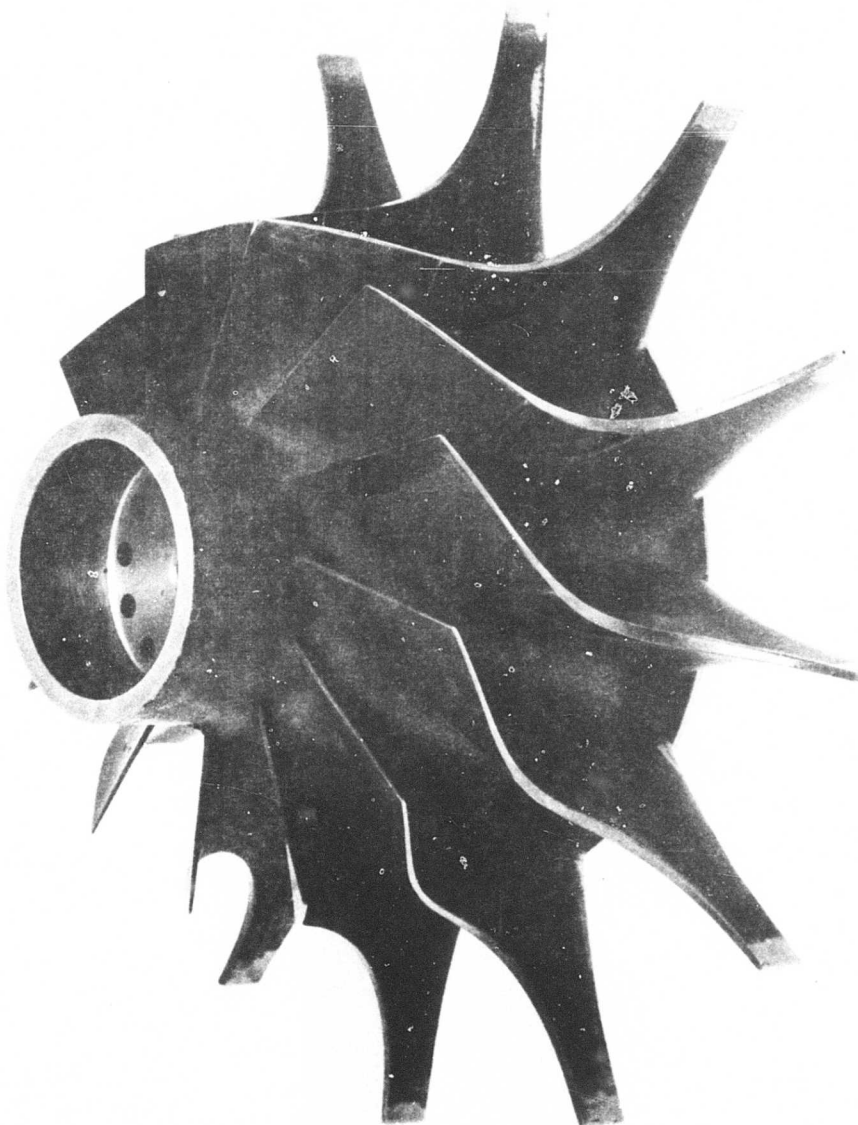
Figure 68. Integrally-Cast Spin Test Rotor.
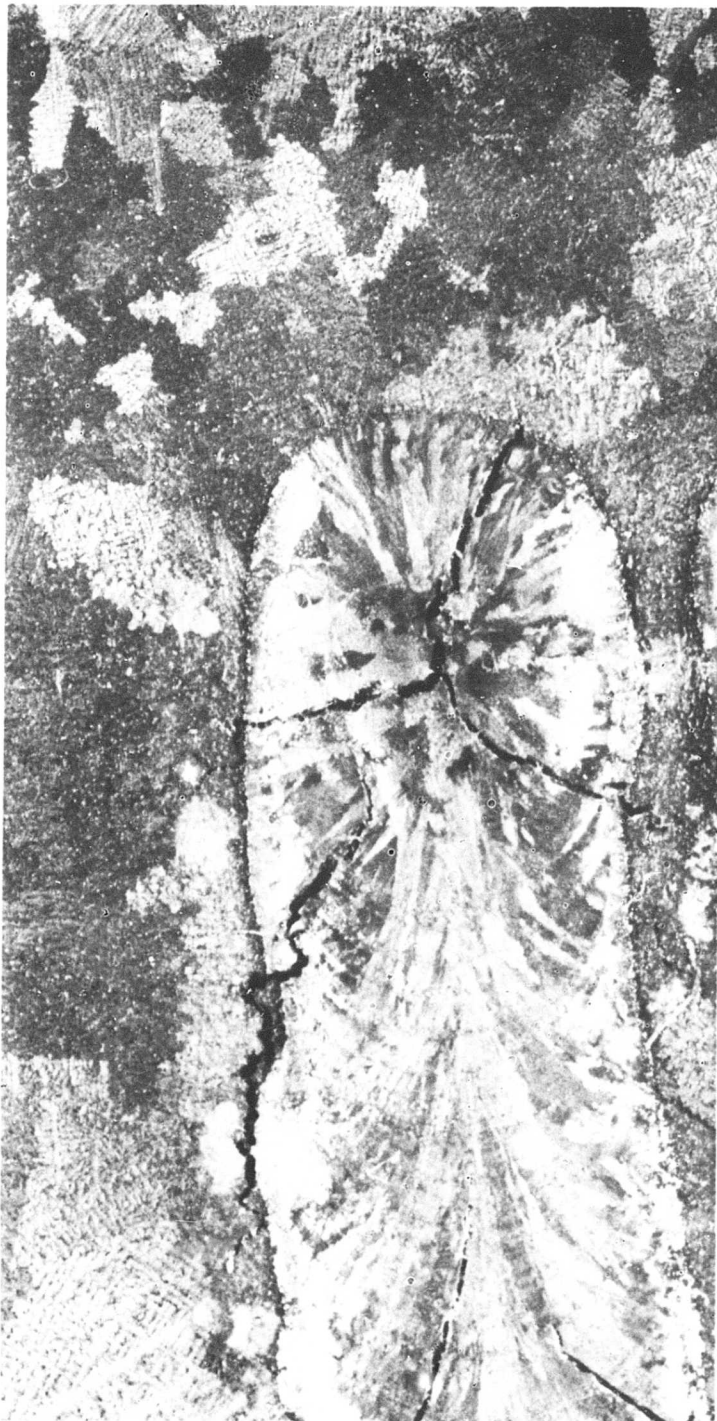
Figure 69. Typical IN100 Weld Cracks.

120
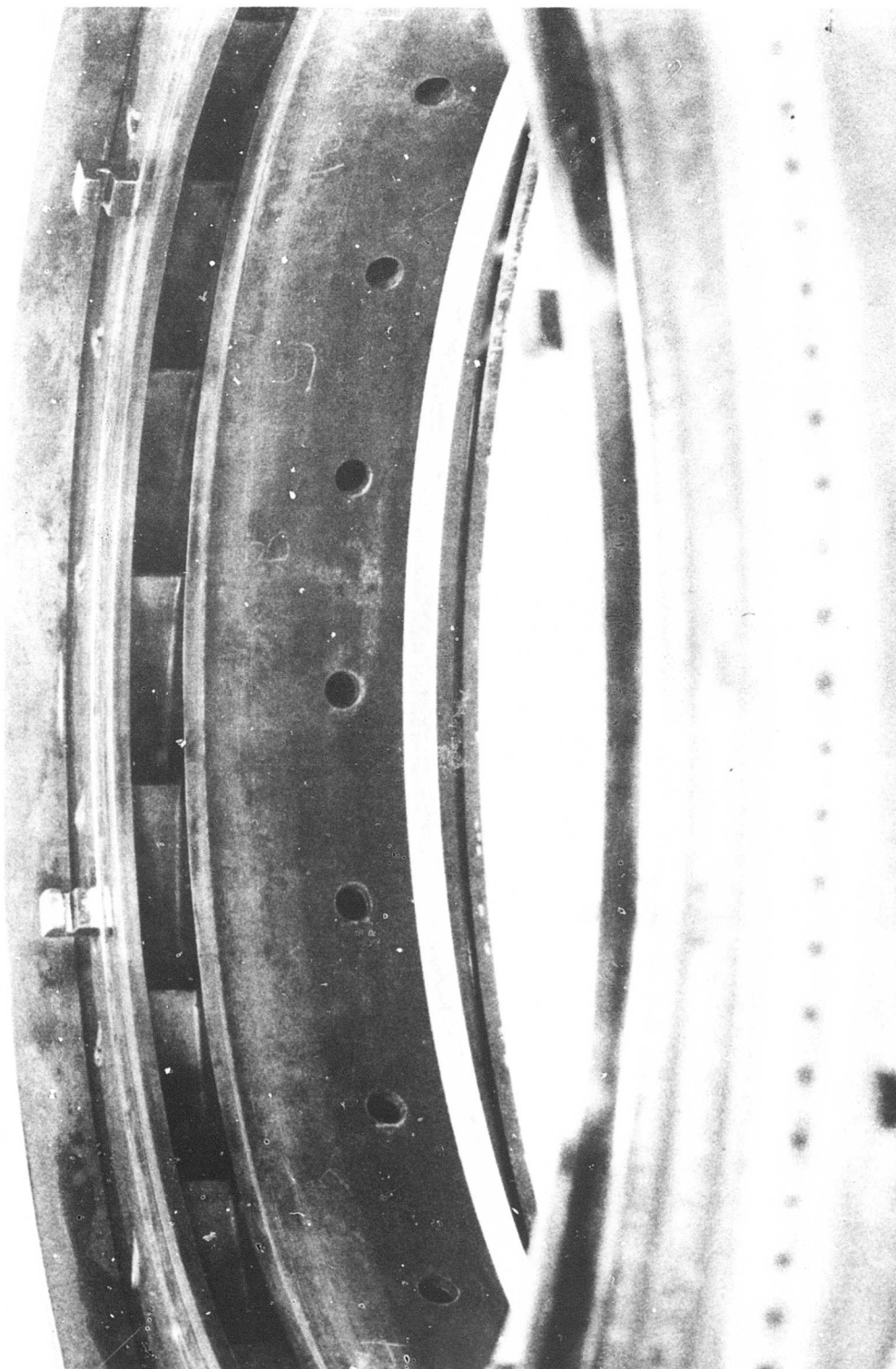
Figure 70. Integral Nozzle Casting After Machining.

Electrodes

Cooling Air Holes
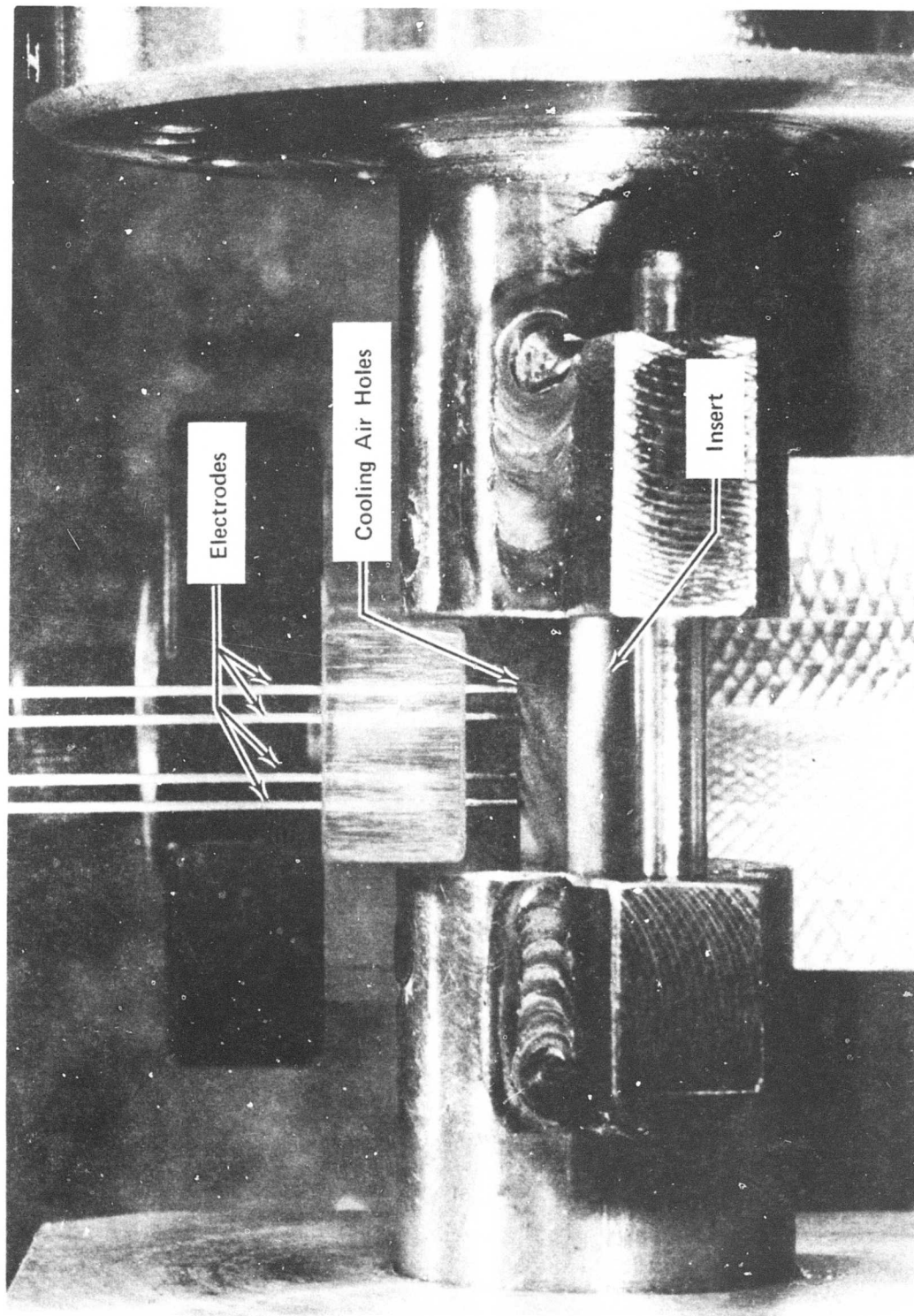
Insert

Figure 71. Cooling Air Insert Machining.
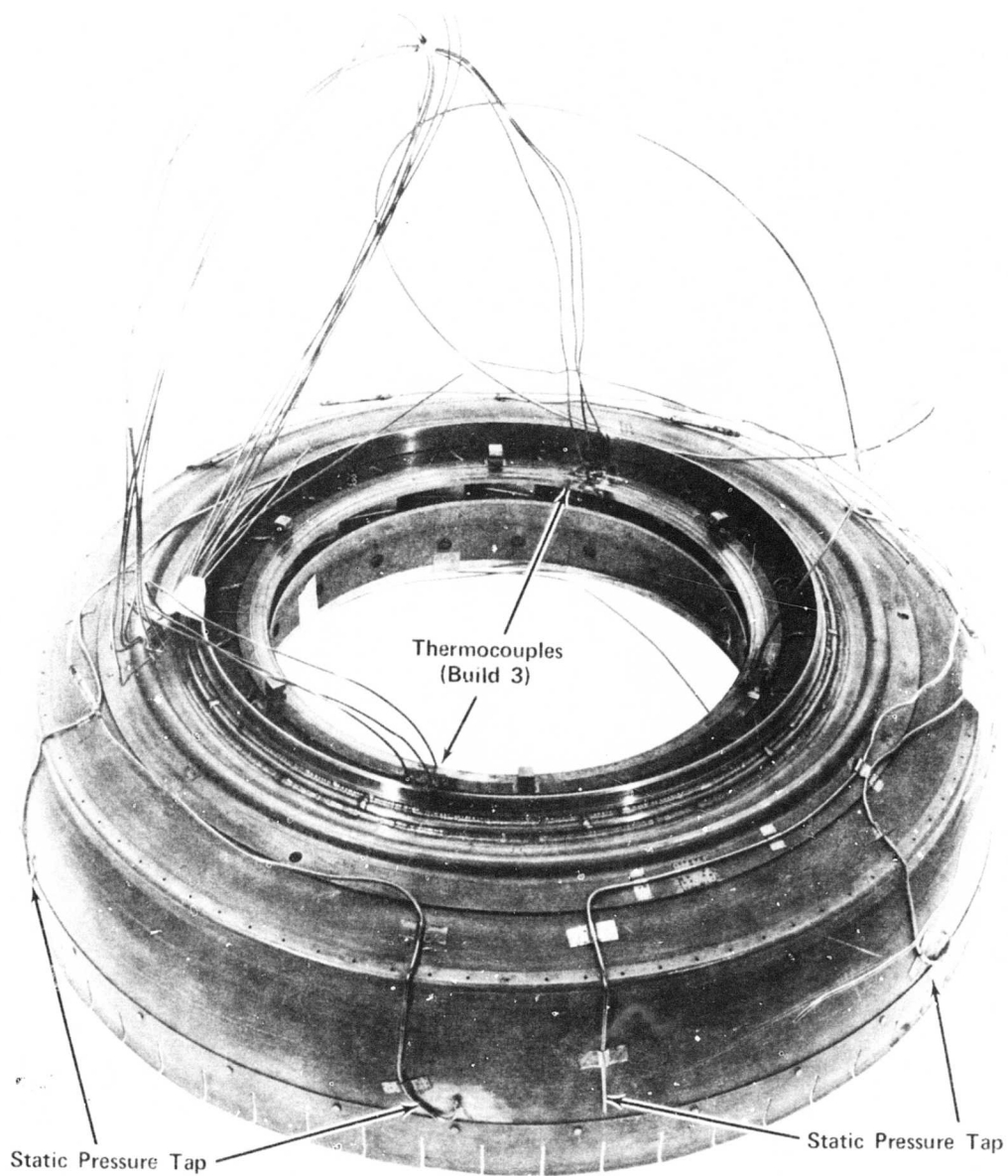
Figure 72. Completed Nozzle Assembly.

Rear Core Support
Holes (Welded)

Tip Bleed Holes
Machined After
Welding
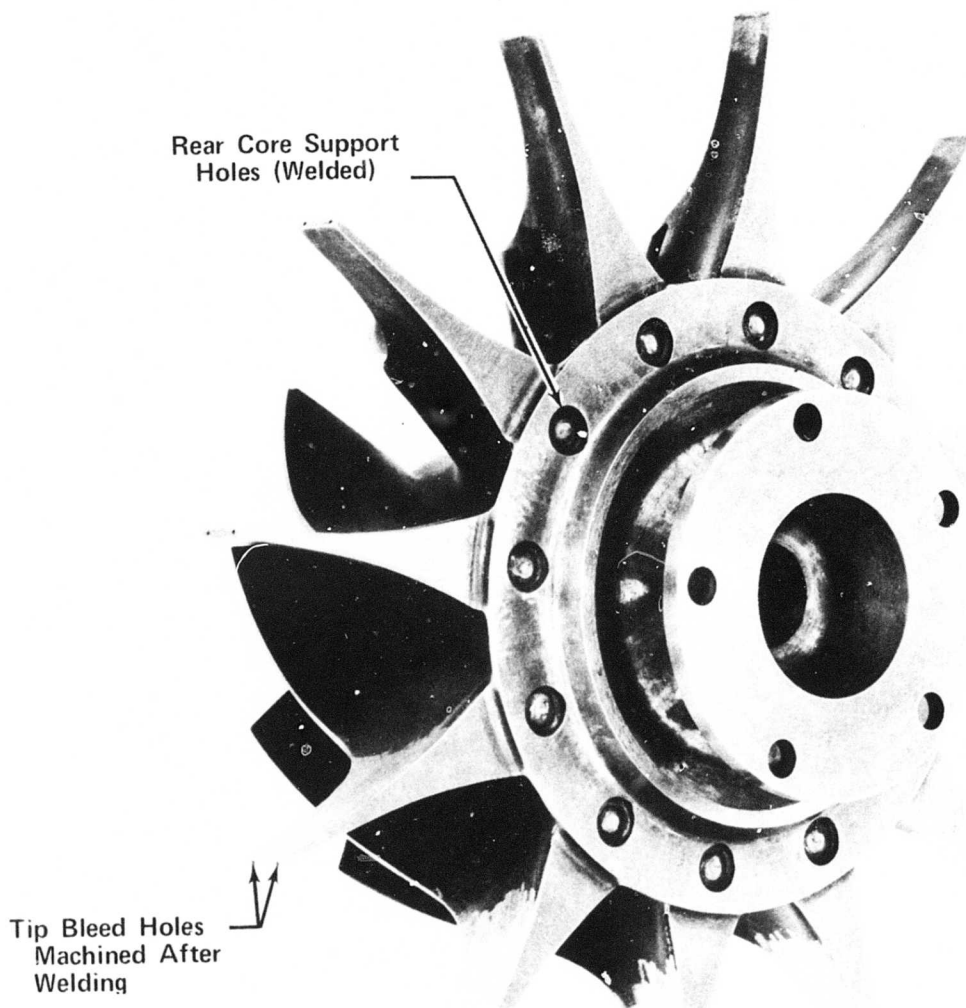
Figure 73. Turbine Rotor (Rear View).

124

0.050R

0.150

0.050R

0.150

Cross Section of Welding Groove
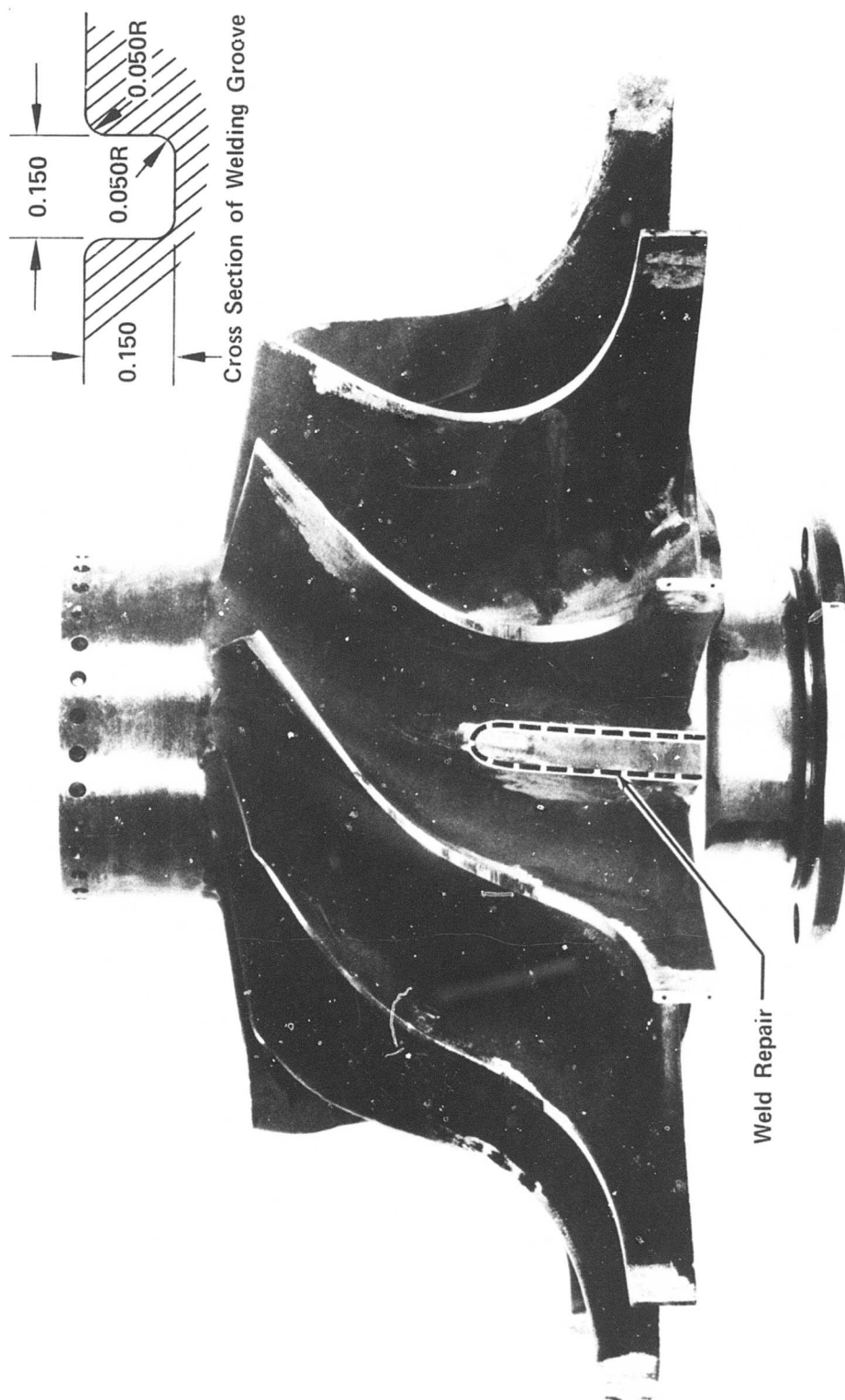
Weld Repair

Figure 74. Weld Repaired Rotor (Side View).

125

0.150

0.150

0.050R

0.050R

Cross Section of Welding Groove

Thermocouple

Weld Repair

Thermocouple
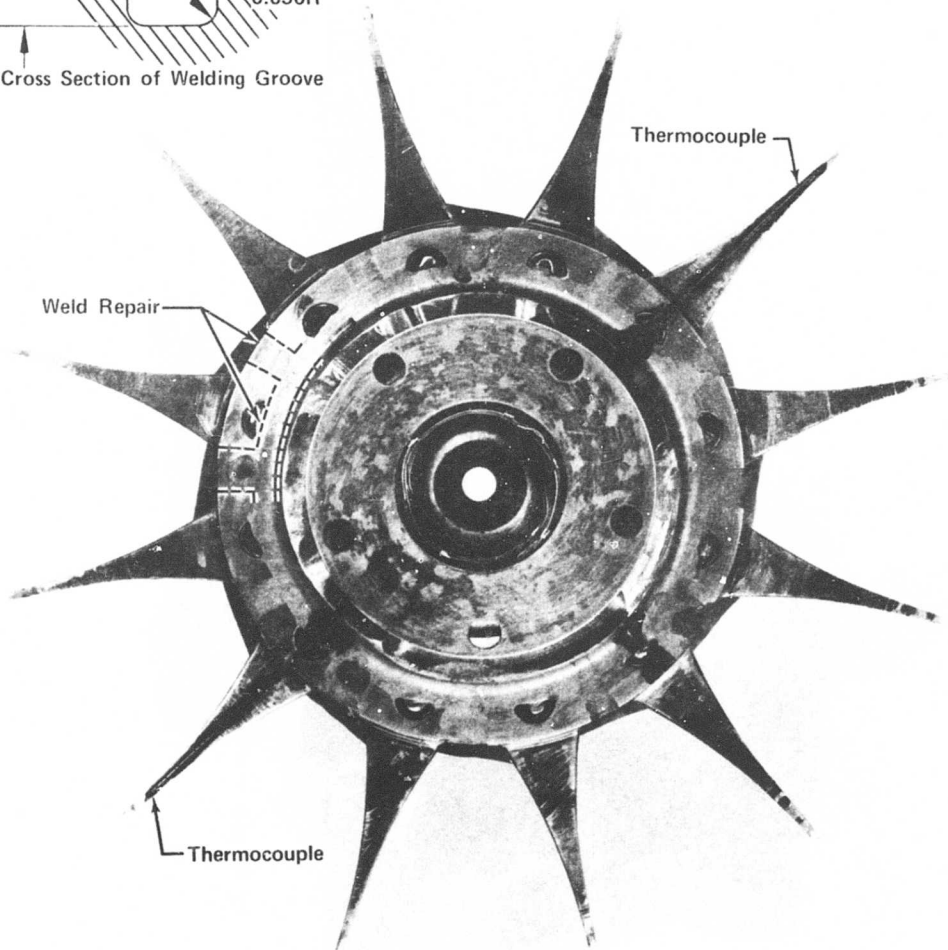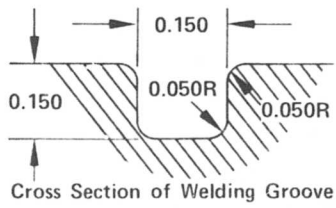
Figure 75. Weld Repaired Rotor (Rear View).

Cooling Air
Inlet Hole
(Typical)
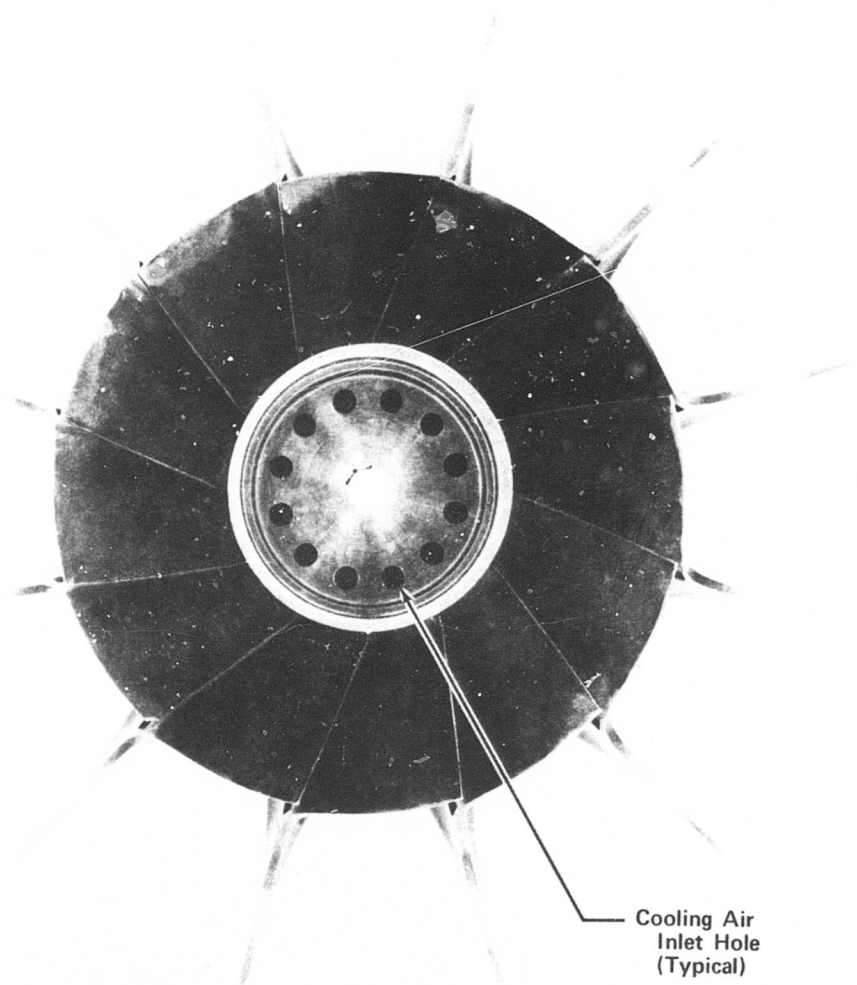
Figure 76.   Turbine Rotor (Front View).
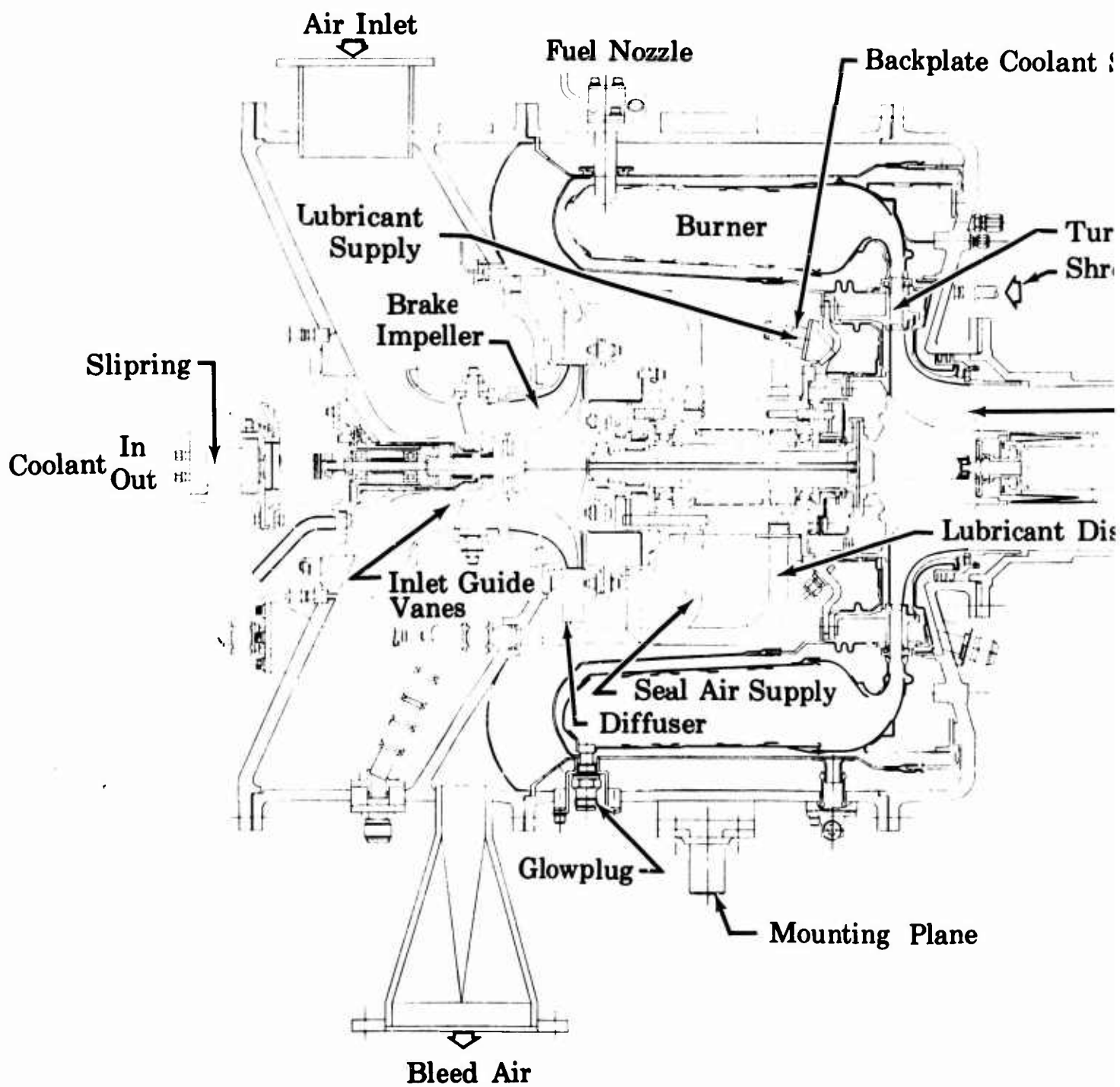
Figure 77. Turbine Test Rig Configuration.

Fuel Nozzle

Backplate Coolant Supply

Burner

Vane Cooling Configuration

Turbine Nozzle

Shroud Coolant Supply

Rotor Cooling Air Inlet

Turbine Rotor

Turbine Exhaust

Lubricant Discharge

Seal Air Supply

Diffuser

Cooling Air

Glowplug

Mounting Plane

Two-Pass Rotor Cooling Configuration

r
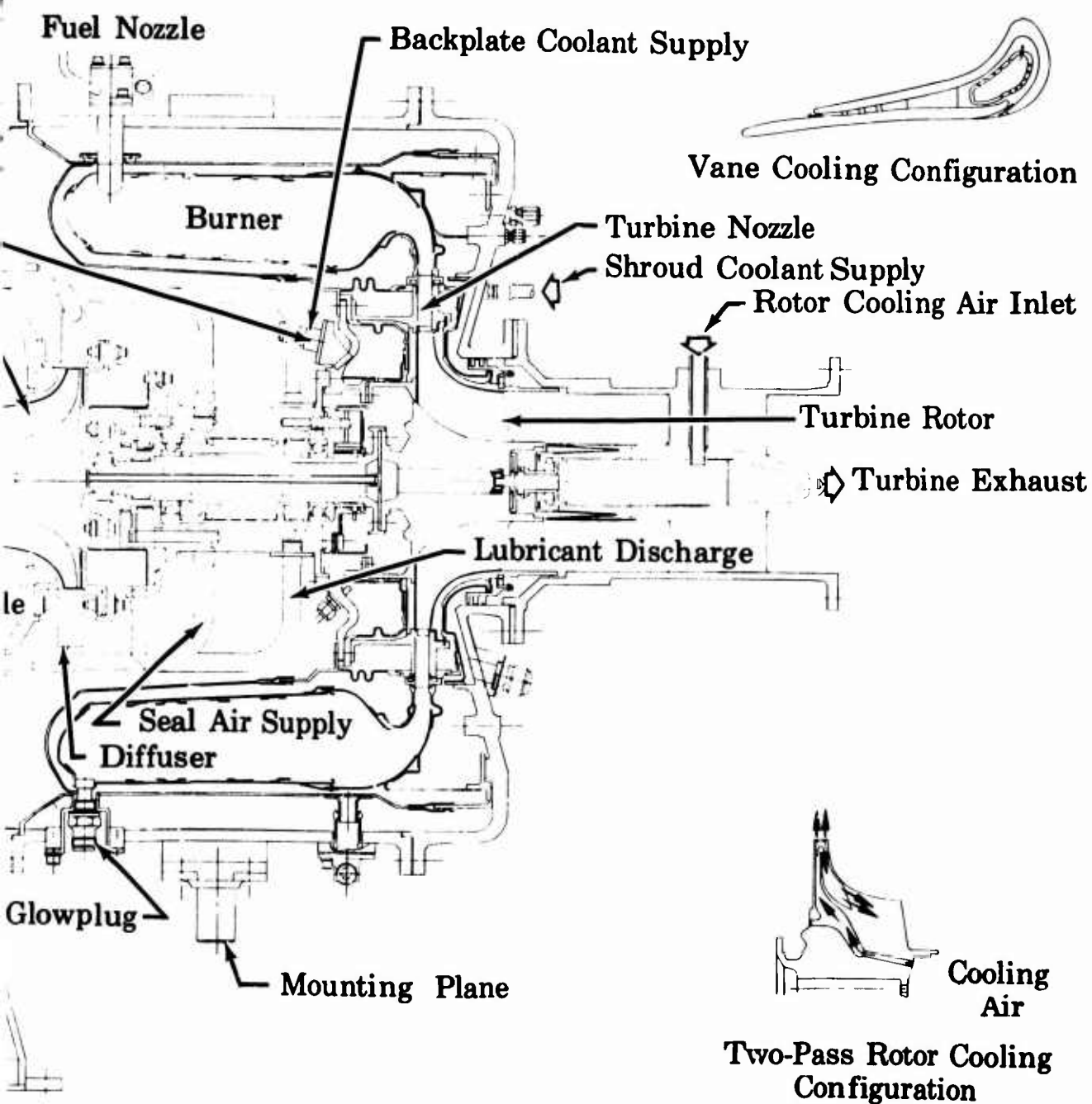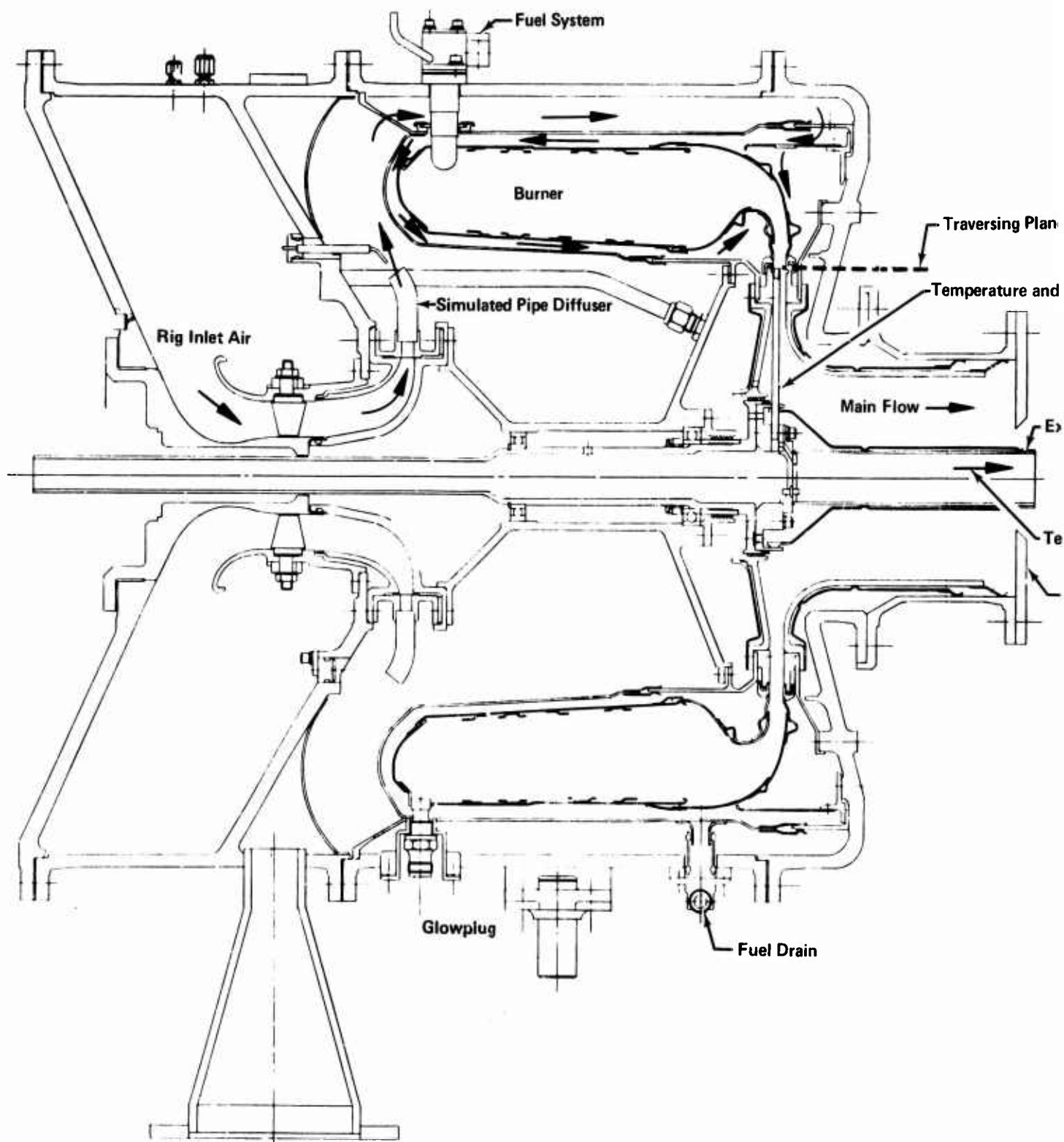
Rig Configuration.

Figure 78. Burner Test Rig Configuration.

—Fuel System

Burner

— Traversing Plane Nozzle Vane Inlet

ed Pipe Diffuser

—Temperature and Total Pressure Probes (Rotates 355 deg)

Main Flow →

— Exhaust Centerbody

—Temperature Probe Aspiration Air

— Backpressure Orifice

—Fuel Drain
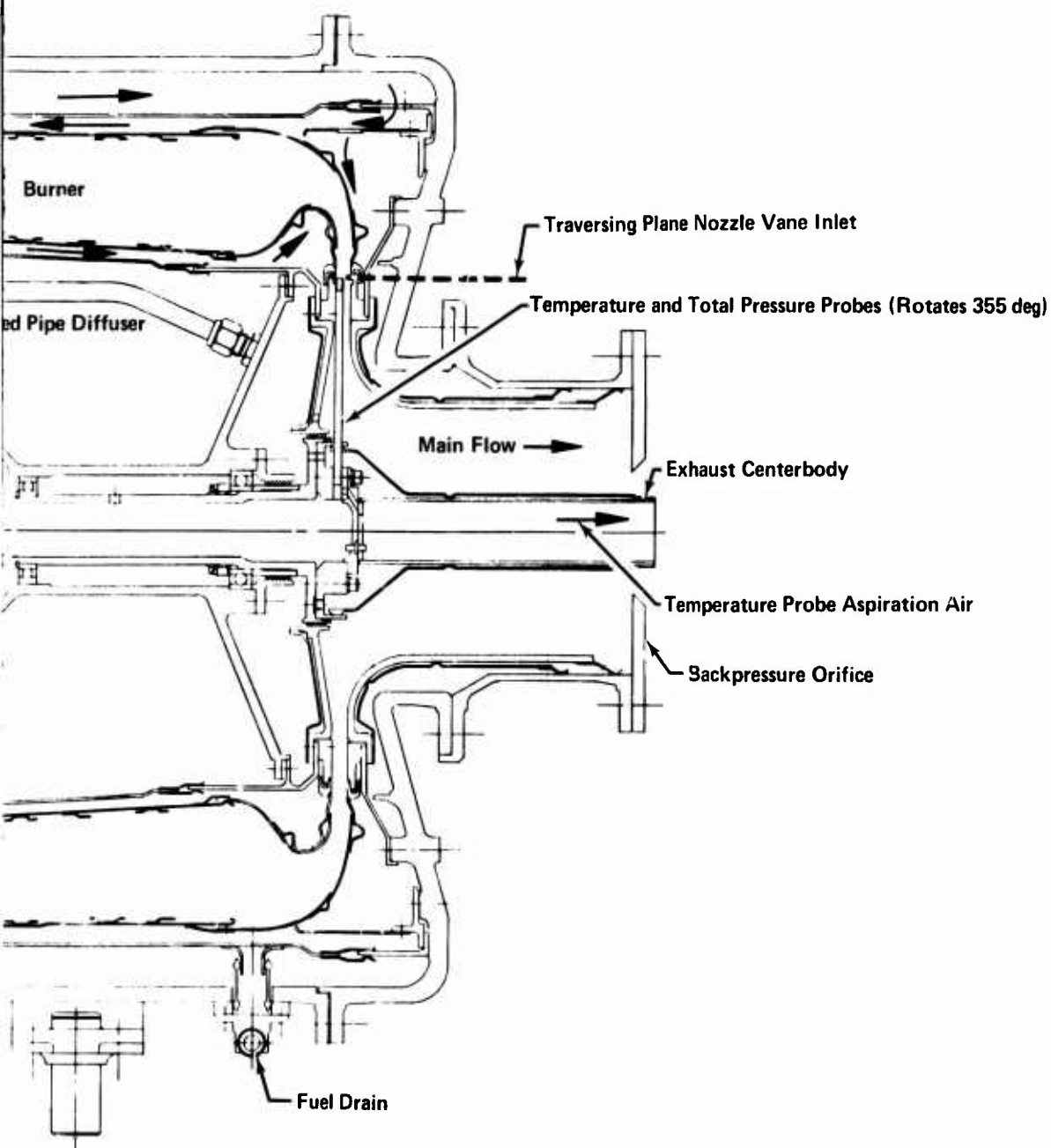
t Rig Configuration.
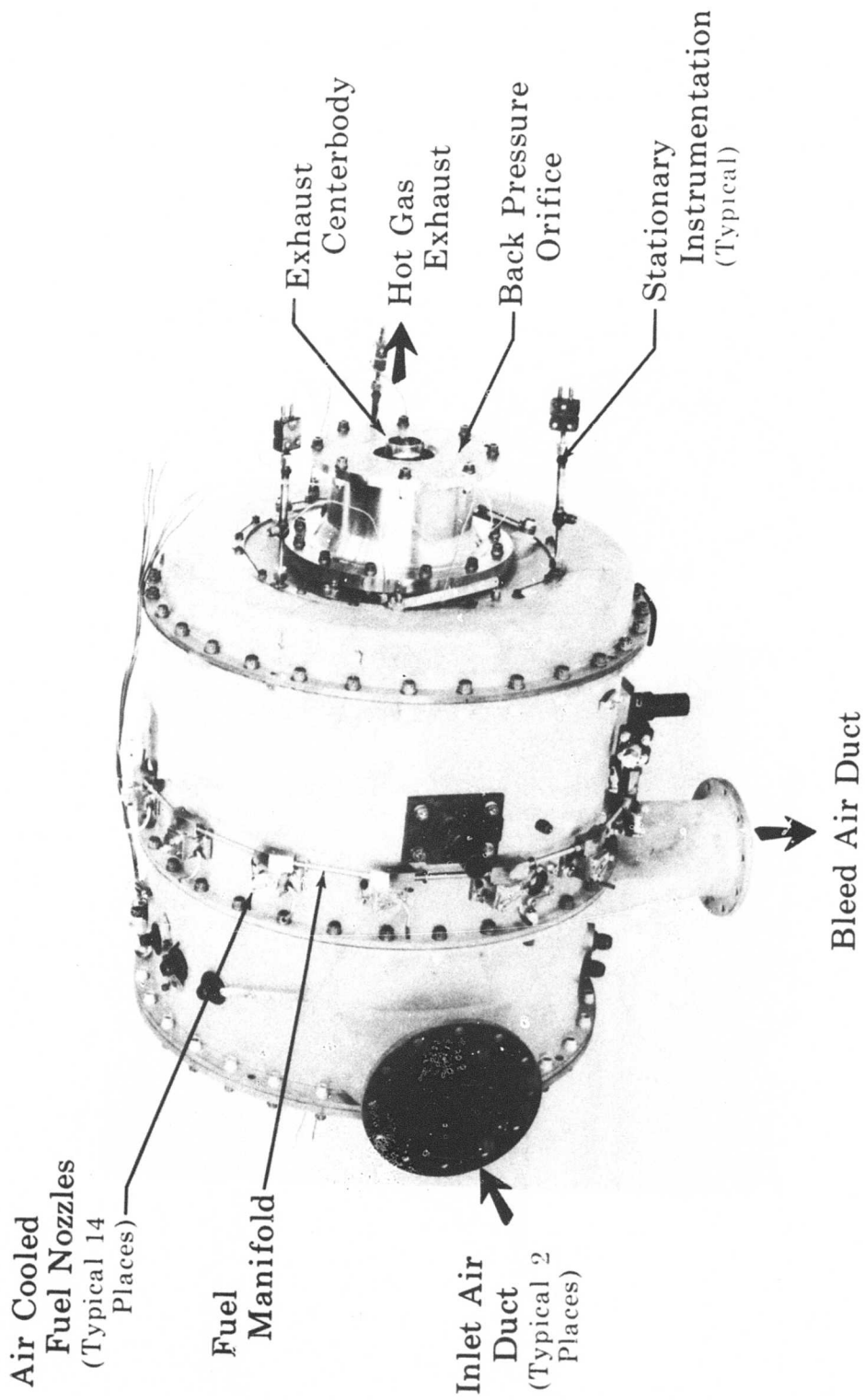
Figure 79. External View of Burner Rig Showing Exhaust Section.

133

Air-Cooled
Fuel Nozzles
(Typical 14
Places)

Fuel Manifold

Bleed Air Duct

Traversing
Instrumentation
Lines

Compressor
Inlet Plenum

Inlet Air Duct
(Typical 2 Places)
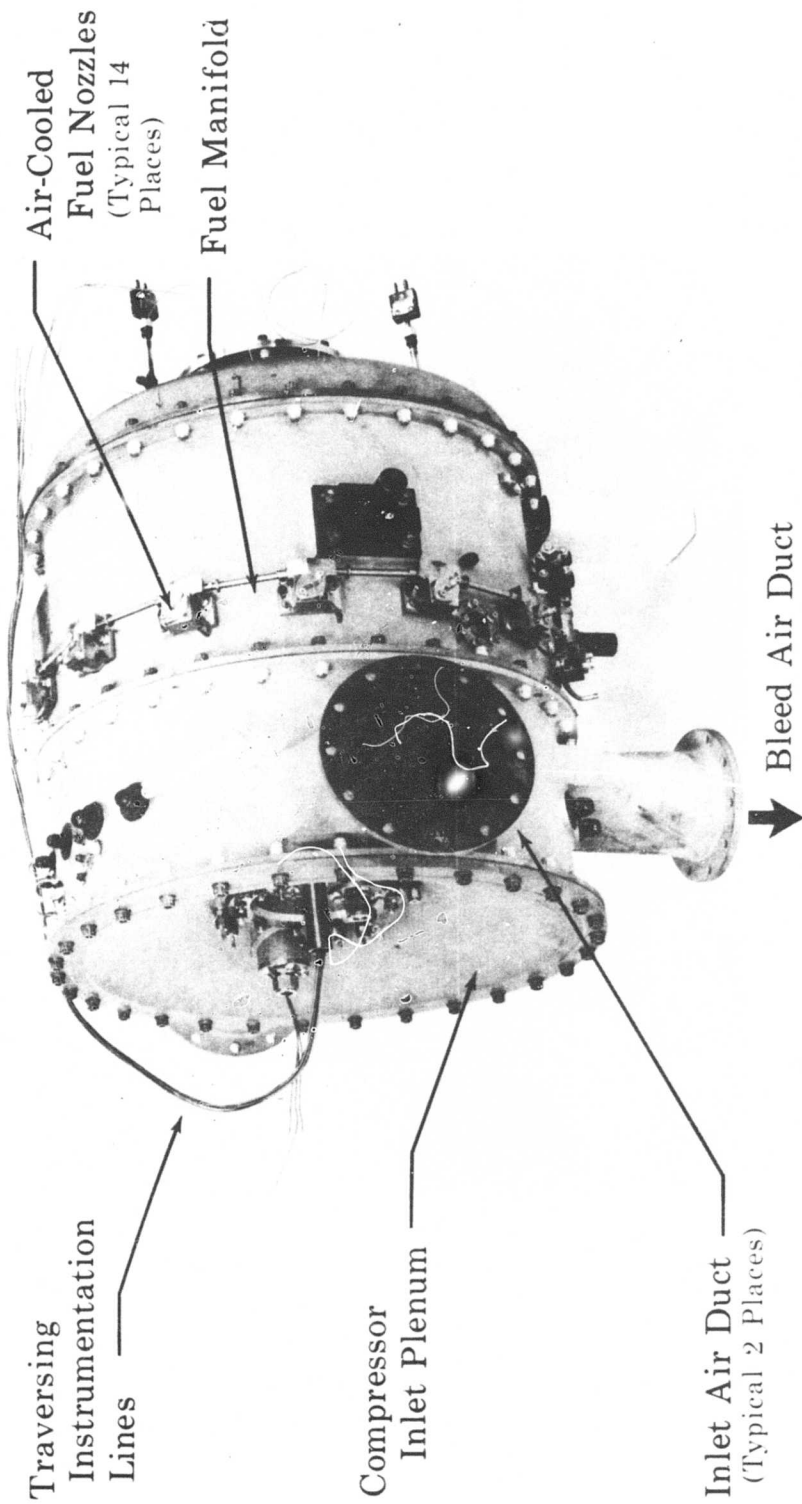
Figure 80.   External View of Burner Rig Showing Inlet Section.

Test Rig

Inlet Lines

Fuel Pump and Control

Air Heater

Air Dryer

Lube Oil System

Bleed Air Line

Lube Oil Scavenge Pumps
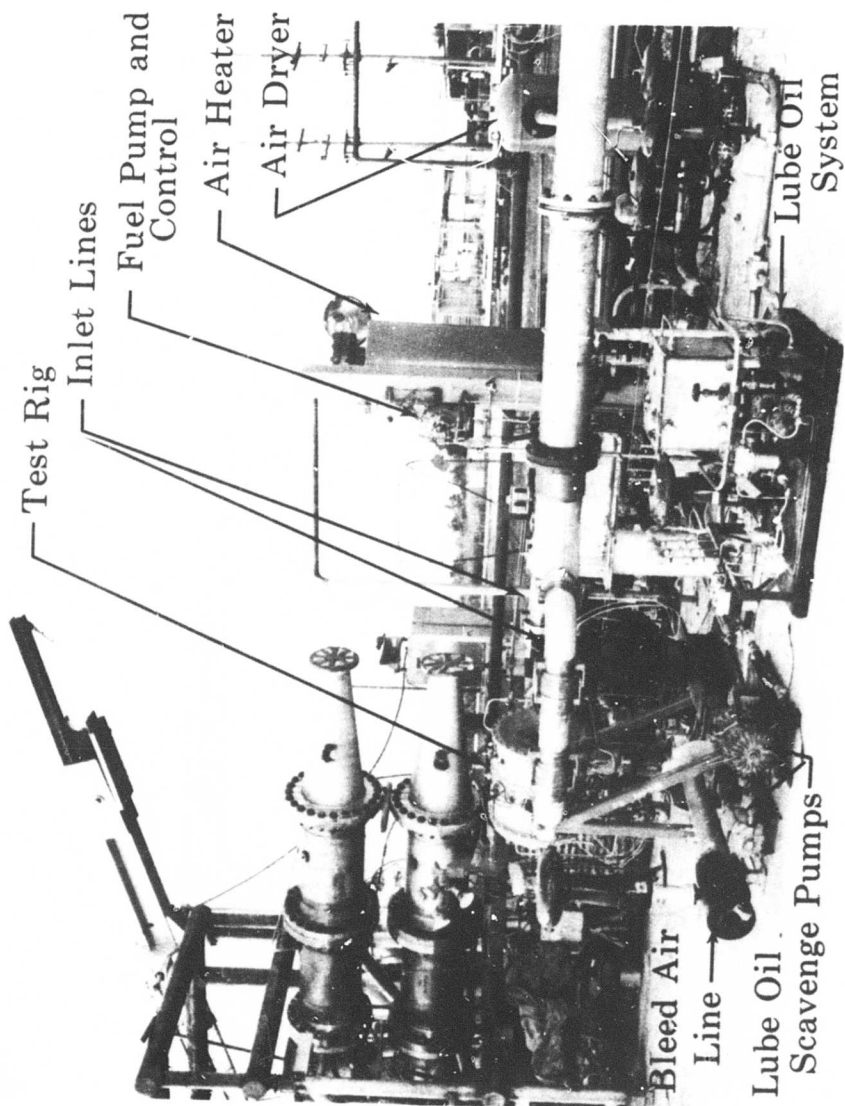
Figure 81.   Burner Test Rig on Test Stand.

135
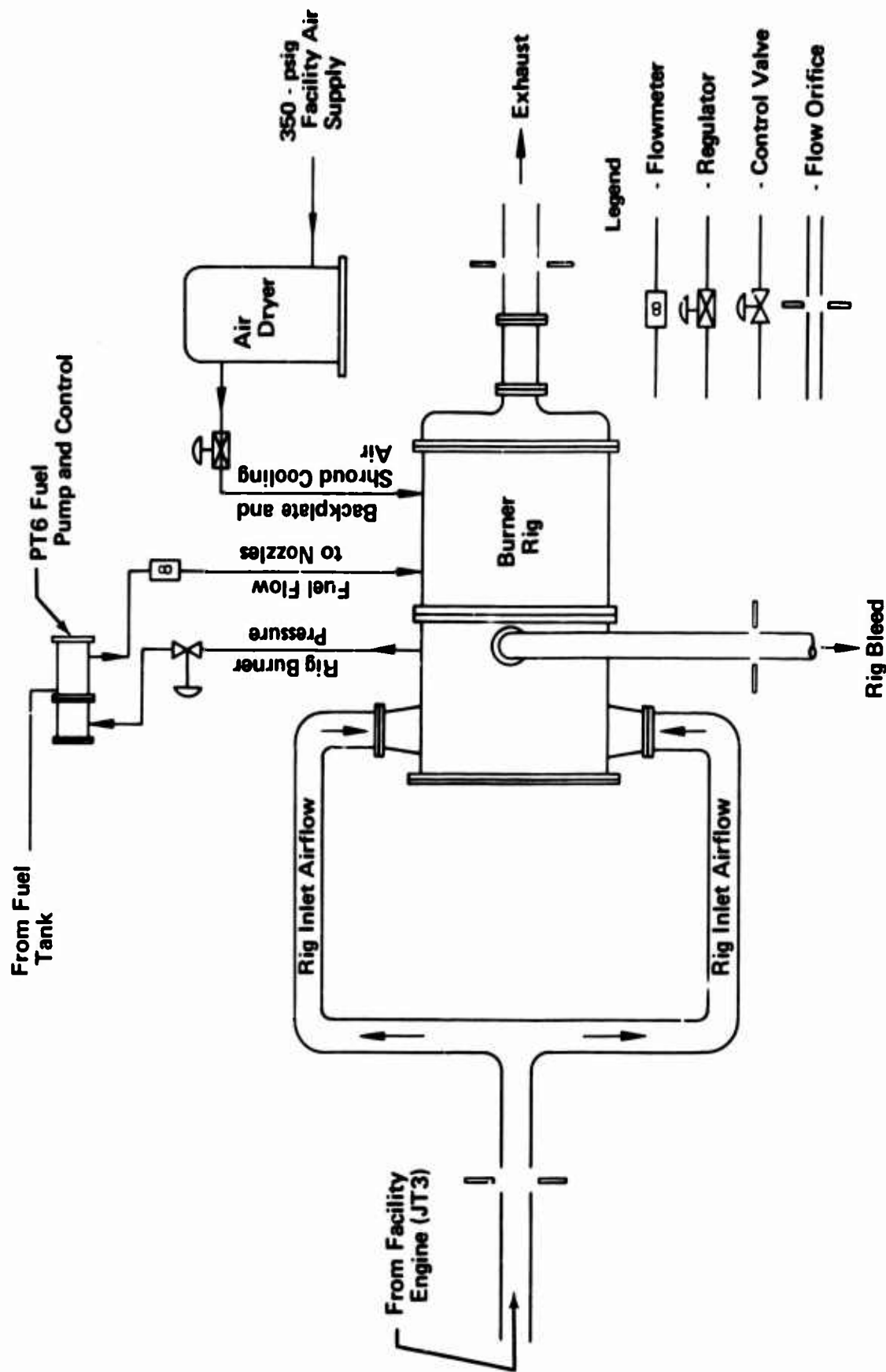
Figure 82. Burner Test Facility Schematic.

136

TEMPERATURE-PRESSURE PROBE

0.170-in. OD, 0.020-in. Wall Tube
80% Platinum, 20% Rhodium

Inconel-Sheathed Pt-PtRh
Thermocouple Assembly

Hot Gas Vented
to Atmosphere

Aspirated

T/C

Hot Gas

Total Pressure

Total Pressure Probe

Platinum

Platinum-Rhodium

0.090-in. OD, 0.014-in. Wall Tube
80% Platinum, 20% Rhodium

Copper Alloy II
to Readout
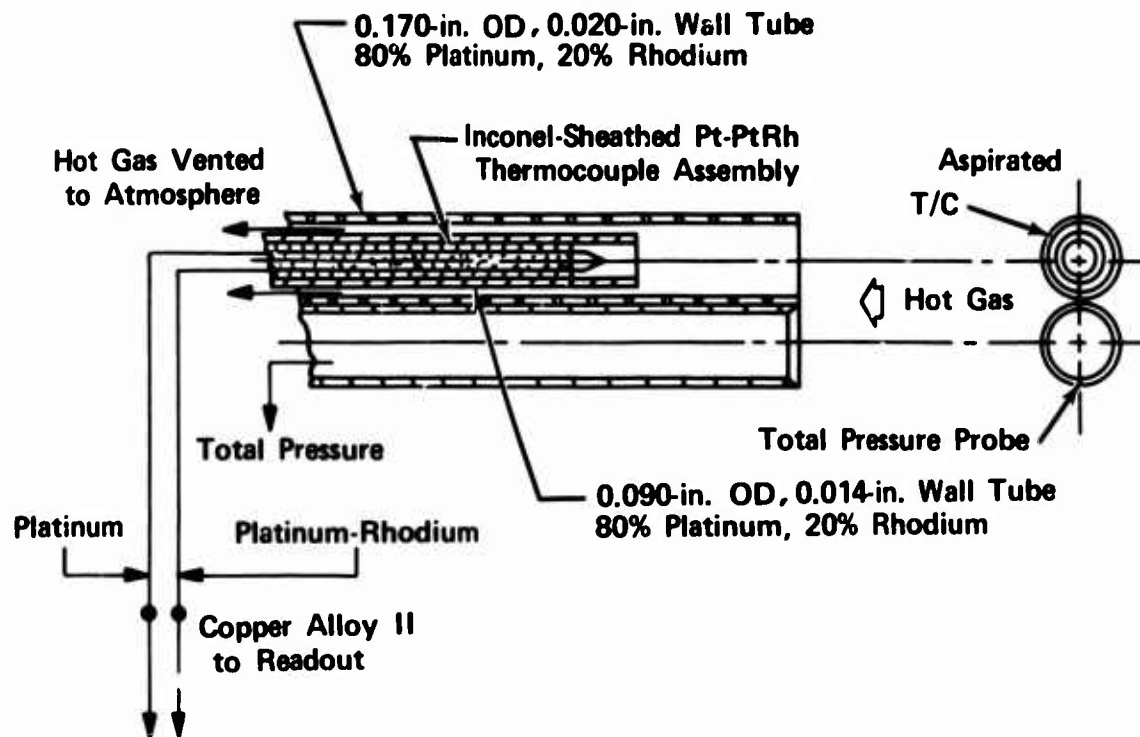
Figure 83. Temperature - Pressure Probe.
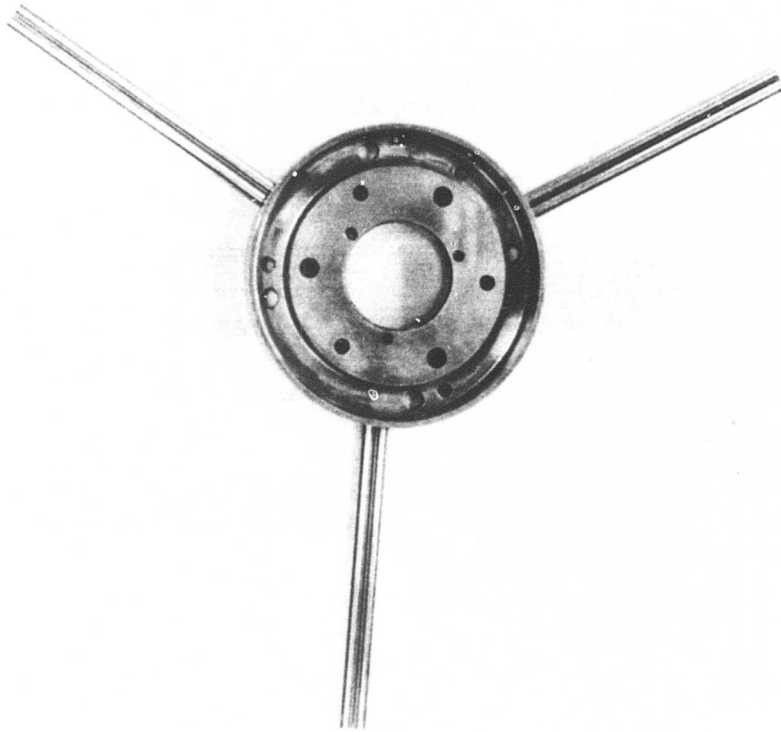
Figure 84.   Temperature – Pressure Probe Assembly.
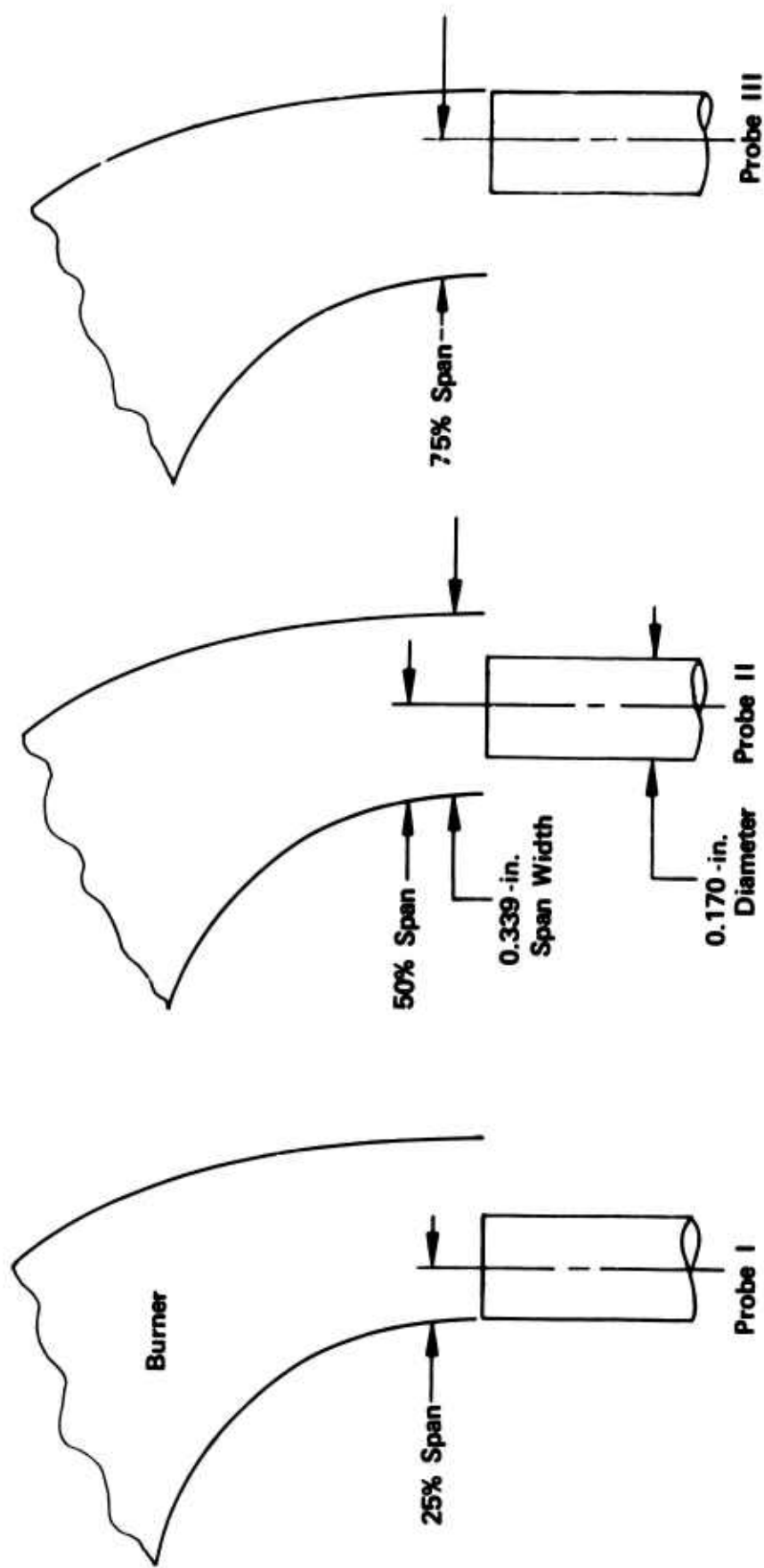
Figure 85. Nominal Spanwise Location of Probes.

Inlet
Air Duct

Total Temperature
Total Pressure
Probes
(Typical 3 Places)

Exhaust
Center Body

Bleed Air Duct
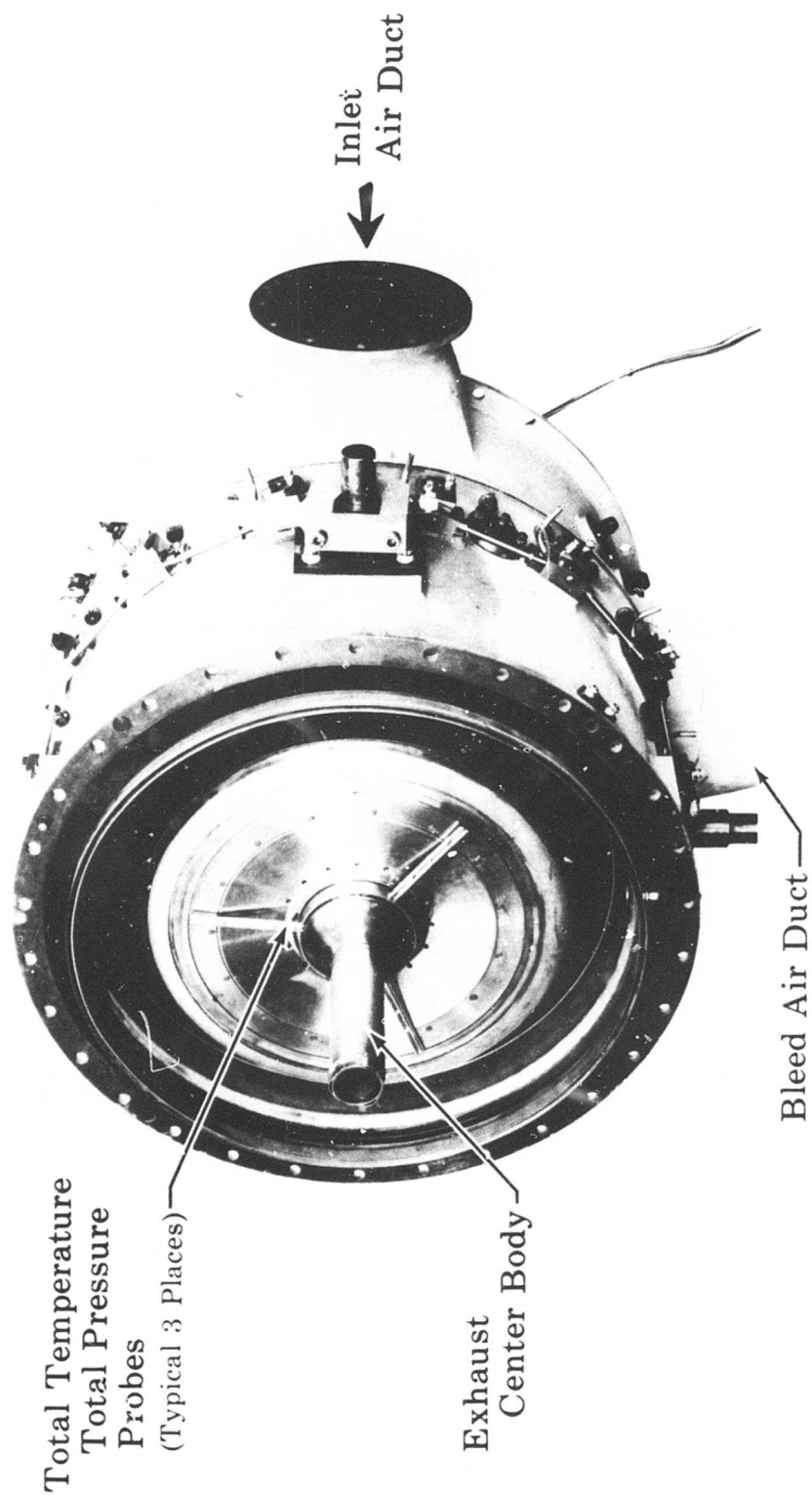
Figure 86. Internal View of Burner Showing Probe Assembly.

140
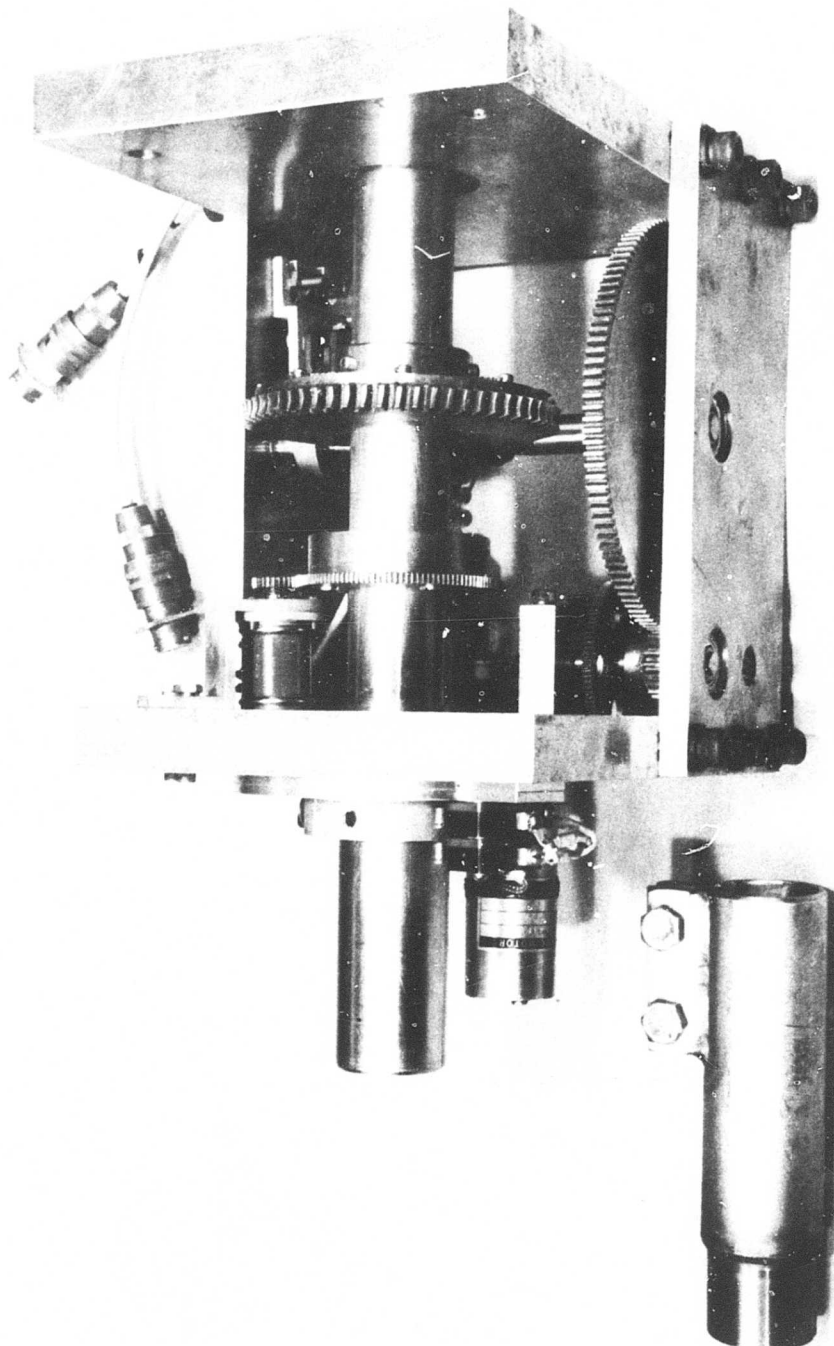
Figure 87. Indexing Gearbox.

141
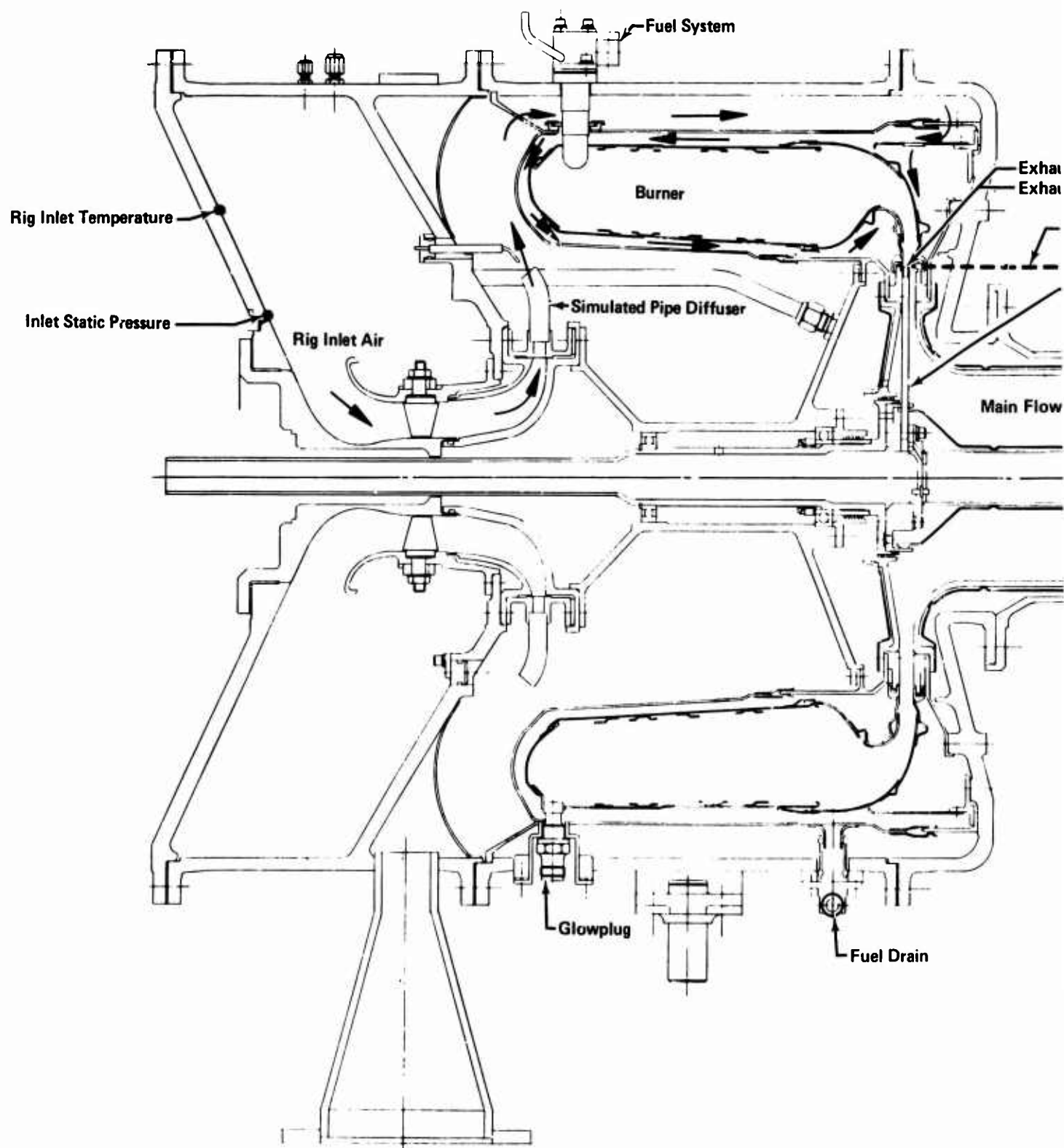
Figure 88. Burner Test Instrumentation.
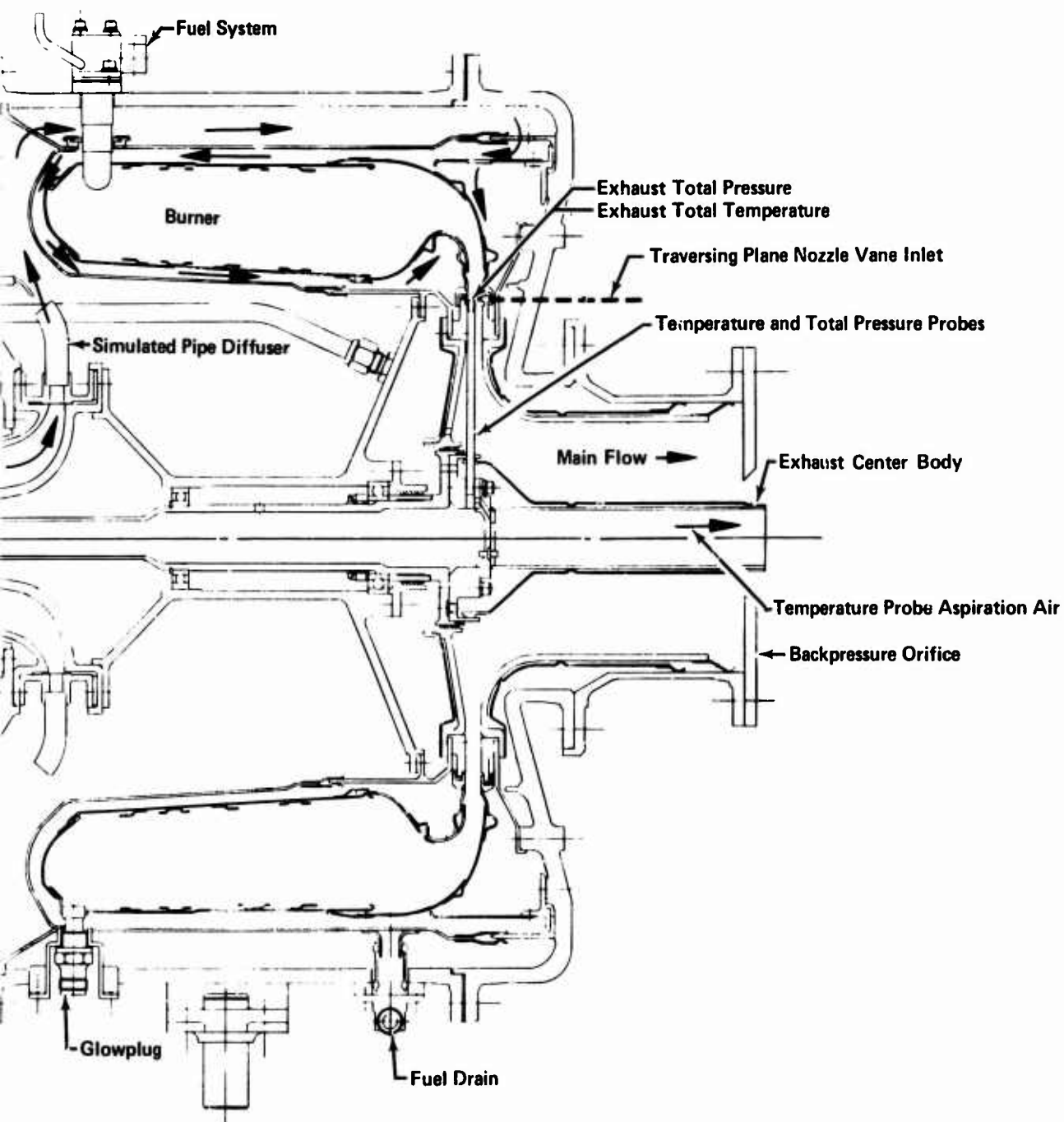
PRECEDING PAGE BLANK

Fuel System

Burner

Exhaust Total Pressure
Exhaust Total Temperature

Traversing Plane Nozzle Vane Inlet

Temperature and Total Pressure Probes

Simulated Pipe Diffuser

Main Flow →

Exhaust Center Body

Temperature Probe Aspiration Air

Backpressure Orifice

Glowplug

Fuel Drain

t Instrumentation.
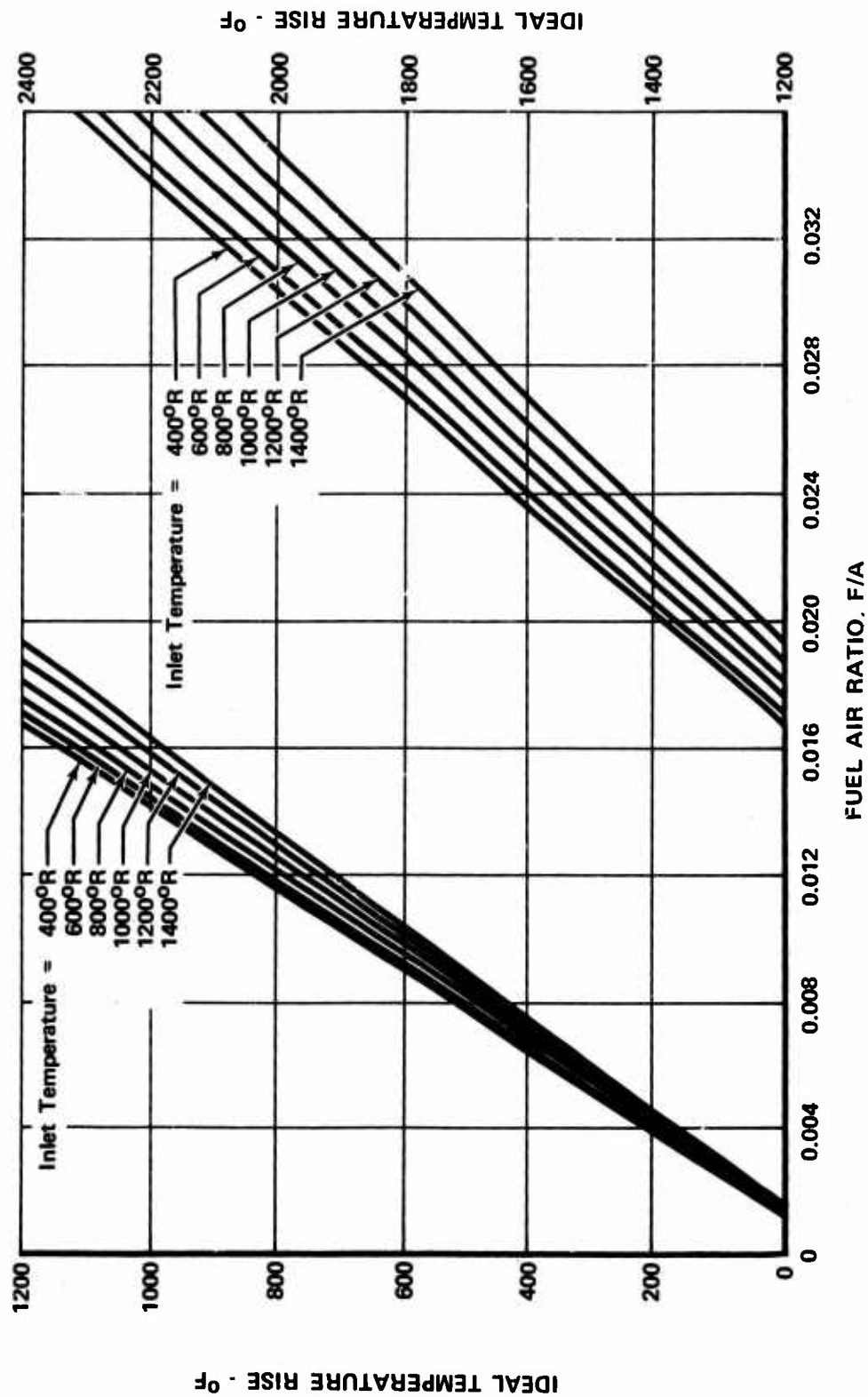
Figure 89. Ideal Temperature Rise for Constant Pressure Combustion of 100/130 Aviation Gasoline.

PRECEDING PAGE BLANK
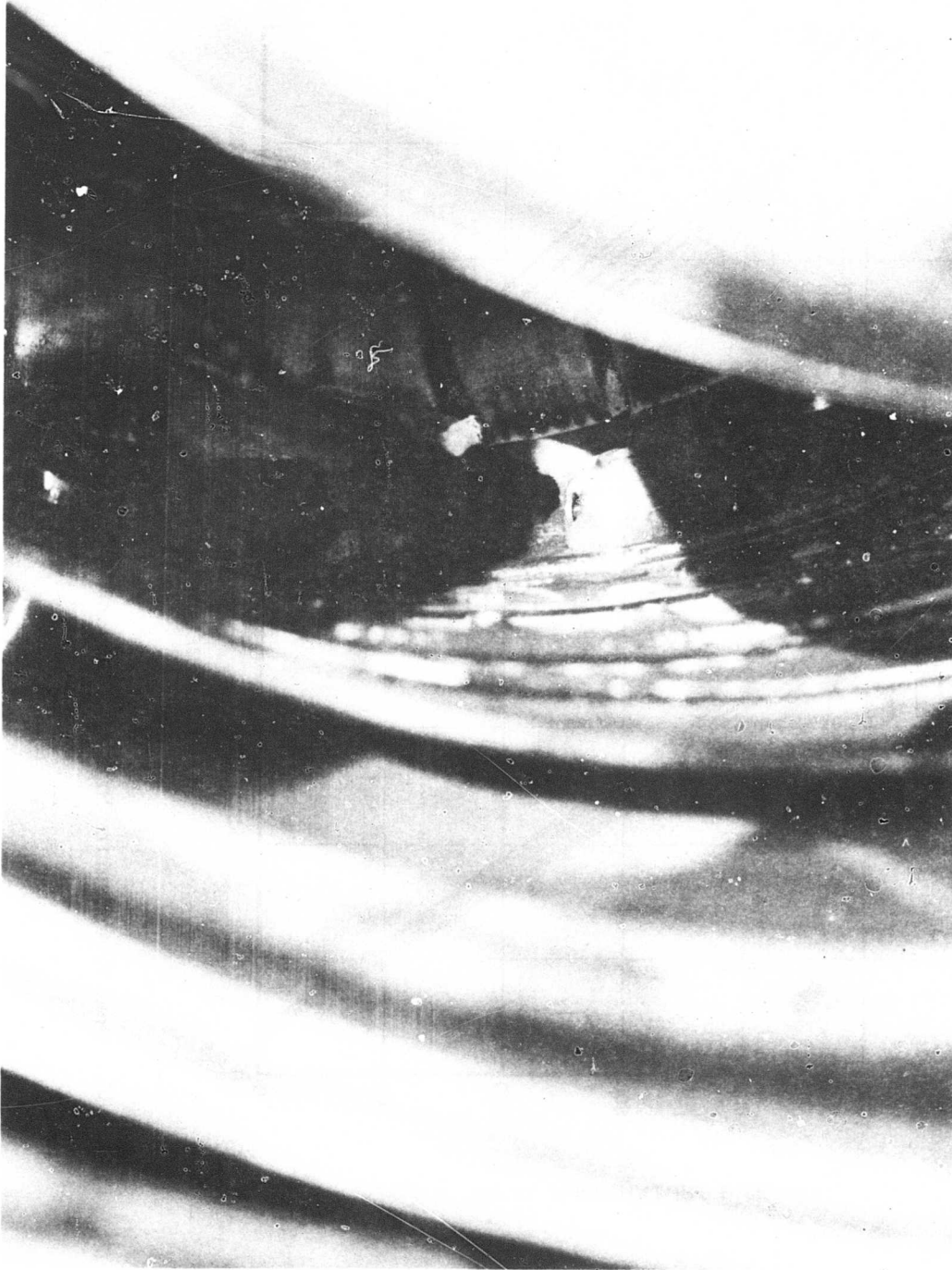
Figure 90. Carbon Deposits From JP5.

Figure 91. Carbon Deposits From JP7.

147
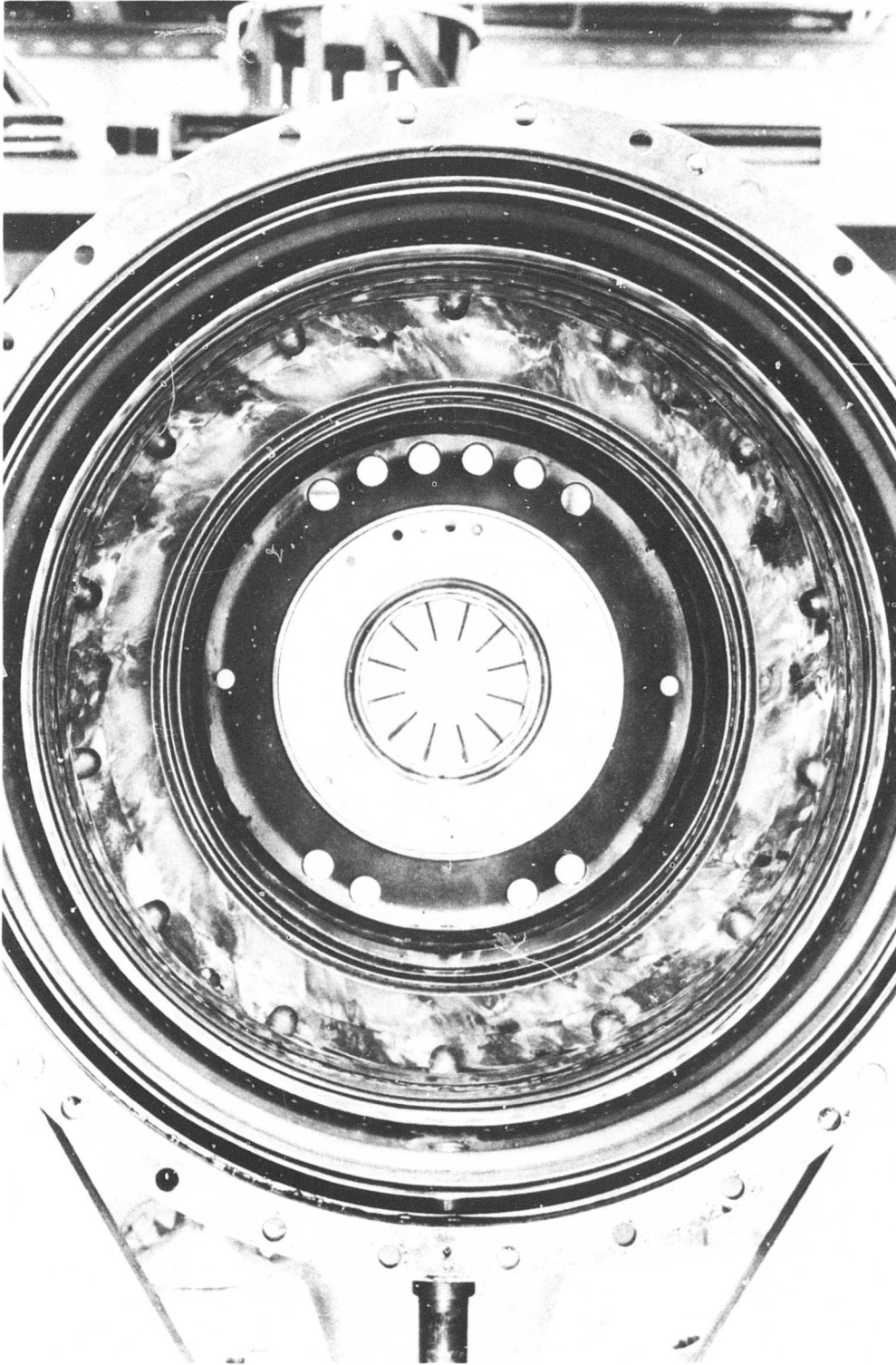
Figure 92. Burner After Testing With AVGAS.
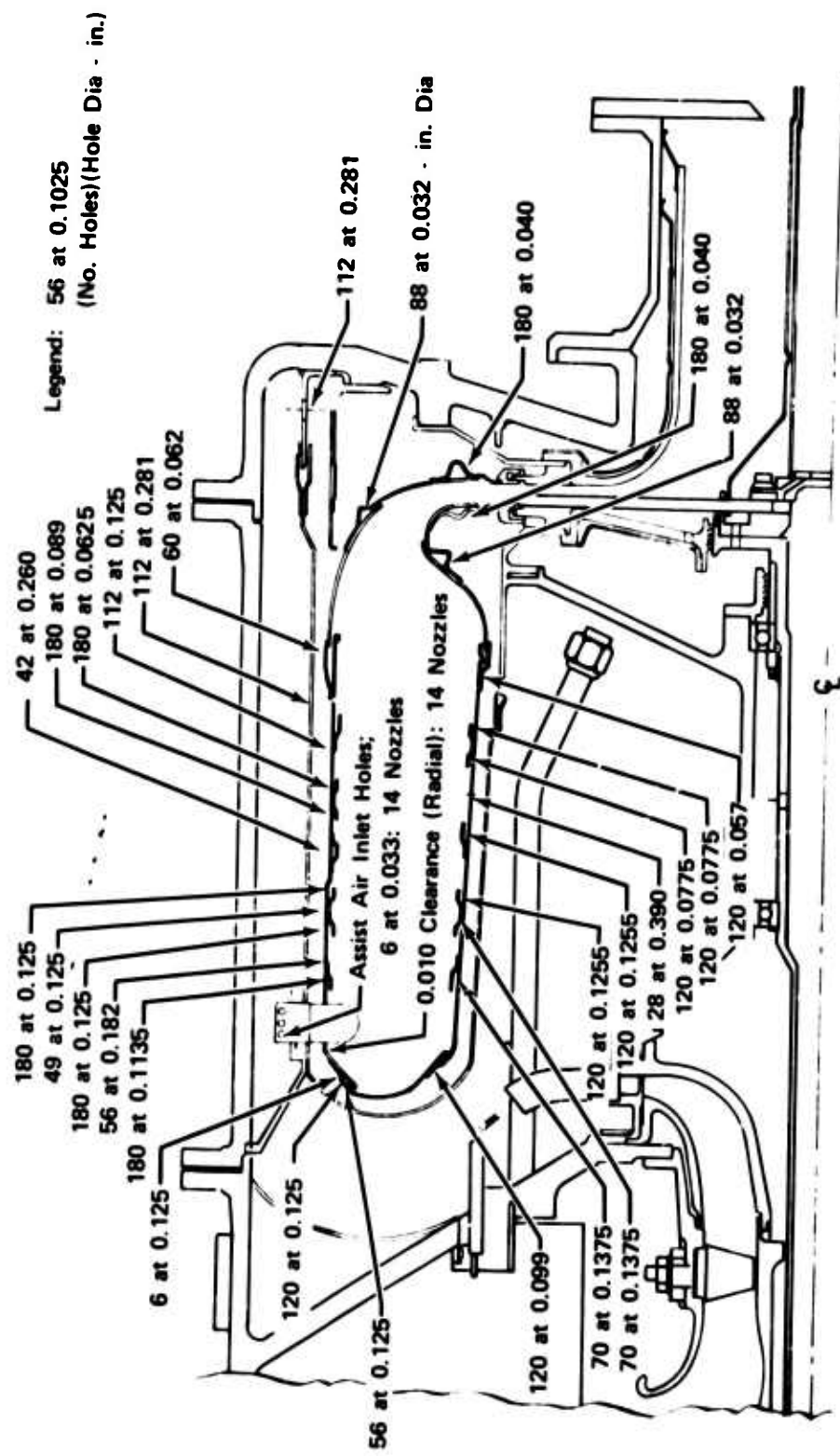
Figure 93. Final Burner Hole Pattern.

149
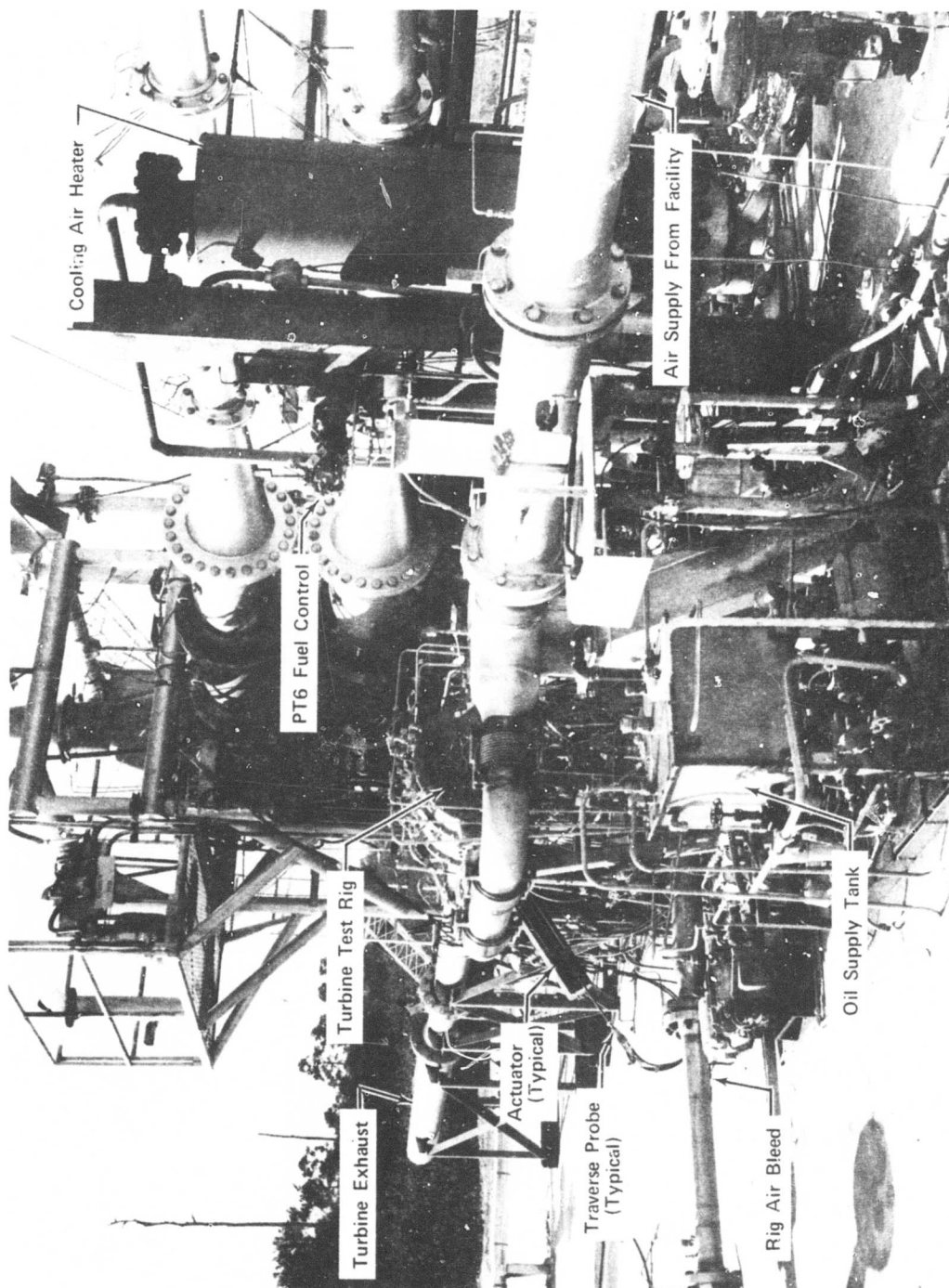
Figure 94. Turbine Test Rig (Front View).

150
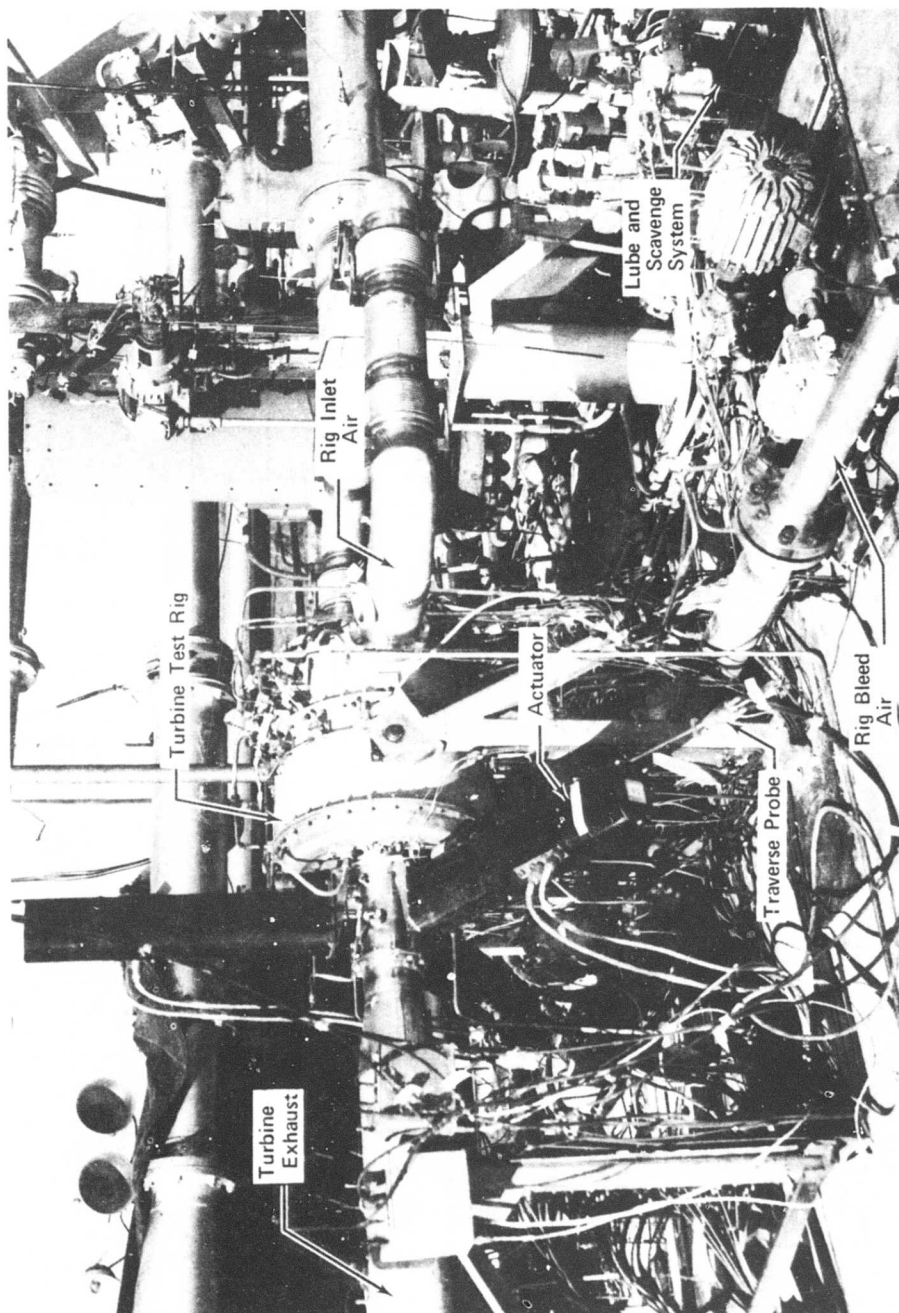
Figure 95. Turbine Test Rig (Rear View).

151
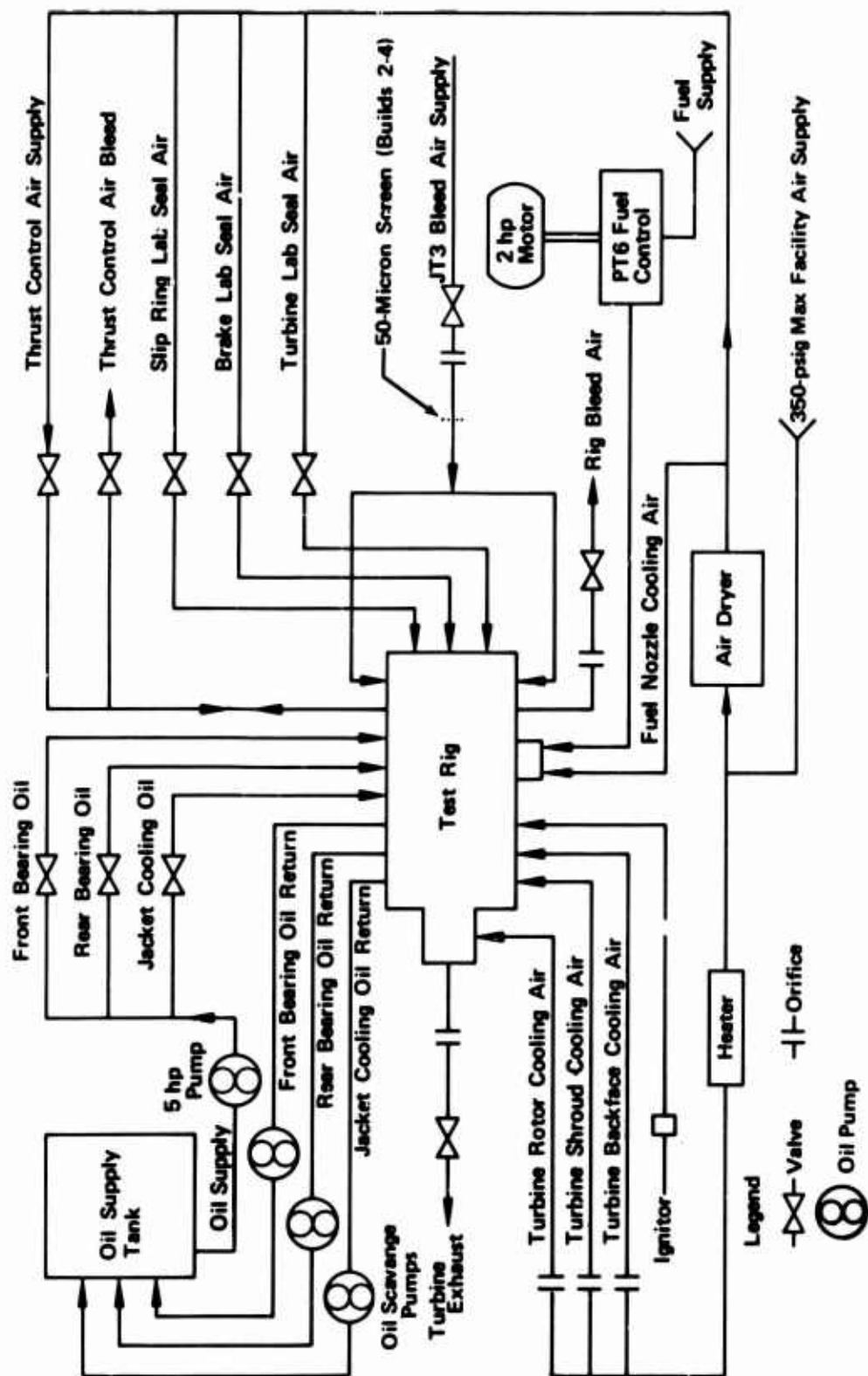
Figure 96. Turbine Test Facility Schematic.

152
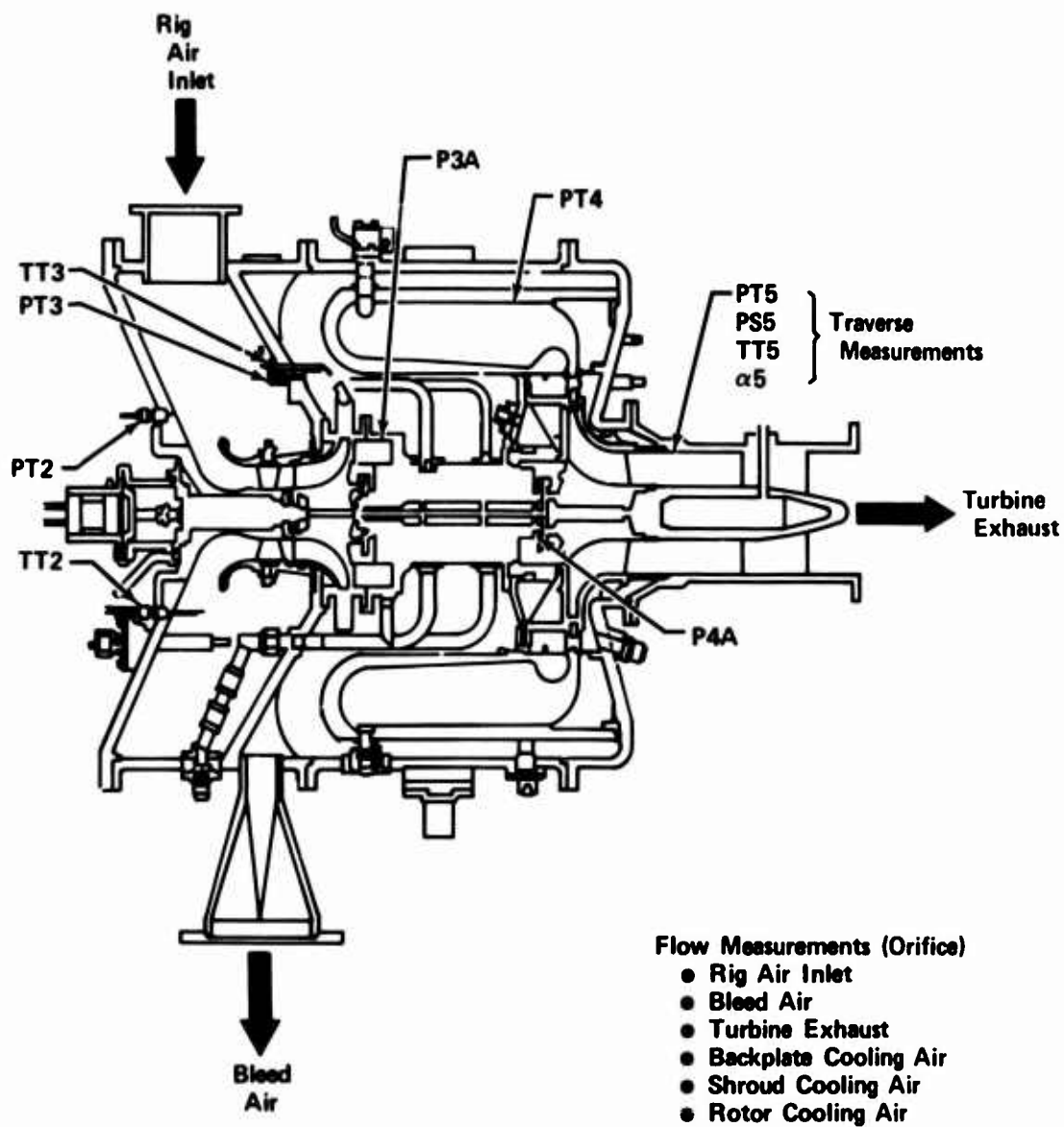
Figure 97. Basic Instrumentation Plan for Turbine Tests.

Figure 98.   Wedge Probe.

154

Fuel Flow (W_{fuel})

$(W_{burn} + W_{fuel})$

Burner Airflow (W_{burn})

Bleed Flow (W_{bl})

Brake Inlet Flow (W_c)

Shroud Cooling Flow (W_{sh})

Backplate Cooling Flow (W_{bp})

Rotor Inlet Flow (W_{tcr})

Turbine Exhaust Flow (W_t)

Rotor Cooling Flow (W_r)

Normal Calculation for Rotor Inlet Flow (W_{tcr}):
$W_{tcr} = W_t - W_r$

Alternate Calculation for Rotor Inlet Flow (W_{tcr})
$W_{tcr} = W_c - W_{bl} + W_{fuel} + W_{bp} + W_{sh}$
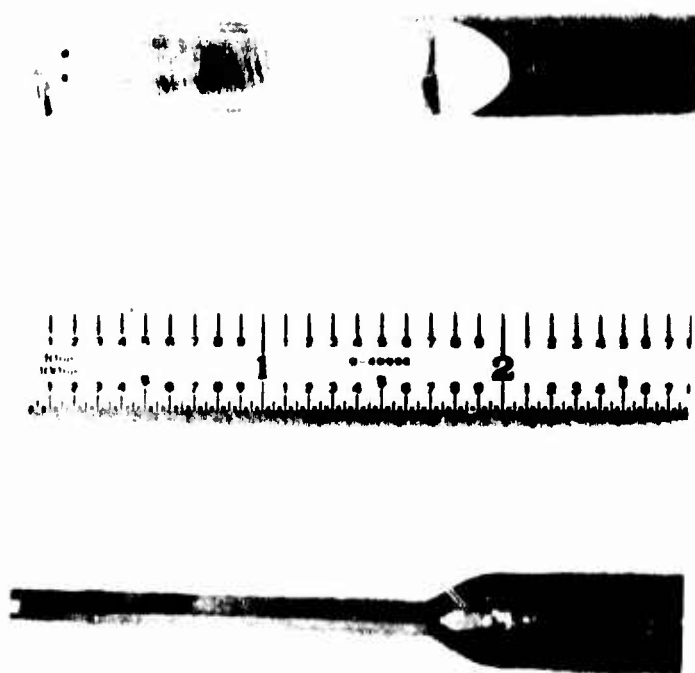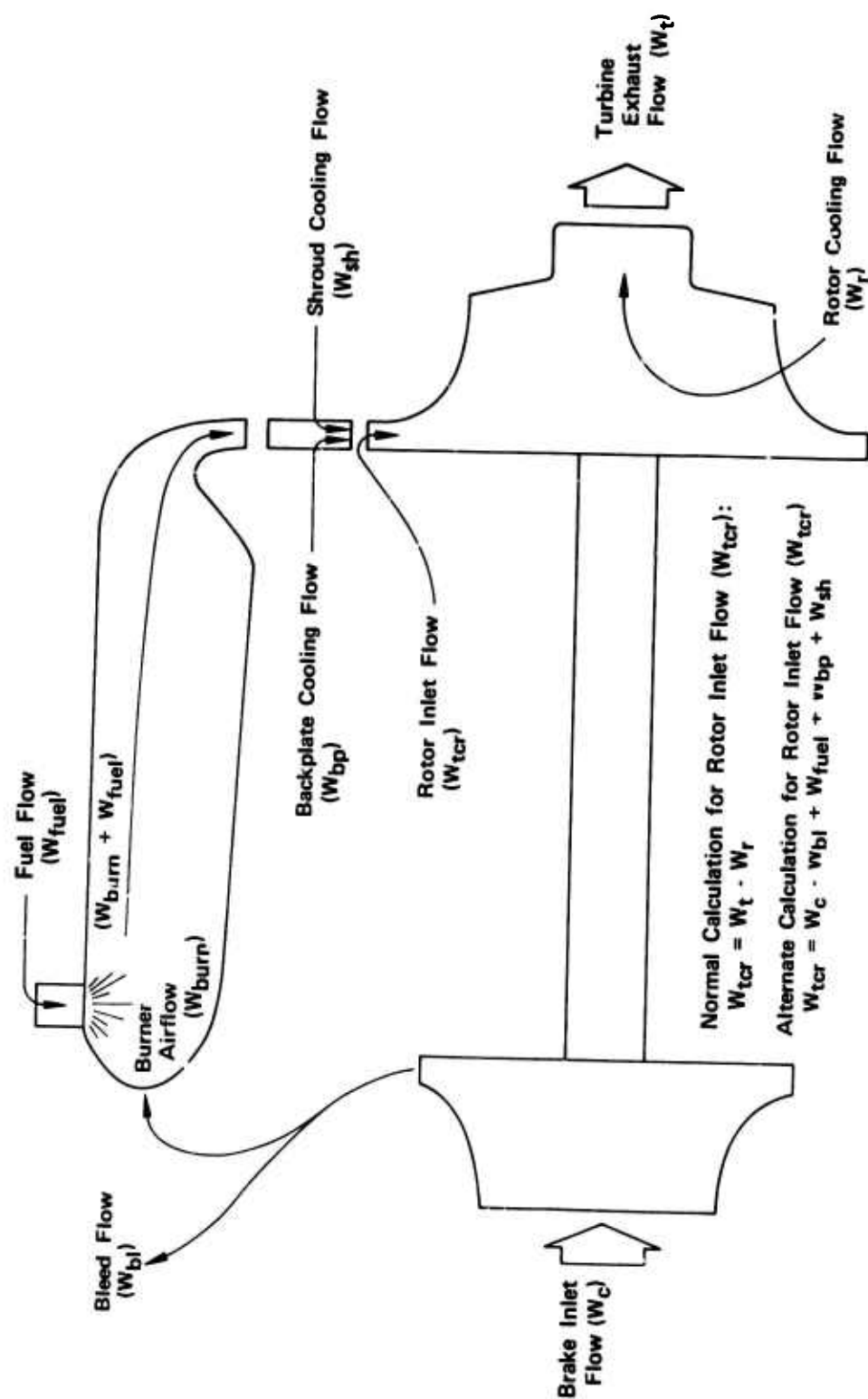
Figure 99. Rotor Inlet Flow Calculation.

155
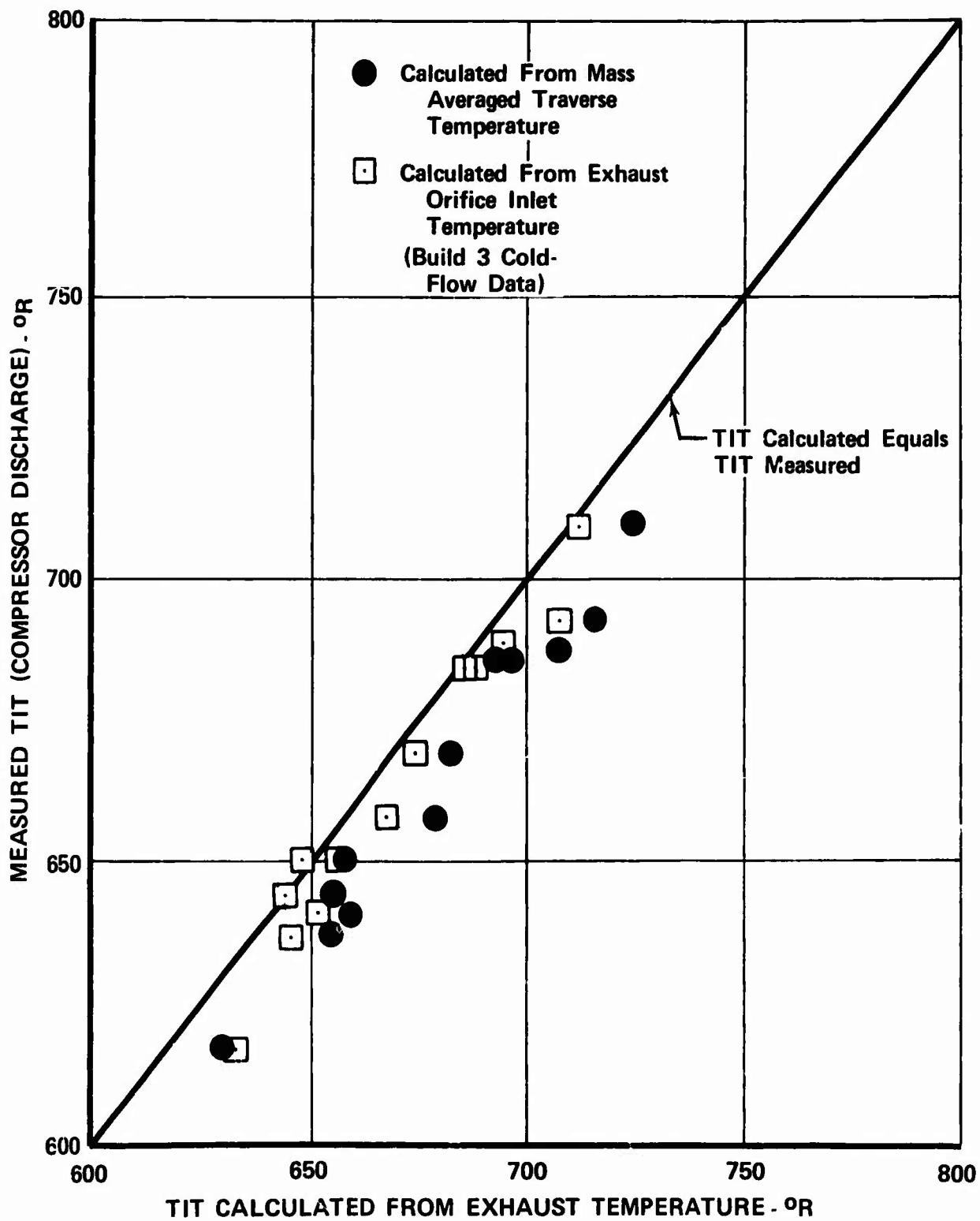
Figure 100. Comparison of Turbine Inlet Temperature Calculations.

156
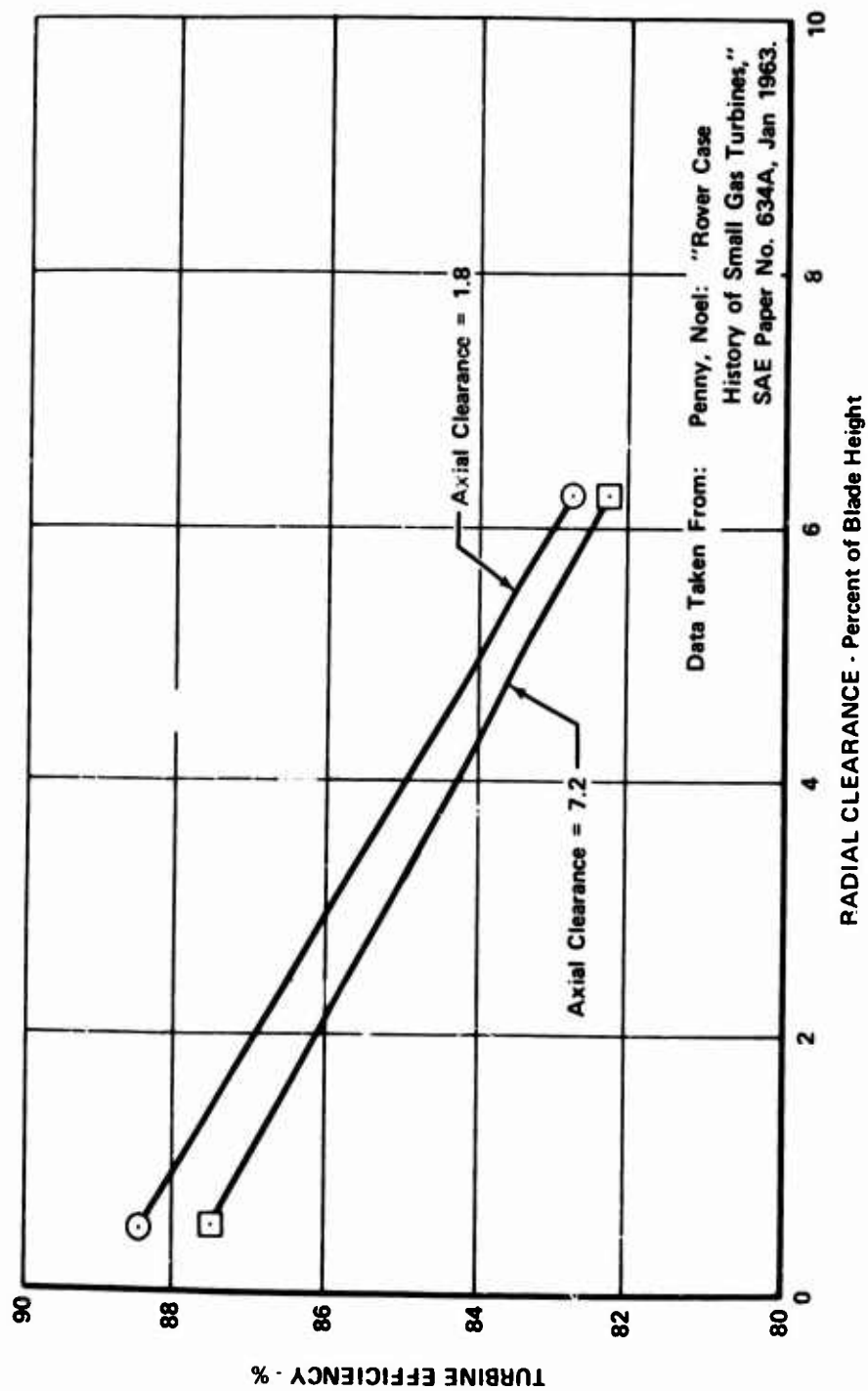
Figure 101. Effect of Rotor Clearances on Radial Turbine Efficiency.

Figure 102. Bearing Chip Detector After Turbine Build 1.
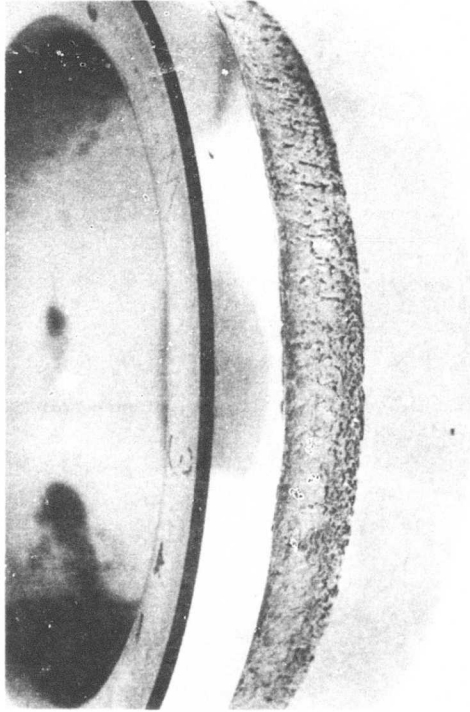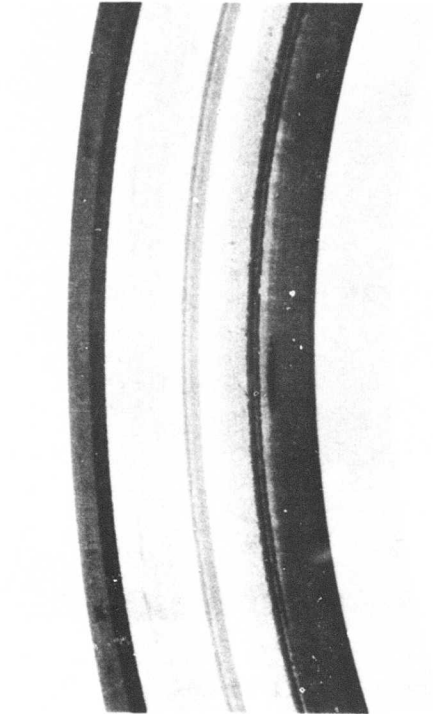
Outer Race

Inner Race

Figure 103.   Bearing Races After Turbine Build 1.
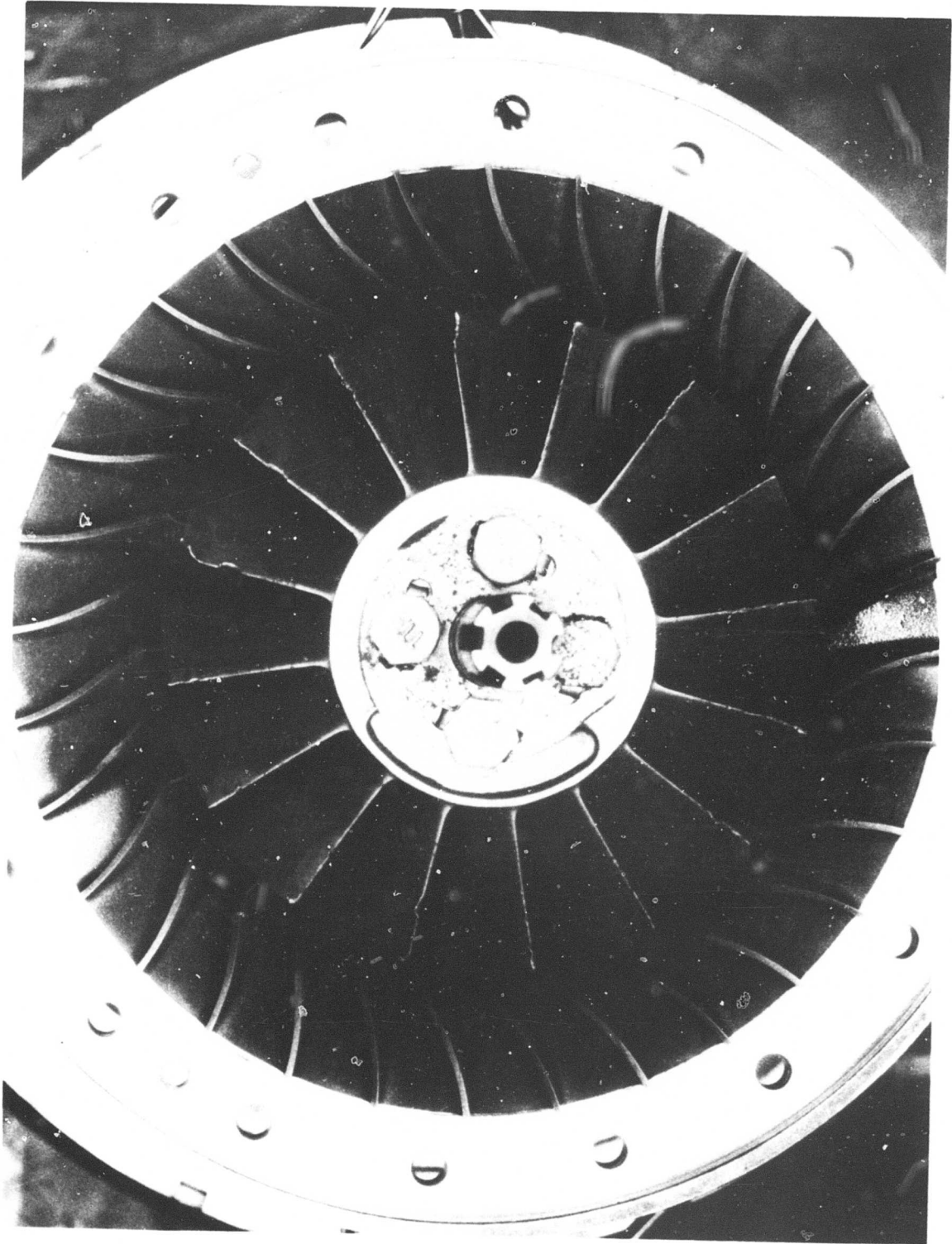
Figure 104. Turbine Build 1 Brake.
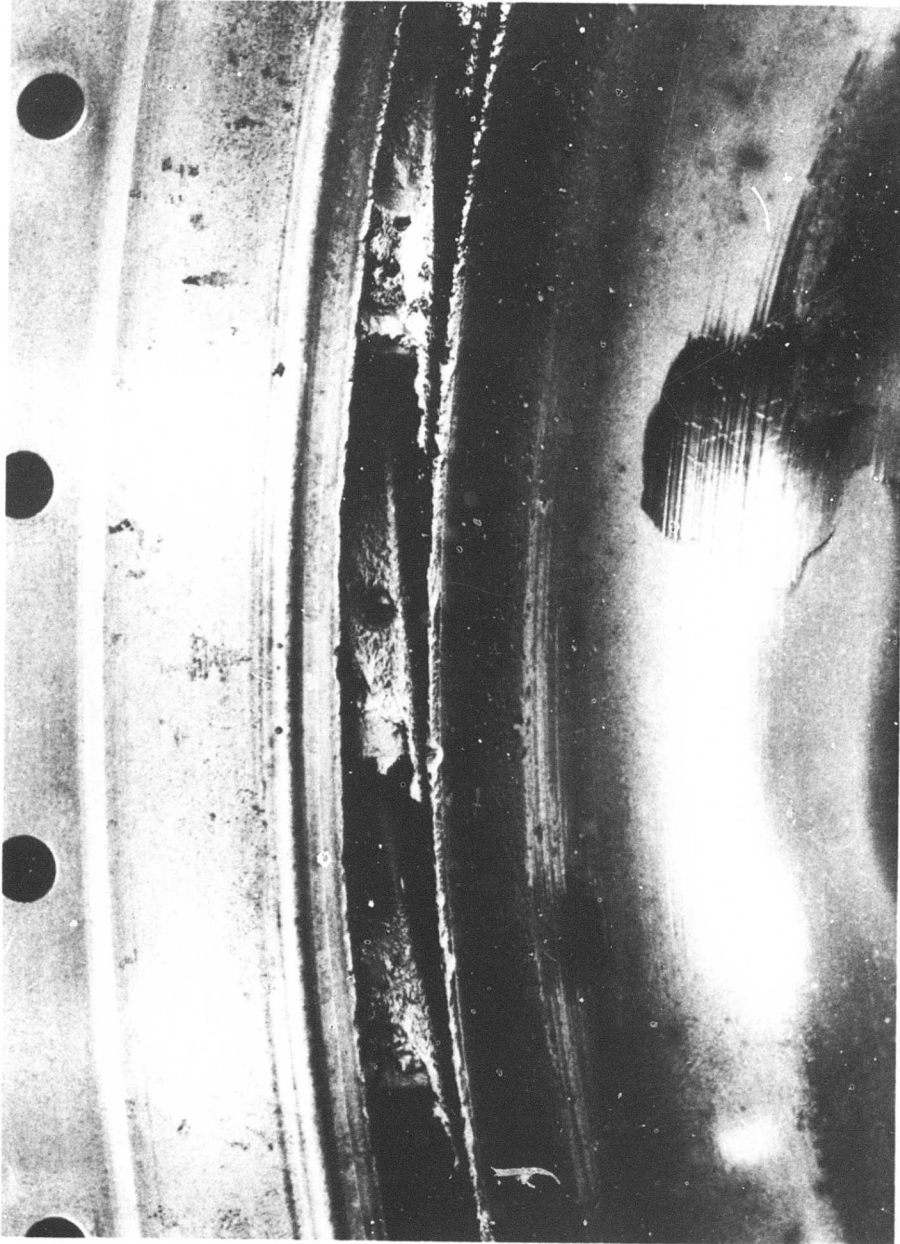
Figure 105. Turbine Build 1 Vane.

161
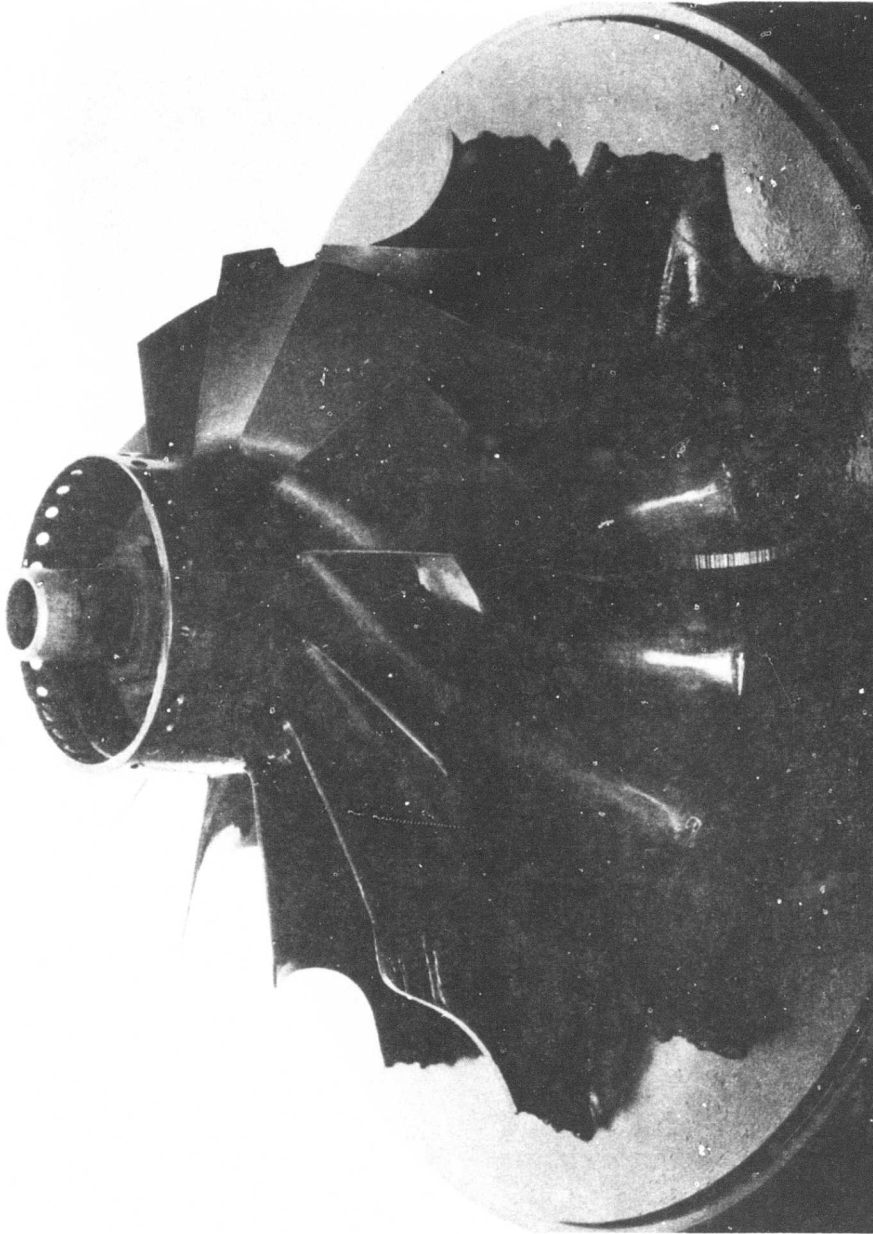
Figure 106. Turbine Build 1 Performance.
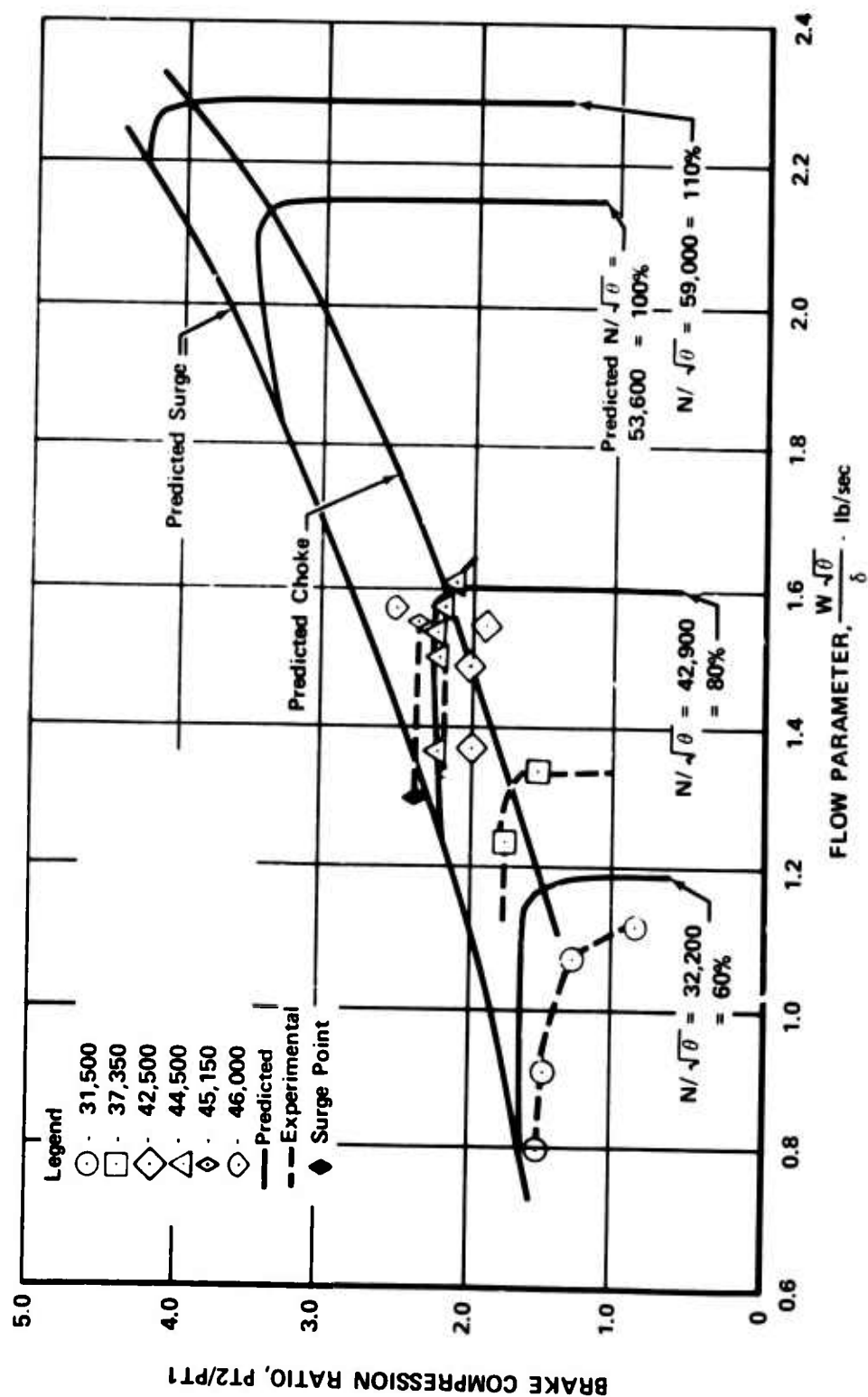
Figure 107. Brake Performance With 26-Pipe Diffuser and Zero Degree Prewhirl.

163
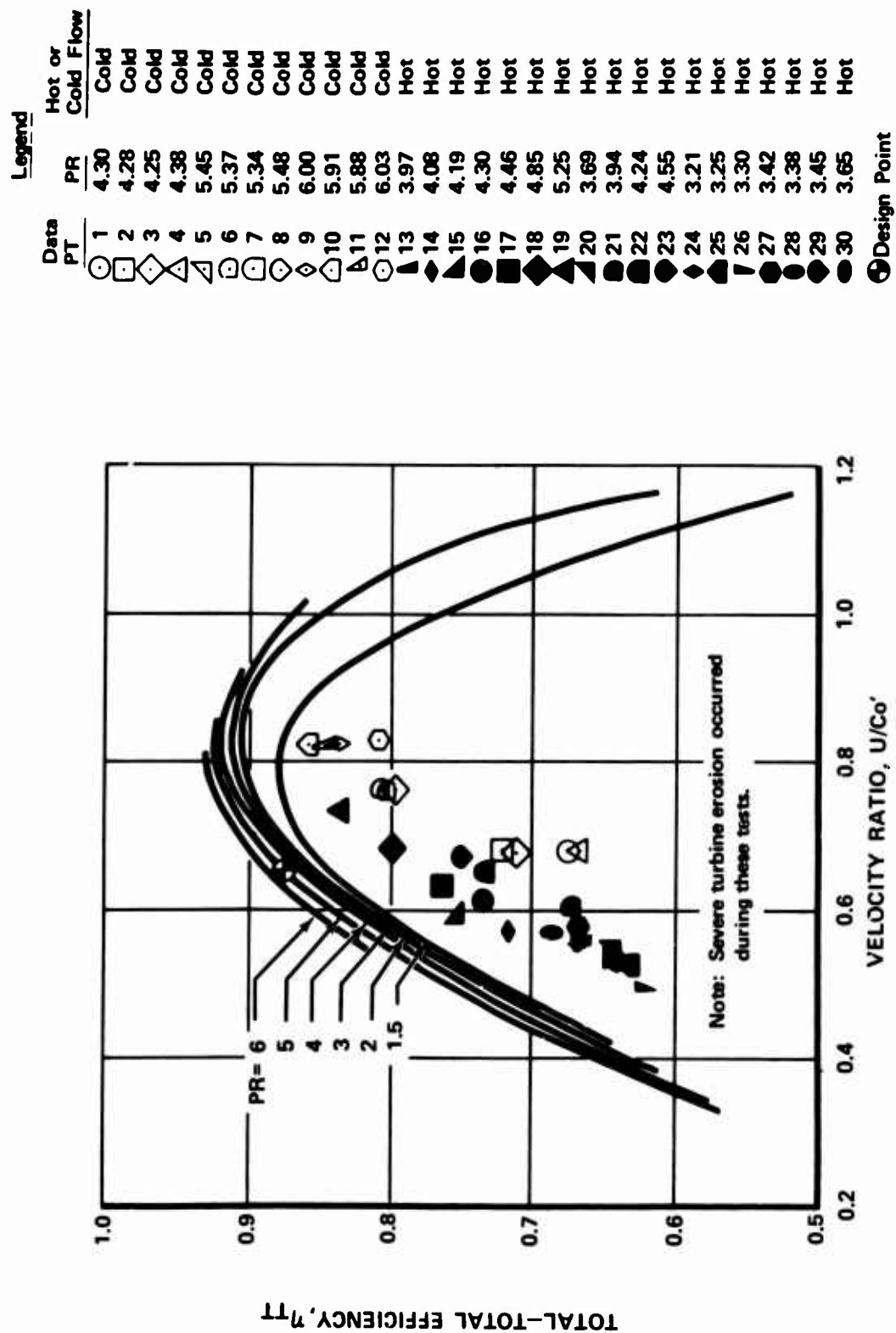
Figure 108. Turbine Build 1 Performance.

164
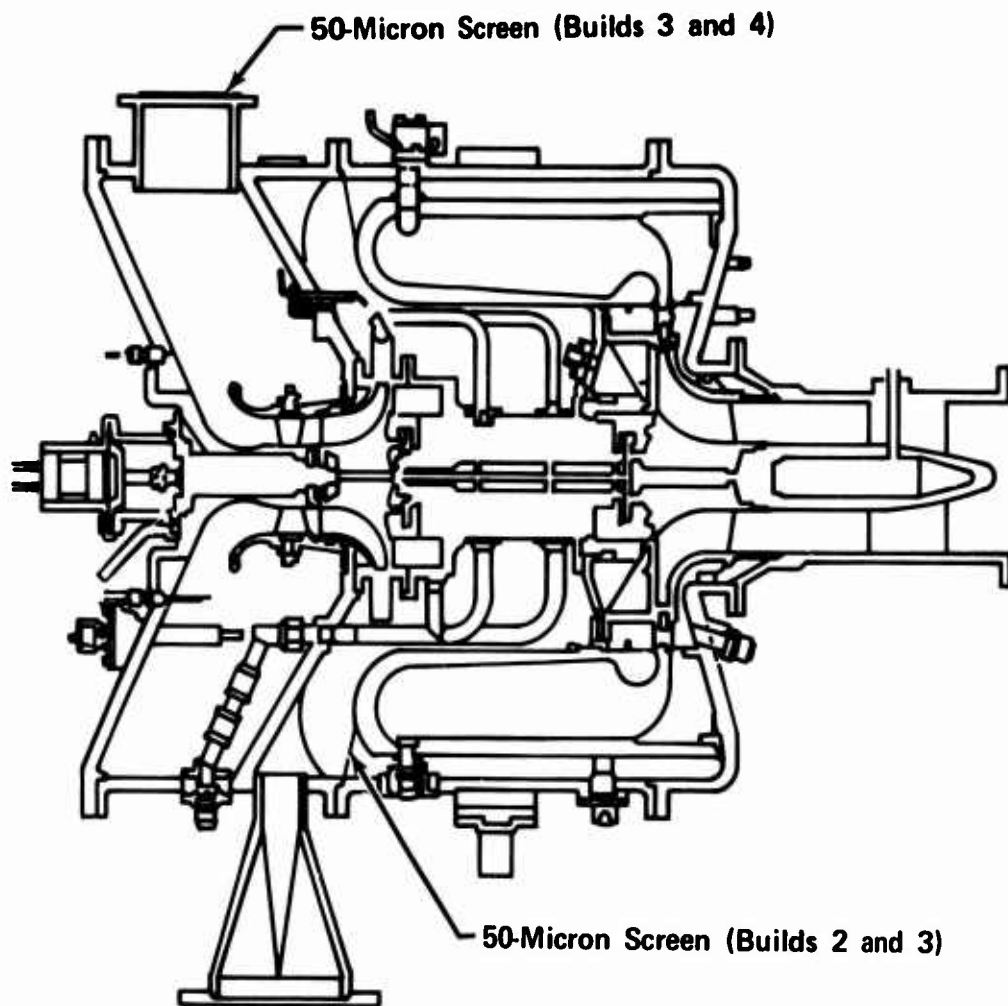
Figure 109. Location of Screening in Rig.
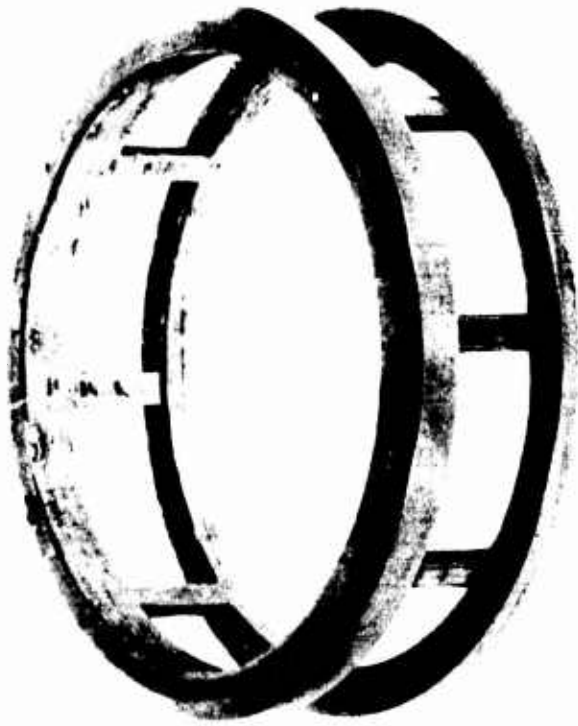
Original Design

Redesign

Figure 110. Original and Redesigned Load Rings.

Original Bellows Section
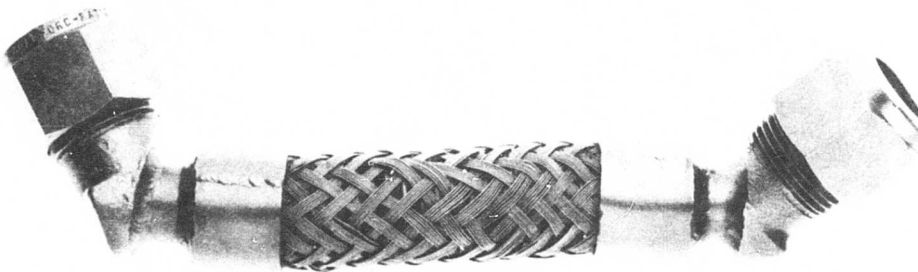
Replacement Bellows Section

Figure 111.   Original and Replacement Bellows Sections.
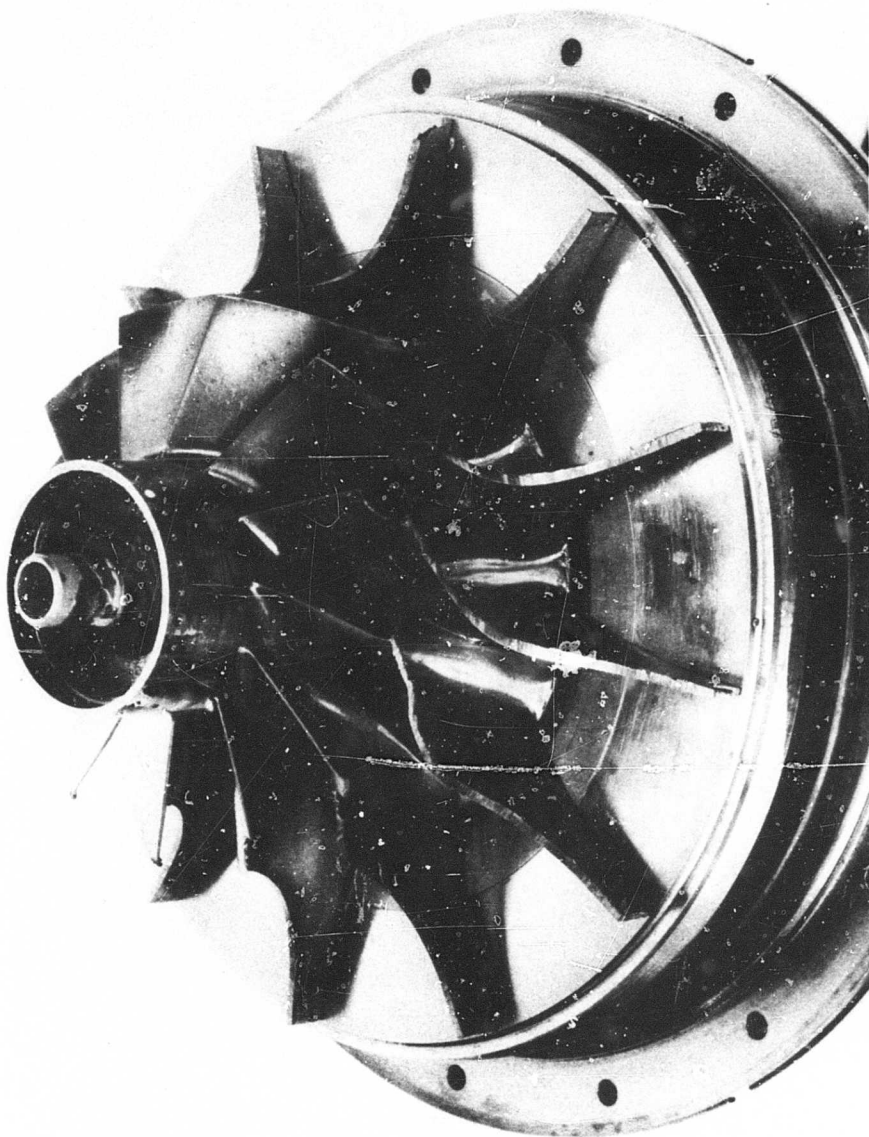
Figure 112. Turbine Build 2 Rotor.
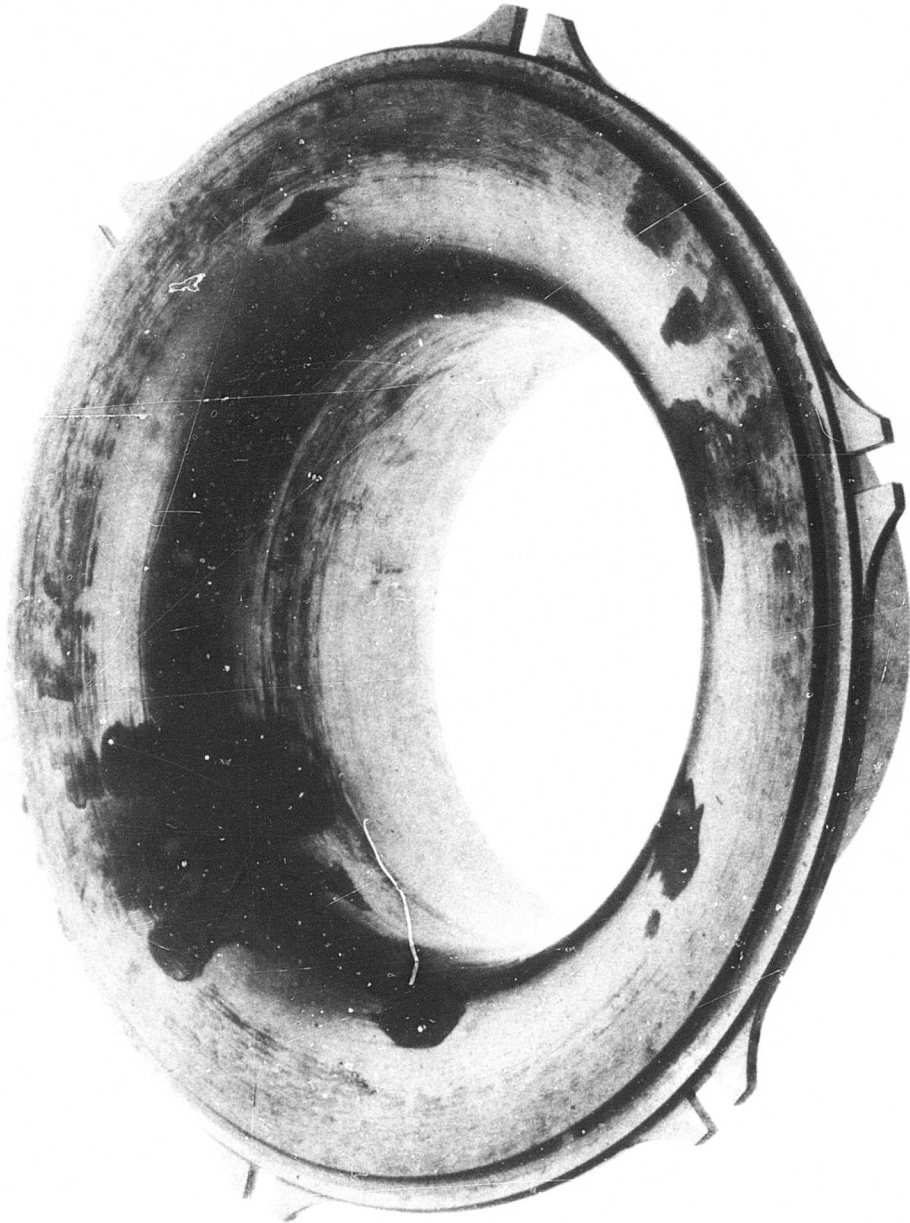
Figure 113. Turbine Build 2 Shroud.

Figure 114. Turbine Build 2 Vane.

170

0.015-in. Clearance (Axial)

0.022 - 0.024 in. Removed From This Face

0.033-in. Clearance (Radial)

1.326 in.

0.357 in.

0.015-in. Clearance (Axial)

Turbine Build 3
Clearances, Percent of Blade Height
Axial = 4.2
Radial = 2.5

0.010-in. Clearance (Axial)

Shroud

0.010-in. Clearance (Radial)

1.350 in.

0.379 in.

Rotor

0.010-in. Clearance (Axial)

Backplate

As Designed
Clearances, Percent of Blade Height
Axial = 2.6
Radial = 0.74

Figure 115.   Turbine Build 3 Rotor Clearances.

171

Meridional View of Turbine

Thermocouples
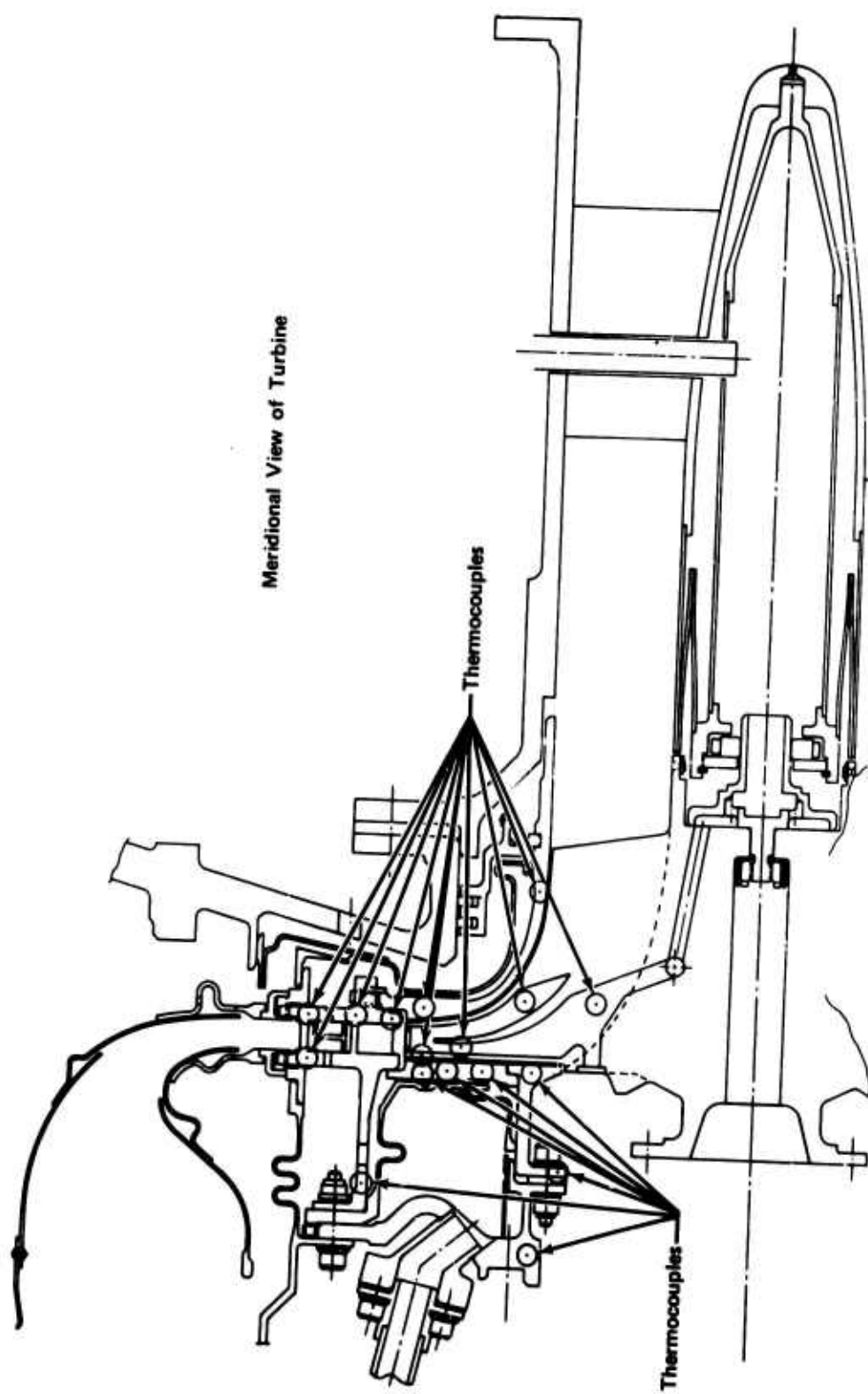
Thermocouples

Figure 116. Turbine Build 3 Thermocouple Locations.
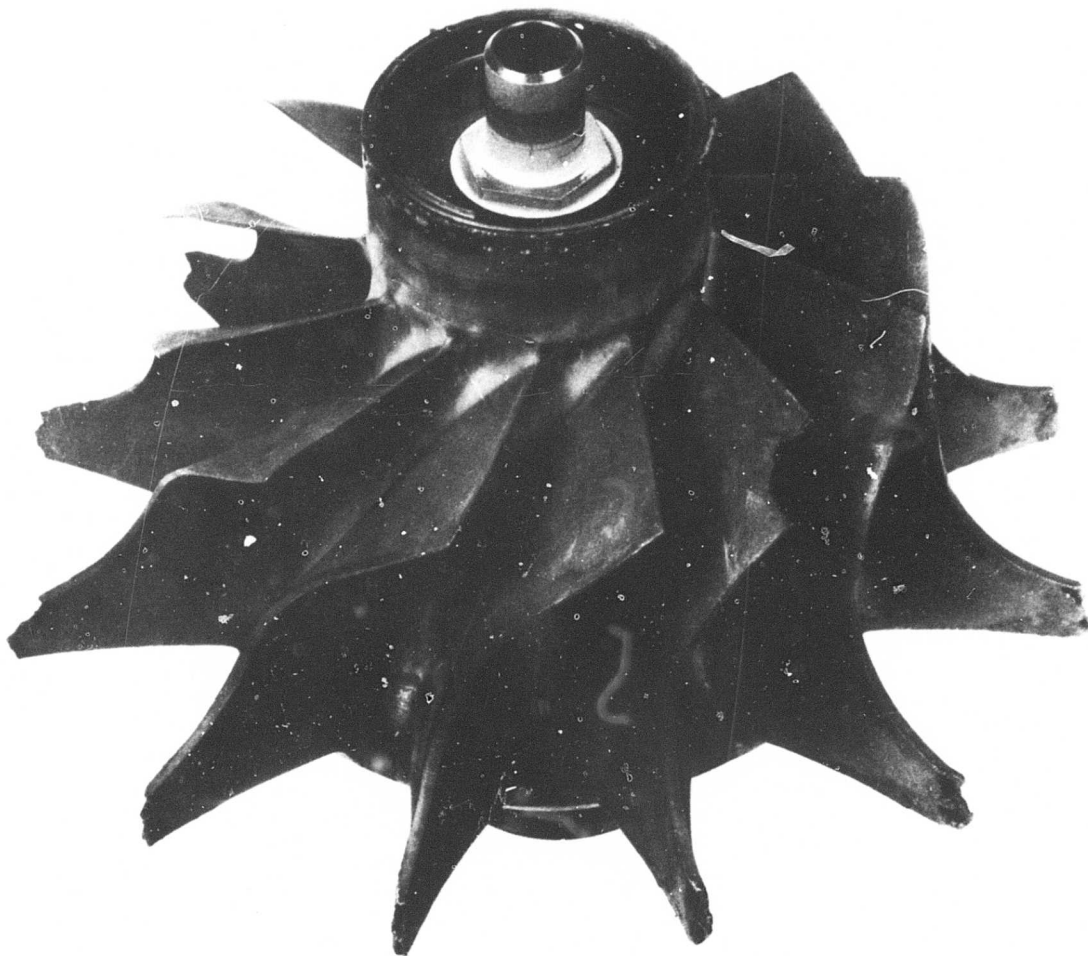
Figure 117.   Turbine Build 3 Rotor.
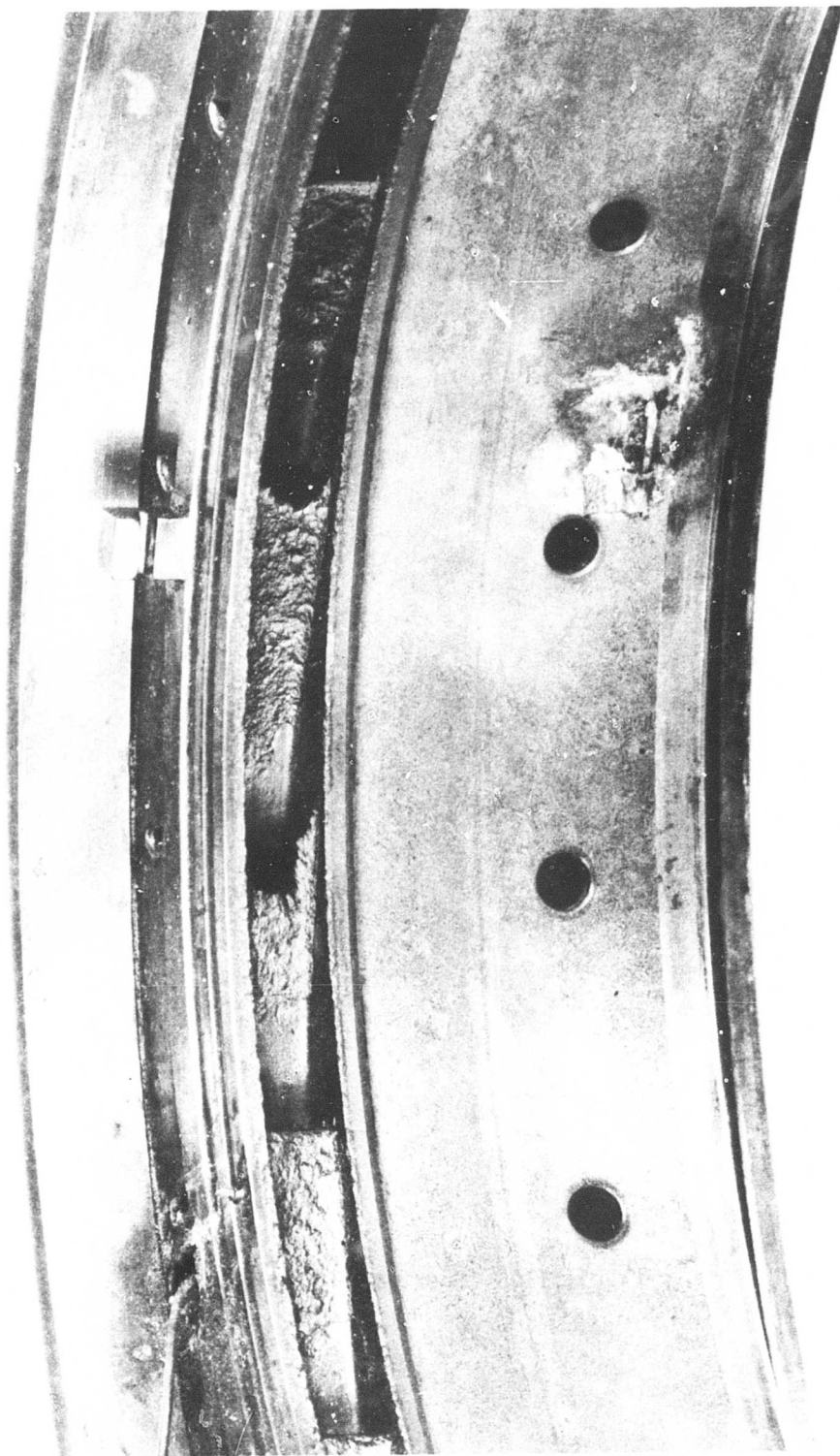
Figure 118. Turbine Build 3 Nozzle Vane Trailing Edge Damage.

174
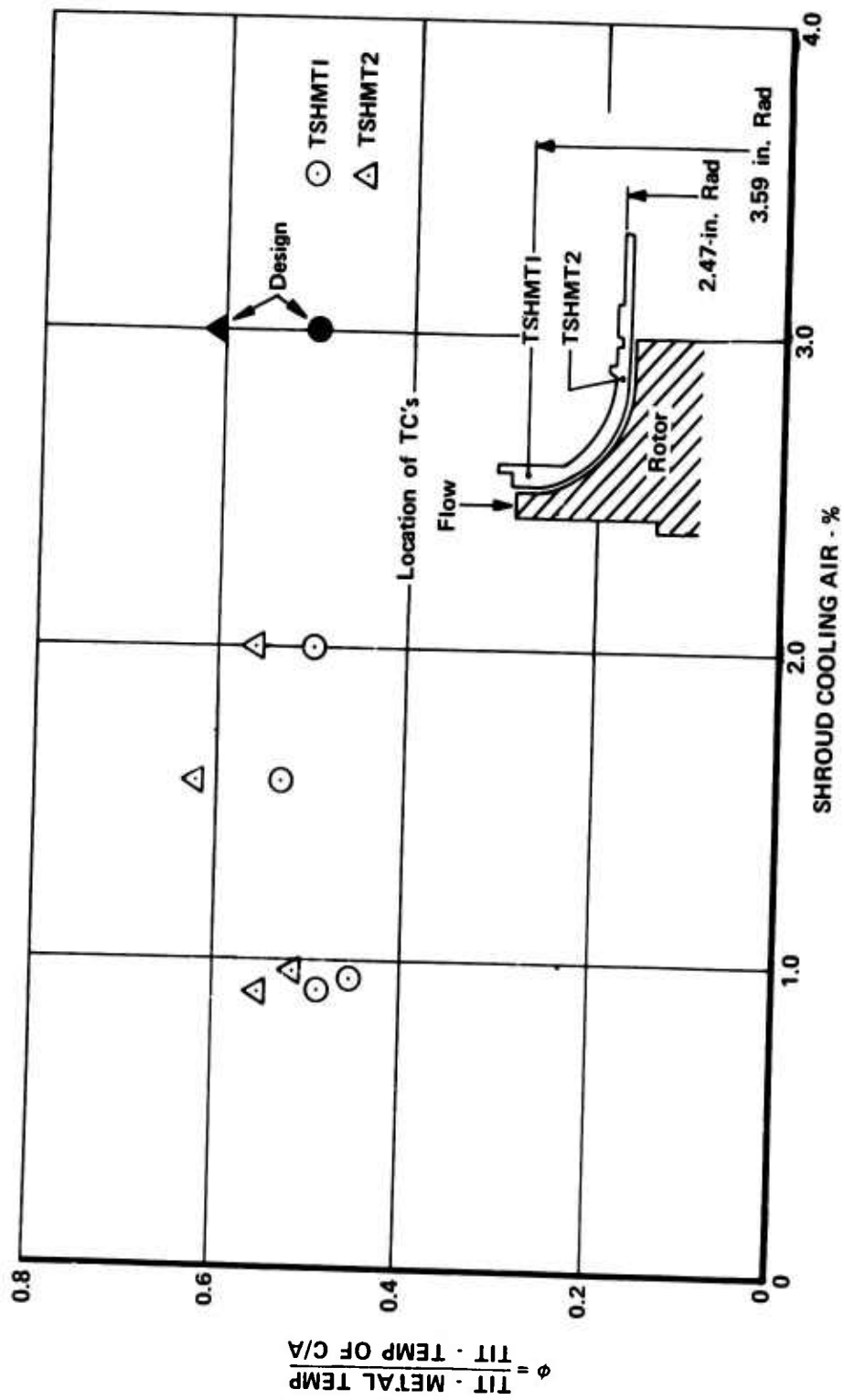
Figure 119. Turbine Build 3 Cooling Effectiveness (Shroud).

175
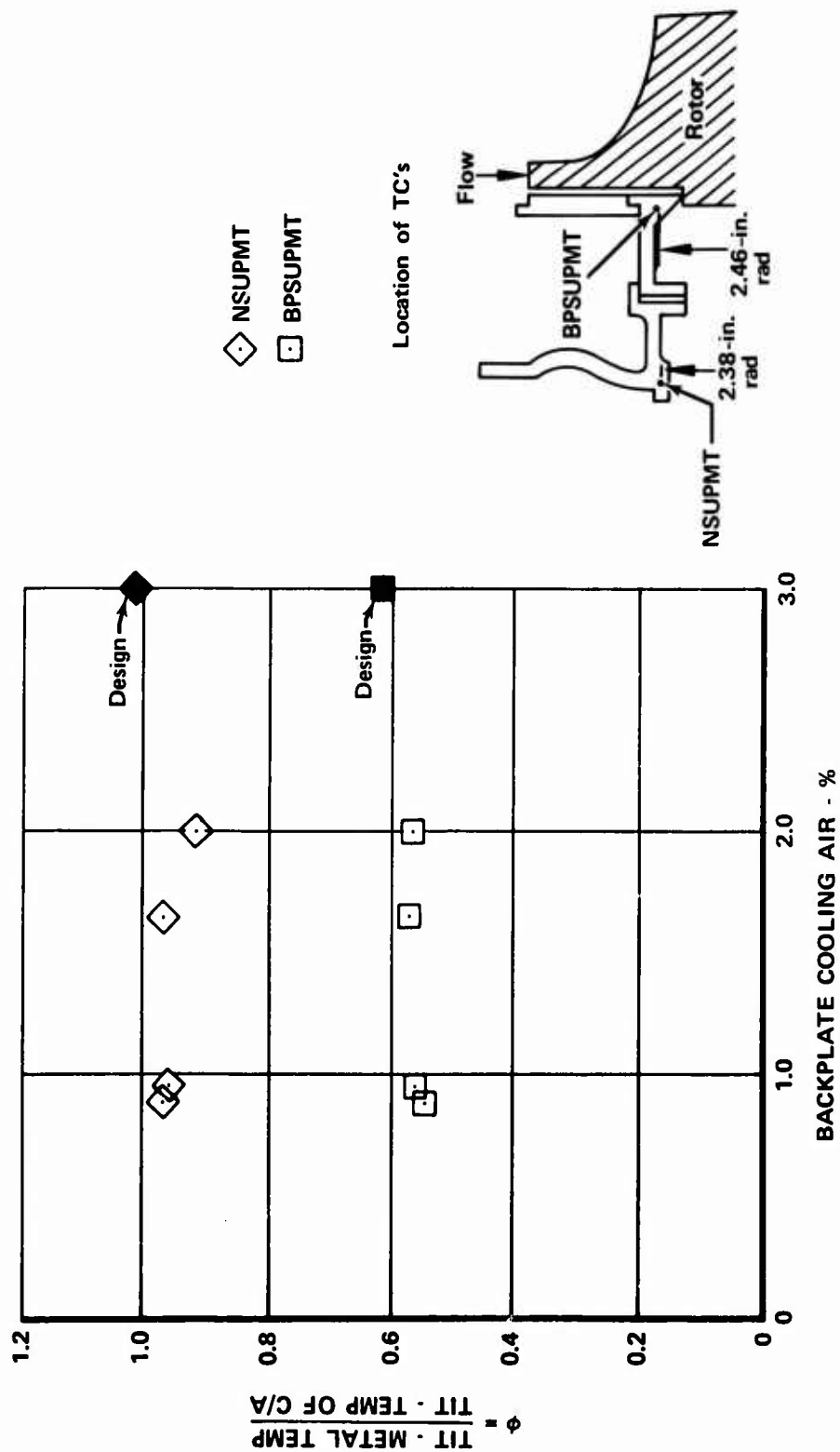
Figure 120. Turbine Build 3 Cooling Effectiveness (Backplate).
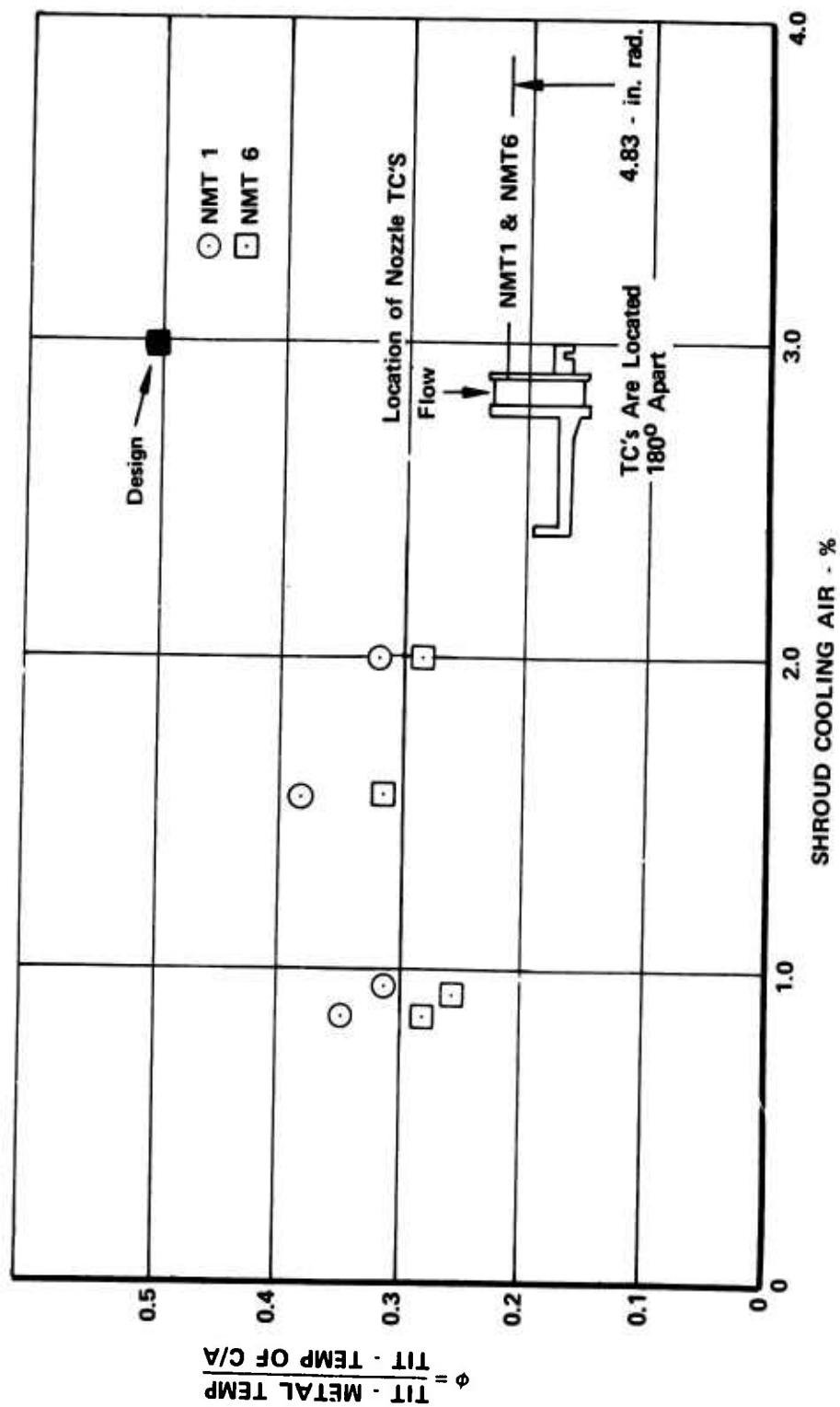
Figure 121. Turbine Build 3 Cooling Effectiveness (Beneath Heat Shield).

177
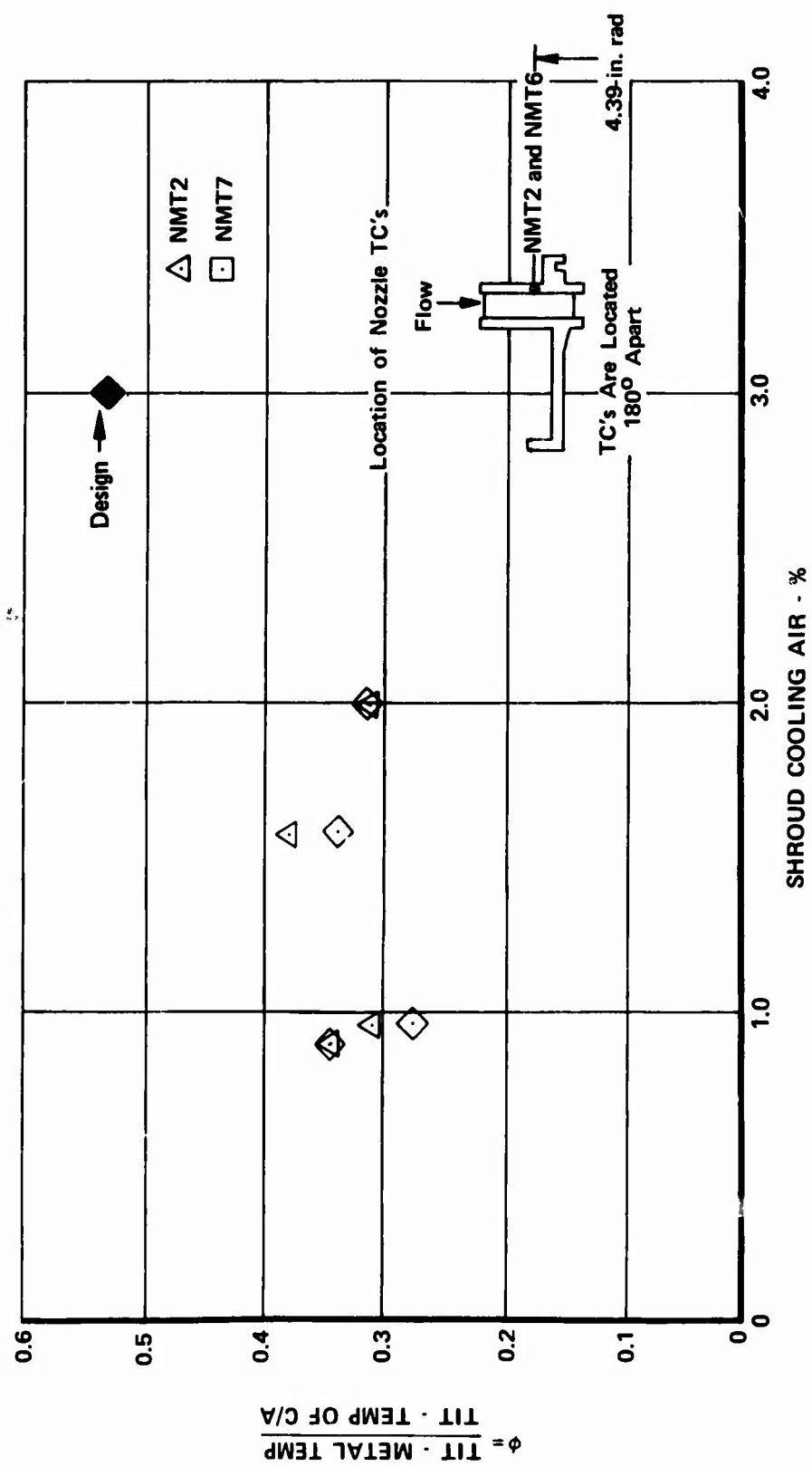
Figure 122. Turbine Build 3 Cooling Effectiveness (Platform).

178
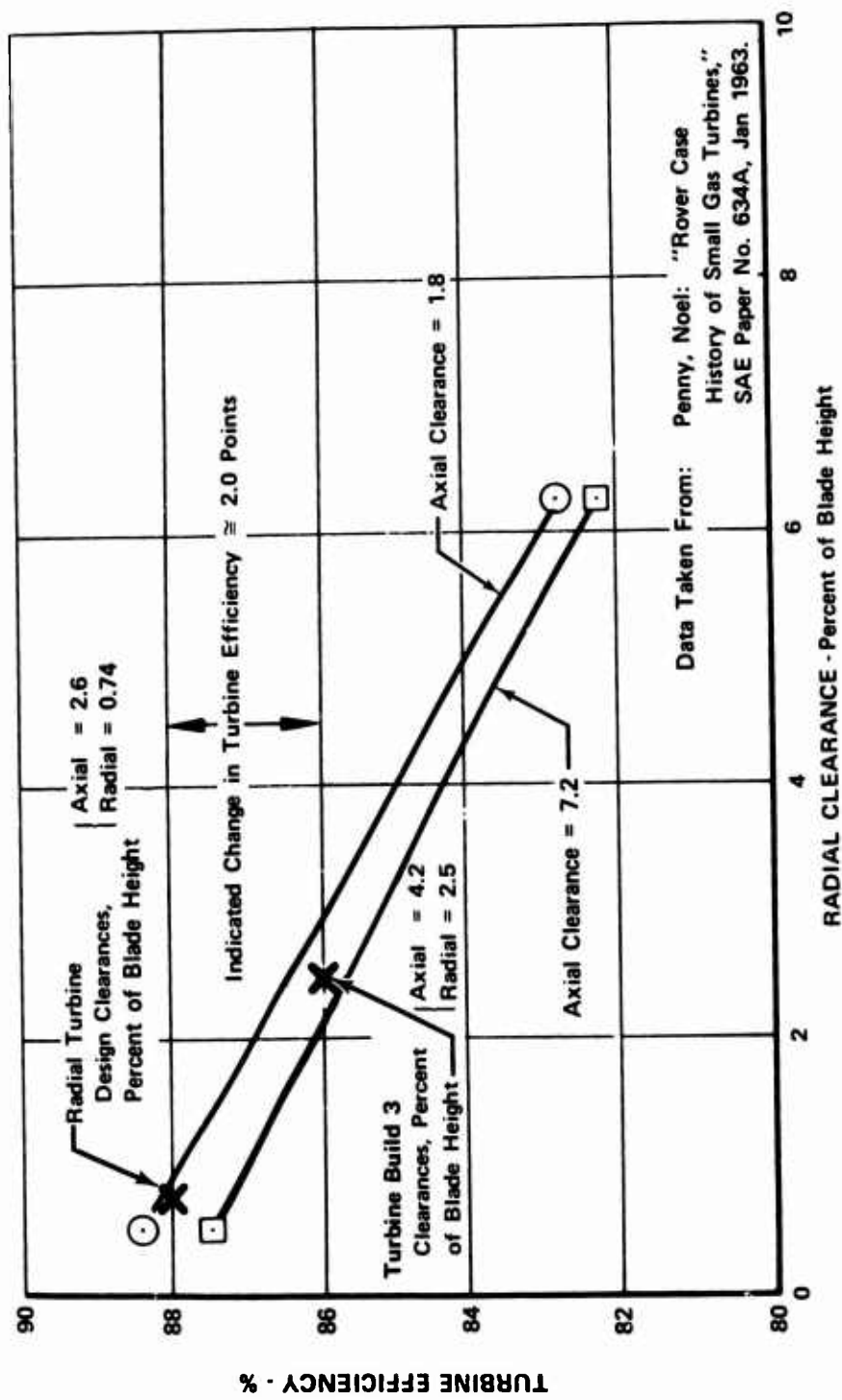
Figure 123. Determination of Clearance Correction for Turbine Build 3.

179
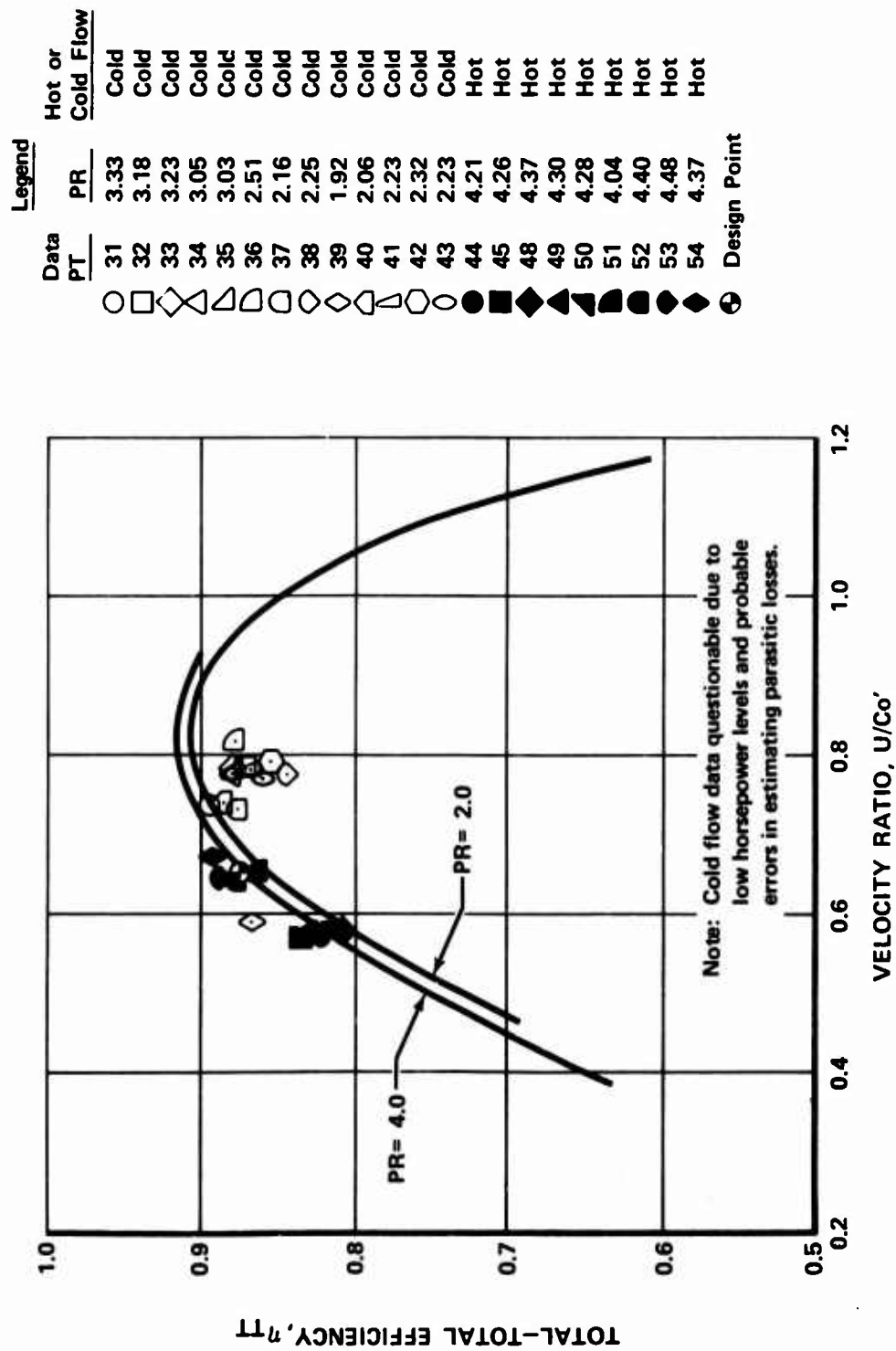
Figure 124. Turbine Build 3 Performance.
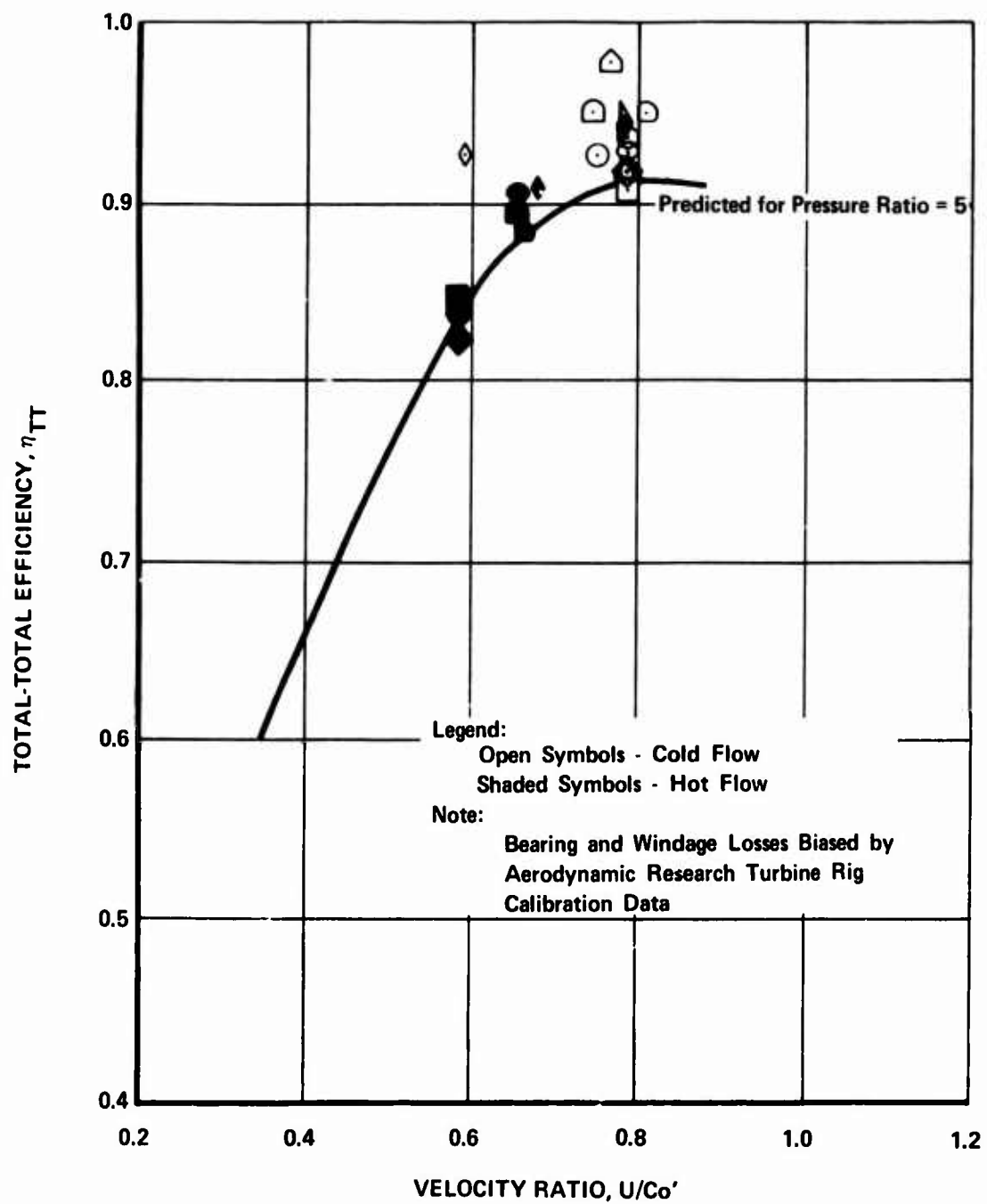
Figure 125. Turbine Build 3 Adjusted Performance.
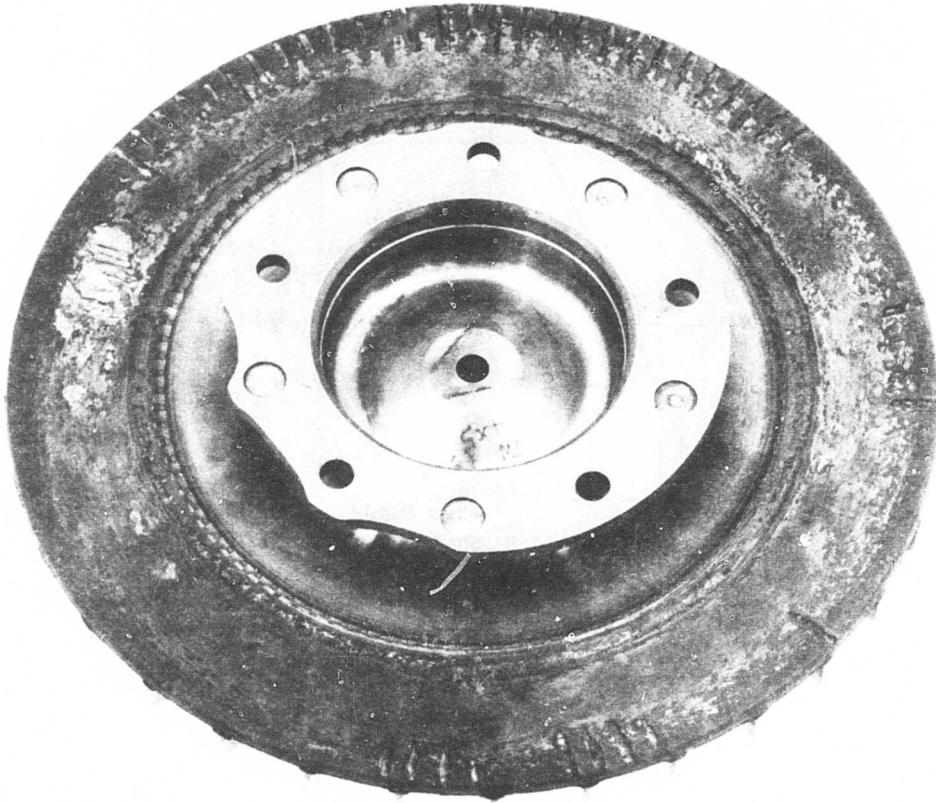
Figure 126.   Turbine Build 4 Brake Impeller.
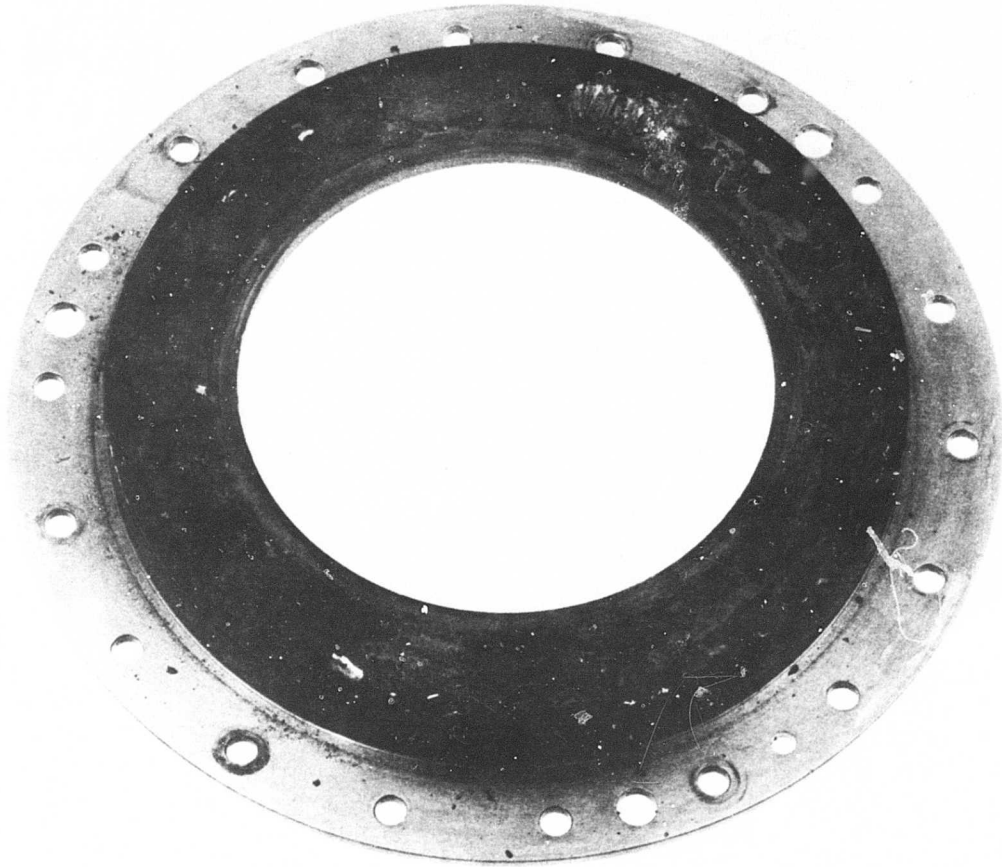
Figure 127.   Turbine Build 4 Brake Backplate.
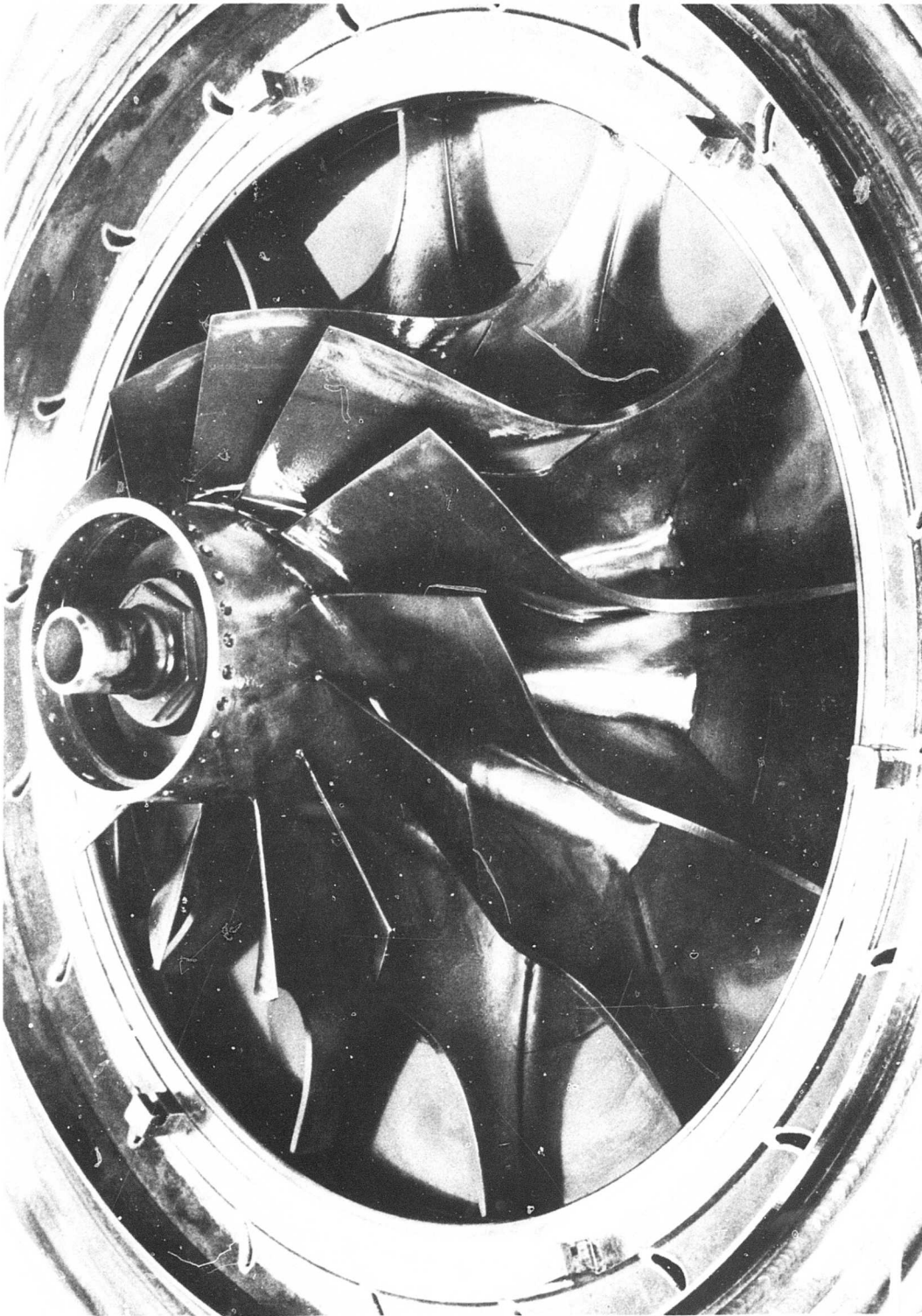
Figure 128. Turbine Build 4 Turbine Section.
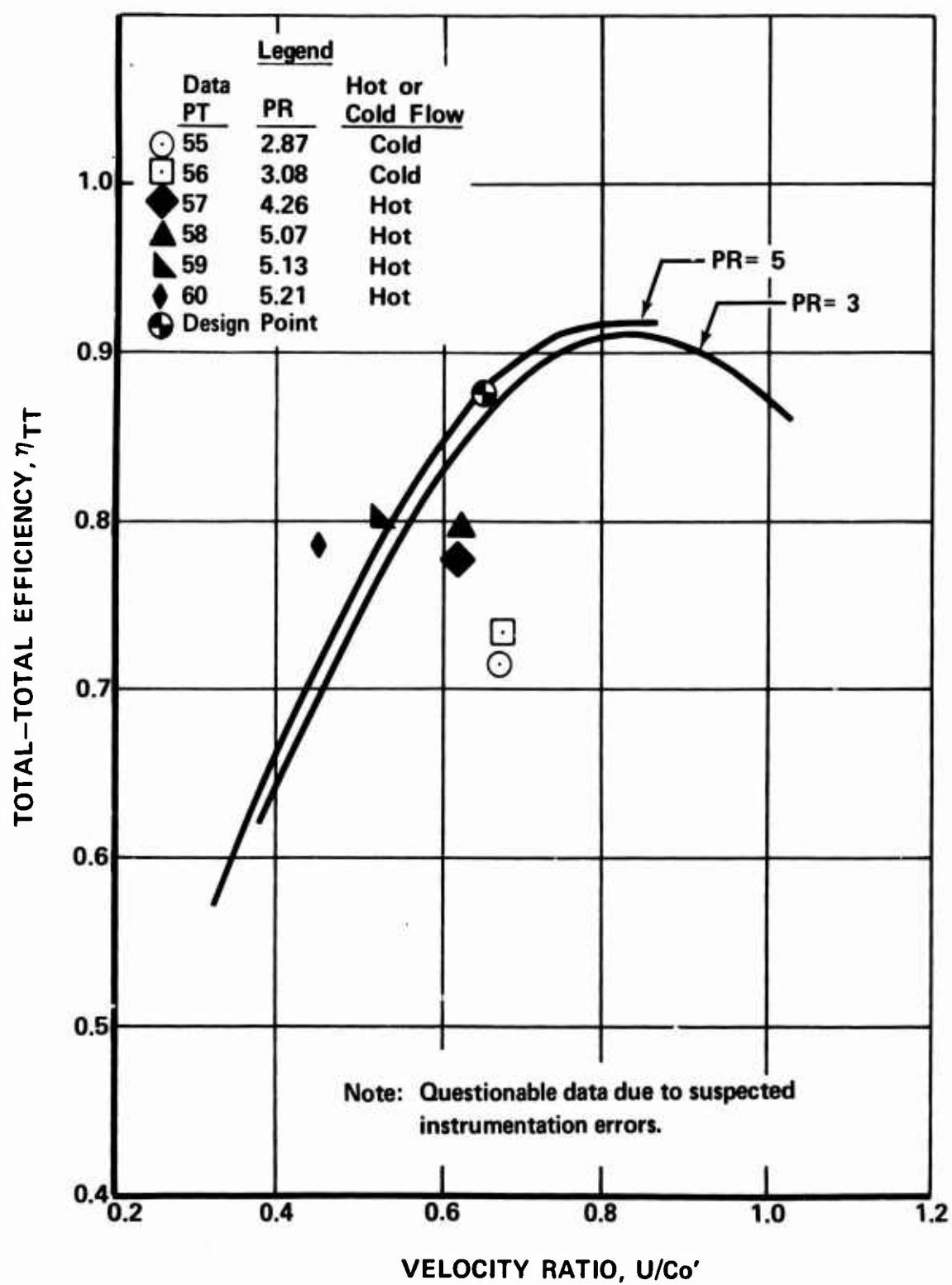
Figure 129. Turbine Build 4 Performance.
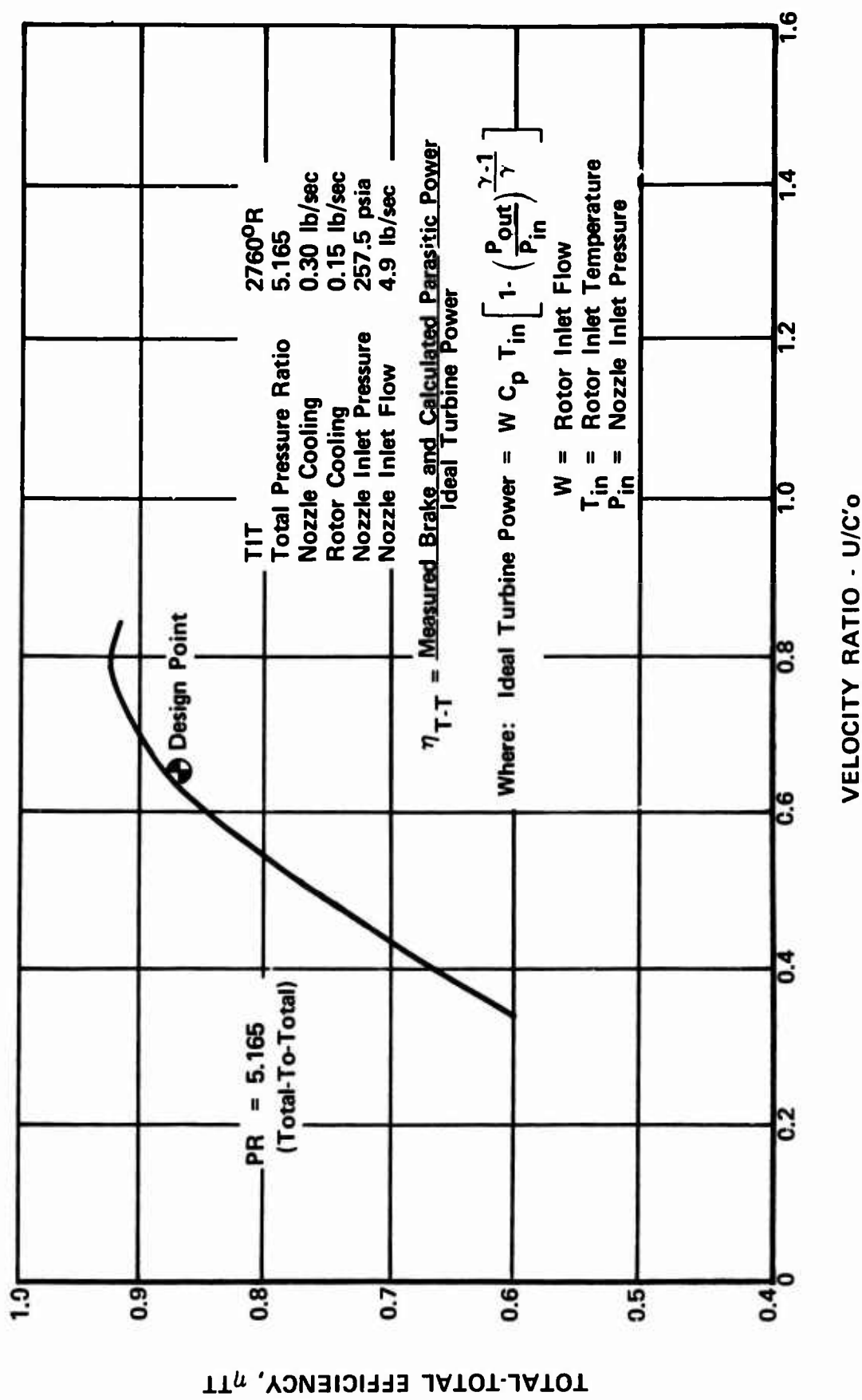
Figure 130. Most Probable Performance at Design Pressure Ratio (Based on Rig Test Data).

APPENDIX I
VANE INSERT BRAZE PROCEDURE

The braze specification used to braze the vane inserts into the vane casting was as follows:

1. Nickel plate braze areas of inserts per AMS 2403 to 0.0055- to 0.0065-in. thickness.

2. Nickel plate braze areas of nozzle casting per AMS 2403 to 0.0010- to 0.0015-in. thickness.

3. Position inserts into nozzle housing. Maximum allowable interference is 0.0005 in. Use Hastelloy shims to achieve a tight fit where clearance exists.

4. Apply braze material (Coast Metals No. 50 paste) to form nominal 0.060-in. fillets at braze joints. Brazing must be accomplished within 8 hr of paste application.

5. Braze in hydrogen atmosphere at 2100°F ± 25°F for 10 min.

6. Open furnace door and allow part to cool to 1700°F. Remove from furnace and air cool to 300°F or lower while maintaining hydrogen atmosphere. Remove from retort.

APPENDIX II
BALANCE AND SPIN PROCEDURES

Balance Procedures

Three different balances were made on the radial turbine rig rotating parts. Each balance was a dynamic balance to 0.001 oz-in. The first of these was the detail balance of each of the rotating parts. The detail balance of the turbine rotor was made with a spin arbor and spindle mounted to the rotor to insure the correct balance for subsequent proof testing in a spin pit. The turbine rotor was balanced by removing material from the raised portion of the rear face and on the ID of the hub at the exhaust end.

The last two balances were made on the rig rotating package during the assembly of the rig for test. The first of these two balances was made with only the rotating parts installed on the bearing housing. Figure 131 shows this assembly mounted on the balance machine. The assembly was balanced by adding weights to the rear face of the brake impeller flange and to the turbine rotor mounting flange on the shaft. After the initial assembly balance, the rotating package was removed from the bearing housing so that the nozzle assembly, turbine and compressor back-plates, and support structure could be mounted on the bearing housing. The rotating package was again installed in the bearing housing, and the final balance of the rotating package was completed (Figure 132). This final balance was achieved by adding weights to the rear face of the brake impeller flange and to the exhaust end of the turbine rotor (hub inside diameter).

Spin Procedure

After the detail balance of the rotor, it was mounted in the spin pit. The spin pit was evacuated to approximately 0.2-mm Hg prior to spin testing to reduce windage friction. Two proximity probes mounted at 90 deg to each other around the rotor hub (monitored on an oscilloscope) gave an indication of the stability of the rotating part. The spin test apparatus included an automatic overspeed abort system. In addition, testing could be aborted manually. The rotor was driven by a small air-driven turbine, and the speed was controlled by regulating the turbine air supply.
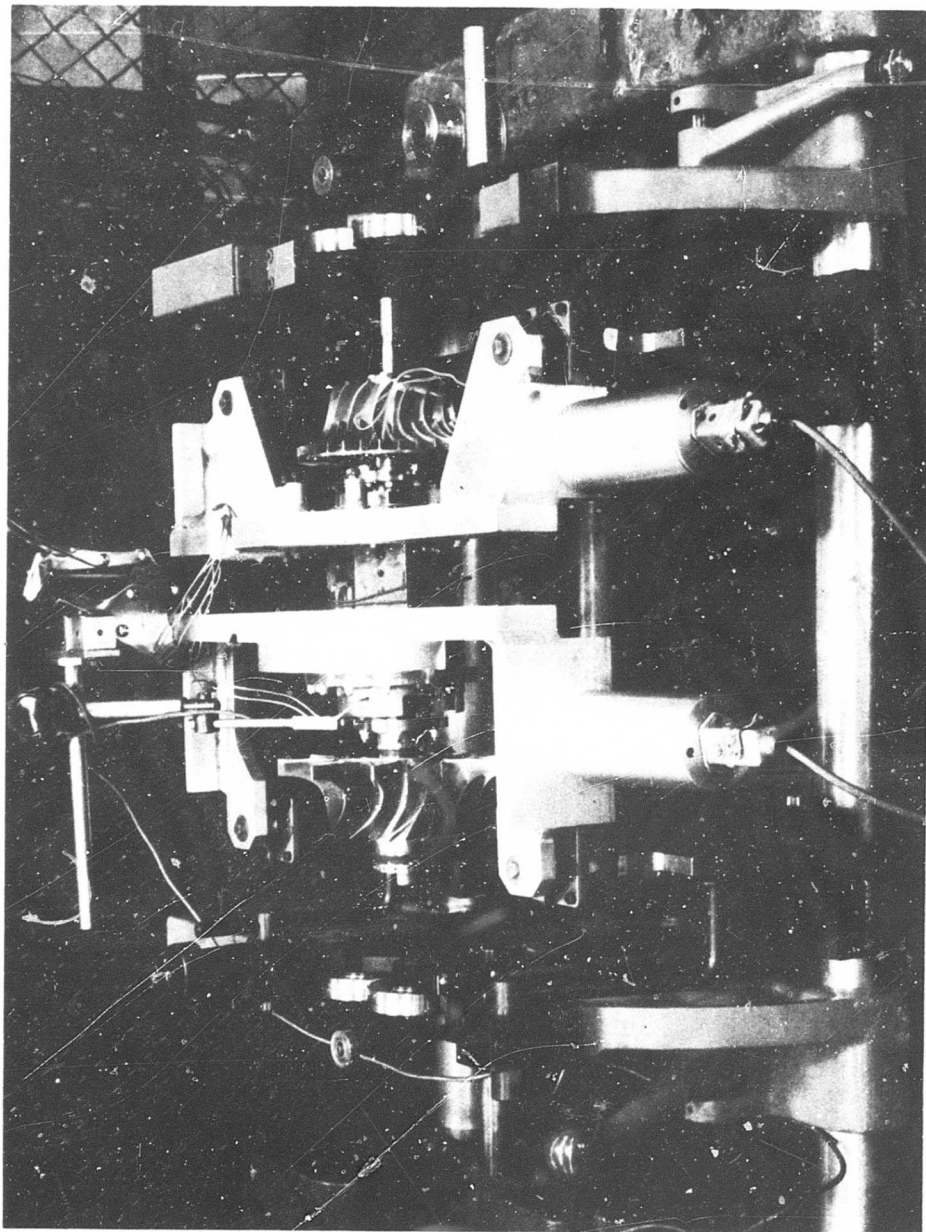
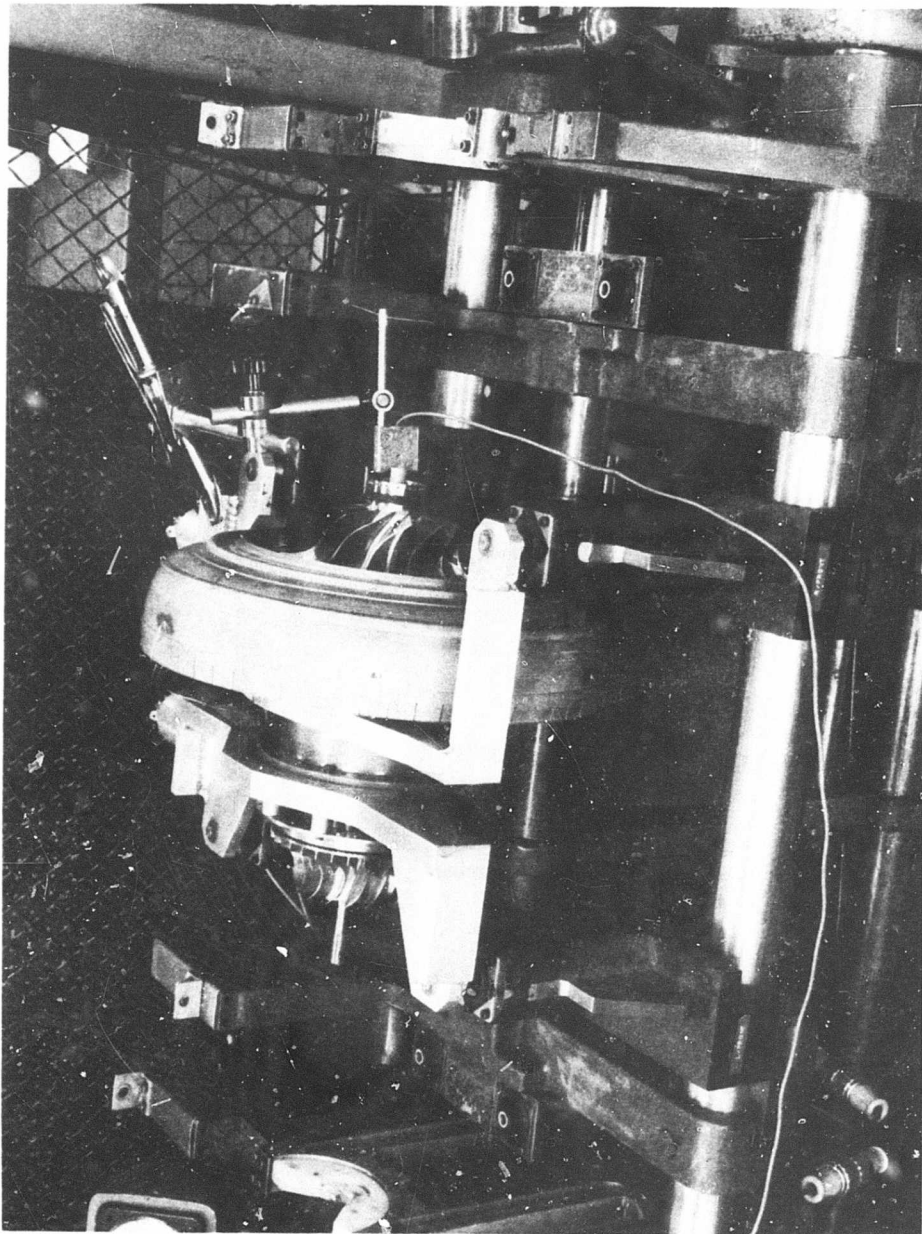Figure 131.   Initial Assembly Balance.
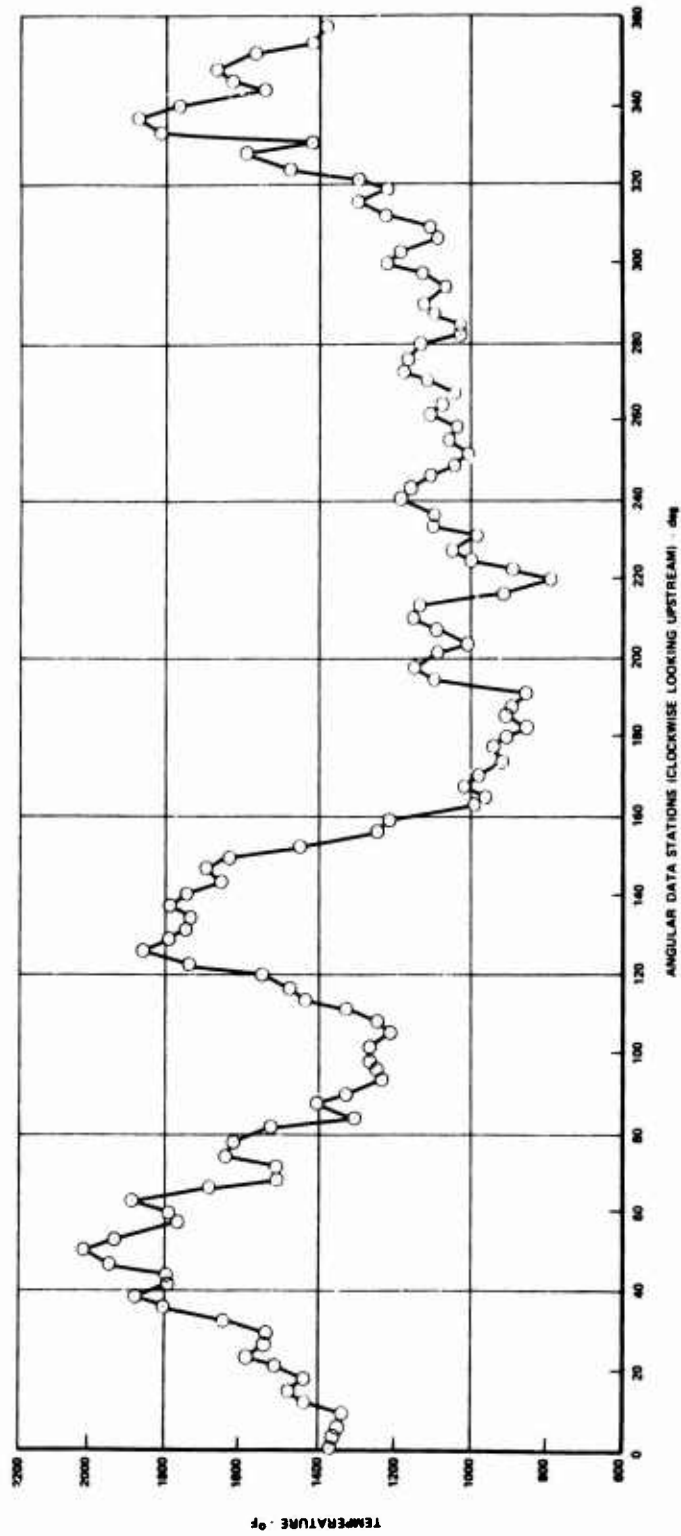
189

Figure 132. Final Assembly Balance.

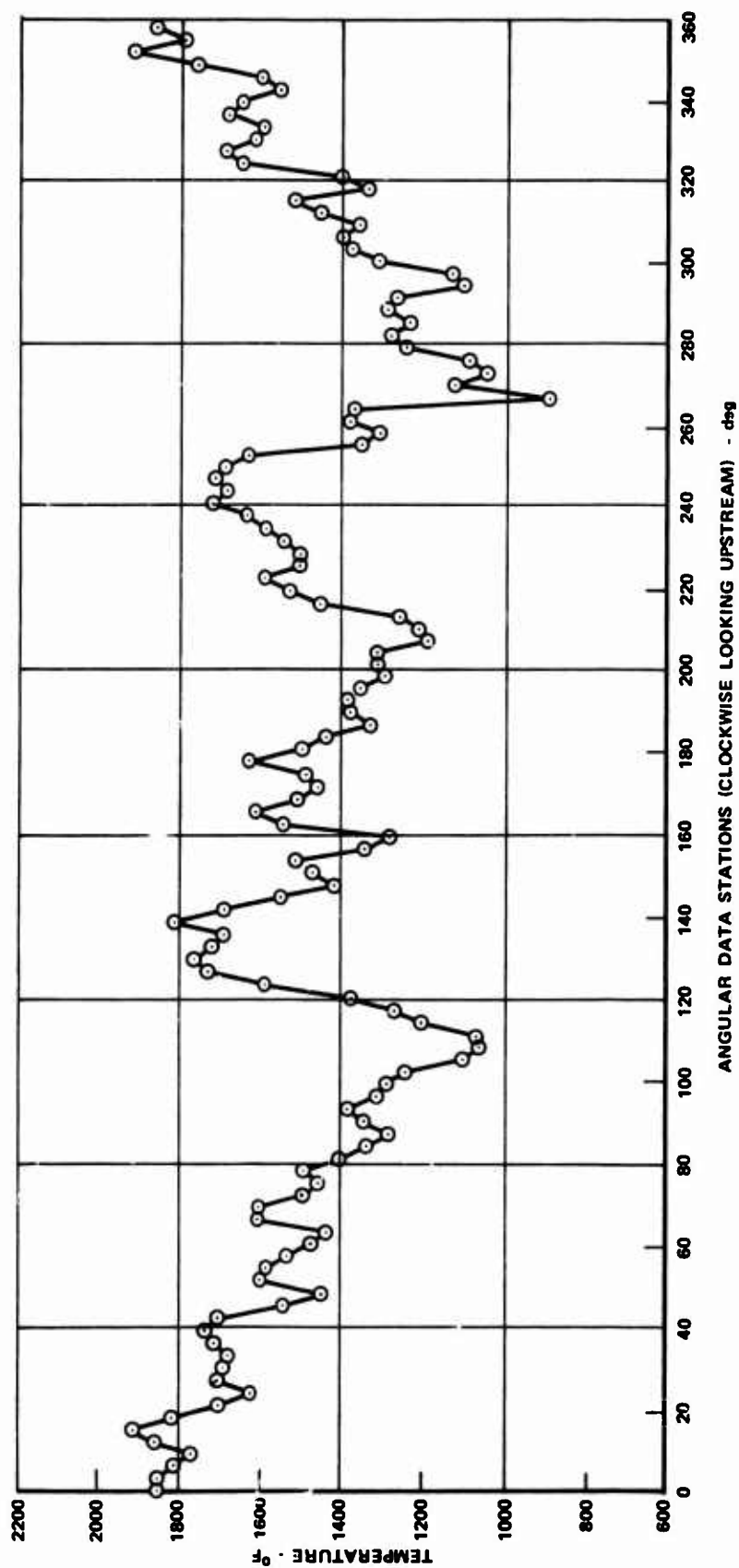Figure 133.   Burner Test 1-1 Temperature Profile.

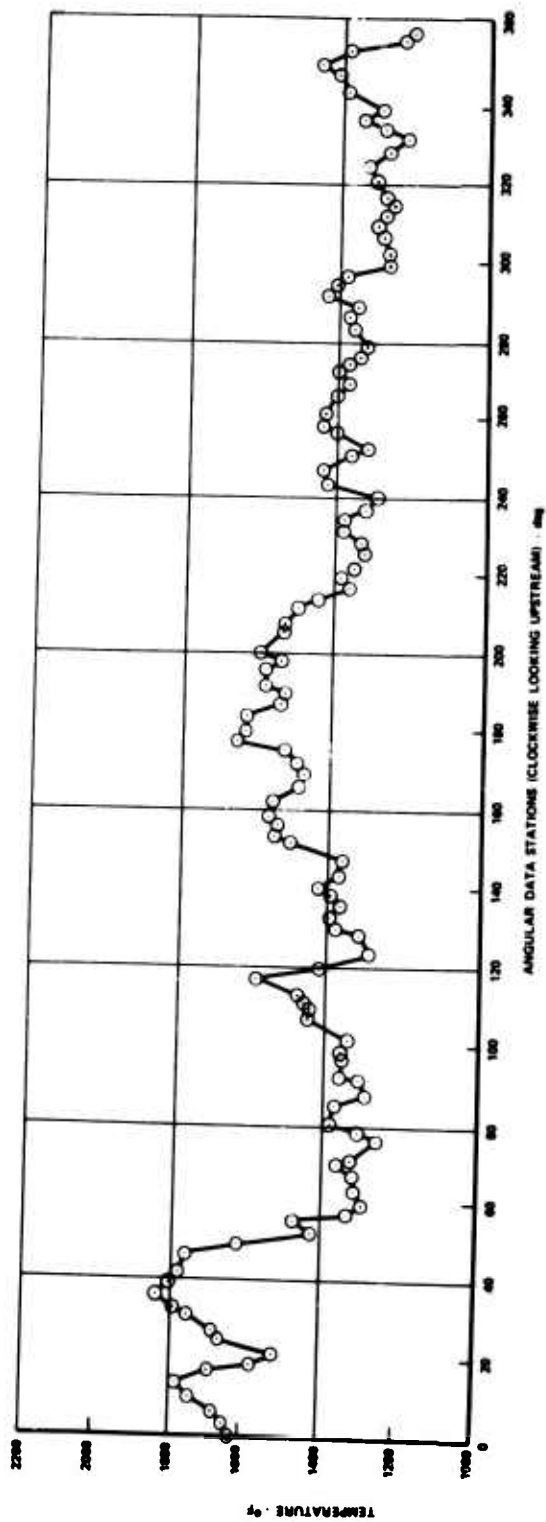Figure 134. Burner Test 2-1 Temperature Profile.
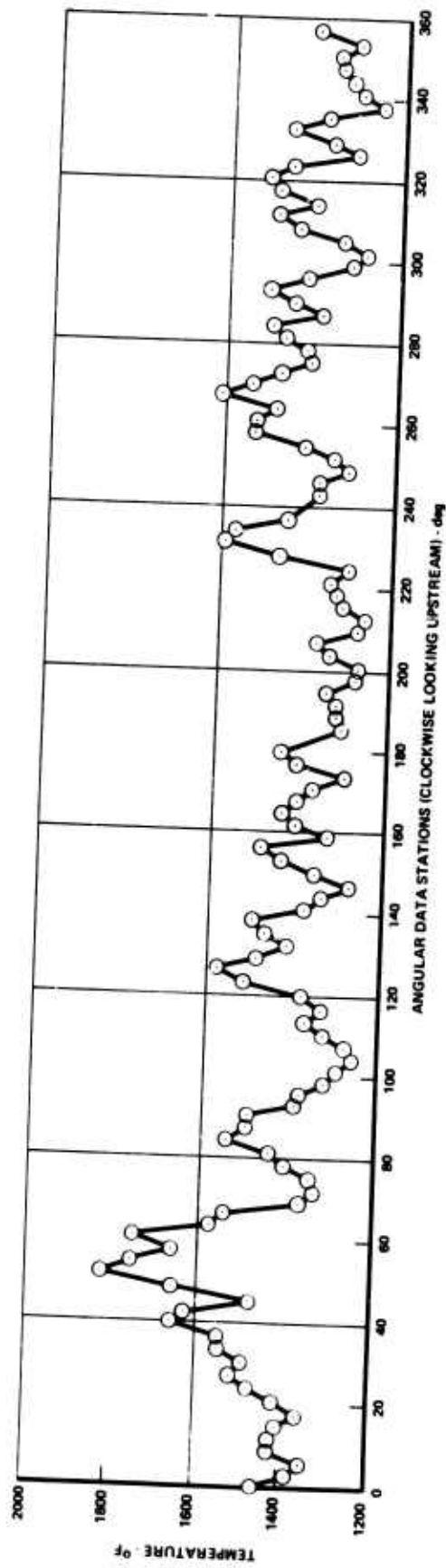
Figure 135. Burner Test 3-1 Temperature Profile.

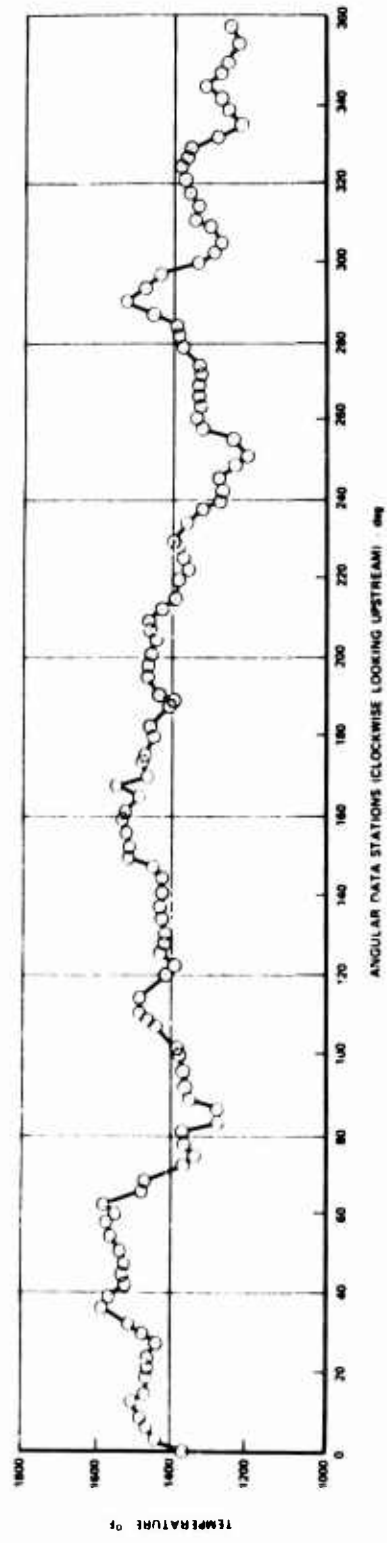Figure 136. Burner Test 4-1 Temperature Profile.

194

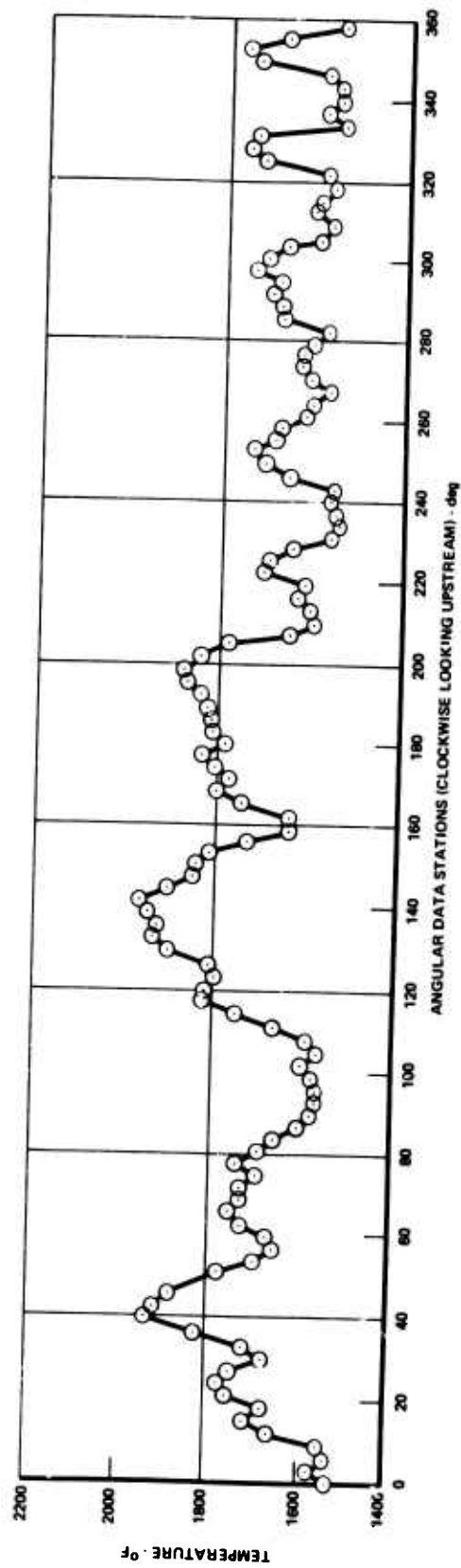Figure 137.   Burner Test 5-1 Temperature Profile.
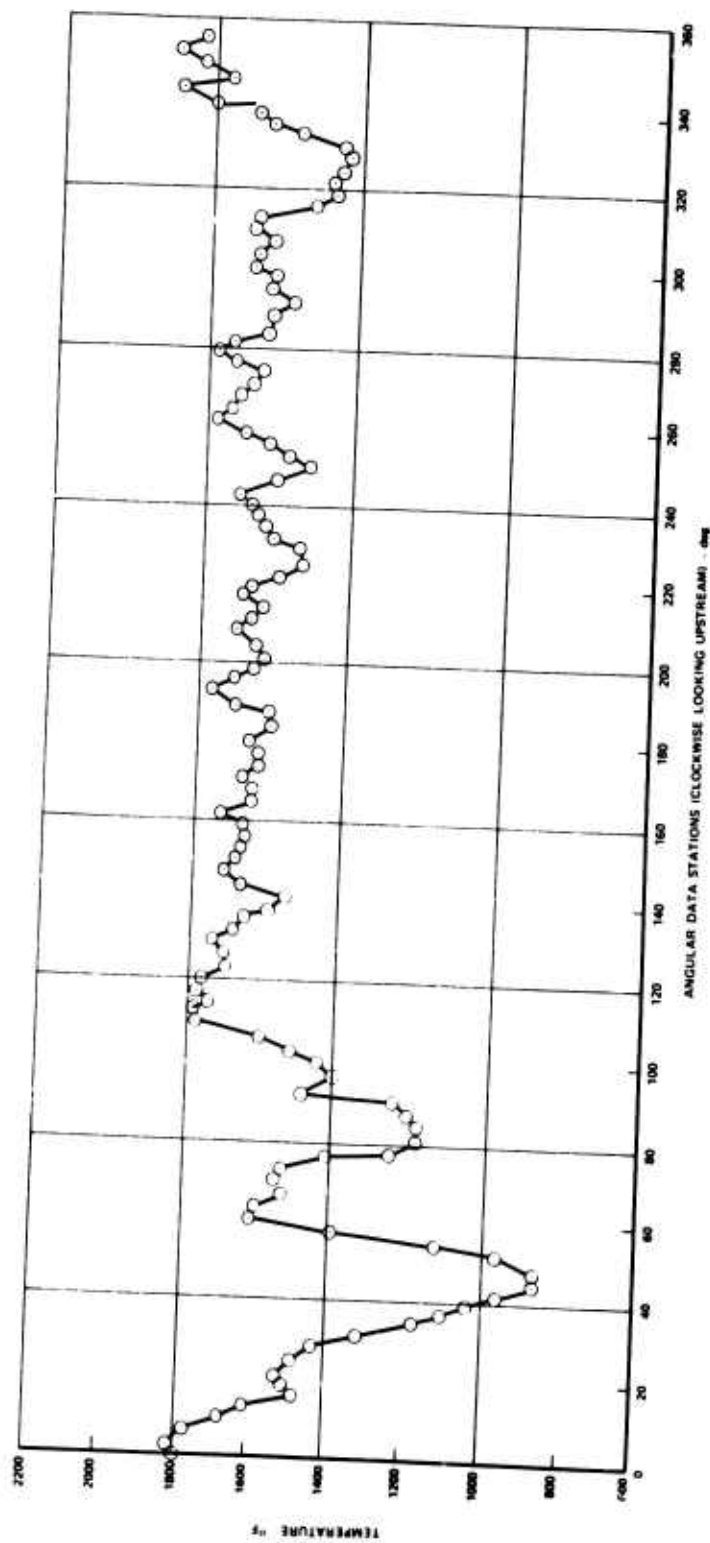
Figure 138. Burner Test 7-1 Temperature Profile.

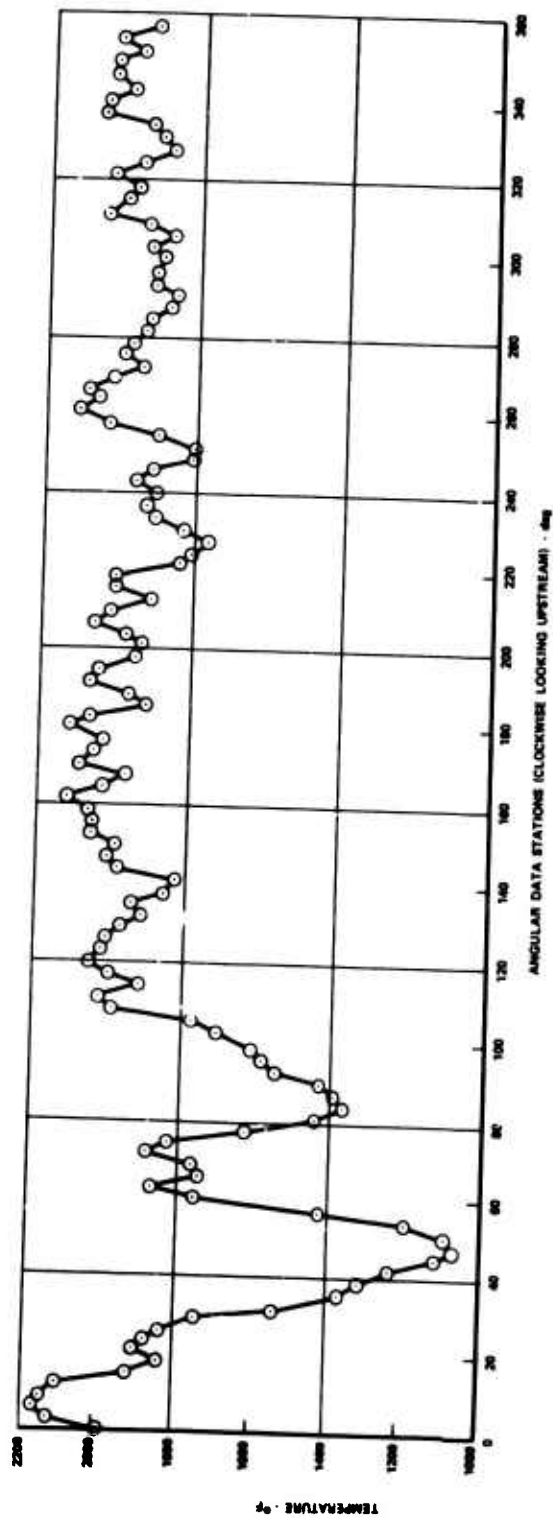Figure 139. Burner Test 8-1 Temperature Profile.

197

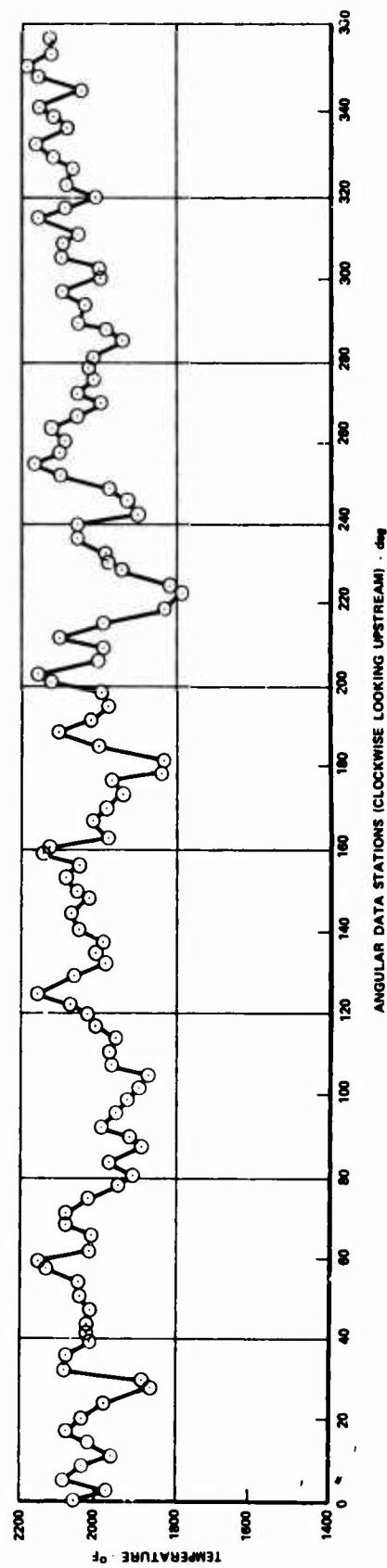Figure 140. Burner Test 8-2 Temperature Profile.
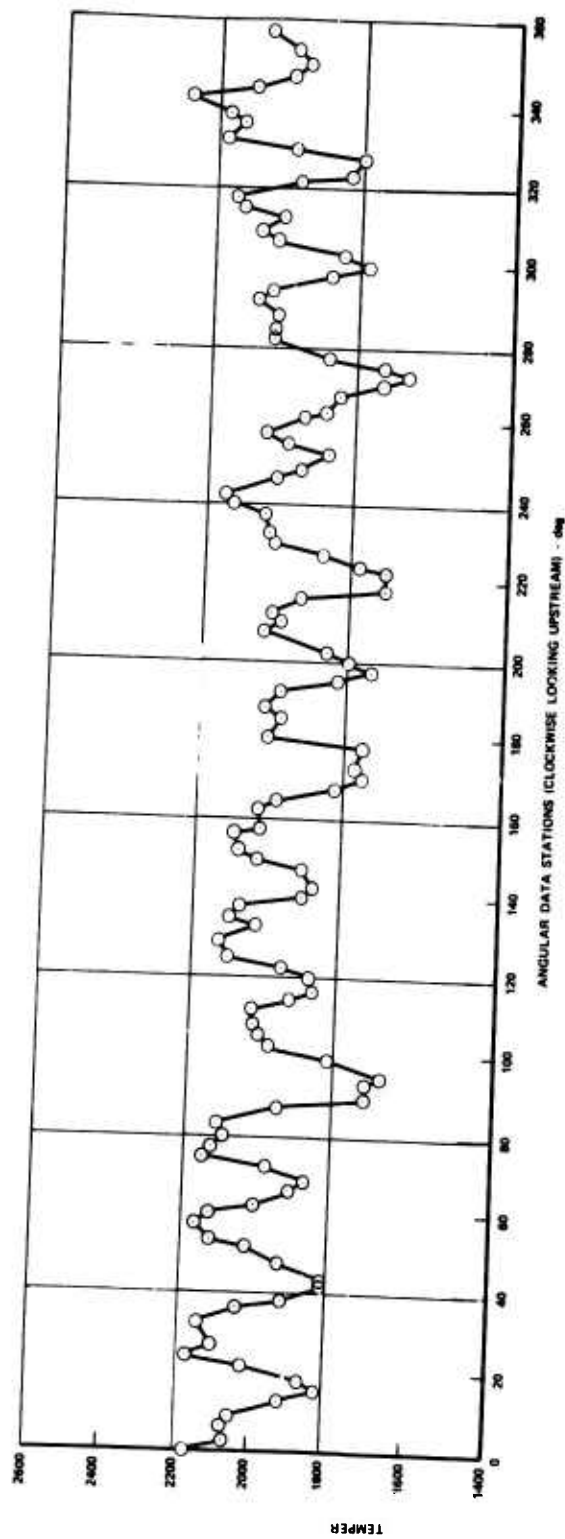
Figure 141. Burner Test 9-1 Temperature Profile.
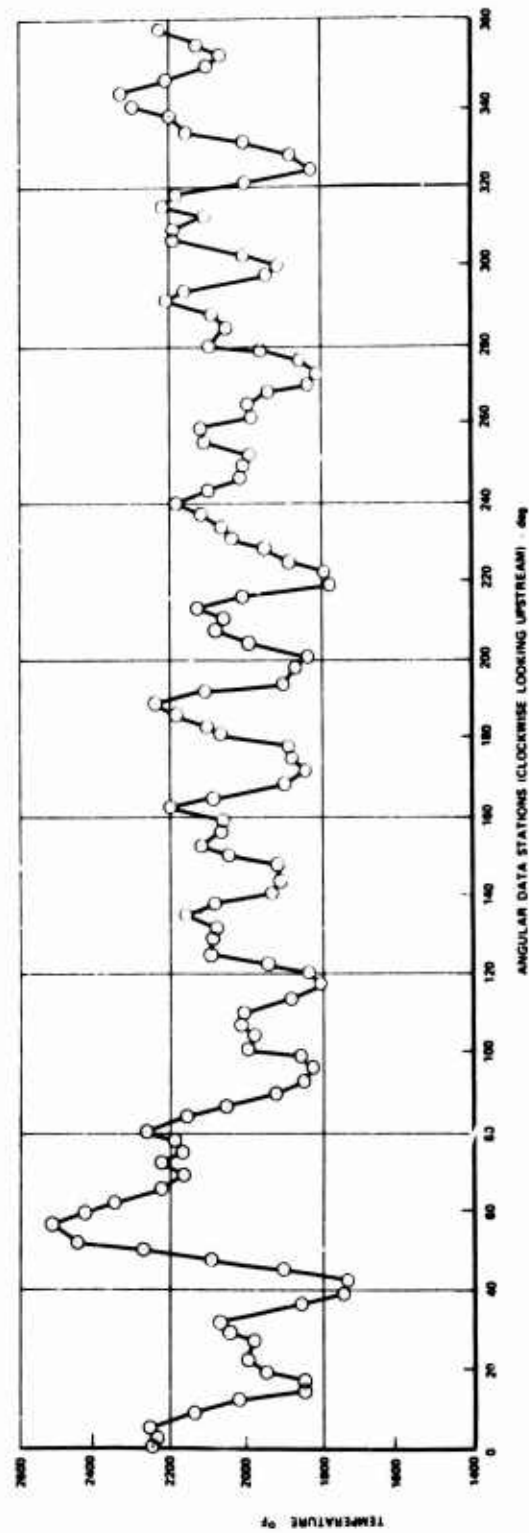
Figure 142. Burner Test 10-1 Temperature Profile.

Figure 143. Burner Test 10-2 Temperature Profile.

APPENDIX IV
UNCERTAINTY ANALYSIS

Using data point No. 54 as a typical hot test condition, the performance calculations were analyzed to determine the uncertainty in the calculated efficiency due to bias and precision errors in the measured parameters. The measurement uncertainty estimates for the efficiency are as follows:

Bias	-0.010 ± 2.937
Precision (1 Standard Deviation)	0.800
Uncertainty	-0.010 ± 4.537

Uncertainty is defined as the maximum possible error that we would reasonably expect to observe.

DISCUSSION OF CALCULATIONS

A measure of the rate of change of efficiency with respect to each variable used in calculating efficiency was needed to obtain an estimate of the precision error and bias associated with efficiency. The existing data reduction computer deck was utilized to calculate the effect of the precision error (S_i) and the bias error (B_i) of each input variable (X_i) on efficiency.

The program was run first at nominal conditions. Then, each X_i was changed by one standard deviation unit (S_i) to obtain estimates of the partial of efficiency with respect to each input variable times the precision error, or

$$\frac{\partial \eta}{\partial X_i} S_i$$

This was repeated twice, once increasing the input by one standard deviation, and once decreasing the input by one standard deviation. The average effect due to the input precision error was calculated to obtain the estimate of effect of the precision of each input variable on efficiency.

Similarly, the partials of efficiency with respect to each input variable times the bias were calculated. Since the bias limits were not always symmetric about zero, it was necessary to have estimates for both the upper limit on bias (B_i^+) and the lower limit on bias (B_i^-), or

$$\text{maximum bias limit effect} = \frac{\partial \eta}{\partial X_i} B_i^+$$

and

$$\text{minimum bias limit effect} = \frac{\partial \eta}{\partial X_i} B_i^-$$

202

Values of $\partial\eta/\partial X_i \ S_i$, $\partial\eta/\partial X_i \ B_i^+$ and $\partial\eta/\partial X_i \ B_i^-$ were calculated for each input variable X_i. Estimates of the precision, bias and uncertainty of efficiency were calculated based on these values.

The calculation of the measurement variance of efficiency S^2, is found by summing the squares of the partial derivative of efficiency with respect to each input variable X_i times the standard deviation, S_i.

$$S^2 = \sum_{i=1}^{n} \left[\frac{\partial\eta}{\partial X_i} S_i \right]^2 = 0.6404$$

or,

$$S = 0.800$$

When the bias limits are symmetric about zero, the recommended practice is to root sum square the individual biases to get the overall bias. For this problem, however, several of the biases were not symmetric about zero. To handle this problem, the average effect of bias was found for each input parameter as:

$$\overline{\frac{\partial\eta}{\partial X_i} B_i} = 1/2 \left[\frac{\partial\eta}{\partial X_i} B_i^+ + \frac{\partial\eta}{\partial X_i} B_i^- \right]$$

The range of the bias was defined as the total of the average bias effects plus and minus the root sum square of the differences between the effect of the maximum bias and the average bias; i.e.,

$$B_\eta = \sum_{i=1}^{n} \overline{\frac{\partial\eta}{\partial X_i} B_i} \pm \left[\sum_{i=1}^{n} \left(\frac{\partial\eta}{\partial X_i} B_i^+ - \overline{\frac{\partial\eta}{\partial X_i} B_i} \right)^2 \right]^{1/2} = +0.010 \pm 2.937$$

Since the degrees of freedom are greater than 30, uncertainty was

$$U = +0.010 \pm \left| 2.937 + 2 (0.800) \right|$$

$$= +0.010 \pm 4.537 \text{ efficiency points}$$

Table IX presents the input values used in the analysis and their effect on calculated efficiency.

TABLE IX. UNCERTAINTY ANALYSIS SUMMARY						
Input				Effect on Efficiency		
Parameter (X_i)	Units	Precision (1 S)	Bias	$\frac{\partial \eta}{\partial X_i} S_i$	$\frac{\partial \eta}{\partial X_i} B_i^+$	$\frac{\partial \eta}{\partial X_i} B_i^-$
W_c	lb/sec	±0.025	+0.070, −0.029	±0.620	+1.737	−0.719
W_t	lb/sec	±0.0193	±0.0386	±0.456	−0.915	+0.915
W_r	lb/sec	±0.000325	+0.0003, −0.0023	±0.013	+0.091	−0.091
TT2	°R	±0.38	+6.13, −7.13	±0.103	−1.666	+1.936
TT3	°R	±0.45	+4.63, −8.63	±0.105	+1.088	−2.043
PT4	psi	±0.105	±0.9	±0.063	−0.534	+0.548
P3A	psi	±0.125	±0.75	±0.002	+0.016	−0.016
P4A	psi	±0.0625	±0.375	0	0	0
PS5	psi	±0.040	±0.10	0	0	0
PT5	psi	±0.020	±0.10	±0.024	+0.120	−0.120
				±0.011	+0.058	−0.058
				±0.017	+0.089	−0.089
T_{exit}	°R	±0.47	±9.15	±0.025	−0.493	+0.493